Nanowire Quantum Dots as Single and Entangled Photon Sources

by

Milad Khoshnegar Shahrestani

A thesis
presented to the University of Waterloo
in fulfillment of the
thesis requirement for the degree of
Doctor of Philosophy
in
Electrical and Computer Engineering

Waterloo, Ontario, Canada, 2014

I hereby declare that I am the sole author of this thesis. This is a true copy of the thesis, including any required final revisions, as accepted by my examiners.

I understand that my thesis may be made electronically available to the public.

Milad Khoshnegar Shahrestani

Abstract

Realization of linear quantum computation and establishing secure quantum communication among interacting parties demand for triggered quantum sources delivering genuine single and entangled photons. However, the intrinsic energy level spectrum of nanostructures made by the nature or developed under a random growth process energetically lacks the expected figures of merit to produce such quantized states of photons.

Here, I present the semi-empirical modeling and experimental investigation on the spin fine structure of strongly confining quantum dots embedded in III-V nanowires. To this end, the quantum dot is numerically modeled via the Configuration Interaction method at two different levels: 1) single-particle level, where its pure energy level structure is resolved in the presence of strain and spin-orbit interaction. 2) Few-particle level, at which the few-body interactions appear as perturbative energy corrections and orbital correlations. I demonstrate the influence of quantum confinement on the binding energies and spin fine structure of excitons in the absence of hyperfine interaction. Importantly, the high-symmetry character of excitonic orbitals in nanowire quantum dots restore the degeneracy of optically-active ground-state excitons, offering an ideal spectrum for the entangled photon pair generation.

To experimentally verify the idea, we design and fabricate defect-free nanowire quantum dots with ultra-clean excitonic spectrum, and construct the time correlation function of emitted photons through performing a series of low-temperature statistical quantum optics measurements. We observe a decent performance in terms of single photon generation under low excitation powers. Moreover, photon pairs emitted from the biexciton-exciton cascade of nanowire quantum dots exhibit color indistinguishability and polarization entanglement owing to the trivial fine structure splitting of the ground-state excitons.

We further extend the idea by proposing the hybridized states of a nanowire-based quantum dot molecule as the potential source of higher-order entangled states. Tracing the field-dependent spectrum suggests the appearance of dominant features under the weak localization of electrons and coherent tunneling of holes. In addition to their Coulomb correlation, excitons also remain spatially correlated, opening new transition channels normally forbidden in the ground state of a single dot. The proposed structure can be exploited to create tripartite hybrid, GHZ and W-entangled states.

Acknowledgements

"Many hands make light work."

John Heywood

I sincerely thank my family who supports me unconditionally through each and every step of my life.

I would like to express my special appreciation to my PhD advisor, Prof. Amir H. Majedi for his consistent support and encouragement during the course of my PhD studies. His tenderness and decency provided me and my fellows a friendly environment to advance our research.

I am deeply indebted to my MSc advisor, Prof. Sina Khorasani who always inspired me to break through the walls of my own ignorance.

I thank Prof. Gregor Weihs who provided me the opportunity to do my experiments in his well-equipped quantum optics laboratory at Institute for Experimental Physics, Innsbruck, Austria. His gentleness and hospitality turned my work in Austria to a great life experience.

I sincerely thank Prof. Jonathan Baugh who brought my attention to the rich physics lying behind nanowires. He never refused to give me insightful advice and helpful consultations on my research.

I express my special acknowledgement to my committee members, Profs. Dayan Ban and Irene Goldthorpe for their helpful comments and suggestions on my PhD research. I deeply thank Prof. Zetian Mi who attended my defence session as the external examiner.

A significant part of the experimental results could never be obtained without the assistance of Tobias Huber and Dr. Ana Predojevic at Institute for Experimental Physics. I would like to thank them for both their worthwhile discussions and hospitality during my stay in Austria.

I specially thank Dr. Dan Dalacu and Dr. Philip J. Poole whose expertise in growing high quality nanowire quantum dots helped me realize my theoretical modelings and numerical simulations. I should also thank Dan for providing me with many SEM and TEM images and initial measurement results on different samples.

I would also like to acknowledge lots of beneficial consultations that Dr. Chris Haapamaki and Prof. Ray Lapierre at McMaster University gave me on InP nanowire growth. Chris has always been a great collaborator and a decent friend to me.

I acknowledge the partial financial support from Waterloo Institute for Nanotechnology, Institute for Quantum Computing, and University of Waterloo.

Many thanks to my colleagues and friends at Integrated Quantum Optoelectronic Lab, Dr. Hamid Reza Mohebbi, Dr. Mohsen Keshavarz Akhlaghi, Amir Jafari Salim, Amin Eftekharian, Haig Atikian and Erika Janitz for their collaborations, fruitful discussions and support.

Finally, thanks to all my close friends who persistently supported me to follow my desires and realize my goals. Our lives and our identities are made of our unforgettable memories. I do owe a great part of my life to those friends who have made my most memorable moments come true.

Dedication

To my father who taught me to see beyond the horizons of my fear

To my mother who taught me never to give up on reaching beyond those horizons

Table of Contents

List of Tables

List of Figures

Chapter 1

Introduction

A photon is a fundamental carrier of information. With various degrees of freedom including energy, polarization, phase, linear momentum, arrival time and entanglement, photons are capable of transporting different bits of information in optical channels. Indeed, a classical communication channel together with a pad encryption algorithm maintains an ideal level of secrecy. However, no classical channel is able to securely deliver the algorithm itself. In this context, the emergence of single photons has paved the way towards realizing secure communication under the fast developing Quantum Key Distribution (QKD) platform [1]. Single photon quantum bits (qubit) can be used for quantum cryptography, where the projective measurement of the photon qubit leads to the safe identification of communicating parties. Accordingly, on-demand quantum photonic sources have become fundamental ingredients of linear optics quantum computing and quantum communication systems primarily because it is straightforward to encode, manipulate and detect quantum bits on individual photons [2, 3]. Although the current technology based on attenuated laser pulses enables simple quantum key distribution, it is demonstrated that genuine single photons can improve the performance considerably [4]. Moreover, a photon as a flying qubit can link between two stationary qubits, such as electron spins, under an initialization, projection and detection process [5].

The current replacements for on demand sources of quantum light, count on weak laser fields and nonlinear phenomena in optical crystals. Although the attenuated coherent state of a laser fundamentally cannot prepare the temporal properties of a single photon stream [6], it is the most convenient substitute available in the absence of a real single photon source in quantum optics experiments, such as long distance quantum key distribution [7, 8] or single photon detector characterization [9]. Nonlinear crystals under optical pumping generate higher wavelength photon pairs, namely signal and idler, through parametric

downconversion (PDC) process [10]. This technique, aside from its relatively low level of efficiency, is being extensively employed for generating time-bin and polarization entangled photons [11, 12, 13, 14, 15]. The efficiency of generating photon pairs in the parametric downconversion process relies on the pumping level, but its random nature enhances the chance of producing double or multiple photon pairs per excitation pulse [16]. The presence of an upper limit of pumping power then restricts the conversion efficiency.

For the mentioned applications, a single photon source is expected to deterministically produce a single photon in response to an external optical or electrical triggering pulse. This means the system must undergo a relaxation period following an emission event. A quantum two level system inherently possesses such a property since it is unable to regenerate a photon immediately after emitting one: in a more simplified picture, an electron is excited to a higher energy level by an input energy pulse. It subsequently relaxes to a lower energy level by emitting a photon [17]. After relaxation, the two-level system is by definition no longer excited until the next input energy pulse arrives. The unique character of a single photon emitter is, or shall be, that it prohibits two or multiple photon generation events even under a very fast pulse excitation regime or continuous pumping. In practice, the effective relaxation time becomes dependent on the pumping intensity and as a result the probability of two-photon emission grows.

To obtain a better sense of the performance of a typical single photon source, its operation can be parameterized based on a few figures of merit. Although the variety of experiment conditions and immaturity of the devices still does not allow for providing independent numbers, the degree of improvement from device to device can be relatively compared through these parameters.

1.1 Performance parameters

Operating wavelength: Ideally, a quantum photon source should have a sharp linewidth tunable over a wide range of wavelength. The transmission of Silica fibers in telecommunication wavelengths are around 1330 and 1550 nm. However, quantum statistical measurements at this range would be challenging as the currently available InGaAs detectors operating at $\lambda > 1\mu m$ have inferior performance compared to their Si counterparts operating at $\lambda < 950$ nm.

Operating temperate: A quantum emitter should preferably operate at room temperature. However, the solid state nature of genuine single photon sources limits their optimal performance to cryogenic temperatures. This is primarily due to their very small dephasing times and broad linewidths at higher temperatures.

Time correlation function: The most important figure of merit for such a source is perhaps its time correlation function (see Sec. 2.5.1), which compares its quantum nature to a classical source of the same average intensity, but emitting photons randomly spaced in time. The time correlation function relies on the time spacing between individual photons in a stream. Photons are bunched in a classical light as they statistically tend to travel in ensembles [18], thus the time correlation function consistently exceeds 1. In an ideal single photon source, however, time correlation drops to zero.

Efficiency: According to M. Varnava et al.'s model, the lower limit of source efficiency η_s times detector efficiency η_d is 2/3 to perform efficient linear optical quantum computation [3]. Taking the limited efficiency of single photon detectors at telecommunication band into account, an efficient source is therefore of great interest. It is essentially impossible to specify a precise, yet general, definition for the single photon emitter efficiency because it involves excitation efficiency, quantum efficiency, extraction efficiency and collection efficiency, all of which are dependent on the other optical components in the system. A more relevant definition for the quantum efficiency is the portion of trigger pulses converted to single photons.

Indistinguishability: In order to be indistinguishable, two photons from a single emitter must have the same coherent wavepacket, wavelength and polarization. To this end, photons ought to have identical coherence time, T_2. The coherence time is determined by $1/T_2 = 1/2T_1 + 1/T^*$, where T_1 and T^* are the exciton lifetime and pure dephasing time, respectively. Dephasing, which is primarily related to the scattering and phonon-interaction processes, randomizes the coherence time. To achieve a fairly decent indistinguishability, the coherence of photons shall be lifetime-limited. However, the spectral diffusion and interactions with the bath keeps the pure dephasing time much shorter than the two-level-system lifetime in solid state structures. This leads to weak indistinguishability.

1.2 Different Quantum light sources

Although the scope of this thesis is based on semiconductor quantum dots (QD) as sources of single and entangled photons, we have chosen to concisely review a few types of existing quantum light emitters here. This gives us the insight to the advantages and drawbacks of QD-based emitters.

Attenuated beam of laser: Possibly the oldest and simplest method to approach to the quantum regime is to decrease the intensity of a coherent state. The Poissonian nature of coherent state, however, hinders crossing the boundary between classical light and quantum light, see Sec. 2.5.1. Moreover, the time distribution of successive single photons is random.

Highly attenuated laser beam is widely used in optical fiber-based single-photon sources in quantum cryptography.

Atoms, ions and molecules: Atoms and ion-traps have well-defined energy levels that can be exploited as clean two level systems. The advantage of an atomic system lies in the fact that all the atoms of a particular isotope are rather indistinguishable and their energy eigenstates are almost identical from sample to sample. Their lifetimes are relatively longer than solid state systems, thus their single photon generation rate is slow [19]. Relevant experiments cool and trap single atoms [20] or ions [21] in a high finesse cavity in order to guide single photons efficiently into a single optical mode. The spectral resonances are narrow and almost dephasing-free. Single photons from atom transitions exhibit a decent time correlation function $g^{(2)}(0) \simeq 0.02$ and long coherence time [22]. The operating wavelength is quite dependent on the type of emitter. The required setups at room temperature with laser cooling, however, are complex enough to make their integration with larger systems very challenging.

A solid state two level system pumped by energy pulses much shorter than its natural lifetime emits a single photon during each excitation cycle. First solid state single photon source was realized by Th. Basche and W. E. Moerner on a single molecule of pentacene in a p-terphenyl host [23]. Afterwards B. Lounis et al. extended the operation of a single molecule single photon source to room temperature [24]. Single photons can be extracted from the so called zero phonon line (ZPL) in the molecule spectrum, which basically connects the ground vibrational states of the ground and excited electronic states. The linewidth of this transition crucially relies on the temperature due to the coincidental fluctuations. Similar to most other solid state systems, the energy eigenstates of molecules are structure dependent and not reproducible. Additionally, the molecule florescence suffers from blinking because of its dark states [25]. The operating frequency of organic molecules lies in the visible band.

NV center in diamond: NV center consists of a substitutional nitrogen atom in the vicinity of a missing carbon atom (vacancy) in the diamond lattice. Single negatively charged nitrogen-vacancy NV^- color centres, which are essentially a neutral NV center NV^0 with a trapped electron, were detected for the first time in 1997 [26]. This prompted the demonstration of single photon generation form color centers in room temperature [27, 28]. The relatively long coherence time of NV-center spin states has introduced them as stable qubit systems convenient for quantum information processing [29]. The typical spectrum of a NV center comprises a ZPL at 637 nm along with a broad phonon side band 637-720 nm. Its wide spectral linewidth enhances the attenuation in the optical fibers. The lifetime of NV center is fixed in the order of ~ 10 ns in bulk diamond. The common method to isolate a single NV center and improve its time correlation function

via suppressing the background light of adjacent centers is etching [30]. The spectral characteristics of NV centers located near the etched edges deteriorate, however. Apart from the fact that implementing optical structures in diamond substrate is demanding, there have been significant advances in coupling NV centers into microcavities and optical waveguides during the past decade [31, 32]. NV^--NV^- spin coupling [33], spin-photon entanglement [34] and tripartite spin entanglement [35] are important demonstrations of NV center capabilities towards realizing scalable quantum networks.

Quantum dots: Nanoscale QDs grown with epitaxial methods show bright emission, good time correlation function ($g^{(2)}(0) < 0.05$), decent stability and lifetime-limited spectral linewidth at cryogenic temperature (5°-10° K), wide range of wavelength tunability (UV to infrared). Epitaxially grown QDs can be easily integrated with other optical components such as waveguides and microcavities to enhance their light emission efficiency. In the next section, we further detail the unique properties and potential drawbacks of single semiconductor QDs as quantum photon emitters. The fundamental concepts of their operation are explained in Chapter 2.

1.3 Quantum dots as quantum photon source

Quantum dots are often called artificial atoms as they localize charge carriers in quantized energy states. Because of the carrier-carrier Coulomb interactions, the quantized states are energetically anharmonic. Most of the devices utilized for quantum information application so far are based on epitaxially grown III-V self-assembled QDs. In 2000, Michler et al. demonstrated that discrete excitonic levels of a single self-assembled QD are able to emit single photons under a pulsed laser excitation ($\sim$ 250 fs) [36]. Although the current techniques mostly rely on single photon emission from the QD neutral exciton, other types of exciton complexes, including biexciton and charged excitons, also generate at most one photon per excitation pulse and could be exploited for single photon emission [37]. In quantum optics experiments, single dots are often pumped non-resonantly or quasi-resonantly [37, 38]. The timing issue to obtain single photons from each excitonic transition is then simple: if the radiative lifetime of an exciton is longer than the recombination time of free electrons and holes in the barrier (or higher shells), then at most one photon emission event is expected from the corresponding transition per excitation cycle. The radiative lifetimes of different excitonic transitions could range from 100 ps to a few ns, giving additional versatility to tailor the repetition rate of the source. The phonon-mediated decay process of carriers from higher shells to the desired state introduces a time jitter and broadens the linewidth, lowering the photon indistinguishability.

The photon indistinguishability of a single photon emitter is measured via two-photon interference experiments described in 2.5.1. The measure of indistinguishability is determined by the so called interference dip: the deeper the dip, the better the indistinguishability. This depth is a function of T_2 and $2T_1$ explained above in Sec. 1.1. If $T_2 \simeq 2T_1$, the dephasing processes are negligible and interference dip of 100% occurs. So far interference dips of 69%, 66% and 75% have been reported by Santori et al. [39], Bennett et al. [40] and Varoutsis et al. [41]. One solution to further improve the indistinguishability is resonant excitation as recently done by Y. He et al [42].

The first realization of an electrically-driven QD single photon source was reported by Z. Yuan et al in 2002. [43]. They used a GaAs p-i-n diode with a layer of low density InAs self-assembled QDs grown inside the intrinsic region. The p-i-n structure was modified afterwards by the same group via embedding the InAs layer inside a cavity defined by a high-reflectivity bottom distributed brag reflector (DBR) [44]. Lack of a clean spectrum in electrically-driven dots as compared to their photoluminescence spectrum, impairs the indistinguishability of photons in p-i-n diodes. However, R. Patel et al. raised the degree of indistinguishability to 64% by temporal filtering those photons which had undergone dephasing [45]. The time correlation function is normally poor under electrical pumping. In addition, the effective exciton lifetime could be manipulated in a p-i-n device, where the escape rate of electrons and holes is electric field-dependent [46].

QD size together with its material decide the operating wavelength. InAs with $E_g = 0.354$ eV looks promising to reach into the telecommunication band. That is the reason the most common quantum optics experiments employ single InAs QDs on GaAs [47]. They are normally grown in the Stranski-Krastanov mode by either molecular beam epitaxy (MBE) or metalorganic chemical vapour deposition (MOCVD). In addition, enlarging the QD size allows for longer wavelengths but weaker oscillator strength. First single photon diode operating at 1.3 μm was fabricated of InAs dots by Ward et al. with $g^{(2)}(0) \simeq 0.19$ [48]. In the visible range, a clear signature of antibunched photons has been observed in spatially isolated InP/InGaP [49], InP/AlGaInP [50], GaN/AlGaN [51], and CdSe/ZnS [52] QDs.

In order to tailor the spontaneous emission rate and enhance the light extraction efficiency the QDs are integrated with either micropillar [39, 53], microdisk [54] or photonic crystal cavities [55]. The general idea is to modify the Purcell factor [56] and increase the density of optical modes the QD dipole could then couple to. The Purcell factor is inversely proportional to the mode volume, thus a higher emission rate and light extraction efficiency demands for smaller cavities with larger quality factors. The optimal coupling into the cavity modes crucially depends on the position of dipole and whether it is in proximity to the nodes or antinodes of the electric field. One important issue in the ear-

liest stages of developing QD-microcavity single photon emitters was the random position of bright self-assembled QDs. Recent advancements in growing site-controlled QDs has greatly overcome this issue [57, 58].

A unique feature of semiconductor QDs lies in their exciton X and biexciton XX energy level structure, see Secs. 2.2.1 and 2.2.2: a single quantum dot in its ground state can host up to two bright excitons and form a biexciton. Upon a cascade recombination, biexciton decays to either of these exciton states and then into the ground state, emitting two photons. Benson et al. for the first time proposed this sequential decay as a source of polarization-entangled photons [59]. Realization of entangled photons had been previously demonstrated in atomic cascades [60] and nonlinear crystals [11, 13]. In the proposal by Benson et al., the polarization character of photons were entangled, meaning that the other degrees of freedom, including energy, had to be indistinguishable. This condition is rare to find in self-assembled QDs since the intermediate exciton states possess different energies [61]. The limited number of experiments reported on generating entangled photon pairs from QDs relied mostly on the post-processing of photons or external perturbations to remove this energy difference. A list of these experiments can be found in Sec. 2.5.2. However, none of these experiments has presented QD structures naturally emitting entangled photon pairs.

1.4 Scope of thesis: Nanowire quantum dots

In the present work, I study the physics of nanowire-embedded quantum dots and their ability to generate quantum states of light. NWQDs offer some unique features in addition to those already explored in self-assembled QDs. The versatility in the axial and radial growth of III-V nanowires [62] allows for manipulating both their electronic and optical properties. As revealed in the following chapters, the excitonic energy states of nanowire quantum dots (NWQD) can be deterministically modified by controlling the growth parameters since the QD formation is not primarily ruled by strain forces. Their symmetry properties promise their superior performance as an entangled photon source. Additionally, single QDs can be easily stacked up in a nanowire [63, 62], offering mixed states with unprecedented design flexibility. The carriers are efficiently captured by the QD segment under an electrical injection, as compared to the single photon diodes based on self-assembled QDs, because the carrier channel is aligned with QD in the semi-1D geometry of nanowire. Accordingly, the control of few-particle electronic states is principally simpler in nanowires as evidenced by the single carrier transport in InP nanowires [64], or local gating of the InAs nanowires [65]. On the other hand, the radial size of III-V nanowires is controllable by optimizing the growth temperature [66]. Adequately thick nanowires support optical modes, improve the

photon collection efficiency and enhance the QD spontaneous emission rate. Of fundamental challenges in nanowires are noticeable chance of surface recombination under electrical pumping and the difficulty of achieving electrical injection as compared to planar quantum dot structures.

The NWQDs investigated here are axially symmetric with a circular cross section (our study on hexanognal NWQDs could be found in Ref. [67]). Analogous to the self-assembled QDs, material and size determine the operating wavelength. A strained InAs segment with a direct energy band gap of 0.345 eV ($\sim$ 3.6 micron) embedded inside a GaAs ($E_g = 1.424$ eV) or InP ($E_g = 1.344$ eV) matrix is able to provide a wide range of frequencies in the near infrared band. The materials of choice here are zinc-blende In(Ga)As/GaAs and In(As)P/InP in theoretical modelings and wurtzite In(As)P/InP in experiments. In principle, the mesoscopic properties of NWQDs we deal with in this work do not represent a substantial difference in zinc-blende and wurtzite structures, unless perhaps in some numerical values. Therefore, at least the qualitative conclusions we draw from theoretical models (zinc-blende structure) hold for the wurtzite NWQDs as well. The QD dimensions are set to obtain a predominant axial quantization, which gives a better control over the electron and hole orbitals, excitonic binding energies and spin relaxation times. Schematic of a typical core-shell NWQD is illustrated in Fig. 1.1(a). Presence of a passivating shell surrounding the QD segment is necessary to preserve the lateral confinement and QD brightness, see Sec. 3.4.2.

Ideally, once the nanowire is optically excited, either by a continuous wave laser or a pulsed laser, the photogenerated electron-hole pairs form in the nanowire continuum states and instantaneously (compared to the average exciton lifetime, $T_1 = 1$-2 ns, we have observed in our devices) decay into the QD energy levels under a phonon-mediated process. Sequential decays eventually initiate the excitons in the QD ground state followed by a photon emission event after T_1. Early experiments on nanowire quantum dots indicate a strong spectral diffusion with exciton linewidth in the order of 1 meV [68, 69], which signifies long pure dephasing times and time jitters. This considerable spectral diffusion is partially attributed to the existence of stacking faults (i.e. zinc-blende sections inside wurtzite phase) in their nanowire structure [70]. The defect-free nanowires used in the present study facilitate achieving clean QD emission with nominal linewidth < 50 μeV.

At low excitation powers (namely 10 nW delivered to 1 μm^2) only the exciton line is observable in NWQD spectrum since the chance of ground state re-excitation during the exciton lifetime is low. We expect to observe a dip in the time correlation function of photons collected exclusively from this line, stating that single photons are regulated in time. By increasing the excitation power (up to 100 nW per 1 μm^2), the biexciton line appears and its intensity gradually grows with the pumping intensity through the

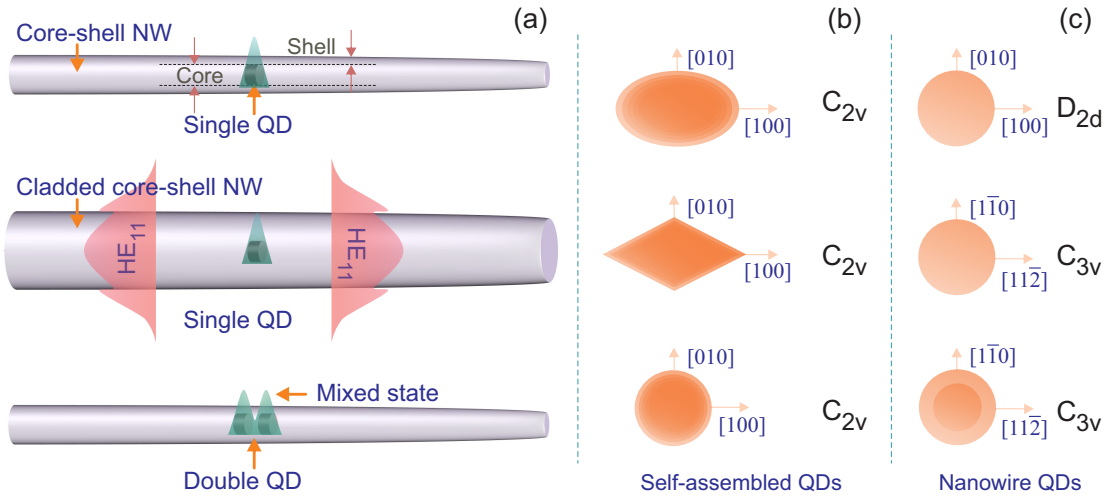

Figure 1.1: (a) Top: Schematic of a core-shell single NWQD with predominant axial confinement. Middle: If the shell is adequately thick with respect to the QD emission wavelength, the fundamental HE_{11} mode can form and efficiently couple to the QD dipole. Bottom: Stacked NWQDs hosting hybrid wavefunctions. (b) Top to bottom: elongated lens shaped, pyramidal and lens-shaped self-organized QDs on (001) substrate. (c) Top to bottom: Cylindrical QD in [001] nanowire, cylindrical and cone-shaped QDs in [111] nanowire.

two-photon absorption process. Due to the binding energy of biexciton with respect to exciton, the biexciton resonance often appears at a different wavelength. To distinguish the biexciton resonance either its nonlinear behaviour versus pumping power or its time correlation with the exciton resonance can be assessed, as explained in Chapter 6. The order of binding energy is tunable by QD dimensions, but its exact value can dynamically be controlled only via Stark effect. The biexciton-exciton binding energy plays an important role in color-matching conditions for generating entangled photons.

Perhaps the key feature of selecting NWQDs in this work is their symmetry properties. Self-assembled QDs grown on (001) substrates mostly show structural anisotropy due to the different surface mobilities along [110] and [1$\bar{1}$0] orientations [71], see Figure 1.1(b) where the lens-shaped and pyramidal QDs are schematically depicted from the top view. The in-plane symmetry of QD geometry is twofold, hence the electron and hole wavefunctions possess C_{2v} symmetry. Even if the QD is circularly symmetric on (001) plane, the strain-induced fields and piezoelectricity, caused by its vertical anisotropy, reduce the net symmetry of wavefunctions to C_{2v} [72]. This low symmetry gives rise to anisotropic ex-

change interaction and splits the twofold degenerate exciton states [73], impeding entangled photon pair generation from the XX-X cascade. In a [001]-oriented nanowire, however, the QD segment does not suffer from axial anisotropy due to its cylindrical symmetry. Even though the global symmetry is eventually reduced to D_{2d} in the presence of strain-induced potentials, exciton states still remain degenerate. A similar situation applies to QDs embedded in [111]-oriented nanowires and the wavefunctions are C_{3v}-symmetric, see Chapter 3. In this case, even axial anisotropy cannot break the C_{3v} symmetry.

Along with many other remarkable features not addressed here, the above advantages of NWQDs have recently drawn the attention of quantum information scientists. Nanowires are able to channel both carriers and optical modes simultaneously and be integrated with other optical and electronic components in an on-chip platform of quantum information processing.

1.5 Goals and objectives

The objective of this thesis is threefold. First, I provide a detailed analysis on the electronic properties of NWQDs based on their structural parameters. To this end, I developed an extensive package of numerical simulation tools based on finite element. It enabled me to model the core-shell NWQDs at two different levels:

a) single particle level, where the pure states of NWQD are numerically calculated based on the modified $\mathbf{k}\cdot\mathbf{p}$ model. The advantage of this modeling, as it will be uncovered afterwards, is a transparent translation between the input parameters and output variables such as single particle energy levels, single particle orbitals, and in a general viewpoint, the underlying band structure. The model incorporates almost all the relevant effects including strain-induced potentials, piezoelectricity, band mixing, spin-orbit interaction, electric field Stark effect and magnetic field Zeeman effect.

b) The model then evolves to an advanced level where the mutual interactions are introduced into the picture. In order to deal with many-body interactions I implemented an all-inclusive geometry-independent configuration interaction (CI) model. The CI model comprises multi-million spatial integrations to take care of orbital deformations in a few-particle system, thus the numerical simulations are demanding technically and computationally. The outcomes, however, deliver deep insight into the practical details of NWQD spectrum. In particular, they bring a clear sense of Coulomb interactions, exchange interactions, correlations and their contribution into the NWQD resonances.

The net result of above calculations altogether enabled me to derive original conclusions on

1) how different components of confinement interplay and lead to high symmetry character of carrier orbitals in various NWQD structures,

2) quantify the influence of spin-orbit interaction and strain-induced potentials on carrier localizations,

3) predict the trend of excitonic binding energies and fine structure splittings under NWQD size variations and external perturbations.

In simple words, proceeding into the next step, i.e. experimental realization, was not feasible without an evaluated design. Most of the design inputs are tailored towards optimizing the NWQD performance as an entangled photon source.

Second, we propose the quantum dot molecule (QDM) as a potential source of higher order entangled states. No doubt that producing higher orders of quantum correlated states [74] is a mandatory requirement in constructing a quantum network. Higher order entangled states have not been realized, nor proposed, in QD structures because establishing strong quantum correlation between the excitons while maintaining the color matching conditions is challenging and urges careful design and fabrication. This is tremendously difficult in self-organized QDs as their formation process is not quite deterministic. We demonstrate that building up such a correlation in nanowire QDMs is achievable by manipulating the electron localization and letting the hole undergo coherent tunneling. Moreover, the calculations show that the interdot spacing is able to change the nature of bound states, adjust the exciton-exciton spatial correlation, and their Coulomb correlation.

Third, we inspect the operation of NWQDs in quantum regime. Bare nanowires exhibit poor optical quality in terms of polarization sensitivity and light extraction efficiency. We address the former issue by exciting the NWQDs axially where the nanowire exhibits similar emission characteristics irrespective of the polarization state we choose. To resolve the latter problem, we clad the core-shell nanowires to obtain a cylindrical waveguide supporting optical modes in the desired wavelength range (900-970 nm), see Figure 1.1(a). The NWQDs we studied show a perfect performance as single photon sources verified by their time correlation function. We observed a very clear signature of XX-X cascade emission by performing cross-correlation measurements under both continuous wave and pulsed excitation. We also measure small fine structure splitting in the NWQD spectrum, by average FSS < 8 μeV, which is a significant improvement compared to the conventional self-organized QDs presenting, by average FSS $\simeq 100$ μeV. This promises for achieving photon pair entangled states from the XX-X cascade without necessity of further post-processings.

This thesis is organized as follows. In Chapter 2, the fundamental concepts and principles of quantum confinement in QDs are explained. Effect of many-body interactions and

their correction to the single particle levels are described. Then it is concisely addressed how directional electric and magnetic field perturb the excitonic states of QD. Finally, the definition of single photon regime is clarified and different schemes of entangled photon generation in QDs are introduced.

In Chapter 3, we study the NWQD single particle states by elucidating on electron and hole dispersion in the presence of various components of total confinement. The method of calculation, symmetry character, energy level structure, and band mixing effects will be detailed. In Chapter 4, the multiexcitonic energy states of NWQDs are explored. We utilize the single particle band structure developed in 3 to construct the wavefunction of multiexcitons. We introduce the orbital-dependent kinetic energy and demonstrate how it compromises with the net confinement to deform the single particle orbitals and minimize the total energy of bound particles. Finally, the effect of exchange interactions on spin relaxation times is scrutinized.

In Chapter 5, we model the QDM structure and analyse the electron and hole localizations against the size of single QDs and the interdot spacing. We show that the weak quantization of electron maintains the correlation between the excitons forming in the ground and first excited state of QDM. By applying electric field, hole tunneling is facilitated and favourable spectral features are brought into resonance. The small detunings between desirable transitions are then controlled via a magnetic field to establish the color matching conditions.

In Chapter 6, the results of our quantum optics experiments on fabricated NWQDS are presented. We elucidate on engineering the nanowire structure to enhance the light collection efficiency. The experimental setup for implementing the micro-PL spectroscopy, autocorrelation, cross-correlation and time resolved PL measurements is introduced. We observe a true manifestation of single photon emission and XX-X cascade emission. As predicted by our numerical modeling, the exciton fine structure splitting is trivial in [111]-oriented NWQDs, offering them as efficient sources of entangled photons.

Chapter 2

Fundamental concepts and overview

In this chapter, the basic physics and fundamental characteristics of quantum dots will be discussed to provide a ground knowledge about the phenomena studied in the rest of this thesis. Most of the physics are borrowed from the literature on self-assembled QDs. However, the way we modify and apply the concepts into NWQDs will be further detailed in the following chapters. Here, in Sec. 2.1, a basic perspective of the quantum confinement in 0D nanostructures is given. In Sec. 2.2, many-particle interactions are concisely described. Different types of few-particle states are introduced and the effect of many-particle interactions on their energy states and other measurable properties, such as oscillator strength (Sec. 2.3), is explained. In Sec. 2.4, we address how an external electric or magnetic fields can perturb a typical QD. Finally, Sec. 2.5 clarifies the concepts of single and entangled photon emission in QDs.

2.1 Quantum confinement in QDs

A semiconductor QD is a 3D potential box in nano scales able to trap electrons and holes in discrete energy levels. In heterostructure QDs, the energy difference between the QD material and the surrounding barrier develops this 3D potential box. Depending on the relative dimensions of QD, it can provide different levels of carrier localization along a particular plane and its normal axis. In our particular case, the QD is embedded inside a nanowire and the localization is stronger along the nanowire axis. An opposite situation is depicted in Figure 2.1(a) where the QD diameter is smaller than its axial thickness. In the absence of the strain induced potentials [75], the height of the confining potentials for electrons (holes) is given by the band edge energy difference at QD-barrier interface,

i.e. E^0_{CB} (E^0_{VB}). In the next chapter it is shown that strain significantly perturbs the confinement energy.

In order to calculate the energy levels and wavefunctions of QDs, we utilize 8×8 $\mathbf{k} \cdot \mathbf{p}$ hamiltonian that incorporates the important effects such as band mixing, spin-orbit interaction and strain [76, 77]. The solution to this hamiltonian describes the QD peoperties at the "single-particle" level where the many-body interactions are neglected. The current method provides a fairly accurate band structure of the QD compared to the more demanding method of atomistic million-atom calculations [78]. The suitability of $\mathbf{k} \cdot \mathbf{p}$ method for modeling the strongly confining QDs decreases with decreasing their size due to the inherent theoretical approximations [76]. The primary limitations are resulted from: a) the validity of the $\mathbf{k} \cdot \mathbf{p}$ model being restricted to the Γ point, b) small number of basis functions employed for expansion of orbitals, c) assumption of identical basis functions throughout the heterostructure, and d) limited ability to consider the lattice symmetry. The advantage of $\mathbf{k} \cdot \mathbf{p}$ scheme, however, lies in the fast and transparent way it links the electronic structure of QDs to their morphological parameters at a reasonable computational expense.

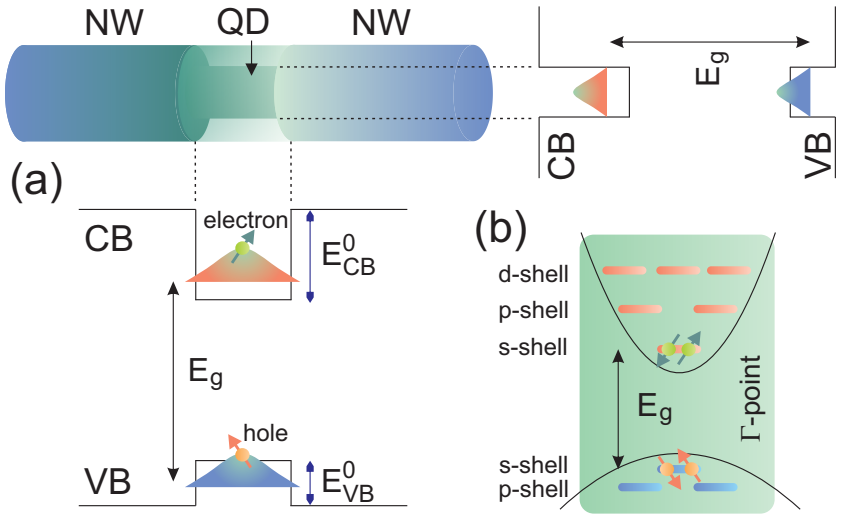

Figure 2.1: (a) Schematic of a QD embedded in a core-shell nanowire and the corresponding energy band diagrams. The QD maintains axial and lateral confinements. Owing the QD symmetry, the electron (hole) wavefunction can be approximated by the multiplication of its axial and lateral envelope functions. (b) QD discrete energy levels denoted by the shell representation.

In $\mathbf{k} \cdot \mathbf{p}$ model for zinc-blende and wurtzite materials, the wavefunction of a particle is described as the multiplication of its Bloch function and envelope function. The Bloch func-

tions that also incorporate the spin state of the particle are classified as $|S = 1/2, S_z = \pm 1/2\rangle$ for electrons, and $|J = 3/2, J_z = \pm 3/2\rangle$ (heavy hole, HH), $|J = 3/2, J_z = \pm 1/2\rangle$ (light hole, LH) and $|J = 1/2, J_z = \pm 1/2\rangle$ (spin-orbit split off, SO) for holes. HH, LH and SO states are achieved by applying a unitary transformation on the p-type atomic orbitals X, Y and Z [79]. This categorization is valid in proximity to the Γ point of the bulk band structure and is a direct consequence of axial confinement in NWQDs. Here J represents the total angular momentum, which is the summation of Bloch angular momentum L_{Bloch} and spin S. The Bloch angular momentum of electrons (holes) in proximity to the Γ point is $L = 0$ ($L_{\text{Bloch}} = 1$). The lateral confinement gives rise to the extra sub-levels known as QD shells. The total angular momentum then should be revised according to the orbital (envelope function) angular momentum of these sub-levels $J = L_{\text{Bloch}} + L_{\text{orbital}} + S$. For example, if $L_{\text{orbital}} = 0$, the energy level is referred to as the s-shell and if $L_{\text{orbital}} = 1$, it is called p-shell. A schematic preview of the QD shell structure is illustrated in Figure 2.1(b). Our numerical calculations in the following chapter shows that the QD shell structure is primarily dependent on the axial confinement, mostly because of the fact that the QD dimension along the axis is smaller than its diameter in our studies and experiments.

The emergence of strain forces in heterostructure QDs directly influences the wavefunction (orbital) of the particles and its magnitude is adequately large not to be treated as a small perturbation. For example, a hole localized in the s-shell of QD possess a dominant HH character since the s-shell is energetically closer to the top of the valence band structure where the HH band of the original bulk material exists. In a strained structure, however, the LH band is shifted accordingly and the hole wavefunction can obtain a non-trivial LH character.

2.2 Effect of many-body interactions

A serious challenge in the modeling of 0D systems comes from the fact that the energy level structure of a QD depends on the population of its levels with charge carriers. Single-particle energy level structure applies strictly to empty QDs only and is valid for the first charge carrier occupying the dot. Immediately after entering the second or more charge carriers in the QD, three major effects must be taken into account: a) direct Coulomb interactions, b) exchange interactions, and c) correlation energies [80]. The balance between the weight of these effects varies depending on the type of many-body state, i.e. the number of confined particles and their charges, and on the QD confinement: in the strong confinement regime where particles are presumed to be weakly correlated, the many-body effect acts as a perturbation to the total confinement. As we will show in the following

chapters, the direct Coulomb interaction dominates the two other effects in the total energy of few-particle states. Within the many-body picture, a given initial single particle state deforms its orbital in order to minimize the total energy of the resulted many-body complex. Indeed, depending on the energy level of the many-body state the contribution from some certain single-particle states would be significant. This is especially correct in the case of weakly correlated bound states within a relatively strong confinement. The deformation of the single particle state is then expanded on a series of namely excited states. The many-body state is then an expansion of various configurations constructed from an initial "ground" state and the corresponding excited states.

The simplest many-body complex, exciton X, consists of an electron and a hole, and the length of its electric dipole is measured by its Bohr radius a_X. Unlike a bulk material, where a_X is only dependent on the electron and hole effective masses, QD confinement renormalizes the size of exciton. In general, the exciton X wavefunction in multilevel system can be written based on the available single-particle bound states as

$$\psi_X = \sum_{a,b} \eta_{ab}[\psi_a^e(\mathbf{r}_1)\psi_b^h(\mathbf{r}_2) - \psi_b^h(\mathbf{r}_1)\psi_a^e(\mathbf{r}_2)] \tag{2.1}$$

where $\psi_a^e(\mathbf{r})$ ($\psi_a^h(\mathbf{r})$) stands for the electron (hole) wavefunction, and a (b) sweeps over available energy levels/bound states. The expansion coefficients η_{ab} for all the exciton states are calculated via diagonalizing the following hamiltonian (Rayleigh-Ritz procedure):

$$\mathcal{H}_X = \mathcal{H}_{\mathrm{CB}} - \mathcal{H}_{\mathrm{VB}} - \frac{e^2}{4\pi\varepsilon_0\varepsilon_r|\mathbf{r}_e - \mathbf{r}_h|} \tag{2.2}$$

where H_{CB} and H_{VB} are $\mathbf{k}\cdot\mathbf{p}$ hamiltonian of electrons and holes, and the dielectric constant $\varepsilon = \varepsilon_0\varepsilon_r$ is assumed to be position-independent. η_{ab} coefficients for the nth exciton state is given by $\mathcal{H}_X\left(\eta_{ab}\right)_n = \xi_{X,n}\left(\eta_{ab}\right)_n$, where $\xi_{X,n}$ denotes the nth exciton energy. The matrix elements of $\mathcal{H}_X$ then reads as

$$\mathcal{H}_X^{abjk} = \left(E_a^e - E_b^h\right)\delta_{aj}\delta_{bk} - \frac{e^2}{4\pi\varepsilon_0\varepsilon_r}\left\langle\psi_a^e\psi_b^h\right|\frac{1}{|\mathbf{r}_e - \mathbf{r}_h|}\left|\psi_j^e\psi_k^h\right\rangle \tag{2.3}$$

with E_a^e and E_b^h being the single particle energies associated with ψ_a^e and ψ_b^h. Calculating sixfold integrals in above equation demands huge computational expense especially when the size of basis set is increased. An efficient scheme to resolve above integral is to first calculate the mean-field potential caused by either of single particles and then find the Coulomb interaction by calculating the energy of the second particle inside this potential. The procedure is further detailed in Chapter 4. Both direct and exchange Coulomb interactions can be estimated by proper indexing of wavefunctions in Eq. 2.3.

2.2.1 Exciton fine structure

Accounting only for the QD s-shell (ground state), four possible exciton configurations can form: $\{\downarrow_e\Uparrow_h, \uparrow_e\Downarrow_h, \uparrow_e\Uparrow_h, \downarrow_e\Downarrow_h\}$. The two first configurations are called bright excitons as they can couple into light after recombination because their total angular momenta are ± 1. The other two configurations are optically dark (± 2). In the QD "excitonic" energy level structure, these four configurations split due to the exchange interactions. The energy spectrum of QD ground state excitons is depicted in Figure 2.2(a): The exciton binding energy corresponds to the electron-hole mutual direct interaction J^s_{eh}. The measure of bright-dark Δ_{bd} and dark-dark Δ_{dd} energy splittings are independent of the QD symmetry properties. The degeneracy of bright excitons, $X^s_{B_1}$ and $X^s_{B_2}$, relies on the orbital symmetries. The short range exchange interaction is described as $\mathcal{H}_{\text{exc}} = \sum_{i=x,y,z}(\alpha J_{h,i} \cdot S_{e,i} + \beta_i J^3_{h,i} \cdot S_{e,i})$, where J_h and S_e are the total angular momentum and spin operator of hole and electron, respectively [81]. Expanding the exchange interaction hamiltonian on the ground state exciton basis set $\{\downarrow_e\Uparrow_h, \uparrow_e\Downarrow_h, \uparrow_e\Uparrow_h, \downarrow_e\Downarrow_h\}$, we obtain

$$\mathcal{H}_{\text{exc}} = \frac{1}{2}\begin{pmatrix} \Delta_{bd} & \delta_s & 0 & 0 \\ \delta_s & \Delta_{bd} & 0 & 0 \\ 0 & 0 & -\Delta_{bd} & \Delta_{dd} \\ 0 & 0 & \Delta_{dd} & -\Delta_{bd} \end{pmatrix}, \tag{2.4}$$

where $\Delta_{bd} = 3/2(\alpha_z + 9/4\beta_z)$, $\Delta_{bb} = 3/4(\beta_x + \beta_y)$ and $\delta_s = 3/4(\beta_x - \beta_y)$. The contribution from the large range exchange interaction can be easily added to δ_s according to Ref. [61]. We calculate the α_i and β_i coefficients through the configuration interaction method described in Chapter 4. Normally, the largest energy scale belongs to Δ_{bd} and the fine structure spectrum resembles Figure 2.2(a). δ_s is a function of in-plane (perpendicular to the main quantization axis) symmetry and vanishes once $\beta_x = \beta_y$. The magnitude of "anisotropic" long range exchange interaction likewise relies on the QD symmetry. As it is demonstrated in the next chapter, QD axial symmetry can manipulate the in-plane symmetry of electron and hole orbitals and give rise to nonzero fine structure splitting (FSS) of bright excitons. Notice that although the HH-LH band mixing violates the validity of strict selection rules, labelling exciton doublets as bright and dark states is often acceptable as long as the LH character of s-shell holes is trivial.

2.2.2 Trion (X^- and X^+) and biexciton (XX)

Trion or charged exciton forms once the QD ground state is occupied with three single particles: negative (positive) trion consists of two electron (hole) and a single hole (electron).

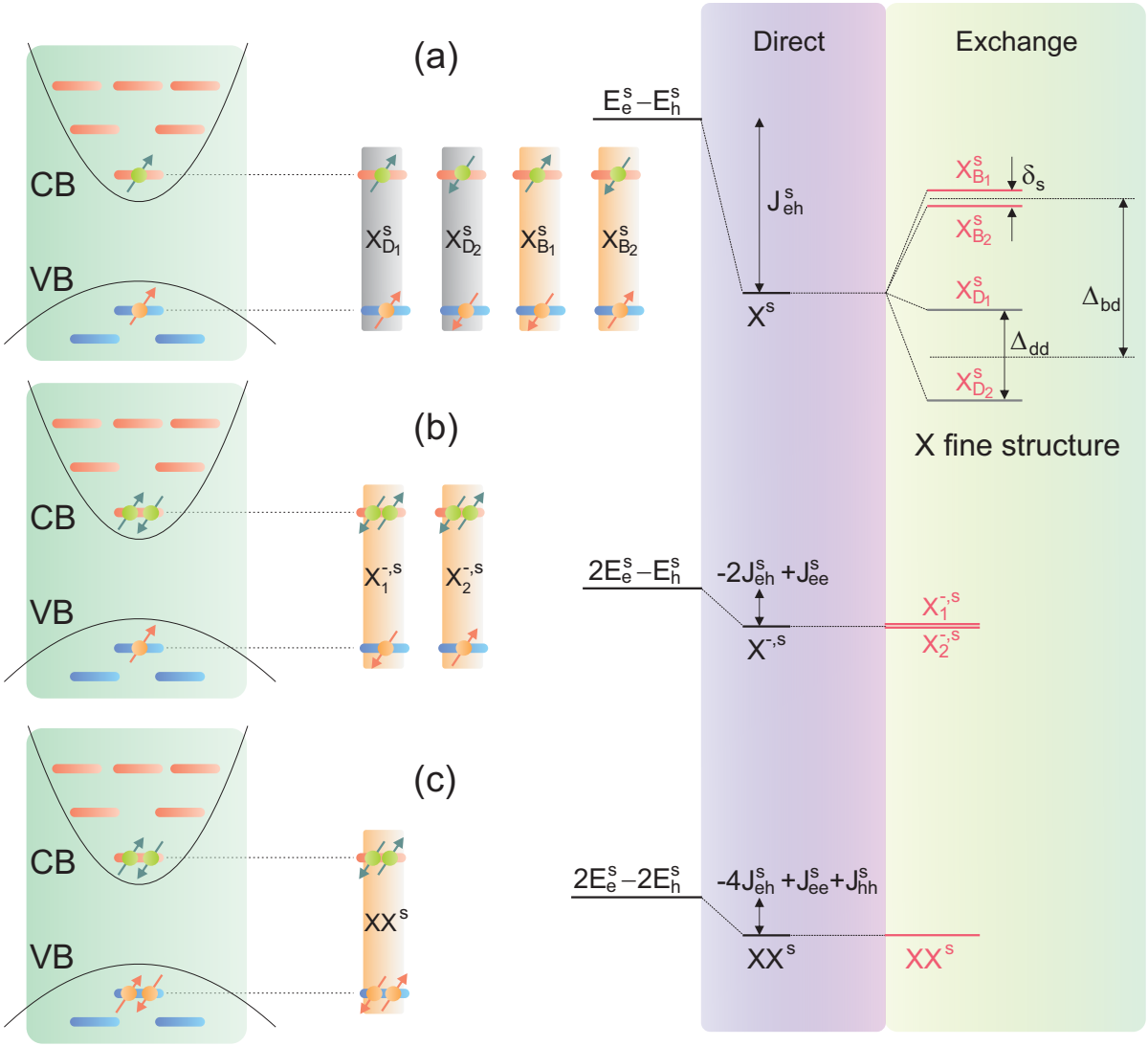

Figure 2.2: (a) Energy level diagram of ground state exciton. Exchange interactions determine the energy ordering in the X^s fine structure spectrum. Only the measure of δ_s is symmetry dependent. (b) Two possible configurations of the ground state negative trion $X^{-,s}$. Owing to the Pauli exclusion principle, the electron pair can form only singlet states. The two configurations are degenerate as the electron-hole exchange terms outweigh each other. (c) Ground state biexciton XX^s has no spin fine structure due to the Pauli exclusion principle.

The binding energy of negative trion $-2J^s_{eh} + J^s_{ee}$, for instance, is a function of electron-hole attractive interactions and electron-electron repulsive interaction, as shown in the energy

level diagram of Figure 2.2(b). The weights of J^s_{eh} and J^s_{ee} are often comparable in the QD studied here, thus $-2J^s_{eh} + J^s_{ee} < 0$ and the trion state is bound. The two electron-hole exchange terms in $X^{-,s}$ total energy are identical and oppositely signed, leading to a doublet state with no fine structure splitting. Indeed, the components of this doublet split under an external magnetic field [82]. Similarly, formation of a biexciton XX^s involves two pairs of electron and hole with oppositely oriented spins in the CB and VB ground states of QD.

The details of QD excitonic energy diagram are extremely important when it comes to the photonics applications. These details determine the color and linewidth indistinguishability of the photons generated by different QD transitions. From the spectroscopy point of view, the binding energy is defined based on the final state to which an excitonic complex transition occurs. For example, a biexciton XX^s decays to either of bright exciton states, $X^s_{B_1}$ or $X^s_{B_2}$, thus its binding energy is $-2J^s_{eh} + J^s_{ee} + J^s_{hh}$ in the QD photoluminescence spectrum, neglecting the small contributions of exchange energies (see Sec. 4.6 for detailed formulation). In order to establish the color matching condition between the $XX^s \rightarrow X^s_{B_1}$ and $X^s_{B_1} \rightarrow G$ photons, the direct Coulomb interactions must be renormalized so that $-2J^s_{eh} + J^s_{ee} + J^s_{hh}$ vanishes. This case is particularly of our interest as the photon entanglement schemes rely on color indistinguishability of XX and X photons. Here, we confine our study to the QD ground state and neglect the formation of complexes with single particles resting in the p or higher shells. The effect of higher energy levels comes into the ground state wavefunctions merely via small correlation energies.

2.3 Selection rules in optical transitions

Within the dipole approximation, the oscillator strength for an optical interband transition between two QD states $|i\rangle$ and $|f\rangle$ with energies E_i and E_f is defined as

$$M_{|i\rangle,|f\rangle} = \frac{2}{m_0} \frac{|\langle i| \, \boldsymbol{e}_{\mathbf{k},\lambda} \cdot \mathbf{P} \, |f\rangle \, |}{E_f - E_i} \tag{2.5}$$

where $\mathbf{P}$ stands for momentum operator, and $\boldsymbol{e}_{\mathbf{k},\lambda}$ is the direction unit vector of electric field having wavevector $\mathbf{k}$ and polarization λ. The dipole moment matrix element of this specific transition is the approximated by

$$\mathbf{P}_{|i\rangle,|f\rangle} = \langle i| \, \boldsymbol{e}_{\mathbf{k},\lambda} \cdot \mathbf{P} \, |f\rangle \simeq \sum_m \sum_n \langle u^m_\sigma| \, \boldsymbol{e}_{\mathbf{k},\lambda} \cdot \mathbf{P} \, |u^n_\sigma\rangle \, \langle \varphi^m_i | \varphi^n_f \rangle \tag{2.6}$$

where u^m_σ and φ^m are the Bloch and envelope parts of the wavefunction, respectively. Based on the symmetry properties of Bloch functions ($|S = 1/2, S_z = \pm 1/2\rangle$, $|J = 3/2, J_z = \pm 3/2\rangle$,

$|J = 3/2, J_z = \pm 1/2\rangle$, $|J = 1/2, J_z = \pm 1/2\rangle$) some certain transitions are optically forbidden.

Considering the fact that circularly polarized photons possess $\pm\hbar$ and $S = 0$, only the transitions following $\Delta J_z = \pm 1$ and $\Delta S_z = 0$ are allowed. Consequently, an exciton containing the heavy hole state $|J = 3/2, J_z = 3/2\rangle$ ($|J = 3/2, J_z = -3/2\rangle$) and electron state $|S = 1/2, S_z = -1/2\rangle$ ($|S = 1/2, S_z = 1/2\rangle$) has a total angular momentum equivalent to $+1$ (-1) and is optically active. Similarly, a light hole in $|J = 3/2, J_z = 1/2\rangle$ ($|J = 3/2, J_z = -1/2\rangle$) state recombines $|S = 1/2, S_z = 1/2\rangle$ ($|S = 1/2, S_z = -1/2\rangle$) electron and generates a circularly-polarized photon. Moreover in nanowires, a photon with linear polarization along the axis can couple to the light hole exciton $|J_z = 1/2, S_z = -1/2\rangle$ (or $|J_z = -1/2, S_z = 1/2\rangle$) [83]. Referring back to Sec. 2.1, total angular momentum of the single particles in different QD shells incorporates an additional angular momentum number associated with its orbital L_{orbital}. Any change in L_{orbital} forbids the transition as $\Delta J_z = \pm 1$ must be consistently obeyed: only electrons and holes from identical shells (s-shell, p-shell, d-shell) can recombine with a nontrivial oscillator strength. Notice that the band mixing effect prohibits assigning a pure HH/LH character to the QD states, thus it is difficult to find a transition whose oscillator strength is absolutely zero.

In addition to the band mixing effect, there exists other phenomena that couple the wavefunctions of dark and bright excitons and activate dark transitions: a) The excitonic wavefunctions of a many-body system are partially correlated. This can be directly inferred from nonzero expansion coefficients in Eq. 2.1. Although the substantial part of each exciton wavefunction is effectively made of a very limited number of single particle states in strongly confining QDs, all components of the band structure contribute to build this wavefunction. The weight of this wavefunction is primarily decided by the energy spacing between the original QD state and the contributing state. It is shown that the dipole moment matrix element of an exciton transition X_i is calculated by $\mathbf{P}^{X_i} = \sum_{a,b} \eta_{ab}^{X_i} \mathbf{P}_{ab}$, where $\mathbf{P}_{ab}$ is the dipole moment matrix element of $|a\rangle \rightarrow |b\rangle$ transition, and a and b span over all the available states [84]. b) Various types of structural asymmetry enhance the band mixing and change the character of quantized states. c) Bright and dark excitons are coupled under magnetic field. This is further elucidated in the following section.

2.4 QDs in external electric and magnetic fields

Stark effect: the influence of the electric field on the QD energy level structure boils down into two effects: a) energy shift in the whole QD band structure. An axial or lateral electric field across the NWQD breaks the potential symmetry and enhances the QD confinement;

see Figure 2.3(a) left panel. This normally reduces the effective s-shell band gap as long as the effective masses of particles allow their orbitals to be squeezed. The oscillator strength drops upon a strong electric field as the electron-hole orbitals relocate oppositely. In our NWQDs, where the axial quantization is dominant, orbitals are more responsive into lateral electric fields. b) renormalizing Coulomb interactions due to orbital deformations. Once the electron-hole dipole spread further, their mutual interaction is suppressed as the overlap decreases. This decrease particularly occurs for all direct and exchange terms in high electric fields. In contrast, an electric field perpendicular to the nanowire axis breaks the confinement in-plane symmetry lifts (increases) the degeneracy (splitting δs) of bright excitons in symmetric (asymmetric) NWQDs; see Figure 2.3(a) right panel.

The feasibility of tailoring the excitonic energies via an external electric field enables us to control the color indistinguishability of transitions. In self-assembled QDs, the in-plane asymmetry of dot along different crystallographic directions, usually [110] and [1$\bar{1}$0], hinders the symmetry of electron-hole wavefunctions, a lateral electric field is able to rebuild symmetric orbitals and diminish FSS [85, 86, 87]. Analogously, the XX-X binding energy ($-2J^s_{eh} + J^s_{hh} + J^s_{ee}$) is field-dependent, thus $XX \rightarrow X$ and $X \rightarrow G$ can brought into resonance. This has been accomplished very recently by simultaneously controlling the strain field of self-assembled QDs and an external electric field [88].

Zeeman effect: the interaction between a magnetic field of arbitrary magnitude and orientation and an electron (hole) spin (pseudo-spin) is given by $\mathcal{H}_{\mathbf{B}} = \mu_{\mathrm{B}} \sum_{i=x,y,z} (g_{e,i} S_{e,i} + g_{h,i} J_{h,i}) B_i$ in its general form, where μ_B is the Bohr magnetron and g, known as g-factor is the dimensionless magnetic moment. The Zeeman effect on QD excitons is commonly studied under two configurations: a) parallel to the main quantization axis or Faraday configuration; b) in-plane (perpendicular to the main quantization axis) or Voigt configuration. In Faraday configuration, the hamiltonian in the exciton basis set $\{\downarrow_e \Uparrow_h, \uparrow_e \Downarrow_h, \uparrow_e \Uparrow_h, \downarrow_e \Downarrow_h\}$, is given by [89]

$$\mathcal{H}_{\mathbf{B};z} = \frac{\mu_{\mathrm{B}} B}{2} \begin{pmatrix} -g_{e,z} + g_{h,z} & 0 & 0 & 0 \\ 0 & g_{e,z} - g_{h,z} & 0 & 0 \\ 0 & 0 & g_{e,z} + g_{h,z} & 0 \\ 0 & 0 & 0 & -g_{e,z} - g_{h,z} \end{pmatrix} \tag{2.7}$$

The diagonal form of the hamiltonian is due to the rotational symmetry around the main quantization axis. The evolution of exciton fine structure under an axial magnetic field is sketched in 2.3(b). The QD here is assumed to have low symmetry and FSS. Bright (dark) exciton states are exchange coupled through δ_s (Δ_{dd}) in Eq. 2.4. Hence, at low magnetic fields, exciton energies evolve in a nonlinear fashion, but eventually enter the linear Zeeman regime introduced above upon adequately large magnetic fields. As can

be deduced form the hamiltonian, Faraday configuration is beneficial to adjust the bright exciton levels without coupling into the dark states.

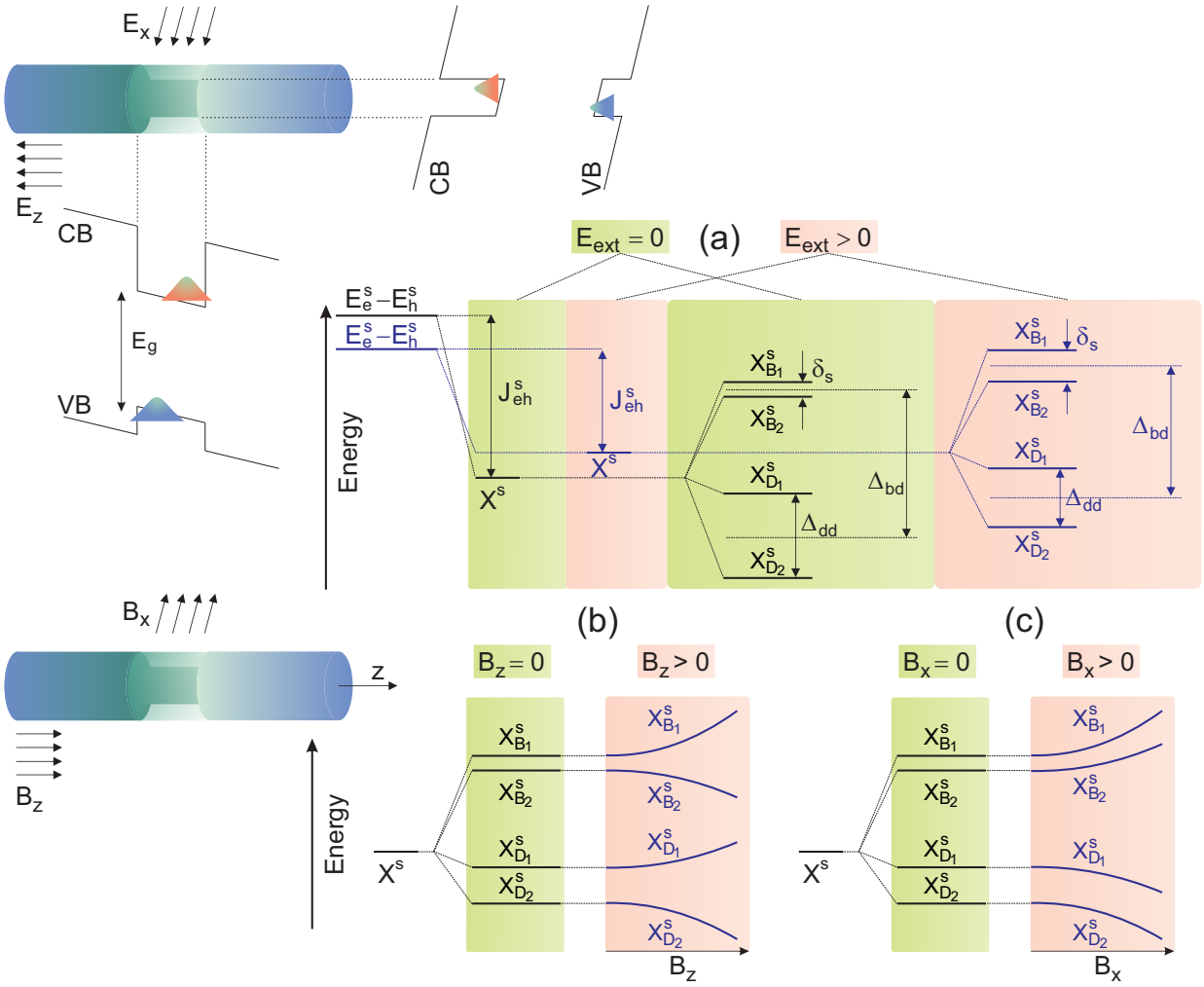

Figure 2.3: (a) Left panel: NWQD under lateral E_x and axial E_z electric fields: the symmetry of QD confinement is broken and orbitals become denser. Right panel: QD exciton fine structure under external electric field, $E_{\text{ext}} > 0$ compared to $E_{\text{ext}} = 0$. The exciton binding energy and exchange interactions are changed accordingly. (b) Exciton fine structure of a low symmetry QD under magnetic field in Faraday configuration. Bright excitons and dark excitons are assumed to be exchange coupled. (c) Exciton fine structure of a low symmetry QD in Voigt geometry.

In the Voigt configuration, the rotational (in-plane) symmetry with respect to the main quantization axis is broken, thus bright and dark excitons mix. The corresponding hamiltonian reads [90]

$$\mathcal{H}_{\mathbf{B}} = \frac{\mu_{\mathrm{B}} B}{2} \begin{pmatrix} 0 & 0 & g_{e,x} & g_{h,x} \\ 0 & 0 & g_{h,x} & g_{e,x} \\ g_{e,x} & g_{h,x} & 0 & 0 \\ g_{h,x} & g_{e,x} & 0 & 0 \end{pmatrix}. \tag{2.8}$$

The dark and bright states are coupled through the spin of either electron or hole. This coupling lifts up the oscillator strength of dark states. The signature of coupling can be observed in QD spectrum as an anti-crossing at small magnetic fields, see Figure 2.3(c). The effective g-factor of higher order excitons (X^-, X^+, XX, XX^-, and so forth) can be resolved by adding the g-factors of the constituting particles and considering the spin-flip couplings [91].

2.5 Quantum light from QDs

2.5.1 Single photon regime

Light fields can be classified based on their photon number fluctuations: a) Thermal light, b) coherent light, c) single photon regime.

Thermal Light: a thermal light results from a thermal equilibrium between a collection of emitters and an optical field. The photon distribution of thermal light is written as $P(n) = \langle n \rangle^n / (1 + \langle n \rangle)^{n+1}$ in accordance with the mean photon number $\langle n \rangle$ [92]. This geometric distribution indicates that the highest probability belongs to $n = 0$ for a thermal emitter and this probability consistently drops by increasing the photon number. The variance of thermal light is found to be $(\Delta n)^2 = \langle n \rangle^2 + \langle n \rangle$ [92].

Coherent light: a well-known example of coherent state is the output of a laser operating above threshold. The photon number probability distribution is given by the Poisson distribution, $P(n) = e^{-\langle n \rangle} \langle n \rangle^n / n!$ with variance of $\langle n \rangle$ [92]. In contrast to the thermal light, the largest probability of a coherent state occurs at $\langle n \rangle$. According to the measure of variance, thermal light has higher photon number fluctuations compared to the coherent light and an emitter radiating thermal light is operating in the "super-Poissonian" regime. From photon number probability distribution introduced for thermal and coherent light, it is straightforward to interpret that merely by attenuating the thermal or coherent

light a single photon emitter is not achievable: for any $\langle n \rangle = 1$, the probability of other photon numbers is not zero $P(n \neq 1) \neq 0$ and the emitter is producing multiple photons as well.

Number state or Fock state: a number state is quantum light where the average photon number exactly equals the number of photons $\langle n \rangle = n$ and the photon number distribution is $P(n) = n\delta_n$, where δ_n is the Kronecker delta. The photon number fluctuations is zero for a number state, and it can be generated only by single photon emitters. Essentially emitters exhibiting a photon number variance less than $\langle n \rangle$ (coherent state) are identified as operating in the quantum regime. Coherent state serves as the boundary between classical light and quantum light.

The time distribution of photons for different classes of light is shown in Figure 2.4(a-c). The concept of time correlation is mathematically elucidated in Sec. 6.4.2, and here we limit ourself to a qualitative description. In thermal regime, the photons are bunched together and their normalized time correlation exceeds 1, implying that photons tend to form an ensemble in time. In contrast, photons are uncorrelated in coherent state but randomly distributed in time. Finally, single photons produced by an ideal quantum emitter arrive at certain time intervals. Their time correlation plotted versus the time delay τ between two different photons shows a dip at $\tau = 0$, stating that the probability of finding two photons emitted concurrently is small [93]. The time correlation counts illustrated in Figure 2.4(d) is a signature of single photon emission.

An excitonic transition of QD is an ideal source of single photons since it emits no photon immediately after a recombination process. Time spacing of photons is in the order of the exciton coherence time, which is ruled by the spontaneous emission rate and dephasing processes such as exciton-phonon interactions or carrier-carrier scattering. Dephasing processes give rise to the uncertainty in the arrival time of photons, known as time jitter. Time jitter is also a consequence of carrier relaxation process from the higher shells of QD, which is motivated by random carrier-phonon scatterings and delays the exciton formation [94]. The indistinguishablity of emitted photons can be measured through interference experiments [39]. This indistinguishablity particularly concerns the similarity in the color and linewidth. The Michelson-type interferometer is utilized to resolve the interference pattern in these experiments [41]. The QD is excited by a pair of pulses with a time spacing larger than the ground state exciton lifetime ($\Delta T \approx$ 2-3 ns) and less than the laser repetition period. The pulse pair sequence is repeated periodically (10-12 ns). During each cycle QD emits two photons from its ground state, which are sent to the Michelson interferometer after polarization filtering. A 50/50 beam splitter divides the optical path into a short arm and a long arm (delayed by $\Delta T + \delta t$, where δt is

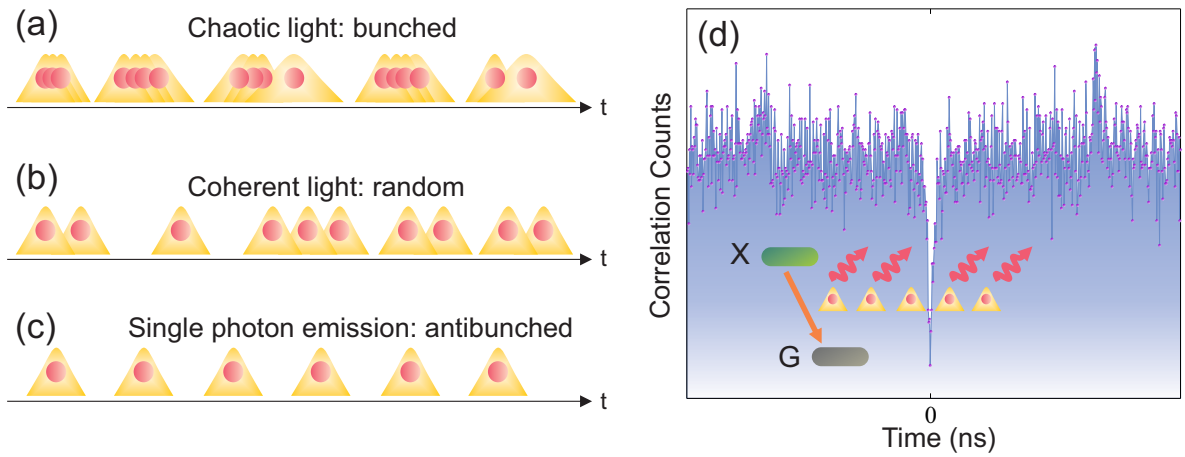

Figure 2.4: (a-c) Time distribution of photons in thermal (bunching), coherent and quantum (antibunching) regimes. (d) Time correlation counts of a QD transition exhibiting a true signature of single photon emission.

mechanically adjustable). The photons are then detected via single photon detectors and the counts are recorded by a correlation card; see Sec. 6.4.2. The value of distinguishablity can be estimated by comparing the areas of the central and the neighbouring interference peaks [39]. According to the Bose-Einstein statistics followed by photons, they tend to bunch. Thus if they are indistinguishable, they exit from one output of beam splitter once the time delay is varied to zero, and the probability of coincidence at zero delay drops.

2.5.2 Entangled photon pair generation in QDs

As mentioned in the previous chapter, in 2000, O. Benson et al. suggested that entangled photon pairs may be produced by the biexciton XX cascade recombination in single QDs [59]. XX radiatively relaxes into the ground level through its constituting bright excitons. $X_{B_1} = \downarrow_e \Uparrow_h$ emits a left-polarized photon ($M = J_z^{\text{tot}} = 1$) while $X_{B_2} = \uparrow_e \Downarrow_h$ emits a right polarized photon $M = -1$. Depending on which exciton recombines first, two different decay paths are available leading to either a $|LR\rangle$ or $|RL\rangle$ biphoton state. The ambiguity of being in what state, or which decay path is chosen, makes the biphoton state entangled $1/\sqrt{2}(|LR\rangle + |RL\rangle)$, where the balanced weight of two terms states that both decay paths are assumed to be equally likely as is expected in a maximally entangled state. The evidence of realizing a XX-X cascade is verified by cross-correlation measurements, demonstrating that the $X \rightarrow G$ photon is more likely to be detected immediately after the $XX \rightarrow X$ has been recorded in the detector; see Sec. 6.4.2. However, how close the actual biphoton state

is to the ideal state, namely $1/\sqrt{2}(|LR\rangle + |RL\rangle)$, depends on a set of parameters. Probably the most important factor influencing the degree of entanglement of two photons is their color matching: any distinction between the energetic of photons impairs the uncertainty in the path information ($|LR\rangle$ or $|RL\rangle$) and entanglement. On the other hand, the linewidth of photons, if broad enough, can hide the energy separation of photons and restore the entanglement [95].

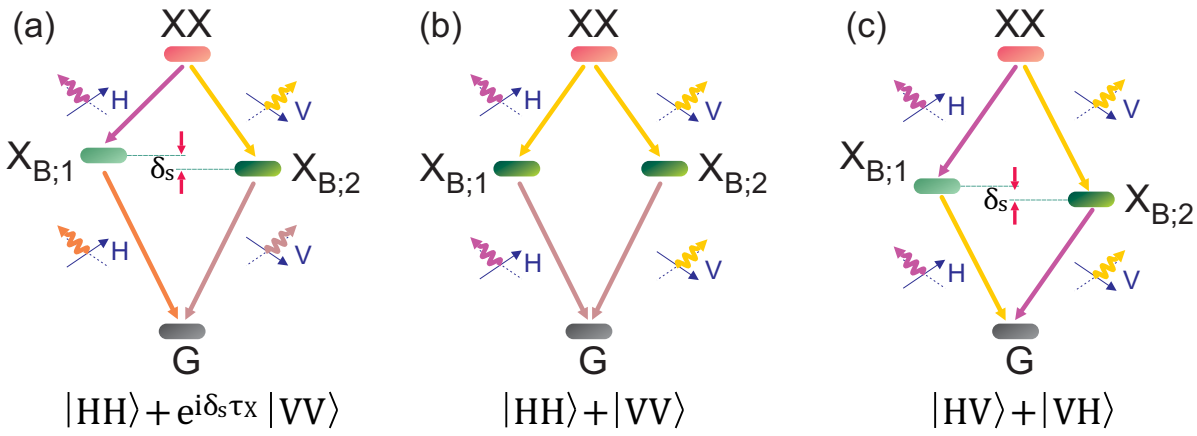

Figure 2.5: XX-X energy level diagram in a single QD: (a) A typical QD with nonzero FSS and XX binding energy. Four components possess different resonance energies. The biphoton wavefunction is given by $|\psi_{\text{biphoton}}\rangle = |HH\rangle + e^{i\delta_s \tau_X} |VV\rangle$ (b) Regular scheme: the FSS is vanished, thus $XX \to X_{B_1}$ ($X_{B_1} \to G$) and $XX \to X_{B_2}$ ($X_{B_2} \to G$) photons have the same energy and the photon pair entangled state is $|\psi_{\text{biphoton}}\rangle = |HH\rangle + |VV\rangle$. c) Time reordering scheme (cross entanglement): the biexciton binding energy is removed. Here, photons across generations, $XX \to X_{B_1}$ ($XX \to X_{B_2}$) and $X_{B_2} \to G$ ($X_{B_1} \to G$) are in resonance and the maximally entangled state $|\psi_{\text{biphoton}}\rangle = |HV\rangle + |VH\rangle$ can be obtained.

According to Sec. 2.2, two energy terms are essential in color matching condition, fine structure splitting δ_s and XX binding energy with respect to X. The energy diagram of XX decay down to the ground level is schematically shown in Figure 2.5(a). The energy difference between $XX \to X_{B_1,B_2}$ and $X_{B_1,B_2} \to G$ is in the order of ~ -10 to 3 meV, typically larger than the exciton linewidth $\Delta\omega \sim$ 30-200 μeV. FSS, however, is comparable to $\Delta\omega$ and ranges between 30 to 100 μeV. Therefore, none of the components shown in Figure 2.5(a) are energetically identical. The biphoton wavefunction can be written as $|\psi_{\text{biphoton}}\rangle = |HH\rangle + e^{i\delta_s \tau_X} |VV\rangle$, where $|H\rangle$ and $|V\rangle$ are the two basis of linear polariza-

tion[1] [96]. Obviously, as the intensity of $|\psi_{\text{biphoton}}\rangle$ decays in course of time, the phase of $|\psi_{\text{biphoton}}\rangle$ rotates. The total phase of the biphoton wavefunction is then randomized over time, and measures of $|\psi_{\text{biphoton}}\rangle$ at different times with opposite phases cancel out each other in a time integrated entanglement [97]. Early experiments after Benson et al.'s proposal reported classical correlation, not entanglement, of QD photon pairs due to the same reason [98, 99]. In order to restore the color matching condition in QD cascade, two types of energy level manipulation, and therefore two schemes of photon entanglement, can be realized.

Regular scheme: it refers to the very early proposal on photon pair entanglement in QDs [59], where the which-path information is erased by vanishing FSS and the maximally entangled state $|\psi_{\text{biphoton}}\rangle = |HH\rangle + |VV\rangle$ is created in a sequential XX decay. Realization of this energy diagram is challenging in self-assembled QDs due to a) lateral asymmetry of QD: dimensions along [110] and [1$\bar{1}$0] are not identical in a [001]-oriented QD, b) vertical anisotropy of QD: this anisotropy enhances the shear strain components in a QD with low in-plane symmetry and lifts the degeneracy of bright excitons, c) piezoelectric potential: it induces an internal electric field that redistributes electron and hole wavefunctions towards different orientations and lowers their symmetry [100].

Time reordering scheme: in the method proposed by M. Reimer [101] and J. Avron [102], photons across generations are entangled. This scheme puts no requirement on the range of FSS, however, the binding energy of biexciton must be set to zero. Irrespective of the measure of FSS, $XX \rightarrow X_{B_1}$ ($XX \rightarrow X_{B_2}$) and $X_{B_2} \rightarrow G$ ($X_{B_1} \rightarrow G$) are in resonance and the biphoton state is expressed as $|\psi_{\text{biphoton}}\rangle = |HV\rangle + |VH\rangle$. The striking difference compared with the regular scheme lies in the timing procedure, as the entangled photons are not being produced sequentially [102].

Restoring photon color matching: there have been numerous efforts attempting to diminish the QD fine structure splitting (FSS) by suppressing above mentioned effects. Some of these works rely on controlling growth conditions and delocalization of electron/hole wavefunction or applying post-growth annealing steps [103, 104]. A. Schliwa et al. reported the effect of annealing on pyramidal and lens-shaped QDs [105]. Their investigations demonstrate that the second order piezoelectric polarization is very sensitive to the interface abruptness of QD. However, they have neglected the intermixing of dot and barrier materials, which usually increases the spatial extent of electron-hole wavefunctions and makes the excitons weakly confined leading to a reduction in exchange interaction.

The quantum confined Stark effect can be utilized to remove the FSS in low-symmetry

[1]Notice that the entangled state expressed in circular polarization can be also written in rectilinear and diagonal representations: $1/\sqrt{2}(|LR\rangle + |RL\rangle) \equiv 1/\sqrt{2}(|HH\rangle + |VV\rangle) \equiv 1/\sqrt{2}(|DD\rangle + |AA\rangle)$ where $|R\rangle = (|H\rangle - i\,|V\rangle)/\sqrt{2}$, $|L\rangle = (|H\rangle + i\,|V\rangle)/\sqrt{2}$, $|A\rangle = (|H\rangle - |V\rangle)/\sqrt{2}$, and $|D\rangle = (|H\rangle + |V\rangle)/\sqrt{2}$.

QDs. As explained in Sec. 2.4, electric field can reshape the electron-hole wavefunctions and their spatial overlap, resulting to a reduction in FSS. This approach was first implemented on gated self-assembled QDs [106], and was recently realized in a GaAs/Al(Ga)As single photon diode by Ghali et al. [107] and A. Bennett et al. [108]. The very same effect enables us to remove small biexciton binding energy (< 3 meV) via applying higher ranges of electric field ($|E| < 30$ kV/cm). The electric field drives an antibinding biexciton deeper into the antibinding regime, pushing the XX line further away from the XX-X resonance point. The requisite to establish the resonance condition is then to develop QDs with binding biexciton, see Sec. 4.8.

A uniaxial or biaxial stress can also tailor the binding energies of excitonic complexes or restore the in-plane symmetry of QD wavefunctions and remove the anisotropic exchange interaction [109, 110]. The QD is simply stressed along specific in-plane orientations by piezoelectric actuators. F. Ding et al. demonstrated it as a robust method to bring the X and XX transitions into resonance [111]. This method has the advantage of fine tuning the excitonic resonances without drastically changing the exciton oscillator strength. It also puts no precondition on the binding or antibinding nature of XX. However, to the best of our knowledge the experiments reported so far have not reached zero FSS limit [112]. Additionally, the maximum achievable variations of FSS relies on the maximum possible stress that the sample can tolerate.

Another technique suggested by A. Schliwa et al. is to grow self-assembled QDs on (111) substrate [80]. Due to the threefold rotational symmetry of the (111) surface, the QD confinement is then expected to show at least C_{3v} lateral symmetry. Unlike QDs grown on (001) substrate, the piezoelectric field does not reduce the in-plane symmetry of QD confinement to C_{2v}. Mohan et al. employed a similar idea by growing lens-shaped In(Ga)As QDs at the apex of inverted pyramids [113]. The geometry and substrate orientation (111) lead to C_{3v} symmetry character of exciton wavefunction. They could not reach zero FSS in their samples and their quantum correlation measurements were further put under question following their retraction.

2.5.3 Fidelity of entanglement

One important indicator of entangled photon pair is the *fidelity* of biphoton wavefunction $|\psi_{\text{biphoton}}\rangle$ to the maximally entangled state, i.e. $|\psi^+\rangle = |HH\rangle + |VV\rangle$. Fidelity with $|\psi^+\rangle$ is calculated by $f^+ = \langle\psi^+|\,\rho_{\text{bi}}\,|\psi^+\rangle$ where ρ_{bi} is the the biphoton polarization density matrix [114, 96]. The fidelity then reads $(\rho_{\text{bi},11} + \rho_{\text{bi},44})/2 + \text{Re}\{\rho_{\text{bi},14}\}$ or equivalently [97]

$$f^+ = (C_R^\tau + C_D^\tau - C_C^\tau + 1)/4 \tag{2.9}$$

where C_R^τ, C_D^τ and C_C^τ are the degrees of correlation in the rectilinear (H,V), diagonal (D,A) and circular (R,L) polarization bases, defined by $C^\tau = (g_{||}^{(2)} - g_{\perp}^{(2)})/(g_{||}^{(2)} + g_{\perp}^{(2)})$ with $g_{||}^{(2)}$ and $g_{\perp}^{(2)}$ being the copolarized and cross-polarized correlation counts of XX and X. The superscript τ indicates the time dependency of all correlation terms. The technique of how to measure the second order time-correlation $g^{(2)}$ is explained in Sec. 6.4.2. The fidelity of a source generating classically correlated photons can never exceed 0.5. In fact, if a source has only classical correlations the off-diagonal components of density matrix become zero, $\rho_{\mathrm{bi},14} = 0$, leading to $|\psi^+\rangle = (\rho_{\mathrm{bi},11} + \rho_{\mathrm{bi},44})/2$ with an upper bound of 0.5 (note that $\rho_{\mathrm{bi},11} + \rho_{\mathrm{bi},22} + \rho_{\mathrm{bi},33} + \rho_{\mathrm{bi},44} = 1$). Although resolving the whole density matrix is required to understand the full details of photon-pair evolution in course of time, a fidelity larger than 0.5 is a strong signature of entanglement.

Chapter 3

Single-particle energies and orbitals in nanowire quantum dots

3.1 Introduction

Nanowire-based QDs are typically heteroinsertions composed of two different band-gap materials commonly found in zinc-blende or wurtzite phases. The precisely controlled morphology and structure of QD segments during the growth process allows for fabricating cylindrical or hexagonal QDs [115, 116, 117], which, due to their symmetric geometry, turn out to be the primary competitors of self-assembled QDs for generating entangled photon pairs. Tailoring the number of charge carriers down to one single particle trapped in a gate-induced QD has been already demonstrated by Bjork et al. [62], opening the same possibility for its heterostructure twins. Moreover, the embedded QD segment covers nearly the entire nanowire cross-sectional area; thus, compared to self-assembled structure the internal quantum efficiency under electrical pumping increases remarkably, having the common surface states removed or suppressed by means of appropriate shell passivation [117]. Upon significant surface recombination, however, electrons and holes find extra channels of radiative decay commonly uncorrelated with the QD resonances, thus the quantum efficiency drops.

While a great deal of theoretical and experimental works focus on self-organized QDs, there is no comprehensive study on single and few-particle states in NWQDs. In contrast to self-organized QDs, the modulated segment barely suffers from any morphological anisotropy along the growth direction and thus intrinsically forbids the formation of low-symmetry (e.g., C_{2v}) piezoelectric confinement. This offers ideal features for producing

polarization-entangled photons under the regular scheme because the indistinguishability of photons is well preserved. Furthermore, direct Coulomb interactions and thus the binding energies of few-particle complexes can be optimally tailored in a field-effect transistor configuration. Entanglement in a time reordering scheme then could be improved through XX_0 binding energy removal.

In this chapter, we first investigate how single-particle characteristics of core-shell NWQDs depend on their structural parameters. For this purpose, orbital symmetry character and band mixing effects are analysed. The impact of single-particle dispersion on its total energy and orbital deformations is discussed. Then a many-body picture is provided to describe the few-particle resonances in the excitonic spectrum of NWQDs. By introducing the orbital-dependent kinetic energy and observing its variations in response to the confining potentials, we are able to predict the evolution of direct interactions and correlation energies. This way, we can engineer NWQD structure to achieve small binding energies for s-shell complexes. It is demonstrated here that trivial binding energies are likely when axial quantization does not exceed the lateral one significantly. Finally, NWQDs are exposed to axial and lateral electric fields so that XX_0 binding energy is removed. Based on the trivial variations of kinetic energy, we prove that correlations are rather insensitive to the electric field in NWQDs studied here. Thus s-shell excitonic resonances move according to direct Coulomb interactions.

3.2 NWQD shapes, dimensions, and growth directions

Here, we model zinc-blende core-shell NWQDs, having their symmetry properties inspired by a number of experiments recently done [115, 117, 69, 118, 119]. We particularly investigate the built-in potential and wave-function symmetries when the growth direction varies from [001] to [111]. As illustrated in Figure 3.1 the geometries of QD insertions include the following:

(A) Truncated pyramidal QD. No modeling is presented for this series and the results only give us the required insight to accomplish useful comparisons between self-assembled and NWQDs.

(B) Cylindrically symmetric NWQDs grown along [001] (B-1) and [111] (B-2) orientations.

(C) Laterally symmetric but axially asymmetric [001]- (C-1) and [111]- (C-2) oriented NWQDs. These cone-shaped zinc-blende QDs qualitatively exhibit properties similar to

those of their wurtzite counterparts originally grown by Minot et al [69].

(D) Laterally elongated [001]-oriented NWQDs.

The diameters of most studied QDs D_D are kept fixed equal to 20 nm (except in a few highlighted cases) for the sake of comparison, while their height h_D varies, changing the vertical aspect ratio, that is, $a_h = h_D/D_D$, between 0.1 and 0.5. The QD/barrier materials are assumed InAs/GaAs for [001]- oriented and InAs/InP for [111]-oriented QDs, comparable to the previously reported experiments [120, 121]. It is noteworthy to mention that the mesoscopic symmetry properties of wavefunctions derived here for [111]-oriented zinc-blende QDs are also extensible to their [0001]-oriented wurtzite counterparts. Additionally, we expect analogous values of Coulomb interactions being observed in wurtzite QDs, since the effective orbital behaviors are rather similar. In series A, two monolayers of QD material are added beneath the pyramid island, serving as the so-called wetting layer.

The variation of QD vertical aspect ratio is selected between 0.1 and 0.5 because of the following reasons. First, we intend to demonstrate the impact of confinement variations in NWs where the effective mass of single particles along one particular coordinate (quantization axis) is principal. The primary character of the hole ground state, h_0 , and the associated exciton, X_0 , then can be easily identified among heavy hole (HH), light hole (LH), and spin-orbit split-off (SO) classifications of the valence bands. This character directly returns a measure of the angular momentum shared by the hole particle in an exciton and, therefore, the polarization of emitted photon after the recombination process. Second, energy of the primary inter- band transition firmly relies on the lowest dimension seen in the QD. We aim to keep the corresponding wavelength within the infrared spectrum, being compatible with other optical components if required. Additionally, this range (0.1-0.5) has been frequently explored by the relevant experimental works on NWQDs. Needless to say, similar transition energies are achievable through higher vertical aspect ratios using a ternary composition of InAs/GaAs or InAs/InP materials as the QD segment.

The lateral elongation of structure, if sufficiently pronounced, is itself a possible origin of FSS in NWQDs since it reduces the symmetry character into C_{2v} even in the absence of a directional piezoelectric field. The net effect of piezoelectricity and elongation can, however, increase or decrease the polarizability of an exciton wavefunction. Here, we do not study the lateral elongation extensively, since our results can be easily revised in the presence of lateral asymmetry.

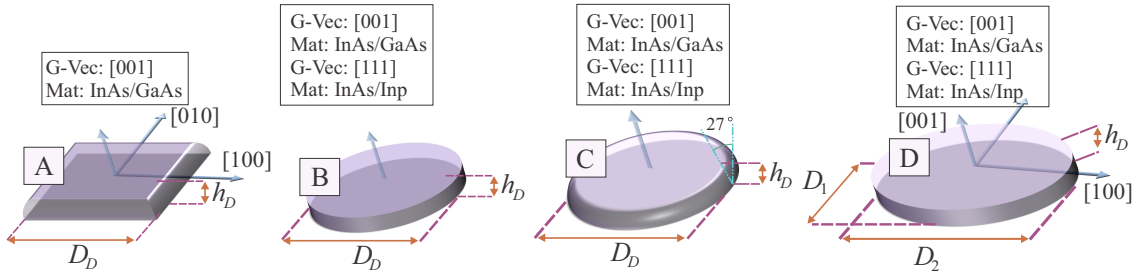

Figure 3.1: Shape of the NWQD insertions modeled in this chapter: (A) truncated pyramidal, (B) cylindrical, (C) cone-shaped, and (D) elongated NWQDs. Growth direction (G-Vec) and QD/nanowire materials (Mat) are specified in each case. The vertical aspect ratio varies between 0.1 and 0.5 for series B and NWQDs. Nanowire core and shell regions are not shown here.

3.3 Polarization anisotropy in NWQDs

Owing to their high refractive index compared to the surrounding ambient, which is normally air or vacuum, III-V nanowires exhibit extensive polarization anisotropy in their emission and absorption characteristics ($\varepsilon_{\text{static}} = 13.2$ for GaAs and 12.5 for InP, respectively). The component of an external electric field parallel to the nanowire axis remains the same inside and outside, ($E_{||;\text{in}} = E_{||;\text{ex}}$), while the perpendicular component weakly penetrates inside $E_{\perp;\text{in}} = 2\varepsilon_{\text{vac}}/(\varepsilon_{\text{in}} + \varepsilon_{\text{vac}})E_{\perp;\text{ex}}$($\varepsilon_{\text{in}}$ and ε_{vac} represent the nanowire and vacuum dielectric constants). Assuming that $\mathbf{e}_{\mathbf{k}\lambda} \in \{||, \perp\}$ symbolizes the polarization vector for an electric field possessing wave vector $\mathbf{k}$ and wavelength λ, the measure of the effective oscillator strength $M_{i,f}^{\text{eff}} = E_{\mathbf{e}_{\mathbf{k}\lambda};\text{ex}}^2 / E_{\mathbf{e}_{\mathbf{k}\lambda};\text{in}}^2 M_{i,f}$ then behave very differently in response to parallel and perpendicular polarizations for an interband transition between states $|i\rangle$ and $|f\rangle$ as $E_{\perp;\text{in}} \ll E_{||;\text{in}}$ ($2\varepsilon_{\text{vac}}/(\varepsilon_{\text{in}} + \varepsilon_{\text{vac}}) \ll 1$) for an arbitrary external electric field unless $E_{\perp;\text{ex}} \gg E_{||;\text{ex}}$. The oscillator strength we refer to throughout this chapter is the intrinsic one $M_{i,f}$.

The symmetry character of a Bloch spinor corresponding to a specific state introduces another source of anisotropy into the interband transitions, which is not exclusive to NWQDs. With the inclusion of band mixing (see Sec. 3.4.1) and neglecting the envelope symmetries, those states exhibiting larger HH (LH) character have $E_{3/2}$ ($E_{1/2}$) symmetry according to the group notation used in Ref. [122]. Electron Bloch spinors possess $E_{1/2}$ symmetry; thus, any transition from CB ground state to HH-like states is allowed only under perpendicular polarization, that is, $\langle c_{E_{1/2}} | \mathbf{E}_{||} \cdot \mathbf{P} | hh_{E_{3/2}} \rangle = 0$. In contrast, interband transitions from CB to LH-like states sharing a similar symmetry are allowed for both types of polarizations, that is, $\langle c_{E_{1/2}} | \mathbf{E}_{||,\perp} \cdot \mathbf{P} | lh_{E_{1/2}} \rangle \neq 0$. Consequently, the effective

oscillator strength drops when the hole effective mass becomes heavier along the nanowire axis (more HH-like). Having these facts in mind, we discuss how the VB ground state is shared by HH and LH bands of the original bulk in Sec. 3.5.4.

3.4 Strain Confinement And Piezoelectricity

Since the confining potentials caused by the strain field are comparable to the original band offsets of III-V compounds, one cannot neglect their influence on the single-particle energy levels and the corresponding wavefunctions, especially when strain becomes highly anisotropic. Having employed the envelope function approximation ($\mathbf{k}\cdot\mathbf{p}$ model) to solve for the single-particle orbitals, we followed the continuum mechanical (CM) model in order to find the strain distribution [123, 124]. The $\mathbf{k}\cdot\mathbf{p}$ Hamiltonian is generally insensitive to the complete details given by atomistic models, such as valence force field (VFF) [125, 126], while with a smaller load of computations, CM can properly fit the restricted number of predefined parameters introducing the strain field into this model. In order to model the strain distribution, we assumed epitaxial growth. A detailed study of the calculation method including initial and boundary conditions along with elastic constants can be found in Refs. [127] and [77].

3.4.1 Band alignment and wave-function coupling

The role of strain in adding extra confinements to the original band alignments of QD-nanowire boils down into three types of potential: (1) hydrostatic $V_{\rm Hy}$, (2) biaxial $V_{\rm Bi}$, and (3) piezoelectric V_p. The origin of the two first types, $V_{\rm Hy}$ and $V_{\rm Bi}$, lies in the diagonal components of strain tensor, that is, $\mathrm{Tr}\{\mathbf{e}\} = e_{\rm Hy} = e_{xx} + e_{yy} + e_{zz}$ and $e_{\rm Bi} = (e_{xx} + e_{yy})/2 - e_{zz}$, where e_{ij} is the strain tensor component, while piezoelectric potential originates from the off-diagonal components. Let us consider the exemplary case of [001]-oriented NWQDs. Proper approximations of QD conduction band (CB) and valence band (VB) energy eigenvalues are given by their energy band alignments having the strain effect included.

(i) The local position of CB at Γ_6 neighborhood in k-space merely depends on the hydrostatic strain: $E_{\rm CB} = E^0_{\rm CB} + a_c e_{\rm Hy}$, where $E^0_{\rm CB}$ denotes the strain-free CB edge and a_c is the CB hydrostatic deformation potential. The above relation implies that higher strain energy developed at QD interfaces lifts up electron eigenvalues in the energy space.

(ii) The position of the VB edge, however, relies upon both hydrostatic and biaxial potentials. The HH band at Γ_8 in k-space curves according to $E_{hh} = E^0_{\rm VB} - a_v e_{\rm Hy} + b_v e_{\rm Bi}$,

where E^0_{VB} is the unstrained VB edge, and a_v stands for the VB hydrostatic deformation potential. In this approximate picture, the energy splitting between HH and LH bands is then $2b_v e_{\mathrm{Bi}}$, where b_v deformation potential along [001] orientation, because $E_{lh} = E^0_{\mathrm{VB}} - a_v e_{\mathrm{Hy}} - b_v e_{\mathrm{Bi}}$. By solving the eight-band $\mathbf{k}\cdot\mathbf{p}$ Hamiltonian at Γ point, one observes that high axial anisotropy in QD structure yields a local crossing between HH and LH bands, leading to the mixture of their associated wavefunctions [76, 128]. This band crossing is attributed to the probable sign-changing of biaxial strain and must be preferably avoided to have purely $\pm 3/2$ ($J_z = \pm 3/2$, where J_z is the z projection of the total angular momentum) or $\pm 1/2$ ($J_z = \pm 1/2$) p spinors for holes residing the ground state.

In addition to the proximity of HH and LH bands, their coupling ratio depends also on the shear strain through

$$\langle lh_2|\,\mathcal{H}_s\,|hh_1\rangle = \langle hh_2|\,\mathcal{H}_s\,|lh_1\rangle = \sqrt{3}/2 b_v(e_{xx} - e_{yy}) - i d_v e_{xy} \tag{3.1}$$

and

$$\langle lhh|\,\mathcal{H}_s\,|lh_2\rangle = -\langle lh_1|\,\mathcal{H}_s\,|hh_1\rangle = -d_v(e_{xz} - i e_{yz}) \tag{3.2}$$

in the $\mathbf{k}\cdot\mathbf{p}$ Hamiltonian $\mathcal{H}_{\mathbf{k}\cdot\mathbf{p}} = \mathcal{H}_k + \mathcal{H}_s$ [77] where $\mathcal{H}_k$ and $\mathcal{H}_s$ indicate kinetic and strain-dependent parts, $|hh_{1,2}\rangle = |J = 3/2, J_z \pm 3/2\rangle$ and $|lh_{1,2}\rangle = |J = 3/2, J_z \pm 1/2\rangle$. As can be realized from the above terms, shear strain components together with the QD lateral asymmetry ($e_{xx} - e_{yy}$) give rise to nontrivial mixture of HH and LH wavefunctions. Conclusively, series B-1 and B-2 flat NWQDs ($a_h = 0.1$) are expected to show minimal impurity in their hole total angular momentum and a single-band representation with the maximum contribution from HH band. In contrast, for series A and C NWQDs, there always exists a non-negligible portion of LH character in their hole angular momentum.

3.4.2 Strain relaxation sensitivity on shell thickness

Before elaborating on piezoelectricity, let us discuss how the shell thickness (in series B and C) may shift the band alignments. Since we assume that NWQDs are grown in the zinc-blende phase, their energy band alignments have been considered to be type I [129]. Compared to VB, the location of the CB bottom edge inside QD then sensitively relies upon hydrostatic strain since $a_c \approx 10 a_v$ [130]. Consequently, when the surrounding shell is suppressed, the strain energy formed in the vicinity of QD sidewalls is not able to relax properly. In particular, this strain inhomogeneity extraordinarily pushes down the CB at the sidewalls, leading to deep confinement of trapped electrons at QD borders instead of its center. Having the hole density mostly concentrated around the center, electron

and hole orbitals spatially separate, resulting in a weak oscillator strength. Thicker shells acting like adequately large barriers also prevent fast recombination of electrons through surface states. The above effect is even more pronounced in InAs/GaAs NWQDs compared with their InAs/InP counterparts since the lattice mismatch $e_{\perp}$ reaches 6.69%, implying a higher compressive force imposed by the majority material. For larger QD insertions, the critical thickness in the vicinity of insertion is enhanced because larger strain energy must be accommodated by the surrounding shell. Choosing the appropriate thickness normally exceeds this critical value [131]. In practice, growth of a passivating shell usually demands for accurate consideration of critical thickness. In this regard, our models contain experimentally verified measures [117, 132].

3.4.3 Symmetry degradation due to Strain-induced potentials and piezoelectricity

The origin of anisotropic fine structure splitting in self-assembled quantum dots is the low symmetry of net confinement. Apart from the asymmetry of quantum dot geometry, strain-induced potentials could lower down the level of confinement symmetry. The symmetry character of electron and hole orbitals are then directly influenced by the low symmetry of strain distribution. Piezoelectricity, known as the accumulation of charge in response to structural deformations, occurs in noncentrosymmetric crystals including zinc-blende or wurtzite phases. Linear piezoelectricity counts exclusively on shear strain components: $\mathbf{P}_a = 2d_{14}(e_{yz}, e_{xz}, e_{xy})$, where d_{14} denotes the first-order piezoelectric moduli [130]. Moreover, one shall not neglect second-order piezoelectric field $\mathbf{P}_b$ once strain components increase in highly mismatched heterostructures like In(Ga)As/GaAs. With the aid of ab initio calculations, Bester et al. showed that the magnitude of quadratic term may compensate or even surpass that of linear term in In(Ga)As quantum wells [100]. This situation particularly applies to QDs where a high degree of anisotropy is observed. In addition to the shear strain, the quadratic term depends also on diagonal components of strain tensor, which are more significant inside the QD. This yields second-order piezoelectric field $\mathbf{P}_b$ to appear predominantly inside QDs or close to their boundaries. Depending on the QD geometry, this internal field may intensify or suppress the impact of $\mathbf{P}_a$.

3.5 Single-Particle Orbitals

In this section we study the global symmetry of electron and hole orbitals along with their associated energies in our QDs. The Bloch components of single-particle wavefunctions are

assumed to be s-like for electrons and p-like for holes, respectively [133]. The geometry of the QD, however, manipulates the symmetry character of the envelope part. In addition to the excitonic energy splittings, orbital symmetry determines the intrinsic oscillator strength $M_{i,f}$ [134]. According to the HH-LH band mixing described in Sec. 3.4.1, general selection rules fail to accurately explain the excitonic transitions. However, the magnitude of intrinsic oscillator strength roughly depends on the type of symmetry shared by electron and hole total wave functions [1].

3.5.1 Calculating Single Particle Wavefunctions

In order to find the single-particle envelope functions corresponding to $|S = 1/2, S_z = \pm 1/2\rangle$ (CB), $|J = 3/2, J_z = \pm 3/2\rangle$ (HH), $|J = 3/2, J_z = \pm 1/2\rangle$ (LH), and $|J = 1/2, J_z = \pm 1/2\rangle$ (SO) Bloch spinors, an eight-band $\mathbf{k} \cdot \mathbf{p}$ Hamiltonian has been diagonalized [76]. All the calculations presented in this chapter are performed with the aid of a home-made code based on finite element method. Details on the calculation of single-particle orbitals are as follows:

(i) *Strain calculation.* To solve for the strain distribution $e_{ij}(x, y, z)$ the strain energy is calculated and minimized for core-shell nanowires using the CM method and generalized minimal residual algorithm (GMRES). The bottom surface is kept fixed (no displacement) while it is assumed that QD stress relaxes at the top surface for some specific points at the shell perimeter (δR_x,δR_y, and $\delta R_x = 0$). Non-uniform discretization has been utilized for better convergence: Refined meshing has been applied to QD and shell regions.

(ii) *Piezoelectric potential V_p.* In order to solve the Poisson's equation associated with the piezoelectric charge density $\nabla \cdot (\mathbf{P}_a + \mathbf{P}_b)$, we utilized the finite element method on an adapted nonuniform three-dimensional grid with gradual growth of the element length outside the shell. Considering a $150 \times 150 \times 150\,\mathrm{nm}^3$ cell, potential was computed on, on average, 2.5×10^7 elements, including 1.26×10^7 elements inside and 1.24×10^7 elements outside the nanowire heterostructure (number of elements slightly changes in different geometries). Periodic boundary conditions were applied along the nanowire axis while Dirichlet boundary conditions were assigned to the cell side walls (perpendicular to the growth direction).

[1] The single-particle total wavefunction in multiband envelope function theory is defined as multiplication of the Bloch spinor state and its associated envelope function, that is, $\Psi_{\sigma;v,c}(\mathbf{r}) = \sum_m \varphi^m(\mathbf{r})\,|U^m{}_{k,\sigma;v,c}\rangle$, where σ denotes the particle spin and the Bloch spinor part is defined as $|U^m{}_{k,\sigma;v,c}\rangle = \exp(\mathbf{k} \cdot \mathbf{r}) u^m{}_{k,\sigma;v,c}(\mathbf{r})$; thus, the symmetry properties of both parts contribute in the total symmetry character.

(iii) *Single-particle states.* An eight-band $\mathbf{k}\cdot\mathbf{p}$ Hamiltonian is diagonalized while applying Dirichlet boundary condition at the nanowire sidewalls (external boundaries of the shell region) and preserving the continuity of probability current across the interior interfaces. The nanowire length was specified to be 150 nm so that the QD energy levels and their envelope functions are not affected by the periodic or Dirichlet boundary conditions at the two hypothetical nanowire ends. The average length of elements inside the QD region was chosen as small as 0.4 nm. This small length was preserved inside shell and nanowire regions close to the QD, growing very slowly toward the nanowire terminating boundaries. GMRES algorithm along with incomplete LU (ILU) preconditioner have been employed to solve $\mathcal{H}_{\mathbf{k}\cdot\mathbf{p}}$. $\mathbf{k}\cdot\mathbf{p}$ parameters used in this chapter have been taken from Refs. [130] and [105].

3.5.2 Symmetry characters of net confinement and orbitals

Series A, self-assembled QDs

Many theoretical works have already been devoted to study the single-particle states in self-assembled QDs. Structures having drawn more attention in these analyses include pyramidal and lens-shaped QDs [105, 80], with their geometries supporting elevated C_{4v} and $C_{\infty v}$ symmetry characters, respectively. The net confinement, however, may contain lower degrees of symmetry depending on the growth orientation. Pyramidal QDs suffer from an extreme axial anisotropy which may be moderated by truncating their top region. This eventually brings down the symmetry of electron and hole orbitals to C_{2v}: In anisotropic [001]-oriented QDs, single-particle orbitals tend to extend toward [110] and $[1\bar{1}0]$ directions as a result of piezoelectricity; thus, the prominent exciton emission lines are seen along these directions. This suggests that the associated bright excitons $X_{B;1,2}$ are polarized along [100] and [010], as the polarization of each emission line is a linear combination of bright exciton polarizations due to the spin-orbit coupling. Any structural defect perturbs the equal weights in this linear combination and thus deviates the polarizations from [110] and $[1\bar{1}0]$ [109]. Schliwa et al. have argued that how properly adding annealing steps may restrain this deviation [105, 135]. Analogous to self-assembled pyramids, orbitals choose C_{2v} symmetry in lens-shaped QDs. However, since the geometry is $C_{\infty v}$ symmetric, replacing (001) substrate with (111) lifts up the net confinement symmetry to C_{3v} leading to a vanishing FSS. Apart from growing highly symmetric structures, strain manipulation, electric field, and magnetic field (acting like an extra SO interaction [6, 81]) may be applied to remove FSS.

Series B-1 and B-2 NWQDs

Unstrained series B-1 NWQDs are $D_{\infty h}$ symmetric. The piezoelectric field, however, follows the symmetry imposed by shear strain components ($e_{yz} = C_z^{\pi/2} e_{xz}$, and $P_z(r < D_D) \approx 0$, since e_{xz} is trivial inside QD), leading to D_{2d}-symmetric potential; see Figure 3.2(a), left panel. Piezoelectric potential is negligible deep inside the QD insertion where the dense parts of electron and hole orbitals commonly exist. Figure 3.2(b) (left panel) illustrates Fourier transform of the s-shell electron and hole orbitals, $\rho_{e_0} = |F(|\varphi_e^s(\mathbf{r})|^2)|$ and $\rho_{h_0} = |F(|\varphi_h^s(\mathbf{r})|^2)|$, along with the differential probability density $\Delta\rho_0 = \rho_{e_0} - \rho_{h_0}$ in k space. ρ_{e_0}, ρ_{h_0}, and $\Delta\rho_0$ are shown on the (001) plane in the vicinity of the Γ point ($2\,\mathrm{nm}^{-1} \times 2\,\mathrm{nm}^{-1}$ large area). $\rho_{e(h)}$ spreadout in k space represents a measure of electron (hole) density in real space: Since ρ_{h_0} is more extended than ρ_{e_0} in k space, we expect its orbital $|\varphi_h^s(\mathbf{r})|^2$ to be relatively denser. $\Delta\rho_0$ is influenced by the piezoelectric effect suppressing e/h spatial overlap; thus, the corresponding oscillator strength $M_{|s_e\rangle,|s_h\rangle}$ and its average value determines e/h dipole.

Noticeable portions of orbitals move toward the QD corners due to the net result of first and second piezoelectric potentials. Figure 3.3(a) shows e/h orbitals $\Phi_{e,h}^{s,p} = \sum_{m_J} |\varphi_{e,h}^{m_J,s,p}|^2$ (m_J sweeps over the total angular momentum numbers) for the s shell $|e_0, h_0\rangle$ (ground state) along with the two excited p shells, $|e_1, h_1\rangle$ and $|e_2, h_2\rangle$. Axial confinement ($\Xi_{v;e} = \Delta_{\mathrm{CB}} + \langle \mathcal{H}_s \rangle_{v;e}$ for electron and $\Xi_{v;h} = \Delta_{\mathrm{VB}} + \langle \mathcal{H}_s \rangle_{v;h}$ for hole) is tight when a_h gets relatively small, for example, ≤ 0.2, preventing flexible orbital deformations. Furthermore, since the piezoelectric potential scales up in proportion to the QD size, the built-in field has not yet penetrated the QD interior considerably: $\langle \Psi_{h_0} | V_p | \Psi_{h_0} \rangle = \langle V_p \rangle_{h_0} = 0.60$ meV and $\langle V_p \rangle_{e_0} = -0.33$ meV. Increasing a_h leads to vertical spreading of electron and hole orbitals. The hole particle then responds sensitively to the confinement variations (comprising piezoelectric effect) because of the higher effective mass m^* it has (the reason is further detailed in the following): $\langle V_p \rangle_{h_0} = 4.37$ meV and $\langle V_p \rangle_{e_0} = -0.74$ meV for $a_h = 0.4$. This behavior can be observed in the $|h_0\rangle$ orbital, where [110] and [1$\bar{1}$0] nodes are not aligned vertically (likewise, $|h_1\rangle$ and $|h_2\rangle$ orbital lobes at the [110] and [1$\bar{1}$0] corners are not in the same level).

In series B-2 NWQDs, all three shear strain components show similar patterns under 120° in-plane rotations, that is, $C_z^{2\pi/3} e_{ij} = e_{i\pm1\,j\pm1}$, where $i, j \in \{x, y, z\}$. The same symmetry character, C_{3v}, belongs to the piezoelectric potential as can be seen in Figure 3.2(a) right panel. Different components of piezoelectric field then add up to build a [111]-directed field: The oppositely signed isosurfaces at the top and bottom interfaces in 3.2(a) right panel, ensure the presence of a non-negligible axial electric field. This axial field may suppress $M_{|s_e\rangle,|s_h\rangle}$ by splitting the electron and hole orbitals. Having considered InP hosting nanowire, the amplitude of piezoelectric potential is not comparable to that of In(Ga)As/GaAs heteroinsertions. Hence, the internal axial field in [111]-oriented

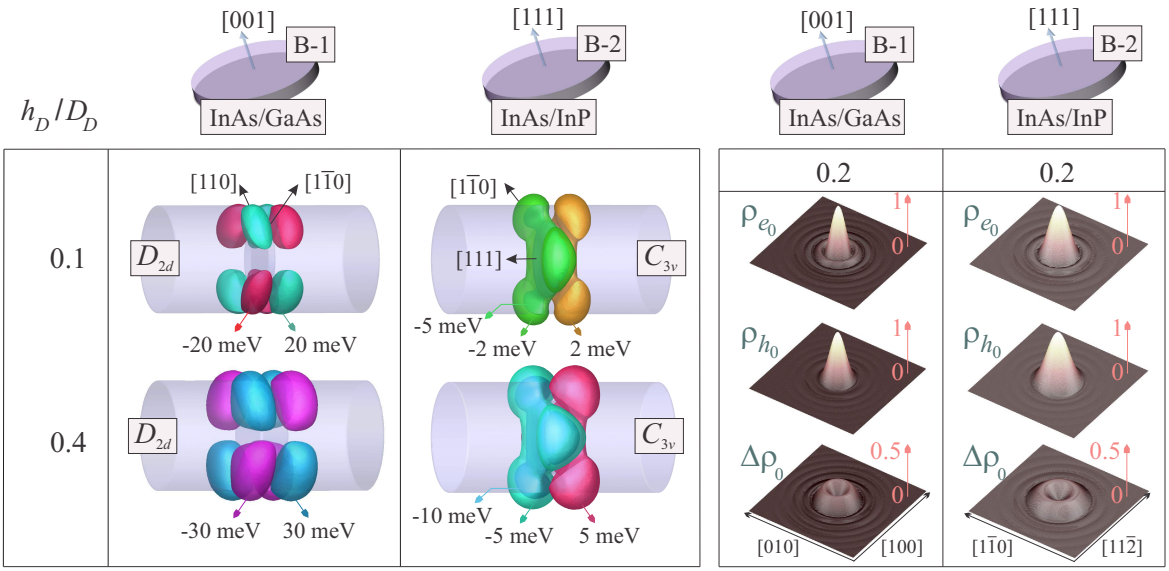

Figure 3.2: (a) Piezoelectric potential in series B-1 and B-2 NWQDs illustrated for a_h equal to 0.1 and 0.4. (Left) 20- (30-) and −20- (−30-) meV isosurfaces shown for series B-1 NWQDs. The potential has D_{2d} symmetry since the top and bottom isosurfaces are equivalent $\langle V_p^U \rangle = -\langle V_p^D \rangle$ and $\langle V_p^U \rangle = e^{i\pi/2} \langle V_p^D \rangle$. (Right) 2- (5-), −2- (−5-), and −5- (−10-) meV isosurfaces for series B-2 NWQDs. The piezoelectric potential exhibits C_{3v} symmetry; $\langle V_p^U \rangle = e^{i2\pi/3} \langle V_p^U \rangle$ and $\langle V_p^U \rangle = -e^{i\pi/3} \langle V_p^D \rangle$. (b) Electron, hole, and differential charge densities shown in k space for seris B-1 (left panel) and B-2 (right panel) with $a_h = 0.2$. Fourier transform is plotted on (001) and (111) planes for series B-1 and B-2, respectively.

InAs/GaAs NWQDs becomes remarkably stronger when indium concentration is large. Nevertheless, $\Delta\rho_0$ in series B-2 ([111]-oriented InAs/InP) is comparable to series B-1 ([001]-oriented InAs/GaAs), implying equivalent e/h dipole; see Figure 3.2(b) right panel.

$D_{\infty h}$ symmetry of QD insertion in series B-2 translates to the conformity of orbital symmetry and that of strain-induced potentials. Our calculations show that the net confinement experienced by e/h has C_{3v} symmetry in s and p states. When a_h is increased $0.2 \rightarrow 0.4$, $\Xi_{v;e,h}$ relaxes and piezoelectric potentials around the top and bottom interfaces increase. The single-particle orbitals then respond freely to the built-in electric field by moving upward or downward, as illustrated in the bottom panel of Figure 3.3. Therefore, we expect at least one pair of degenerate bright states ($|\pm 1\rangle_{hh}$ or $|\pm 1\rangle_{lh}$) having pure and isotropic in-plane polarization for the ground-state excitonic transition.

Before proceeding further, let us clarify why electrons and holes adapt differently to the geometrical variations and potential distortions. Owing to the small effective mass of electron m_e^*, its average dispersion $E(k)$ is sharply curved in k space, leading to an abrupt change of kinetic energy in response to any small variation of wavefunction in the real space. Thus, the electron orbital is rather resistant to any potential deformation. The hole orbital, on the other hand, accepts any trivial detail of the confinement to keep its potential energy minimized (dissimilarity between electron and hole behaviours is further detailed in Sec. 4.5). This can be clearly observed in $|h_0\rangle$ orbitals, where the main character of wavefunction comes from the HH band: Even for $a_h = 0.2$, the $|h_0\rangle$ orbital has been to some extent shifted toward the top interface, where negative piezoelectric potential exists; see Figure 3.2(a). Further enlargement in [111] direction lifts the hole orbital remote from the electron orbital since a nearly uniform electric field $\langle p_z \rangle$ exists in this region. The expectation values given in Table 3.2 affirm the dissimilarity of electron and hole s orbitals: Once a_h increases, $\langle V_p \rangle_{h_0}$ grows because $|h_0\rangle$ orbital immediately attempts to save its spatial overlap with negative piezoelectric potential. Conversely, $\langle V_p \rangle_{e_0}$ gets suppressed despite the increase of $\langle V_p \rangle$ as $|e_0\rangle$ orbital follows the positive piezoelectric potential very slowly.

Series C-1 and C-2 NWQDs

Piezoelectric potential is shown for series C-1 in Figure 3.4(a) left panel. Irrespective of their opposite signs, piezoelectric isosurfaces at the top interface become slightly different from their bottom counterparts given larger a_h. Although the discrepancy of the top and bottom interfaces results in a global C_{2v} symmetry, but as long as the ratio between top and bottom facet areas is not considerably below 1, for example, ≥ 0.8, one can still assign this series a $\sim D_{2d}$ symmetry. This symmetry reduction would occur in envelope functions

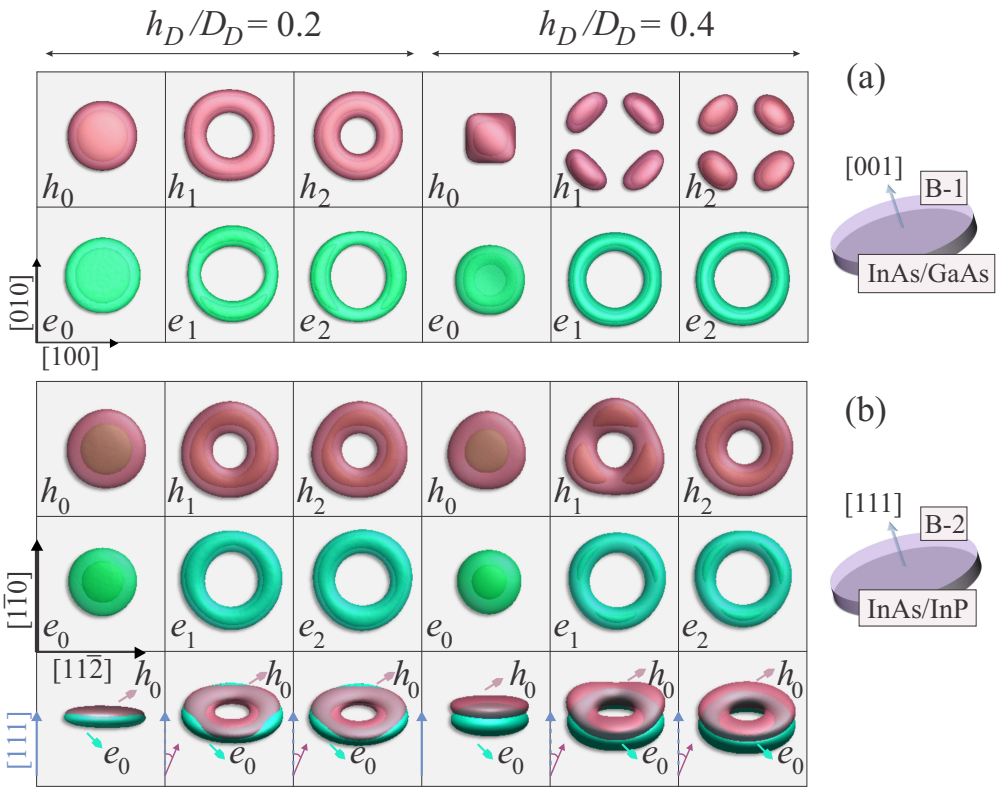

Figure 3.3: Comparison of the s-shell and p-shell electron and hole orbitals in (a) series B-1 and (b) series B-2 NWQDs for a_h equal to 0.2 and 0.4. (a) Series B-1 electron and hole orbitals represent D_{2d} symmetry. Symmetry character becomes clearer for $a_h = 0.4$ since the tightness of $\Xi_{v;e,h}$ is reduced and orbitals reshape with less restriction. (b) Probability densities exhibit C_{3v} symmetry in series B-2 NWQDs irrespective of a_h. (Bottom panel) Side view shows the relative position of electron and hole orbitals. For the sake of clarity, the coordinate system is slightly rotated for p states. Increasing the QD height leads to the spatial separation of electron and hole probability densities.

	a_h	$\langle V_p \rangle_{e_0}$	$\langle V_p \rangle_{h_0}$	$\langle V_{\mathrm{Hy}} \rangle_{e_0}$	$\langle V_{\mathrm{Hy}} \rangle_{h_0}$	$\langle V_{\mathrm{Bi}} \rangle_{h_0}$
Series B-1	0.1	−0.09	0.12	295	−34.9	148
	0.2	−0.33	0.60	325	−34.1	136
	0.3	−0.55	1.77	301	−29.6	112
	0.4	−0.74	4.37	267	−24.5	94.2
	0.5	−0.93	9.26	234	−20.6	83.2
Series C-1	0.1	−0.10	0.15	296	−34.6	147
	0.2	−0.33	0.83	329	−33.5	135
	0.3	−0.76	3.37	308	−28.8	115
	0.4	−0.71	6.01	276	−25.3	105
	0.5	−0.68	6.56	241	−23.6	103

Table 3.1: Expectation values of piezoelectric V_p, hydostatic V_{Hy}, and biaxial V_{Bi} potentials for ground-state electrons and holes in series B-1 and C-1 NWQDs. $\langle V_p \rangle_{e,h}$ reaches saturation in series C-1 for $a_h \geq 0.4$ due to the competition between geometry confinement and piezoelectric effect. Values are given in meV.

and thus $\rho_{e(h)}$. Figure 3.4(b) illustrates ρ_{e_0}, ρ_{h_0}, and $\Delta\rho_0$ on (001) plane ($2\,\mathrm{nm}^{-1} \times 2\,\mathrm{nm}^{-1}$ large area) in k space. ρ_{e_0} (ρ_{h_0}) exhibit C_{2v} symmetry polarized along $[1\bar{1}0]$ ($[110]$). This polarization is more pronounced for ρ_{h_0} due to the hole's larger effective mass. Due to the same reason ρ_{h_0} undergoes further deformation when confinement relaxes ($a_h = 0.2 \rightarrow 0.4$). Moreover, rapid growth of $\Delta\rho_0$ implies e/h dipole enhancement in response to strain-induced potentials.

Figure 3.5(a) depicts the s- and p-shell electron and hole orbitals in series C-1 NWQDs, where the slight axial anisotropy introduced to the geometry breaks the D_{2d} symmetry down to C_{2v}: hole and electron orbitals extend along $[110]$ and $[1\bar{1}0]$, respectively. Since the polarization of exciton follows the symmetry character of electron and hole orbitals,we expect the appearance of FSS in this case. As implied from the right panel ($a_h = 0.4$), QD height shall be maintained small in order to avoid further polarization. During the modelings we observed that the first- and second-order piezoelectric potentials have opposite signs in these series of NWQDs, thus attempting to cancel out each other. However, linear term heavily dominated the quadratic term in contrast to the full pyramid or lens-shaped QDs, where the second order competes with the first order or even rules the total piezoelectric polarization [105]. In Series B-1, enlarging h_D cannot change the ordering between the two terms. Conversely for series C-1 NWQDs, enhancing a_h increases the shear strain besides its overlap with strain diagonal components, leading to a stronger quadratic term. Table 3.1 shows the calculated expectation values of strain-induced potentials ($\langle V_p \rangle$, $\langle V_{\mathrm{Hy}} \rangle$,

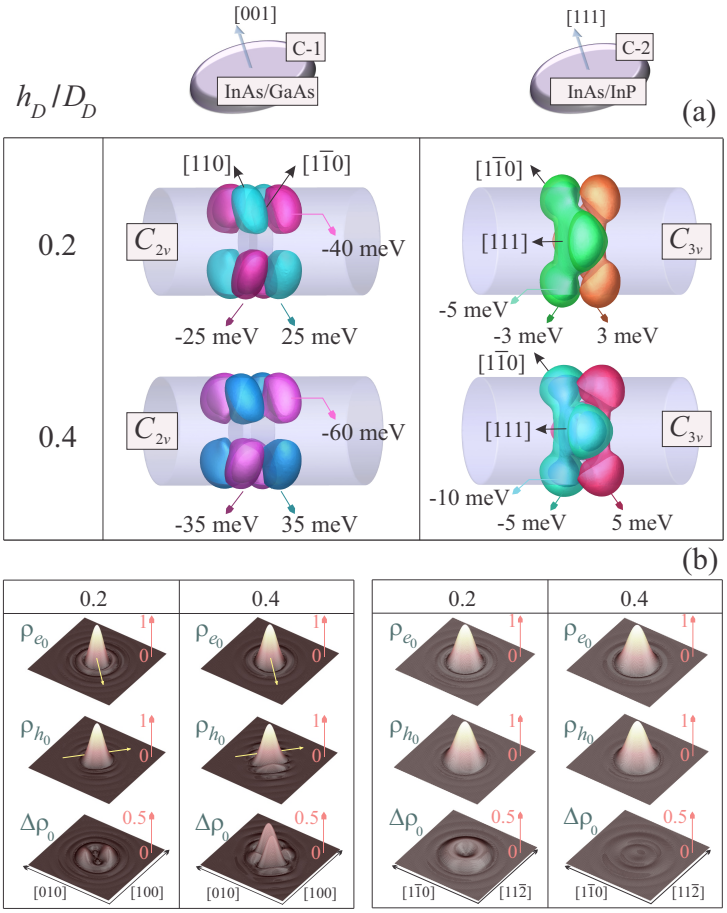

Figure 3.4: (a) Left panel: Piezoelectric potential in series C-1 and C-2 NWQDs illustrated for a_h equal to 0.2 and 0.4. (Left) 25- (35-), -25- (-35-), and -40- (-60-) meV isosurfaces shown for series C-1 NWQDs. The potential has C_{2v} symmetry since the amplitudes of top and bottom isosurfaces are not equivalent; $\langle V_p^U \rangle \neq -\langle V_p^D \rangle$. (a) Right panel: Piezoelectric potential in series C-2 NWQDs illustrated for a_h equal to 0.2 and 0.4. -3-, (-5-), 3- (5-), and -5- (-10-) meV isosurfaces for series C-2 NWQDs presenting C_{3v} symmetry; (b) Left panel: Electron, hole, and differential charge densities shown in k space on the (001) plane for seris C-1 NWQDs with $a_h = 0.2$ and 0.4. All densities are polarized due to the C_{2v} symmetry of orbitals in real space. Right panel: Electron, hole, and differential charge densities shown on (111) plane for series C-2 NWQDs with $a_h = 0.2$ and 0.4. $\Delta\rho_0$ is suppressed for $a_h = 0.4$ since $\Xi_{v;h}$ pushes $|h_0\rangle$ orbital against the built-in piezoelectric field.

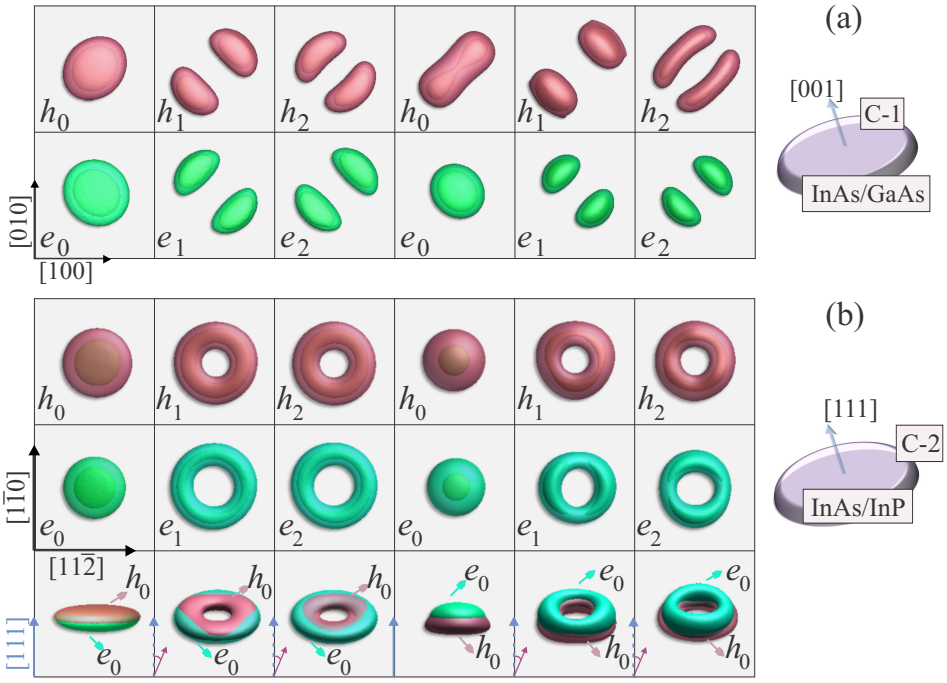

Figure 3.5: S-shell and p-shell electron and hole orbitals in (a) series C-1 and (b) series C-2 NWQDs for a_h equal to 0.2 and 0.4. (a) Symmetry of the single-particle orbitals decrease in cone-shaped NWQDs (C_{2v}) due to the pronounced role of non-symmetric piezoelectric potential. (b) S- and p-shell orbitals of hole and s-shell orbital of electron represent C_{3v} symmetry. (Bottom panel) Probability density of electrons and holes do not have the maximum spatial overlap as a result of internal electric field.

and $\langle V_{\mathrm{Bi}} \rangle$) for series B-1 and C-1 NWQDs. Both hydrostatic and biaxial deformation potentials experienced by the e_0/h_0 orbitals diminish via enlarging the QD size, leading to (1) higher excitonic band gaps and (2) smaller HH-LH energy splitting.

Looking at their axial anisotropy, cone-shaped NWQDs are the moderated version of their lenslike twins with $C_{\infty v}$ symmetry. In lens-shaped QDs, however, the top interface smoothly curves providing distinct boundary conditions for the strain distribution and piezoelectric potential. We note that this mesoscopic view carelessly ignores the possible defects or dissimilarities in the atomic scale which may distinguish the top and bottom interfaces even in isotropic geometries [136]. We emphasize again that the CM model essentially neglects these kinds of imperfections, where an intrinsic but hidden source of FSS lies in the structure. Nevertheless, the conclusions given here for series C-2 NWQDs

	a_h	$\langle V_p \rangle_{e_0}$	$\langle V_p \rangle_{h_0}$	$\langle V_{\mathrm{Hy}} \rangle_{e_0}$	$\langle V_{\mathrm{Hy}} \rangle_{h_0}$
Series B-2	0.1	−0.24	0.41	136	−21.4
	0.2	−0.52	1.48	157	−18.7
	0.3	−0.58	2.62	147	−15.7
	0.4	−0.46	3.77	131	−13.3
	0.5	−0.28	5.11	115	−11.9
Series C-2	0.1	−0.07	0.54	139	−21.1
	0.2	0.18	1.6	155	−18.2
	0.3	0.78	1.73	146	−15.1
	0.4	1.46	−0.03	131	−12.5
	0.5	2.24	−1.84	116	−10.9

Table 3.2: Expectation values of piezoelectric and hydostatic potentials for ground-state electrons and holes in series B-2 and C-2 NWQDs. The expectation value of biaxial strain is trivial because diagonal components of strain tensor become equal in weight when the growth direction is [111]. Sign of $\langle V_p \rangle_{e_0,h_0}$ is inverted in series C-2 since axial confinement pushes probability densities against the piezoelectric field. Values are given in meV.

are extensible to self-assembled lens-shaped QDs at least from the viewpoint of confinement symmetry.

As could be understood from the above discussions regarding the previous geometries, one of the principal templates resolving the confinement symmetry is the NWQD growth direction. Consequently, similar to series B-2 NWQDs, we predict a C_{3v}-like symmetry for series C-2. This can be easily deduced looking at their piezoelectric isosurfaces in Figure 3.4(a). The appearance of oppositely signed potentials at both sides reflects [111]-oriented dipole and possibly dropping $M_{|s_e\rangle,|s_h\rangle}$. This drawback seems to be a unique feature of QDs grown on (111) substrate although it is partially moderated in cone-shaped geometries: $\Delta\rho_0$ gets suppressed when $a_h = 0.4$, as shown in Figure 3.4(b). In fact, the tendency of the hole orbital to cover all of the details of confinement causes a significant part of it to leak toward the bottom side of NWQD despite the presence of an up-pushing electric field.

C_{3v} symmetry of the hole orbitals in both s and p shells indicates how precisely they follow the potential spreadout [see Figure 3.5(b)]. For electrons, however, only the ground state (s shell) represents an elevated C_{3v} symmetry, while p-shell orbitals have a mainly C_{2v} character, especially when QD height increases. This behavior can be attributed to the electrons reluctance of accepting the small contribution reserved by piezoelectric effect in the total confinement. The hydrostatic potential V_{Hy} also exhibits almost a constant

value over the NWQD interior with tiny variations adjacent to the borders. Although these variations provide it with a C_{3v} character, only dilute parts of electron orbital feel this symmetry while the denser parts see the constant landscape thus primarily obey the geometry.

Series D NWQDs

Any lateral elongation imposed on NWQD structure even more complicates the interplay between the potentials contributing in the total confinement. Basically in series B and C, the $D_{\infty h}$ and $D_{\infty v}$ symmetries of geometry reduce to D_{2h} and C_{2v}. When piezoelectricity comes to play, the single-particle wavefunctions are already polarized; thus, any elongation along each arbitrary in-plane axis pronouncedly disturbs the exciton net polarization. The total outcome is then summarized to how these two effects might support or cancel each other out. Here we analyze the impact of elongation on series B-1. The overall description is then credible to some extent for the other series. Elongation puts no distinction between the two orthogonal in-plane directions [110] and [1$\bar{1}$0] since QD is $D_{\infty h}$ symmetric. We elongated the QD insertion 50 % in [100] orientation. There is no experimental evidence reporting such a large amount of lateral elongation [115, 117, 69, 118, 119]. We chose this uncommon value to demonstrate the ultimate deviation of orbitals from their usual spreadout. As illustrated in Figure 3.6(a), s-shell orbitals extend along the axis of elongation giving rise to excitons polarized in the same direction. Since the original piezoelectric potential is D_{2d} symmetric, s states have been predominantly influenced by lateral relaxation rather than piezoelectric field. In the case of p states, a trade-off between these two arises as a_h, and thus piezoelectric potential near top and bottom interfaces, increase. It is known that degeneracy of p-state $|e_{i=1,2}\rangle$ energies for the electrons relies on the polarization of the corresponding orbitals and thus the underlying confinement [137]. As we see in the next section, p-state energy splitting notably diminishes for highly symmetric NWQDs due to the absence of sizable shear strain. Figure 3.6(b) shows that electron p states are initially degenerate, but the degeneracy is lifted up considerably after prolonging the QD. The energy separation becomes larger for $h_D/D_1 = 0.4$. We ascribe this to different measures of $\Xi_{v;e,h}$ present in the two QDs. Electron states are less confined in the second QD; thus, the related p-shell orbitals freely reshape deviating further from their counterparts.

3.5.3 Single-particle energies

In the previous section we demonstrated that as long as the morphological symmetry with respect to the growth axis is preserved, the vertical aspect ratio cannot break the

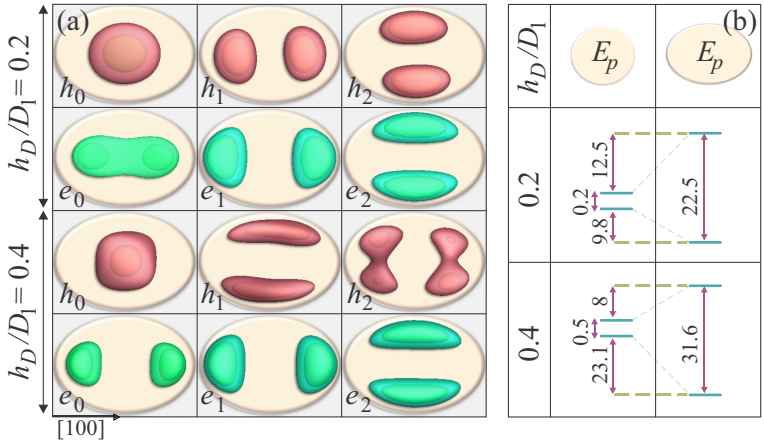

Figure 3.6: (a) S- and p-shell electron and hole orbitals in a [100]-elongated (50%) NWQD grown along [001] orientation; $D_1 = 20$ nm and $D_2 = 30$ nm. Geometry dictates C_{2v} character for all orbitals irrespective of the strain-induced potentials. Electron orbitals are rather insensitive to the QD height as they resist piezoelectric potential variations. (b) Electron p-state splitting as a function of a_h. Values are given in meV.

orbital symmetry. It, however, easily manipulates the single-particle localization energy. In this regard, two major processes are affected by a_h. The first one is the interplay between hydrostatic and biaxial strains. Let us consider series B-1 NWQDs. Biaxial strain deep inside the QD is negligible provided that the diameter and height are almost equal ($a_h = 1$). Hydrostatic strain is negative due to the compressing forces exerted by the surrounding nanowire and shell. Decreasing QD height perturbs the balance established between the in-plane strain components (e_{xx}, e_{yy}) and the perpendicular component (e_{zz}). Enhanced lateral forces then cause the QD insertion to spread axially, leading to a relative dominance of e_{zz} component over e_{xx} and e_{yy}. This gives rise to a measurable negative biaxial strain separating the HH-LH bands: $\mathcal{H}_s^{hh} = -a_v e_{\mathrm{Hy}} + b_v e_{\mathrm{Bi}}$, $\mathcal{H}_s^{lh} = -a_v e_{\mathrm{Hy}} - b_v e_{\mathrm{Bi}}$, $a_v > 0$, $b_v < 0$. Accordingly, uniform increase of biaxial strain over the QD space lifts the HH band, yielding a local increase of hole ground-state energy E_0^h. Meanwhile, the absolute value of hydrostatic strain grows and pushes the hole energies upward. The overall impact of strain on the single-particle energies can be seen in Figure 3.7: The upward shift observed in hole energies moving from $a_h = 0.5$ down to 0.2 returns to the increase in the absolute values of hydrostatic and biaxial strains. Since both $\langle V_{\mathrm{Hy}} \rangle_{h_0}$ and $\langle V_{\mathrm{Bi}} \rangle_{h_0}$ evolve monotonously versus a_h (see Table 3.1), the nonmonotonous change of hole energies is attributed to the second process.

Second process is the axial confinement experienced by each particle along the quanti-

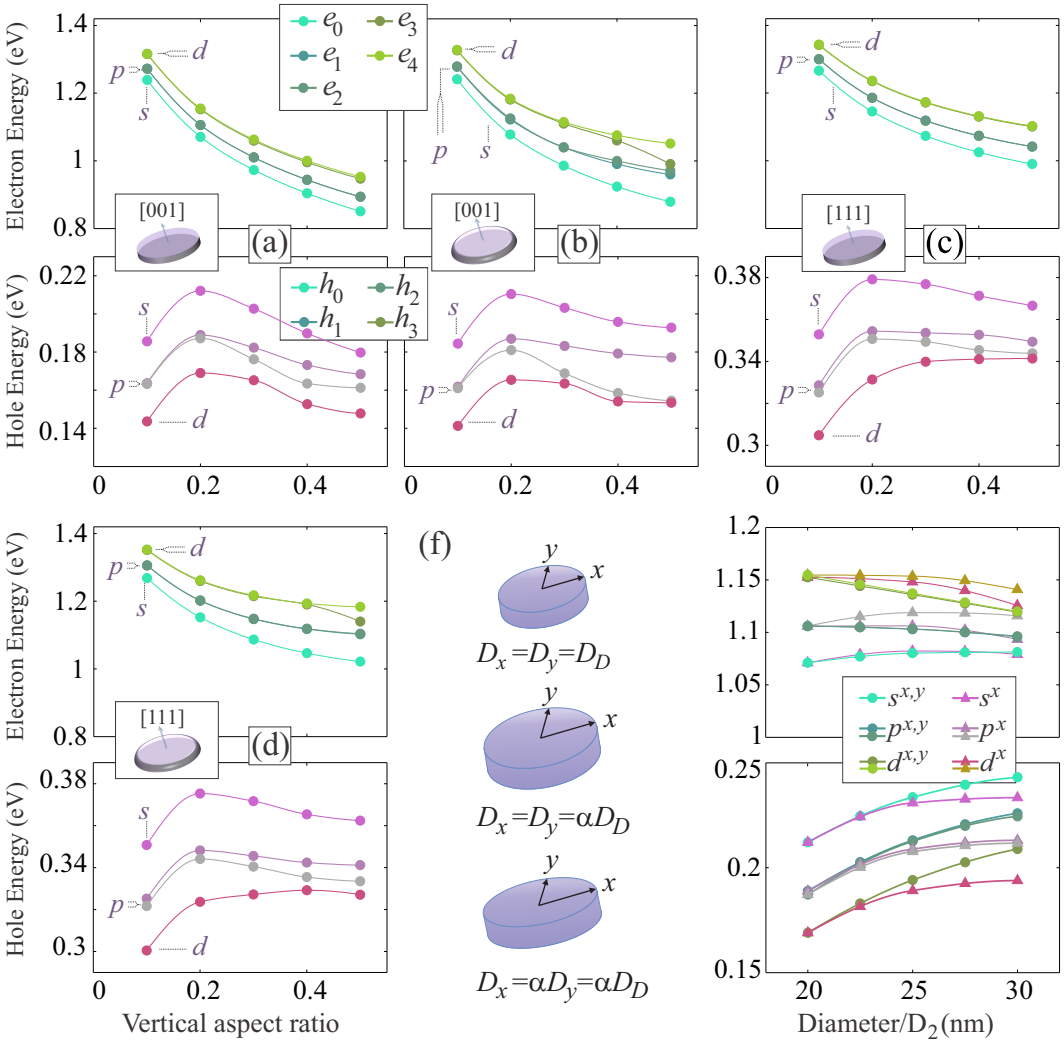

Figure 3.7: Electron and hole energies at the single-particle level shown for series (a) B-1, (b) B-2, (c) C-1 and (d) C-2 QDs against vertical aspect ratio. Reference energies are the VB edges of homogeneous GaAs and InP nanowires; that is, $E^0_{\mathrm{VB,GaAs}}$ and $E^0_{\mathrm{VB,InP}}$. Curves are interpolated data displaying the evolution of single-particle energies. (e) Effect of lateral enlargement for series B-1 (D) NWQDs: s-, p-, and d-shell energies are illustrated versus the QD diameter (D_2) for uniform (x-directed) elongation. x and (or) y state that NWQD is elongated in the [100] and (or) [010] crystallographic directions. The QD height is kept fixed equal to 4 nm.

zation axis which becomes important for lower a_h. Development of biaxial strain e_{Bi} during the reduction of a_h suppresses the LH fraction participating in the hole s state. This results in a higher effective mass $m^*_{h;z}$ felt by holes residing in the ground state (either $\sigma = \Uparrow$ or $\Downarrow$). The corresponding orbital, therefore, adapts more sensitively to the confinement profile. When a_h drops below ~ 0.2, $\Xi_{v;h}$ compresses the hole orbital. Its large effective mass provides it a semi-flat dispersion around Γ_8 and allows it to remain inside QD accumulating further kinetic energy (see Sec. 4.5). Due to the same reason, the hole orbital cannot swell out into the nanowire core and gain potential energy. Considering that both $|\langle V_{\mathrm{Hy}}\rangle|_{h_0}$ and $|\langle V_{\mathrm{Bi}}\rangle|_{h_0}$ are ascending for $a_h = 0.2 \rightarrow 0.1$, we ascribe the ~ 30 meV redshift seen in the hole energies to the second process. For the entire range shown in Figure 3.7, electron energies experience a blueshift moving backward ($a_h = 0.5 \rightarrow 0.1$), because of the following. (1) $a_c \gg a_v$; hence, hydrostatic strain affects electron localization energies significantly. (2) The electron orbital shrinks while QD height approaches smaller values, raising its kinetic energy. For a_h lower than ~ 0.2, the electron orbital diffuses into the nanowire and accumulates potential energy.

An inverse situation occurs when QD height remains fixed while its diameter extends [see Figure 3.7(e), where the energy levels are plotted versus the QD diameter]. Two types of QDs are examined: series B-1 and D. Irrespective of the energy shifts happening to the electron and hole states, 1D elongation in series D (C_{2v} symmetric) is responsible for the splittings between p and d shells. Blueshifts are saturated for the hole states as [100]-oriented effective mass $m^*_{h;x}$ (assuming [100]-directed elongation) rapidly gets lighter; thus, the hole orbital becomes insensitive to any further size variation in this direction and stops exchanging its kinetic energy.

As can be deduced from Figure 3.7, single-particle energies in all the highly symmetric NWQDs exhibit a similar behavior versus a wide range of variations in a_h. P-state splittings do not exceed 1 meV in series B-1 and B-2. Even in series C-1 and C-2, splittings are small particularly for flat QDs where shear strain is trivial. They, however, strongly depend on the angle between the growth axis and the QD side facets, as it determines the strength of axial anisotropy. In addition, energetic separation of the ground and excited states in the VB reflects the measure of effective mass: The smaller the splitting, the lager the effective mass. Consequently, effective masses along the quantization axes, $m^*_{[001]}$ and $m^*_{[111]}$, are almost equivalent as no serious distinction can be made between the VB splittings seen in all plots.

3.5.4 HH-LH and HH-SO band mixing

As described in Sec. 3.4.1, band mixing is a direct consequence of lateral or axial anisotropy. The strength of wave-function coupling and state impurity has been well studied for pyramidal QDs in both theoretical and experimental works. Results given by Karlsson et al., based on their polarization-sensitive micro-PL measurements on In(Ga)As/Al(Ga)As QDs, indicate that a relatively pure character exists in the upmost valence bound states [138]. Niquet and Mojica theoretically showed that this purity seemingly relies upon a_h [139]. Their results demonstrate that enlarging a_h increases the LH percentage in the ground state. This can be explained through the reduction occurring in biaxial strain and relaxation of $\Xi_{v;h}$, which makes in-plane and perpendicular quantizations comparable, thus ending up to higher LH character obtained by the hole ground state. We expect that the same rule applies to series C-2 QDs as they respond analogously to both strain-induced confinement and $\Xi_{v;h}$.

Figure 3.8(a) depicts HH and LH contributions in the ground-state wavefunction of series B-1, C-1, and D NWQDs versus a_h. In series B-1, the angular momentum quantization axis is [001]. The hole orbital expectedly redistributes when $\Xi_{v;h}$ slightly quenches. Meanwhile, HH-LH splitting tends to vanish as the biaxial strain relaxes. Both effects result in higher LH percentage in the s-shell wavefunction. Qualitatively, similar phenomena occur in series C-1 NWQDs except that shear strain more effectively takes part in the band mixing. According to Sec. 3.4.1, the presence of nontrivial shear strain then justifies higher LH fractions observed for series C-1 comparing to series B-1 NWQDs. The impact of lateral elongation on HH/LH proportion is also examined. HH percentage remains fixed for a 50% additional elongation in [100] ([010]) direction, while the LH fraction decreases. This reduction translates to larger, although small, SO character gained by the bound state. The weak response of the hole ground state can be attributed to its large effective mass $m^*_{[001]}$: For this range of a_h, $\Xi_{v;h}$ is dominant. The hole particle then becomes lighter along the in-plane directions, thus hesitating to adapt the lateral variations of geometry.

The SO band is energetically away from the ground state (in the order of Δ_0), thus weakly participates in s-shell envelope function. Figure 3.8(b) illustrates the contribution of each character (HH, LH, and SO) in the s-shell nonexcitonic oscillator strength $M_{|s_e\rangle,|s_h\rangle}$. Although $M^{so}_{|s_e\rangle,|s_h\rangle}$ relies also on $|e_0\rangle$-orbital and SO-orbital overlap, its very small amplitude confirms that $|\varphi^s_{h;so}|^2 \ll |\varphi^s_{h;hh}|^2$ and $|\varphi^s_{h;lh}|^2$. The SO character generally grows with a_h as can be understood from the single-particle Hamiltonian, where HH-SO coupling is a direct function of shear strain: $\langle hh_2|\,\mathcal{H}_s\,|so_2\rangle = -\langle so_1|\,\mathcal{H}_s\,|hh_1\rangle = (e_{xx}-e_{yy}) - i\sqrt{2}d_v e_{xy}$ and $\langle so_2|\,\mathcal{H}_s\,|hh_1\rangle = \langle hh_2|\,\mathcal{H}_s\,|so_1\rangle = -1/\sqrt{2}d_v(e_{xz}-e_{yz})$. Accordingly, we observe larger SO character in cone-shaped QDs. The SO orbital becomes non-negligible in p states where energy spacing to SO band is reduced.

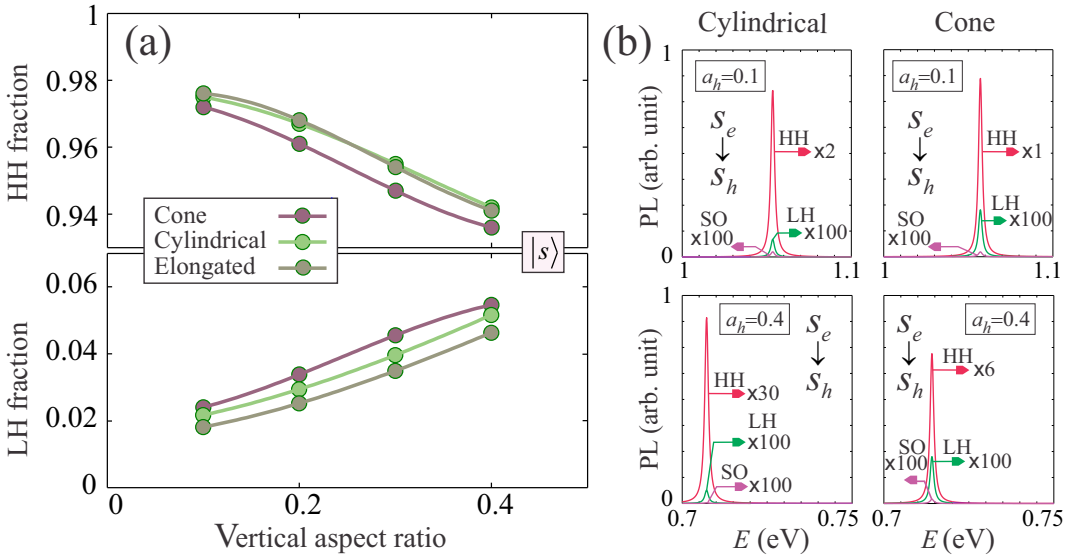

Figure 3.8: HH and LH fractions in the hole ground-state $|s_h\rangle$ wavefunction plotted against the a_h for series B-1, C-1, and D NWQDs. (a) Reduction of $\Xi_{v;h}$ along with the biaxial strain redistribution enhances the LH contribution. Shear strain further increases the LH fraction in series C-1 QDs compared to their B-1 counterparts. In series D QDs, the s-shell hole particle exhibits an insignificant response to in-plane variations as it is quantized strongly along the [001] direction. (b) HH, LH, and SO nonexcitonic oscillator strengths calculated for the $|s_e\rangle \rightarrow |s_h\rangle$ transition in series B-1 and C-1 QDs. LH and SO oscillator strengths generally grow with a_h.

3.5.5 Summary

In this chapter, the electronic structure of core-shell NWQDs is studied at the single-particle level, in which symmetry characters of s- and p-shell orbitals, overlap of e/h probability densities and their spreadout in k space were discussed in detail. We quantitatively demonstrated how strain-induced potentials (including $\langle V_{\mathrm{Hy}}\rangle_{e,h}$, $\langle V_{\mathrm{Bi}}\rangle_{e,h}$, and $\langle V_p\rangle_{e,h}$) change the orbital symmetry, e/h dipole, and s-shell hole character. It was particularly shown that flat NWQDs, even if suffering from axial anisotropy, gain low contribution from LH and SO characters in their s-shell oscillator strength. In the end of this section, we summarized our numerical analysis on NWQDs in Table 3.3 along with data for self-assembled QDs compiled form relevant literature. In addition to the symmetry characters, electron p-state splittings and ground state HH/LH percentages have been compared. These data imply that improving the degree of symmetry and keeping the NWQDs relatively flat suppress LH-band contribution in the ground state, and electron p-state splitting.

Nanowire-QD	Symmetry		Base	Height	Electron p-state	Ground-state	Ground-state
	Shape	Piezo	(nm)	(nm)	splitting (meV)	HH	LH
[001], disk, InAs/GaAs	$D_{\infty h}$	D_{2d}	20	2-8	0.1-0.5	97.5% ($h_D = 4$ nm)	2.17% ($h_D = 4$ nm)
[001], disk, InAs/GaAs	$D_{\infty h}$	D_{2d}	25	4	0.22	97.9%	1.83%
[001], disk, InAs/GaAs	$D_{\infty h}$	D_{2d}	30	4	0.67	98.5%	1.32%
[001], cone, InAs/GaAs	$C_{\infty v}$	C_{2v}	20	2-8	0.8-9.2	97.2% ($h_D = 4$ nm)	2.4% ($h_D = 4$ nm)
[111], disk, InAs/InP	$D_{\infty h}$	C_{3v}	20	2-8	0.4-0.6	95.2% ($h_D = 4$ nm)	2.42% ($h_D = 4$ nm)
[111], cone, InAs/InP	$C_{\infty v}$	C_{3v}	20	2-8	0.6-1.2	93.9% ($h_D = 4$ nm)	3.03% ($h_D = 4$ nm)
[001], elongated, InAs/GaAs	D_{2h}	C_{2v}	20/30	2-8	18.4-31.6	96.8% ($h_D = 4$ nm)	2.53% ($h_D = 4$ nm)
Self-assembled							
[001], pyramid InAs/GaAs	C_{4v}	C_{2v}	17	0.68-8.5	10.2 ($h_D = 3.6$ nm)	$< 93\%$ ($h_D = 0.68$ nm)	$2.8\% - 9.2\%$
[001], lens InAs/GaAs	$C_{\infty v}$	C_{2v}	17	2.9-8.5	0.3 ($h_D = 3.6$ nm)	$< 93\%$ ($h_D = 2.9$ nm)	$2.8\% - 14.4\%$
[111], lens	$C_{\infty v}$	C_{3v}	NA	NA	NA	NA	NA
[111], triangular In(Ga)As/Al(Ga)As	D_{3h}	C_{3v}	16	1.5	NA	89%	$< 11\%$

Table 3.3: Symmetry character, electron p-state splitting and ground-state HH/LH percentages of NWQDs studied here, along with the same data compiled for self-assembled QDs form other theoretical results. Electron p-state splitting increases by enlarging the NWQD height: Minimum and maximum correspond to the smallest and largest heights, respectively. Ground-state HH/LH percentages are given only for a_h equal to 0.2 ($h_D = 4$ nm) in the case of NWQDs. In self-assembled QDs, h_D is mentioned for the available data (NA, not available).

Chapter 4

Few-particle states in Nanowire-QDs

4.1 Introduction

A serious challenge in the modeling of 0D systems comes from the fact that the energy level structure of a QD depends on the population of its levels with charge carriers. The considerations of the previous chapter apply strictly to empty QDs only and are credible for the first charge carrier occupying the dot. Immediately after entering the second or more charge carriers in the QD, three major effects must be taken into account: a) direct Coulomb interactions, b) exchange effects, and c) correlation effects [80].

The balance between these three effects depends on the type of few-body state, that is the number of confined particles and their charges, and on the QD confinement in particular its size and symmetry. In the strong confinement regime where excitons are presumed to be weakly correlated, few-body effect acts as a perturbation to the total confinement. As we will show in the following, the direct Coulomb interaction, i.e. on-site repulsion or attraction, dominates the two other effects in the total energy of few-particle states such as exciton X or biexciton XX. We should notice that in this treatment a strict correspondence between a few-body state and a given single particle state does not exist anymore. This arises from the fact that single particles in our system are correlated to some extent. An initial single particle state deforms its distribution in order to minimize the total energy of the resulted few-body state. Indeed, depending on the energy level of the few-body state the contribution from some certain initial states would be significant. This is especially correct in the case of weakly correlated bound states within a relatively strong confinement. Notice that in our QDs, where a set of orthonormal basis from CB and VB exists, this deformation of an initial single particle state can be expanded on a series of

namely excited states. The few-body state is then an expansion of various configurations constructed from that initial "ground" state and the corresponding excited states. In this description, the correlation exhibits itself as the importance of more than one configuration in each expansion.

The necessity of accounting for the above three effects becomes clear by the following explanations: First, the total wavefunction of two bounded single particles, namely electron and hole in a exciton, could not be simply approximated by the product of their individual wavefunctions (Hartree model). In fact Hartree approximation puts each single particle in the mean field potential of the other one, thus the conditional probability of finding one single particle for a fixed position of the other one is still unaffected. This description fails to present few-body properties since in a few-body complex the carriers are correlated through their spin and Coulomb interactions. Second, the simple single-particle picture fails to describe the binding energies and the spin fine structure splittings of a typical QD, while the precise energy level spectrum is necessary to resolve once delicate phenomena such as photon entanglement are studied in a QD.

We exploit configuration interaction (CI) method to modify our model and include above correlations. Notice that two fundamental assumptions are made in this modification: first, the eigen states of empty QD (single particle bound states) provide a proper, although not unique, set for few-body states expansion. This assumption is proved to be appropriate in the strong confinement regime [125], since the configuration basis are similar to weakly correlated states, confirming that choosing single particle states provides the quick convergence requirements. Second, these correlations are presumed as weak perturbations with respect to a QD strong confinement. As a rule of thumb, the direct Coulomb interaction energies (40-60 meV) are one order of magnitude larger than correlation energies (1-10 meV) and this ratio is a direct function of axial localization in NWQDs. Exchange interactions energies, on the other hand, are approximately tenfold smaller than correlation energies (a few μeVs to 0.4 meV) and contribute in the spin fine structure of multi-particle states.

In this chapter we study the behavior of ground state exciton X_0 (s-shell exciton), positively and negatively charged excitons $X_0^{\pm}$ and biexciton XX_0 in different series of NWQDs introduced in the previous chapter. Our primary concern is to compare the binding energies of these few-particle states under geometrical variations of QD insertion and external perturbations. This provides necessary information on how external fields might be applied to appropriately control the spectral resonances in the regular or time reordering schemes.

4.2 Configuration interaction method

A reliable approach to cover the correlation effects is expanding the true wavefunctions of few-particle states on a set of Slater determinants rather than a single one, as proposed in modified Hartree Fock (HF) approximation. A linear combination of these Slater determinants $|\Theta_{\alpha,\beta}\rangle$ then would be a refined guess for each actual wavefunction: $|\Psi^{nX^m}\rangle = \sum_{l,p;\sigma_e,\sigma_h} \gamma^{nX^m}_{\alpha_l;\sigma_e,\beta_{p;\sigma_h}} |\Theta^{nX^m}_{\alpha_l;\sigma_e,\beta_{p;\sigma_h}}\rangle$, where the expansion coefficients $\gamma_{\alpha,\beta}$ depend on the number of constituting particles in the few-particle state nX^m, $\alpha_l = \{e_{0;\uparrow}, e_{0;\downarrow}, e_{1;\uparrow}, e_{1;\downarrow}, \ldots, e_{l;\uparrow\sigma_e}\}$ and $\beta_p = \{h_{0;\Uparrow}, h_{0;\Downarrow}, h_{1;\Uparrow}, h_{1;\Downarrow}, \ldots, h_{p;\sigma_h}\}$, and the size of the basis set. This combination includes all possible configurations that can be constructed from the available single-particle states, here provided by $\mathbf{k}\cdot\mathbf{p}$ band structure. The number of $\mathbf{k}\cdot\mathbf{p}$ orbitals contributing in $|\Theta_{\alpha,\beta}\rangle$ determines the speed of convergence and accuracy of correlation energies. The weight of correlation coming from the excited shells, $|p_i\rangle$ and $|d_i\rangle$, in the expansion coefficients depends on their energy spacing together with the symmetry of corresponding orbitals.

In our studied NWQDs, the average dielectric constant and dimensions are adequately large so that excitons are considered Wannier type [140]. Thus CI method is able to calculate the state couplings and orbital deformations. The spin part of the bound states is incorporated in their wavefunctions, and its separation from the orbital part is impossible as long as spin-orbit interaction exists. Furthermore, according to the previous chapter, the QD biaxial and shear strain lead to the band mixing between bulk HH and LH bands, suspending the reliability of total angular momentum selection rules. However, the basic model of the excitonic fine structure is still ruled by total angular momentum and these mixing effects enter the model as a perturbation. From the computational point of view, larger energy spacing between the conduction levels allows for truncating to lower excited states. Based on the energy splittings between the higher shells we sometimes change the number of single particle levels involved in the calculations for different series of NWQDs, but it is always maintained above 7 and 9 ($l = 14$ and $p = 18$ states by spin inclusion) for electron and hole, respectively. The hamiltonian for the multiexciton complex can be written as [141]:

$$\mathcal{H}_{nX^m} = \sum_i E^e_i c^\dagger_i c_i - \sum_i E^h_i h^\dagger_i h_i + \frac{1}{2}\sum_{ijkl} J^{d,ee}_{ijkl} c^\dagger_i c^\dagger_j c_k c_l + \frac{1}{2}\sum_{ijkl} J^{d,hh}_{ijkl} h^\dagger_i h^\dagger_j h_k h_l - \sum_{ijkl} J^{d,eh}_{ijkl} h^\dagger_i c^\dagger_j c_k h_l + \sum_{ijkl} J^{\mathrm{exc},eh}_{ijkl} h^\dagger_i c^\dagger_j c_k h_l. \quad (4.1)$$

In above expression, nX^m symbolically stands for a few-particle complex made of n exciton (X) or trion (X^+ or X^-) or alternatively their possible combinations. Summation indexes i (l) and j (k) contain all the information related to the single-particle states (spin included). $h^\dagger$ ($c^\dagger$) denotes the creation operator for holes (electrons). E_e (E_h), J^d , and J^{exc} represent electron (hole) energy, direct and exchange Coulomb interactions, respectively. After diagonalization, the correlation part associated with the off-diagonal terms reveals in the total energy of the excitonic complex.

Since we primarily deal with s-shell complexes (X_0, $X_0^\pm$ and XX_0), we restrict our formulation to the s-shell electron and hole orbitals a their interactions. For an s-shell exciton the direct attractive interaction energy is

$$J_{00}^{d,eh} = \langle \psi^e_{0;\uparrow,\downarrow}(\mathbf{r}_e)\psi^h_{0;\Uparrow,\Downarrow}(\mathbf{r}_h)|\, C\, |\psi^e_{0;\uparrow,\downarrow}(\mathbf{r}_e)\psi^h_{0;\Uparrow,\Downarrow}(\mathbf{r}_h)\rangle = e\,\langle \psi^h_{0;\Uparrow,\Downarrow}(\mathbf{r}_h)|\, V^e_{0;\uparrow,\downarrow}\, |\psi^h_{0;\Uparrow,\Downarrow}(\mathbf{r}_h)\rangle \quad (4.2)$$

where $C = e^2/4\pi\varepsilon_r\varepsilon_0|r_e - r_h|$ and $V^e_{0;\uparrow,\downarrow}$ is the mean-field potential established by s-shell electron $e_{0;\uparrow}$ or $e_{0;\downarrow}$. Both spin degrees of freedom are acceptable since the measure of direct interaction disregards spin configuration, $\{\uparrow,\downarrow\}$ for electrons or $\{\Uparrow,\Downarrow\}$ for holes. Similarly, $J_{00}^{d,hh} = e\,\langle \psi^h_{0;\Uparrow}(\mathbf{r}_h)|\, V^h_{0;\Downarrow}\, |\psi^h_{0;\Uparrow}(\mathbf{r}_h)\rangle$ and $J_{00}^{d,ee} = e\,\langle \psi^h_{0;\uparrow}(\mathbf{r}_h)|\, V^e_{0;\downarrow}\, |\psi^h_{0;\uparrow}(\mathbf{r}_h)\rangle$ where Pauli exclusion principle restricts the spin configuration of identical particles occupying the same state. To obtain mutual Coulomb interactions, the mean-field potential caused by each single particle $V^{m(n)=e,h}_{\sigma_1(\sigma_2)=\uparrow,\downarrow;\Uparrow,\Downarrow}$ shall be calculated through solving Poissons equation:

$$\nabla\cdot\left(\varepsilon_0\varepsilon_r\nabla V^{m,n}_{\sigma_1,\sigma_2}\right) = e^2\,\langle\psi^m_{\sigma_1}|\psi^n_{\sigma_{21}}\rangle \quad (4.3)$$

where m (n) sweep over all possible levels. Above equation was solved inside an adequately large cell, $300\times300\times300\,\text{nm}^3$. Dirichlet boundary conditions were assigned to the cell side walls. After expanding the multiexciton hamiltonian of Eq. 4.1 on the new Hilbert space of all possible configurations l, p, σ_e, σ_h, few-particle resonances were calculated by numerical diagonalization. The diagram shown in Figure 4.1 illustrates the transition from single particle level to the few particle level and the corresponding outputs in each level.

4.3 Binding energies of ground-state complexes

Following some mathematical simplifications, one can readily deduce from the general hamiltonian Eq. 4.1 that the energy separations between ground-state complexes, that is,

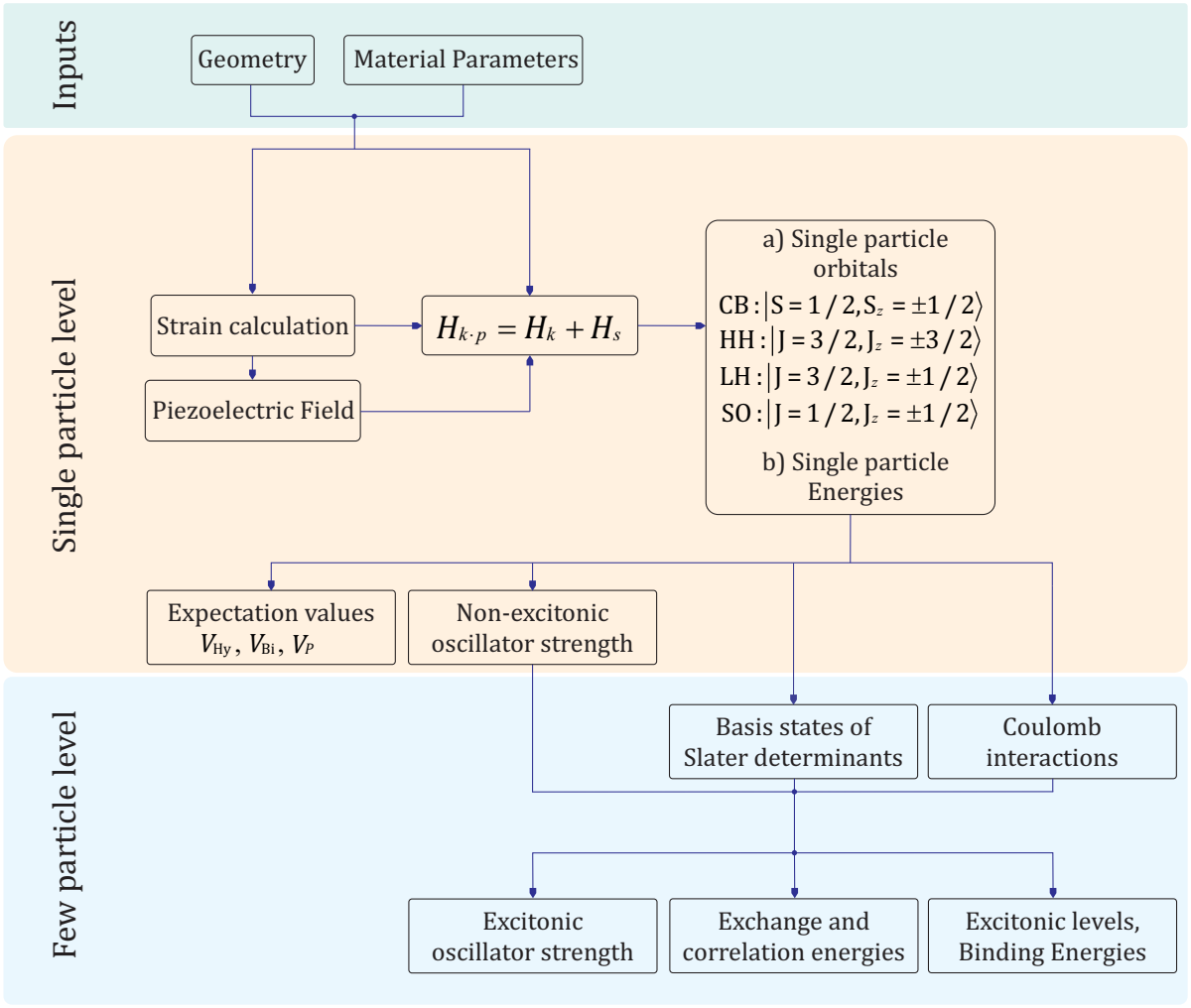

Figure 4.1: Diagram showing different calculation steps and outputs in either of the single particle or few particle levels.

their binding energies with respect to exciton $E(X_0) = E_0^e - E_0^h + J_{00}^{d,eh} + J_{00}^{\rm corr}(X_0) + J^{\rm exc}(X_0)$ read [84],

$$\delta(X_0^-) = -J_{00}^{d,ee} - 2J_{00}^{d,eh} + J^{\rm corr}(X_0) - J^{\rm corr}(X_0^-) + J^{\rm exc}(X_0) - J^{\rm exc}(X_0^-), \tag{4.4}$$

$$\delta(X_0^+) = -J_{00}^{d,hh} - 2J_{00}^{d,eh} + J^{\rm corr}(X_0) - J^{\rm corr}(X_0^+) + J^{\rm exc}(X_0) - J^{\rm exc}(X_0^+), \tag{4.5}$$

and

$$\delta(XX_0) = -J_{00}^{d,ee} - J_{00}^{d,hh} - 2J_{00}^{d,eh} + 2J^{\rm corr}(X_0) - J^{\rm corr}(XX_0) + 2J^{\rm exc}(X_0) - J^{\rm exc}(XX_0) \tag{4.6}$$

Here, $q^{\rm corr}(nX^m)$ is the total correlation energy of a particular complex nX^m. Configurations associated with above complexes include two configurations for each bright or dark exciton ($c^\dagger_{\uparrow,\downarrow} h^\dagger_{\Uparrow,\Downarrow} |s_e, s_h\rangle$), two configurations for positive or negative trion (X_0^+ : $c^\dagger_{\uparrow,\downarrow} h^\dagger_{\Uparrow} h^\dagger_{\Downarrow} |s_e, s_h\rangle$ and X_0^- : $c^\dagger_{\uparrow} c^\dagger_{\downarrow} h^\dagger_{\Uparrow,\Downarrow} |s_e, s_h\rangle$), and one configuration for biexciton (XX_0 : $c^\dagger_{\uparrow} c^\dagger_{\downarrow} h^\dagger_{\Uparrow} h^\dagger_{\Downarrow} |s_e, s_h\rangle$). Here, $c^\dagger_\sigma$ and $h^\dagger_\sigma$ each create an electron and a hole with spin σ in ground states $|s_e\rangle$ and $|s_h\rangle$, respectively. More variety of configurations was possible if higher shells could be occupied. Energy ordering of direct Coulomb interactions then falls within four common situations:

(i) Electron and hole probability densities are spatially separated, suppressing the attractive Coulomb interaction $J_{00}^{d,eh}$. This situation mostly occurs in QDs suffering from (exposed to) internal (external) electric fields. For instance, [111]-oriented and laterally elongated NWQDs exhibit this feature. (i-a) The hole possesses a denser orbital; thus, $J_{00}^{d,hh}$ becomes larger than $J_{00}^{d,eh}$ and $J_{00}^{d,ee}$. Strong piezoelectric field or small a_h, tightening the hole localization, may develop this situation. (i-b) The electron possesses a denser orbital making $J_{00}^{d,ee}$ the largest energy value among direct interactions. This situation may occur in highly anisotropic and relatively large QDs, where the hole orbital extends to cover the negatively charged regions while the electron orbital remains rather unaffected. A relevant example of this case would be series C NWQD when a_h is sufficiently increased ($a_h > 0.4$). Neglecting the correlation energies, trion spectral lines fall in between those of bright excitons and biexciton.

(ii) The next situation regularly occurs when the spatial overlap of electron and hole orbitals is large enough so that $J_{00}^{d,eh}$ exceeds $J_{00}^{d,hh}$ or $J_{00}^{d,ee}$. (ii-a) The hole probability density encompasses the electron orbital. This situation is likely to take place in [001]-oriented NWQDs having large a_h, where the size of the hole envelope function becomes dominant. (ii-b) The hole orbital gets denser compared to the electron orbital when $\Xi_{v;e,h}$ is enhanced, leading to a significant hole-hole interaction. In contrast to case (i), biexciton and bright excitons spectral lines are sandwiched by those of trions in the two latter cases (ii-a) and (ii-b).

4.4 Direct Coulomb interactions and binding energies versus QD shape and size

To investigate the impact of NWQD size and shape on direct Coulomb interactions, the trade-off between two primary effects must be considered: (1) axial and lateral confinements and (2) strain-induced potentials. Principally, enlarging the dimensions of a field-free QD leads to a reduction in the mutual interaction between two single particles, as their orbital size grows in real space. This rule of thumb, however, might not be valid for particles having a low effective mass, for example, electron or LH. As described in Sec. 3.5.2, electrons resist being exactly adapted to the confinement variations. For small a_h, the electron spreads its orbital beyond the QD insertion boundaries toward the nanowire core. This is shown in Figures 4.2(a) and (c) for series B-1 and B-2 NWQDs with $a_h = 0.1$, where projections of the electron e_0 and hole h_0 normalized orbitals, $\Phi_{e_0} = |\varphi_{e_0}|^2$ and $\Phi_{h_0} = |\varphi_{h_0}|^2$ are plotted along the nanowire axis.

In Figure 4.2(c), positions of the s-shell electron and hole orbitals deviate from the NWQD center due to the piezoelectric field, producing an axially oriented dipole. The larger portion of electron probability density Φ_{e_0} shrinks inside the NWQD when a_h smoothly exceeds 0.1, yielding a denser orbital. Further enhancement of a_h consistently results in the vertical spread of the electron orbital, inside the QD borders this time, thus lowers the density. Further on, lateral forces induced by the surrounding shell suppress upon enlarging a_h. Since we have restricted our analysis to $a_h \leq 0.5$, $\Xi_{v;h}$ maintains dominant and determines the strength of Coulomb interactions.

With the inclusion of V_p in $\mathcal{H}_s$, Φ_{e_0} and Φ_{h_0} are not allowed to extend freely in proportion to the QD size. The piezoelectric field reduces the spatial overlap of e_0/h_0 orbitals $\langle s_{e_0}|s_{h_0}\rangle$, and thus the mutual attractive interaction $J_{00}^{d,eh}$. Moreover, it enhances the magnitude of repulsive interaction terms, $J_{00}^{d,ee}$ and $J_{00}^{d,hh}$, through accumulating the orbitals near the charge centers. Depending on the strength of piezoelectricity with respect to other

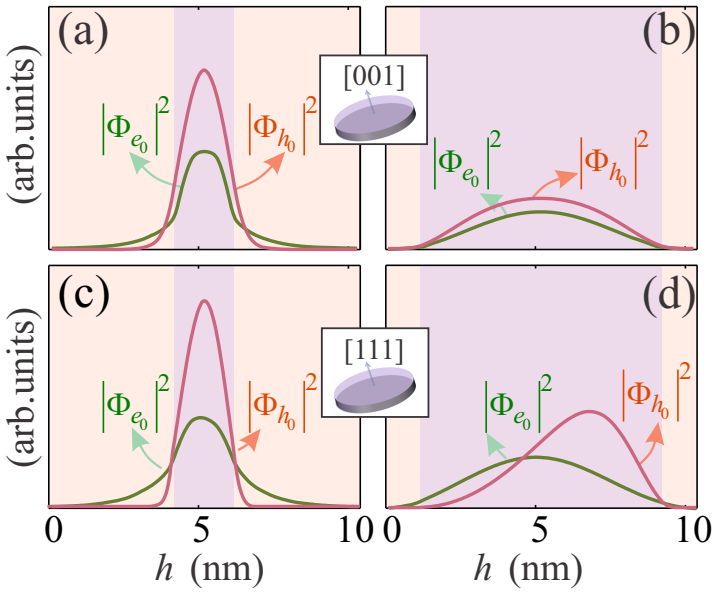

Figure 4.2: Projections of the electron and hole s-shell orbitals on the nanowire axis: (a) and (b), series B-1 NWQD with $a_h = 0.1$ and 0.4. The probability densities are symmetric along the axis as a consequence of trivial piezoelectric potential close to the QD center; (c) and (d), series B-2 NWQD with the same vertical aspect ratios. Electron and hole orbitals do not share same centers of mass due to the axial piezoelectric field.

potential terms in $\mathcal{H}_s$, the evolution of Coulomb interaction terms versus a_h is treatable as follows.

(i) The feature of being continually restricted to the QD boundaries shown by the ground-state hole orbital Φ_{h_0} usually translates to a persistent reduction of $J_{00}^{d,hh}$ upon increasing the QD size. In the case of [001]-oriented NWQDs, the relaxation of confinement and growth of V_p compete together. The hole orbital reacts more sensitively toward $\Xi_{v;h}$ rather than piezoelectricity, as could be concluded from Figures 4.3(a) and 4.3(b), where $J_{00}^{d,hh}$ consistently drops versus the QD height. In [111]-oriented NWQDs, the relatively strong built-in piezoelectric field along the nanowire axis, however, may overcome the impact of axial relaxation for larger aspect ratios ($0.4 \leq a_h \leq 0.5$); see Figure 4.3(c). We also observe that $J_{00}^{d,hh}$ follows the same trend in cone-shaped [111]-oriented NWQDs, but grows slighter for $0.4 \leq a_h \leq 0.5$ since Φ_{h_0} occupies a larger volume despite the stronger piezoelectric field; this is further detailed in (iv).

(ii) Evolution of $J_{00}^{d,ee}$ against a_h could be divided in two regimes: (1) Starting from flat NWQDs, both V_p and $\Xi_{v;e}$ cooperate to enhance the orbital density and therefore $J_{00}^{d,ee}$. (2) Proceeding further toward larger ratios, they begin to oppose each other; thus, $J_{00}^{d,ee}$ smoothly drops.

(iii) Variation of $J_{00}^{d,eh}$ comprises both regimes of evolution discussed in (i) and (ii). Since Φ_{e_0} and Φ_{h_0} possess D_{2d} and C_{2v} symmetries, it seems not trivial to precisely predict how they overlap over the space. According to Figure 4.3, $J_{00}^{d,eh}$ resembles $J_{00}^{d,ee}$ in terms of growing initially and receding eventually. This behavior could be inferred from Figure 4.2, where the axial overlap of Φ_{e_0} and Φ_{h_0} is greater for $a_h = 0.4$ and expected to decrease for larger ratios. The average measure of the electron-hole Coulomb attraction term agrees with the previous theoretically and experimentally estimated values [121, 139].

(iv) A comparison between the interaction terms in series B-1 and B-2 (C-1 and C-2) NWQDs for each specific a_h clarifies the role of piezoelectricity. Larger V_p existing in [001]-oriented cone-shaped NWQDs lightly increases the repulsive interactions. The QD steep side walls also make the effective volume felt by the orbitals smaller. For large a_h, this amplifies the effect of piezoelectricity in repulsive interactions, but competitively attempts to enhance the electron-hole overlap. In [111]-oriented NWQDs, instead, the axial piezoelectric field attempts to collect Φ_{h_0} near the top interface; see Figure 3.2(a), right panel. Steep sidewalls in the cone-shaped type push Φ_{h_0} toward the QD center; see Figure 3.3(b). Hence, the net impact of $\Xi_{v;h}$ and piezoelectric field appears as a small suppression in both repulsive and attractive interactions compared to the cylindrical type.

(v) All direct Coulomb matrix elements decay hyperbolically ($1/D_D$) by relaxing the lateral confinement ($\Xi_{l;e,h} = \Delta_{\text{CB,VB}} + \langle \mathcal{H}_s \rangle_{l;e,h}$) irrespective of the particle type; see Figures 4.3(e) and 4.3(f). Their analogous evolution stems from the fact that effective masses

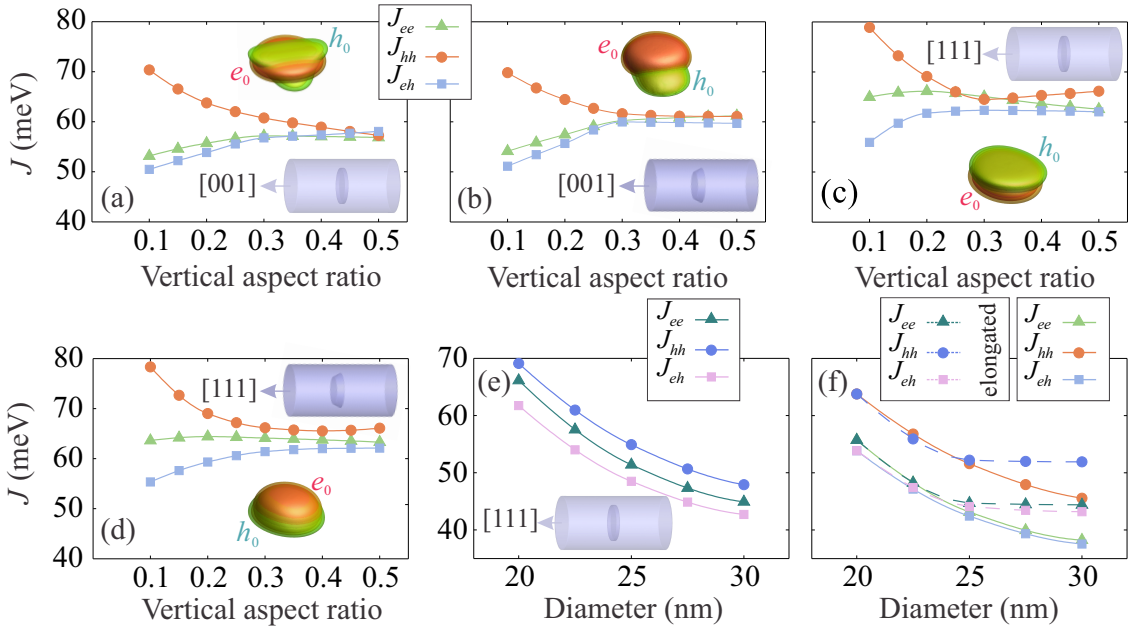

Figure 4.3: (a-d) Direct Coulomb interaction terms for the ground-state electrons and holes in different series of NWQDs. Temporary increase in $J_{00}^{d,ee}$ and $J_{00}^{d,eh}$ results from the reversed penetration of the electron orbital from the nanowire core into the insertion region. Insets show the s-shell electron and hole respective positions for $a_h = 0.4$, where $J_{00}^{d,ee}$, $J_{00}^{d,hh}$, and $J_{00}^{d,eh}$ become comparable. (e), (f) Enlarging the QD diameter pronouncedly decreases the Coulomb terms in a similar fashion ($1/D_D$); QD height h_D is kept fixed equal to 4 nm. (g) [001]-oriented NWQDs are elongated in the [100] direction less than 50%. Electrons and holes hardly spread laterally, having $D_1/D_2 > 1.25$; thus, direct Coulomb terms approximately remain fixed.

of electrons and holes are comparable perpendicular to the nanowire axis. The decaying behavior seems to be moderated in [100]-elongated NWQDs after a certain amount of 1D elongation (here, ~ 1.25 for series D). This can be explained through e/h dispersions:Once the QD is laterally extended along the [100] direction, the corresponding hole effective mass in this orientation $m^*_{hh,[001]}$ becomes lighter, while $m^*_{hh,[010]}$ undergoes a negligible change. The relatively steeper dispersion resulting from $m^*_{hh,[001]}$ allows only dilute parts of Φ_{h_0} to extend along the [100] direction; otherwise, it would cost a considerable exchange of kinetic energy (see Sec. 4.5). Φ_{e_0} , on the other hand, splits parallel to the elongation axis and gets dilute along the main quantization axis [001]. The electron-induced mean-field potential felt by e_0, $\langle\psi^e_{0;\uparrow,\downarrow}|\, V^e_{\uparrow,\downarrow}\,|\psi^e_{0;\uparrow,\downarrow}\rangle$, or h_0, $\langle\psi^h_{0;\Uparrow,\Downarrow}|\, V^e_{\uparrow,\downarrow}\,|\psi^h_{0;\Uparrow,\Downarrow}\rangle$, however, turns out not to change significantly under this orbital splitting.

4.5 Dependence of electron and hole kinetic energies on orbital extent and QD size

Any effort expended by the few-particle complexes for minimizing their total energy in response to the size or shape variations is reflected in their corresponding orbital spread-out. In this regard, the amount of kinetic energy obtained by each one of the constituting particles can be estimated through its expectation value: $E_k = \langle\psi(\mathbf{k})|\,\mathcal{H}_k\,|\psi(\mathbf{k})\rangle \simeq \langle\psi(\mathbf{k})|\,E(\mathbf{k})\,|\psi(\mathbf{k})\rangle$. E_k is then directly linked to the dispersion relation $E(\mathbf{k})$ and the orbital extent in k space. According to this relation, the sensitivity of each individual envelope function to any kind of structural variation relies not only on its effective mass, dictated by $E(\mathbf{k})$, but also upon its original size of probability density within the real space. The above relation also implies that a for a fixed value of effective mass, a larger extent of an orbital in the real space leads to a lower gain of kinetic energy.

By scrutinizing the evolution of direct Coulomb interactions in Figure 4.3, we observe that $J^{d,hh}_{00}$ exhibits a greater sensitivity to the size variations for smaller a_h. This behavior can be explained by taking the roles of both effective mass and piezoelectricity into account: (i) having a_h increased, Φ_{h_0} grows and becomes more responsive to any additional size variation. (ii) Meanwhile, the effective mass along the nanowire axis ($m^*_{hh,[001]}$ or $m^*_{hh,[111]}$) gets lighter due to the relaxation of $\Xi_{v;h}$ (LH percentage becomes larger). This moderates the orbital sensitivity by enhancing the potentially available amount of E_k that may be gained by any tiny spreading out. (iii) As mentioned before, the piezoelectric field attempts to squeeze Φ_{h_0} at large a_h, thus partially compensating the role of QD size. Eventually, having one electron and one hole involved in each mutual attractive interaction, it evolves as a mixture of electron-electron and hole-hole repulsive interactions

	Series B-1		Series B-2		Series C-1		Series C-2	
a_h	ζ_e	ζ_h	ζ_e	ζ_h	ζ_e	ζ_h	ζ_e	ζ_h
0.1	0.295	−0.056	0.298	−0.057	0.203	−0.071	0.201	−0.073
0.2	0.239	−0.040	0.245	−0.041	0.198	−0.045	0.195	−0.045
0.3	0.201	−0.030	0.213	−0.031	0.180	−0.037	0.175	−0.035
0.4	0.177	−0.025	0.199	−0.030	0.163	−0.033	0.159	−0.032
0.5	0.162	−0.028	0.198	−0.034	0.151	−0.036	0.147	−0.044

Table 4.1: Orbital-dependent kinetic energy defined as $\langle H_k \rangle_{e_0} - E^0_{\mathrm{CB}}$ ($\langle H_k \rangle_{h_0} - E^0_{\mathrm{VB}}$) for electrons (holes) versus the vertical aspect ratio in different series of NWQDs.

to some extent. To examine how QD flatness affects E_k acquired by each type of carrier, we defined a renormalized orbital-dependent kinetic energy as $\zeta_{h_0,e_0} = \langle \mathcal{H}_k \rangle_{h_0,e_0} - E^0_{\mathrm{VB,CB}}$ for e_0 and h_0 discarding the heterostructure band offsets, and calculated it for $a_h = 0.1$ to 0.5 (see Table 4.1). The orbital-dependent parts of electron and hole kinetic energies grow as we keep flattening the NWQDs since the associated $\rho_{e_0}(\mathbf{k})$ and $\rho_{h_0}(\mathbf{k})$ swell out. ζ_{h_0} also grows given larger aspect ratios ($a_h > 0.4$) because of the further LH character the hole particle obtains.

4.6 Exchange, correlation and binding energies

Considering the fact that all NWQDs studied here, except series C-1, possess high symmetry characters, the anisotropic exchange interaction, representing FSS is less than 1 μeV within our numerical accuracy. However, the weights of exchange interactions become important upon any sort of morphological asymmetry, including any small variation in homogeneity of QD insertion: in a simple picture where the correlations are excluded, the FSS is given by $2\langle \psi^e_{0;\downarrow}\psi^h_{0;\Uparrow}| \mathcal{C} |\psi^h_{0;\Downarrow}\psi^e_{0;\uparrow}\rangle = 2\langle \psi^h_{0;\Uparrow}| V^{e,h}_{\downarrow,\Uparrow} |\psi^e_{0;\uparrow}\rangle$. This overlap integral, if not zero, is by average dependent on the orbital overlaps of electrons and holes in the ground state. We experimentally observe such a size dependency of anisotropic exchange interaction (FSS) in Chapter 6. Other terms of exchange interaction leading to dark-bright splitting, or dark-dark splitting show this size dependency likewise. The measure of dark-bright splitting is important in terms of spin relaxation times. This will be further detailed in Sec. 4.7.

The correlation energy that the ground state shares with higher excited states is essentially determined by a number of parameters including (a) size and position of single-particle orbitals $\Phi_{e,h}$, (2) energy spectrum, (3) number of particles existing in the complex, and (4) kinetic energy variations δE_k. In the few-particle picture, once a carrier resting in

one particular state correlates its wavefunction with other orbitals, it is looking for any deformation stabilizing the complex. This mechanism involves direct interactions established between the carrier and other single particles, that is, how the associated orbital reshapes to minimize the total energy affected by attractive and repulsive Coulomb interactions. Returning to Figure 4.3, repulsive terms, $J_{00}^{d,hh}$ and $J_{00}^{d,ee}$, are much stronger than $J_{00}^{d,eh}$ in flat NWQDs although e_0 and h_0 share rather the same centers of mass. This is due to the tight $\Xi_{v;h}$, which keeps the orbital sizes small. We observe larger correlation energies in this range almost for all series of NWQDs [see Figure 4.4(a-d)]. According to the reasons explained in Sec. 4.4, the interplay between the dominant $\Xi_{v;e,h}$ and piezoelectric effect causes the Coulomb interactions to approach each other while increasing a_h up to 0.5. The correlation energies thus choose a descending evolution in accordance with the differences between $J_{00}^{d,hh}$, $J_{00}^{d,ee}$, and $J_{00}^{d,eh}$.

The orbital-dependent part of kinetic energy $\zeta_{e,h}$ is plotted for Series B and C NWQDs in Figure 4.5 based on the data given in Table IV. The reduction rate drops for both ζ_{e_0} and ζ_{h_0} when the size of QD increases. For e_0, the dispersion relation $E_{e_0}(\mathbf{k})$ is barely influenced when the orbital e_0 slowly grows. For the hole particle, we face two competing effects. On the one hand, enlarging the QD axially enhances the LH character of the h_0 thus its dispersion $E_{h_0}(\mathbf{k})$ gets steeper. Meanwhile, the orbital is spreading out rapidly. The former attempts to increase ζ_{h_0} while the latter acts oppositely. For $a_h < 0.4$, the dispersion curve is not steep enough to overcome the effect of orbital growth, respecting the fact that the hole particle accelerates gaining LH character for larger a_h [see Figure 3.8(a)]. Finally, for $a_h > 0.4$, kinetic energy gained by $|h_0\rangle$ orbital ζ_{h_0} is enhanced due to the steeper dispersion curve.

Regardless of two above regimes of variation for holes in [001]-oriented NWQDs, they lose (gain) less kinetic energy than electrons in response to any size variation and thus become more flexible to correlate their orbitals with excited states; see Figures 4.5(a) and (b). Hence, we generally expect X_0^+ (having contribution from two h_0 and one e_0) to exhibit larger correlation energy than X_0^- (having contribution from two e_0 and one h_0). In contrast, the hole obtains kinetic energy comparable to that of the electron in [111]-oriented NWQDs for this range of a_h [see Figures 4.5(c-d)]. This can be attributed to the existing axial piezoelectric field which squeezes the orbital in the real space. Consequently, the trade-off between dispersion and orbital extent is further motivated by piezoelectricity in these types of NWQDs; this means that $J^{\text{corr}}(X_0^-)$ may even exceed $J^{\text{corr}}(X_0^+)$ wherever the impact of orbital size becomes dominant.

Binding energy is primarily determined by direct Coulomb interaction terms since they are much stronger than correlation energies in our studied NWQDs. As shown in Figure 4.4, XX_0 and X_0^+ are deeply antibinding in flat NWQDs due to their large $J_{00}^{d,hh}$. This behavior

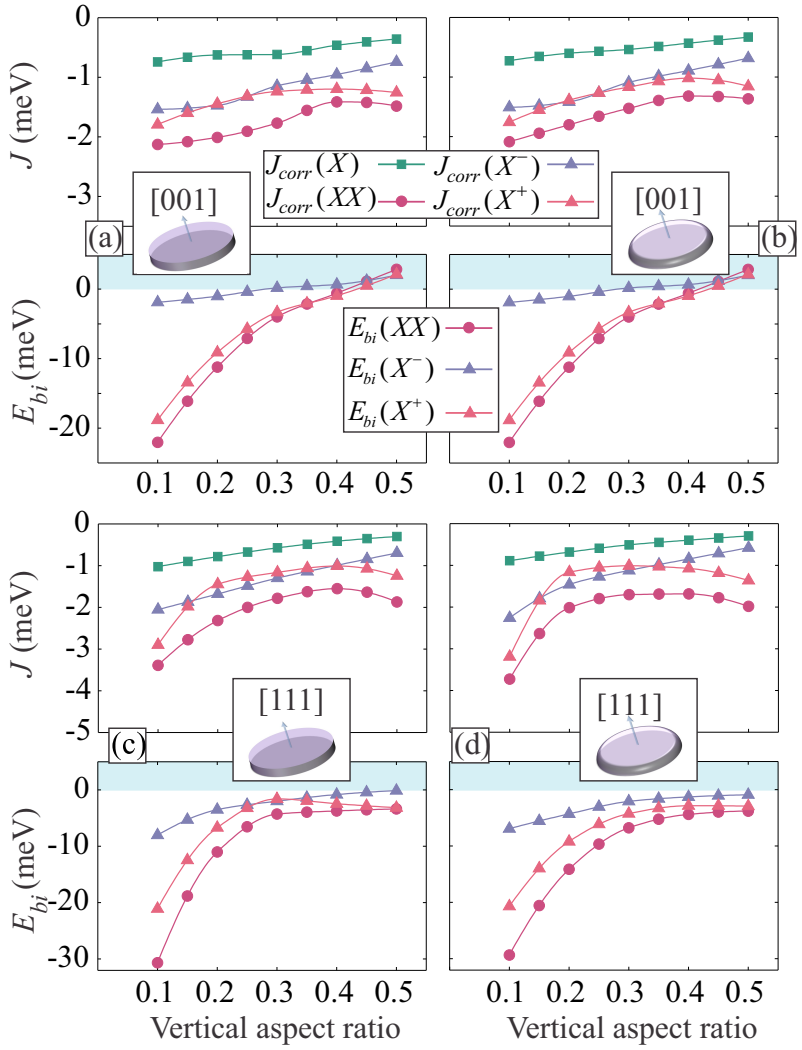

Figure 4.4: Coulomb correlation and binding energies in different series of NWQDs plotted for s-shell X_0, XX_0, X_0^+, and X_0^-. Correlation energies are larger wherever the repulsive interaction terms significantly exceed the attractive term. They also grow for larger a_h where the chance of exchanging kinetic energy becomes smaller.

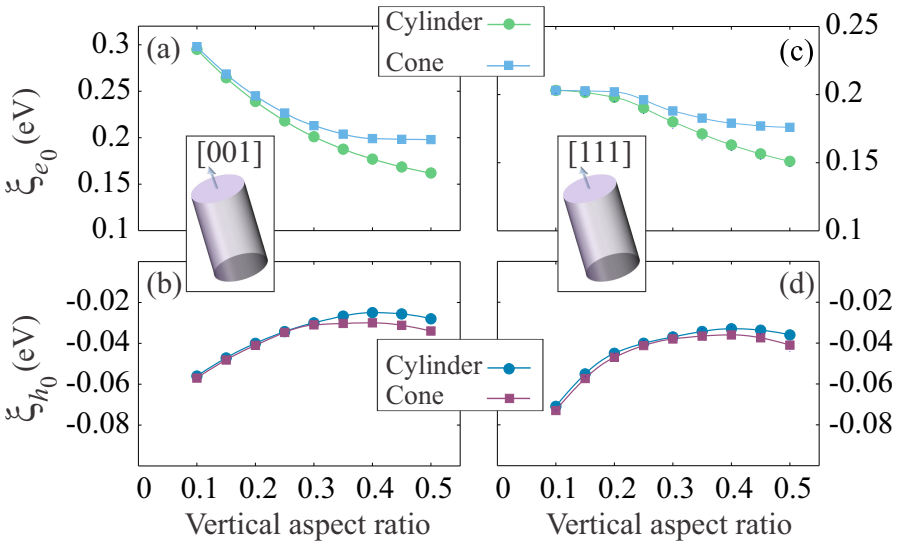

Figure 4.5: Orbital-dependent kinetic energy of electrons ζ_{e_0} and holes ζ_{h_0} plotted for [001]-oriented (a), (b) and [111]-oriented (c), (d) NWQDs. No remarkable distinction exists for flat QDs as they possess similar orbital spreadout and hole LH character. For larger QD heights, electrons and holes in cylindrical type gain the least ζ_{e_0,h_0} having the smaller orbital extent (and LH contribution for holes). Dispersion is steeper in cone-shaped QDs, plus that hole orbital is pushed downward, occupying a larger area despite the stronger piezoelectric field and smaller QD size.

has been experimentally observed in Ref. [142]. Our range of dimensions offers no binding biexciton except for cylindrical [001]-oriented NWQDs and merely for a_h larger than ~ 0.45. One may reach binding regime for the other types as long as QD size, either laterally or axially, becomes larger so that direct Coulomb terms approach each other and further correlation energies are obtained. The binding energy of negative trion X_0^-, however, behaves much more smoothly since $J_{00}^{d,eh}$ and $J_{00}^{d,ee}$ merge closely. Finally, we should notice that the exact measure of binding energy for each complex is quite fragile, incorporating the realistic amount of correlation energy; however, the trend under which it changes for a homogeneous QD is explained above.

4.7 Spin relaxation and exciton cross dephasing

During the decay process of a neutral biexciton toward ground state, a temporary hybrid wavefunction of the emitted photon and the remained exciton, known as the exciton-photon state, develops after the first exciton is recombined and lives until the second exciton lifetime gets terminated [96]:

$$\psi_{\mathrm{ex-ph}} \propto |\lambda_1^{XX} X_{\lambda_1}\rangle + |\lambda_2^{XX} X_{\lambda_2}\rangle \tag{4.7}$$

where λ_i $(i = 1, 2)$ represents the polarization state of the photon and X_λ symbolically stands for the remained exciton which has to recombine after a certain time interval, emitting another λ_i-polarized photon (we assumed rectilinear or diagonal basis; otherwise polarization state changes for the second photon in a circular basis). This hybrid state eventually ends up with a two-photon state, which its time evolution and degree of entanglement crucially relies on FSS. Any spin-flip occurrence amid the existence of intermediate exciton-photon state randomizes not only the relationship between its present and previous phases in the course of the time, $\phi_{\lambda_i}(t)$ and $\phi_{\lambda_i}(t-\tau)$, but also the relationship between the phases of two intermediate wavefunctions belonging to the two different decay paths [97]. The cross-dephasing characteristic time is typically larger than the exciton lifetime, but this ordering may be affected by the QD size and temperature.

Cross-dephasing time is determined by the spin longitudinal relaxation time τ_1 of the exciton-bound electron and hole. Two primary mechanisms are responsible for exciton spin-flip process depending on the strength of QD confinement [143, 144]. The first mechanism originates from both electron-hole exchange interaction $\mathcal{H}_{\mathrm{exc}} = -\Delta_{bd}\mathbf{S}\cdot\mathbf{J}$ and the phonon-induced deformation $\mathcal{H}_{\mathrm{ph}}$. Here, $\mathbf{S}$ and $\mathbf{J}$ are electron spin and hole total angular momentum operators, and Δ_{bd} is the exchange energy splitting between the dark and

bright doublets. Expanding on the basis of the bright HH and LH states, $|J=\pm1\rangle_{hh}$ and $|J=\pm1\rangle_{lh}$, the total Hamiltonian reads

$$\mathcal{H}_{\text{exc}}+\mathcal{H}_{\text{ph}}=\begin{pmatrix} 0 & 0 & \frac{\Delta_{bd}}{\sqrt{3}} & R^* \\ 0 & 0 & R & \frac{\Delta_{bd}}{\sqrt{3}} \\ \frac{\Delta_{bd}}{\sqrt{3}} & R^* & \Delta_{hh-lh} & 0 \\ R & \frac{\Delta_{bd}}{\sqrt{3}} & 0 & \Delta_{hh-lh} \end{pmatrix} \tag{4.8}$$

Δ_{hh-lh} represents the energy spacing between HH and LH excitons originated from strain forces. In the case of [001]- oriented nanowires, for instance, in which x and y label the in-plane inequivalent vectors (x = [100] and y = [010]), R is $\sqrt{3}/2b_v(e_{xx}-e_{yy})-id_ve_{xy}$, where b_v and d_v denote shear deformation potentials along [001] and [111] orientations, respectively. As described in the multiband picture of zinc-blende crystals, the deformation term R comes from the structural anisotropy and directly contributes to the HH-LH level splitting; see Sec. 3.4.1. Cross dephasing occurs between the two bright exciton states that are now energetically separated, but perturbatively mixed with the introduction of anisotropy. Both electron and hole spins are assumed to simultaneously flip in this mechanism. The corresponding matrix element then reads

$$\langle X_{B;1}|\,\mathcal{H}_{\text{exc}}+\mathcal{H}_{\text{ph}}\,|X_{B;2}\rangle \propto \frac{\Delta_{bd}}{\Delta_{hh-lh}}b_v(e_{xx}-e_{yy}) \tag{4.9}$$

Considering only one acoustic-phonon mode among the whole phononic spectrum, the relaxation time inversely relates to the corresponding oscillator strength $|\langle X_{B;1}|\,\mathcal{H}_{\text{exc}}+\mathcal{H}_{\text{ph}}\,|X_{B;2}\rangle\,|^2$, which means

$$\frac{1}{\tau_{\text{deph}}} \propto \frac{\Delta_{bd}^2}{\Delta_{hh-lh}^2}b_v^2(e_{xx}-e_{yy})^2 \tag{4.10}$$

Equation 4.10 states that the rate of spin relaxation in this mechanism depends on QD lateral asymmetry and decreases when the strained HH band is sufficiently away from the nearest LH band. FSS also contributes in the spin flip rate through phonon emission and absorption accompanying this process; i.e. $1/\tau_{\text{deph}} \propto \delta_s^3$ provided that $\delta_s D_D/2\pi\hbar \leq \nu_s$, where ν_s is the sound velocity [143]. By changing the QD shape or dimensions Δ_{bd} remains

nonzero independent of in-plane symmetry. In small QDs hosting Frenkel excitons (typically $D_D < 15$ nm), electron-hole short-range exchange interaction predominantly causes Δ_{bd}, but long-range exchange interaction further contributes as the QD size becomes larger. Conclusively, symmetric QDs (where $|X_{B;1}\rangle$ and $|X_{B;2}\rangle$ are not energetically separated) remain rather safe against simultaneous spin-flip process $|s_{e,\uparrow}, s_{h,\Downarrow}\rangle \leftrightarrow |s_{e,\downarrow}, s_{h,\Uparrow}\rangle$.

The second mechanism includes an intermediate transition to one dark state (electron and hole spins flip sequentially), where spin-orbit interaction stimulates the process and exchange splitting serves as an external magnetic field. Notice that Dresselhaus spin-orbit interaction permanently exists regardless of the structure inversion symmetry since the underlying zinc-blende crystal lacks any inversion center. This mechanism seems to be dominant in QDs with large axial confinement (small height; e.g., $h_D \ll \{D_D, a_B\}$, where a_B is the exciton Bohr radius) but weak lateral quantization, i.e. $a_h \leq 0.2$ and $m_e^* \sim m_{h\perp}^*$, or large effective diameter 25 nm. As discussed in the following sections, HH-LH mixing is also negligible for this type of QDs ($\Delta_{hh-lh} > 10$ meV). For $\Delta_{bd} < 2\pi\hbar\nu_s/D_D$ the electron (hole) spin-flip rate is effectively determined by coupling to the long-wave phonons. Assuming a simplified harmonic potential in the vicinity of Γ point in k space, the spin relaxation rate for the exciton-bound electron (hole) then could be approximated as [144]:

$$1/\tau^{e,h} \propto \frac{\Delta_{bd}^5}{\hbar^2\omega_0^2(\hbar\omega_0 + \Delta_{bd})^2} \left(\frac{m_{e,h\perp}^*}{m_e^* + m_{e,h\perp}^*}\right) \beta_{e,h}^2 (N_{\text{ph}} + 1) \tag{4.11}$$

where $\hbar\omega_0$ stands for the lateral quantization energy ($\omega_0 = 1/D_D^2$), $\beta_{e(h)}$ denotes the electron (hole) spin-orbit coupling coefficient, and N_{ph} is the phonon occupation factor which prescribes the quantity of available phononic modes. Under the limit $D_D < 2\pi\hbar\nu_s/\Delta_{bd}$, spin relaxation rate grows in proportion to $\sim \Delta_{bd}^5$ ($\Delta_{bd} \ll \hbar\omega_0$) and $\beta_{e(h)}^2$ when coupled to one phonon mode. The relaxation rates estimated below and measured in [145] suggest that this type of single-particle spin flip may even occur during the exciton lifetime (in the order of a 10 ns or shorter).

Our calculations show that the dark-bright energy splitting Δ_{bd} ranges between ~150 and 280 μeV for series B and ~270 and 410 μeV for series C, generally larger for cone-shaped NWQDs. Referring back to Sec. 4.6, this increase could be attributed to further electron-hole overlap in series C. In order to quantitatively demonstrate the impact of quantization and symmetry on spin relaxation times, we examined series C-1 and C-2 NWQDs. Indeed in the following, the variation trend of spin relaxation rates is of our interest and not their absolute values. Let us consider the first mechanism above. We label the longitudinal relaxation time associated with this mechanism by subscript "a".

In series C-1 both δ_s (FSS) and Δ_{bd} increase with respect to a_h, leading to an abrupt drop in $\tau_{1,a}$ as it changes proportional to $1/\Delta_{bd}^2$ and $1/\delta_s^3$. Figure 4.6(a) and (b) show the calculated $\tau_{1,a}$ versus temperature in series C-1 and C-2 for different vertical aspect ratios. We used the explicit formulas derived in Refs. [143] and [144] along with the the parameters (δ_s, Δ_{bd}, Δ_{hh-lh}) we obtain from CI method to calculate these spin relaxation times. In series C-2, δ_s is sub-μeV and considered equal to 0.6 μeV, and only Δ_{bd} grows with a_h; thus, the sensitivity of $\tau_{1,a}$ against h_D drops considerably; see Figure 4.6(b). Regardless of QD type, $\tau_{1,a} \gg \tau_X$, exciton lifetime, indicating that simultaneous spin-flip processes ($|s_{e,\uparrow}, s_{h,\Downarrow}\rangle \leftrightarrow |s_{e,\downarrow}, s_{h,\Uparrow}\rangle$) barely randomize the phase difference between the two bright exciton decay paths.

The second mechanism primarily relies on lateral quantization (or equivalently D_D) along with Δ_{bd} rather than FSS, as the transitions occur between bright X_B and dark X_D excitons. Each bright exciton $|s_{e,\uparrow}, s_{h,\Downarrow}\rangle$, ($J = -1$) or $|s_{e,\downarrow}, s_{h,\Uparrow}\rangle$ ($J = 1$) can switch to either $|s_{e,\uparrow}, s_{h,\Uparrow}\rangle$, ($J = 2$) or $|s_{e,\downarrow}, s_{h,\Downarrow}\rangle$ ($J = -2$) dark states only by flipping one electron or hole spin. Figures 4.6 (c) and (d) show $\tau^e_{J=1\to 2}$ and $\tau^h_{J=1\to -2}$ for $X_B \to X_D$ transition in series C-1 and C-2 NWQDs. Two QD diameters are examined, 20 and 30 nm, while the height h_D is kept fixed equal to 4 nm. The corresponding X_B-X_D exchange splittings are $\Delta_{bd} = 242$ and 93 μeV calculated for series C-1 and $\Delta_{bd} = 345$ and 136 μeV for series C-2 NWQDs. Results show that spin-flip process involving exciton-bound electron generally occurs quicker than the one of the hole. Also, QD having larger diameter exhibits longer $\tau_{1,b}$ when its height is fixed (subscript "b" refers to the second mechanism). This is interpretable when $\hbar\omega_0 \gg \Delta_{bd}$ and thus $\tau_{1,b} \propto D_D^8/\Delta_{bd}^5$, implying that the strength of axial quantization enhances the spin coherence. Δ_{bd} is sufficiently small in series C-1 NWQDs so that $\tau_{1,b} \gg \tau_X$ even for higher temperatures. The larger X_B-X_D splitting in series C-2 NWQDs, however, decrease spin-flip times significantly where $\tau_{1,b}$ becomes comparable to the typical exciton lifetimes. Spin-flip times $\tau^{e,h}_{J=2\to 1}$ of $X_D \to X_B$ transition present similar trend in terms of $\tau^h_{J=2\to 1}$ ($\tau^e_{J=2\to 1}$) and $\tau_{1,b}$ being in the order of τ_X for series C-2 NWQDs. As suggested by Figures 4.6 (e) and (f), exciton dark state X_D remains resistant to spin flip in very low temperatures since the process is phonon-mediated.

4.8 Controlling Coulomb interactions via electric field in NWQDs

The binding energies of few-particle complexes in our studied NWQDs are strongly governed by direct Coulomb interaction terms rather than correlation energies. Owing to the larger correlation energy of biexciton XX_0 compared to bright exciton $X_{0,B}$, we may find

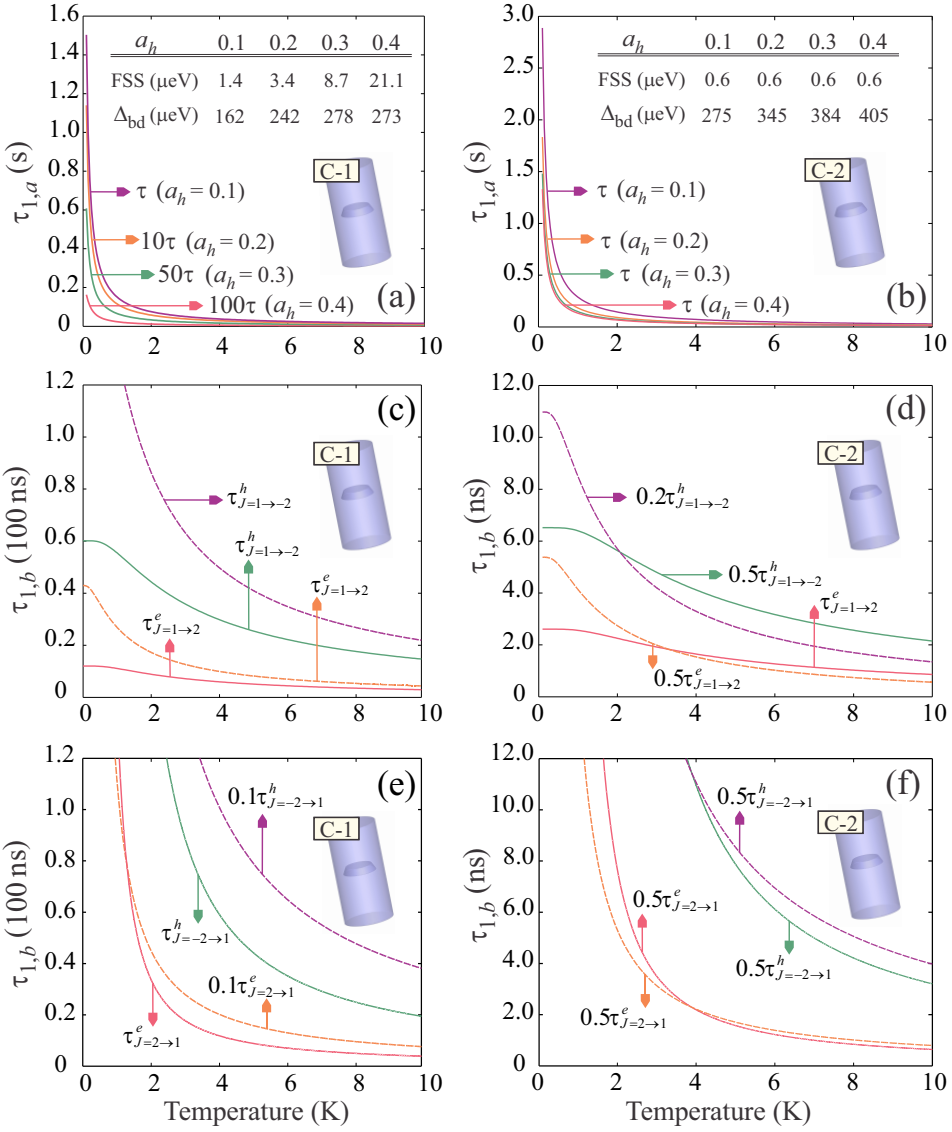

Figure 4.6: Relaxation times, due to the first ($\tau_{1,a}$) and second ($\tau_{1,b}$) spin-flip mechanisms are compared for [001]- and [111]-oriented cone-shaped NWQDs. In the first mechanism, both exchange energies δ_s and Δ_{bd} contribute to the relaxation time. (a) $\tau_{1,a}$ rapidly drops for larger aspect ratios since both Δ_{bd} and δ_s grow with a_h in series C-1 QDs; $\tau_{1,a} \gg \tau_X$. (b) $\tau_{1,a}$ is plotted for maximum δ_s in our calculations. C_{3v} symmetry character of exciton in series C-2 QDs is independent of a_h; thus, δ_s is ideally zero and only Δ_{bd} tunes the relaxation time; $\tau_{1,a} \gg \tau_X$. (c),(d) $\tau_{1,b}$ ($X_B \to X_D$) versus temperature calculated for series C-1 and C-2 QDs with two different diameters, 20 nm (solid lines) and 30 nm (dashed lines), and $h_D = 4$ nm. (d),(f) $\tau_{1,b}$ ($X_D \to X_B$) for the same structures in (c) and (d), respectively.

its energy level appearing below that of $X_{0,B}$ when QD size brings the amount of direct interactions to very similar values. We observed such small biexciton binding energies in our NWQD grown by chemical beam epitaxy; see Chapter 6. A controllable external perturbation, such as the Stark effect, then enables us to delicately tailor these terms and, therefore, the resultant binding energy $\delta(nX^m)$. In general, exerting an external electric field introduces the following effects. (1) It redshifts and blueshifts the e_0 and h_0 energies, respectively, thus attempting to reduce the s-shell transition energy $E_{e_0 \to h_0}$. (2) It spatially separates the electron and hole orbitals, hence diminishing their attractive interaction $J^{d,eh}$. This reduction in the exciton binding energy, partially cancels the redshift in $E_{e_0 \to h_0}$. (3) It can be visualized as an external piezoelectric field, capable of enhancing the repulsive interaction terms by squeezing Φ_e and Φ_h. (4) It renormalizes the binding energies by manipulating Φ_e and Φ_h along with the mean-field potentials. (5) A lateral electric field ruins the symmetry character of wavefunctions. Therefore, under a sufficiently high local electric field, FSS becomes large enough to exclude the possibility of employing the regular scheme. Moreover, a lateral electric field can decrease the radiative recombination lifetime of ground-state complexes, yielding the emergence of higher-order complexes in which one or a number of single particles reside in p states [146].

In this section we study two specific situations where perpendicular (lateral) and parallel (axial) electric fields are applied to [001]- and [111]-oriented NWQDs possessing small XX_0 binding energies. According to the earlier discussions in Sec. 4.4, the biexciton is 2.84 meV binding in series B-1 NWQD with $a_h = 0.5$. Though a part of this energy comes from the correlation terms, zero XX_0 binding energy could be realized through spatially splitting e_0 and h_0, and henceforth delicately reducing $J_{00}^{d,eh}$. Introducing the external perturbation $\langle \psi_{e,h} | \, eV_{\text{ext}} \, | \psi_{e,h} \rangle$ into the total Hamiltonian $\mathcal{H}_k + \mathcal{H}_s$ for this purpose requires a relatively strong electric field due to the considerable difference between dielectric constants inside (ε_{in}) and outside (ε_{vac}) the nanowire. Moreover, mean field potentials produced by each particle are large scale and thus exhibit trivial deformations in response to the electric field-induced orbital distortions.

We modeled an artificial lateral gate by introducing a constant [100]-directed electric field, labeled as E_x in Figure 4.7, into the structure and recalculated the single-particle orbitals for the average internal electric fields $\left\langle E_{[001]} \right\rangle_{V_D}$ equal to 3.61, 10.8, and 18 kV/cm (V_D is the QD volume). These values correspond to 25, 75, and 125 kV/cm external fields, respectively. By performing CI calculations we found that along with separating e_0-h_0 orbitals, the Stark effect also enhances the repulsive interactions, $J_{00}^{d,hh}$ and $J_{00}^{d,ee}$, by shrinking Φ_{e_0} and Φ_{h_0}; thus, binding energies quickly approach zero during the dipole formation. Expectedly, $J_{00}^{d,ee}$ and $\delta(X_0^-)$ have the least variations. Correlation energies very slightly decrease in response to the $eV_{\text{ext}} \approx 36$ meV polarizing potential across the

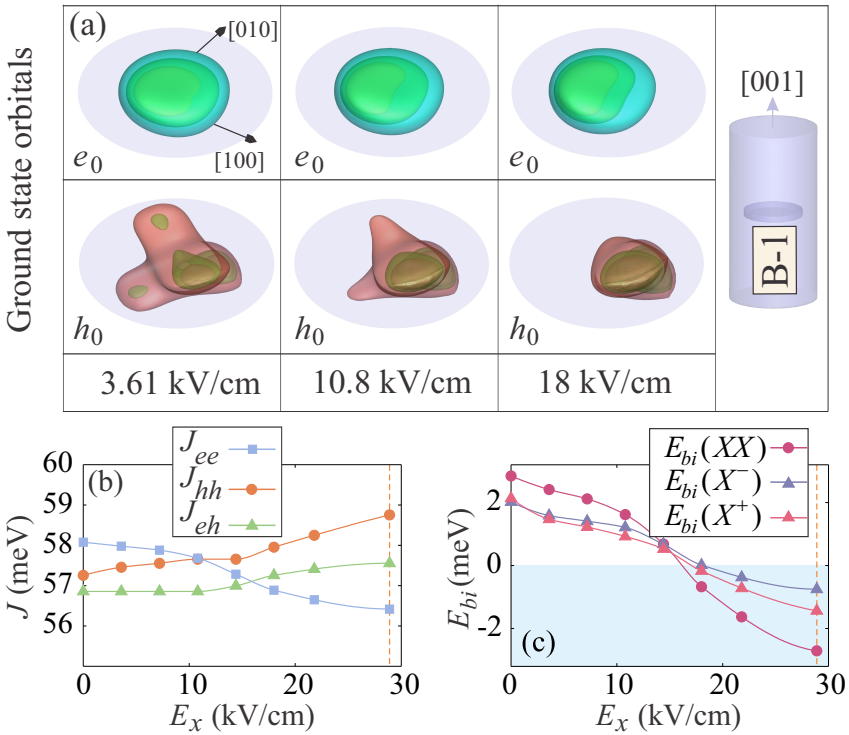

Figure 4.7: (a) Hole and electron orbitals respond to $E_x||[100]$ by squeezing their associated orbitals. The effective field amplitudes E_{eff} indicated above correspond to 25, 75, and 125 kV/cm external electric fields, respectively. The destruction of D_{2d} symmetry gives rise to noticeable anisotropic exchange interaction. The hole orbital flexibly moves due to the small cost of kinetic energy it spends by reshaping. (b) Direct Coulomb interactions versus E_x. Range of variations due to the electric field is quite trivial compared to the variations in response to $\Xi_{v;e,h}$. (c) Ground-state complexes show a binding to antibinding transition. Correlation energies are barely affected; thus, binding energies follow the evolution of direct interaction terms.

$E_{[001]}$(kV/cm)	HH (%)	LH (%)
0	92.6	6.59
25	91.9	5.62
75	91.0	7.20
125	90.6	8.02

Table 4.2: HH and LH percentages of the ground-state orbital in series B-1 NWQDs against a [001]-oriented external electric field.

QD because (1) orbitals are tightened and (2) the LH character is enhanced in the presence of a strong electric field as shown in Table 4.2. Moreover, anisotropic long-range exchange interaction grows rapidly as a result of symmetry breaking and reorders the fine structure energy δ_s.

A parallel electric field is also able to restore the color coincidence between XX_0 and X_0 without breaking the orbital symmetries. Depending on the respective positions of single-particle orbitals, it can shift XX_0 resonance into or bring it out of the binding regime. In the particular case of [111]-oriented NWQDs, an axial dipole already exists as a result of piezoelectric potential pushing XX_0 resonance toward the antibinding region: $J_{00}^{d,hh} + J_{00}^{d,ee} > 2J_{00}^{d,eh} + \Delta J_{X_0,XX_0}^{\text{corr}}$. An equivalent parallel electric field, $|E_{\text{ext}}| \simeq E_{[111]}^{\text{piezo}}$, but oppositely directed then may compensate the built-in polarization. e_0 and h_0 orbital distributions versus E_{ext} are demonstrated in Figure 4.8 for series B-2 NWQD with $a_h =$ 0.5 where a_h =0.5 where $\delta(XX_0) = -3.37$ meV. The $|h_0\rangle$ orbital touches the top interface in relatively weak electric fields. By increasing E_{ext} up to 17.4 kV/cm, the axial component of the internal piezoelectric field is almost canceled out and Φ_{h_0} occupies the entire QD space encompassing Φ_{e_0}. A temporary rise in the spatial overlap and $J_{00}^{d,eh}$ then occurs, leading to a binding XX_0 [$\delta(XX_0) \approx 0.8$ meV]; see Figure 4.8. Note that $J_{00}^{d,hh}$ experiences a transient drop until the electric field becomes strong enough, $E_{\text{ext}} = 26.2$ kV/cm, to collect Φ_{h_0} near the bottom interface. At the same time we observe a trivial minimum happening in ξ_{h_0} once Φ_{h_0} spreads out axially. In contrast, Φ_{e_0} and thus its resultant mean-field potential $V_{0,\sigma}^{e}$ stay stiff, while the associated kinetic energy ξ_{e_0} delivers very limited variations (< 0.1 meV).

4.9 Summary

In this chapter, the energy levels of s-shell excitonic resonances X_0, $X_0^{\pm}$, XX_0 were discussed in terms of direct, exchange, and correlation energies. We defined and calculated orbital-dependent kinetic energy to explain orbital deformations and track the interaction

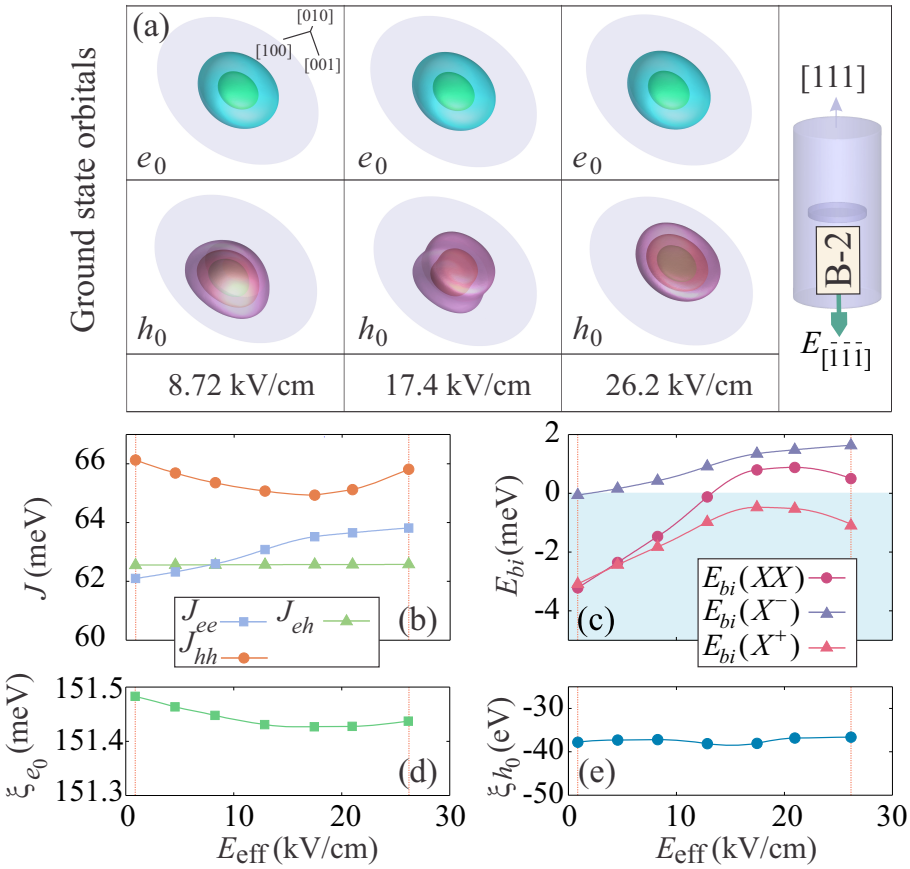

Figure 4.8: (a) Electron and hole orbitals in the presence of an axial electric field E_{ext} in [111]-oriented QDs. The hole is well-confined beneath the top interface when the parallel component of piezoelectric field dominates the effective applied field ($E_{\text{eff}} = 8.72$ kV/cm). The hole orbital moves downward as a function of effective electric field until reaching the bottom interface. The electron orbital, however, stands unmoved. (b) Direct Coulomb interactions are shown against E_{eff}: e_0 and h_0 spatial overlap is improved while $J_{00}^{d,hh}$ undergoes a transient decrease; meanwhile, the h_0 orbital spreads vertically. (c) Binding energies of the ground state complexes. The biexciton becomes weakly binding at $E_{\text{eff}} \approx 12$ kV/cm. (d), (e) Hole and electron orbital-dependent kinetic energies versus the axial electric field.

terms in the few-particle complexes. (a) The energy difference between attractive (J^{eh}) and repulsive (J^{hh} and J^{ee}) interaction terms drops when axial and lateral localizations become comparable. (b) Mean-field potentials barely obey tiny structural details. (c) Correlation energies get important when axial localization is considerably dominant. (d) Accumulating correlation energy is prohibited wherever orbital distortion causes non-negligible gain of kinetic energy. We specifically examined the variations of XX_0 and $X_0^{\pm}$ binding energies versus the vertical aspect ratio: Achieving binding XX_0 and $X_0^{\pm}$ is unlikely in flat NWQDs, where J^{hh} noticeably exceeds J^{ee} and J^{eh}. For the same reason, time reordering scheme cannot be implemented with flat NWQDs. Spin relaxation times were calculated according to fine structure of excitonic resonances, Δ_{bd} and δ_s. We found that the spin flip process which may destroy the phase of exciton-photon wavefunction during XX_0 recombination is dependent on Δ_{bd} rather than FSS. Also, exciton-bound hole spin exhibits more stability than electron spin. Binding energies of XX_0 and $X_0^{\pm}$ were manipulated by applying axial and lateral electric fields. XX_0 binding energy could be effectively erased merely through adjusting direct interactions since correlations turned out to be almost unaffected under external electric field. We particularly showed that it would be possible to have $\delta(XX_0) = 0$ and $\delta_s = 0$ simultaneously in [111]-oriented NWQDs. This could lead to the realization of an entangled photon source emitting photons with an identical color in every sequence.

Chapter 5

Few-particle states in quantum dot molecules: an approach towards hybrid entanglement

5.1 Introduction

Strong localization of charge carriers in quantum dots, maintains sufficiently long coherence time of their spin quantum bits (qubits), easing the realization of quantum correlation between the carrier spin and flying photons which is a compulsory step toward developing secure quantum communication [147]. Experimental evidences reported so far on photon (or spin) qubit entanglement in isolated quantum dots (QD) [59, 107] are valid manifestations of their ability in this context. Although realizing bipartite quantum entanglement has been increasingly studied in the recent years, there exists no theoretical proposal on generating higher order entangled states in real quantum dot structures. In the simplest picture, the reason lies in the anharmonic energy level spectrum of a typical QD that impedes color matching amid its absorption energies, making the excitonic transitions distinguishable [148, 95]. Since the entangled degree of freedom is mostly defined based on the polarization of photon (or spin state of carrier), this color distinguishability reduces the degree of entanglement even in a bipartite system.

As described before in Sec. 2.5.2, current solutions offered to establish the coincidence in the energetic of photons are often perturbational [107, 85, 149, 150] or architectural [134, 151, 67], allowing for creating up to bipartite quantum correlated states. Actualizing higher order entangled states, however, seems unlikely in a single QD due to the absence

of more than two color-matching excitons X in its optical spectrum [152]. Experimental demonstration of tripartite entanglement has so far succeeded merely for spin states in diamond NV centers [35] and photon states via spontaneous parametric downconversion [74].

Considering the fact that photon entanglement in QDs relies on the sequential decays of correlated excitons [95], preserving the spatial overlaps of excitonic orbitals in the QDM is a requisite to maintain this correlation. Creating higher order entangled states thus demands for excitons spatially spreading across the entire QDM, rather than a single QD, otherwise the excitons localized in different dots are partially correlated merely via their Coulomb interactions. This means that one constituting particle of the exciton, that is electron or hole, has to be weakly quantized to establish a strong correlation between the two dots. In contrast to the previous experiments [153], here we show that weakly-localized electron orbitals with relatively large tunneling energy retain the correlation and give rise to optically-active indirect (interdot) excitonic recombinations, opening new channels of entangled photon emission. The QDM in our model consists two axially stacked In(Ga)As quantum dots embedded in a GaAs nanowire [154]. An axial electric field then can be exploited to drive the interdot hole tunneling, and eventually to entangle or disentangle electron-hole pairs [155, 156]. In contrast to electron, the hole tunneling energy is noticeably renormalized by the spin-orbit interaction in III-V materials [157]. Moreover, the emergence of new entanglement channels strongly depend on the spin fine structure of holes. Thus a detailed quantum mechanical treatment is required to address all the underlying phenomena, including spin-orbit and Coulomb interactions, in a few-body populated QDM.

In this chapter, we study the capability of quantum dot molecules as potential sources of higher order entanglement. We show that the configurations of multiexcitons can be deterministically controlled by tunnelling mechanism between the hybridized s-shells via an external source of electric field. We analyse the particular case of hybrid entanglement in which the spin of a carrier resting in the metastable ground state is correlated with the polarization of twin photons. To this end, we confine our model to the sequential decays of a negatively (positively) charged biexciton, XX^- (XX^+), down to the singly charged electron (hole) state, $XX^- \rightarrow X^- \rightarrow e$ ($XX^+ \rightarrow X^+ \rightarrow h$), yet the scheme can be generalized to higher orders with more complexity. We demonstrate that only a limited number of transitions are favorable in the field-dependent spectrum of QDM due to the few-body interactions and tunnelling effects.

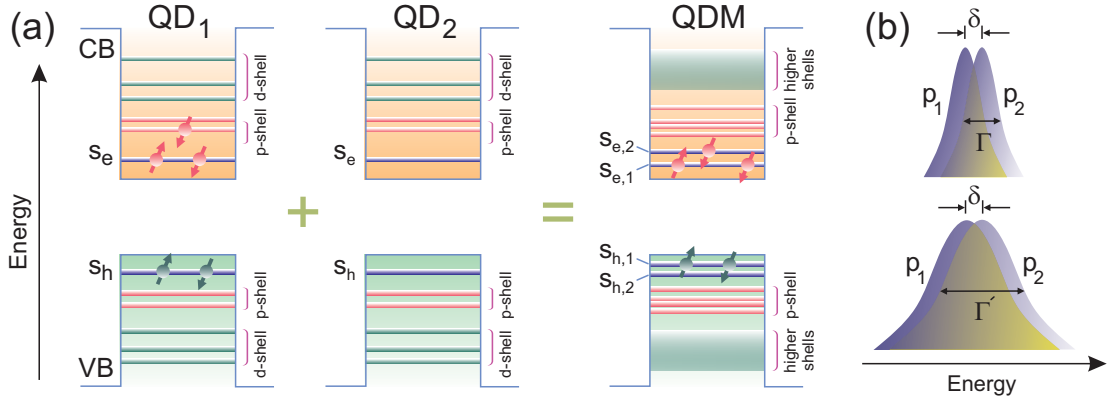

Figure 5.1: (a) Energy level spectrum of a single QD comprising s (s_e,s_h), p, d and higher shells in both conduction and valence bands. Two uncoupled identical QDs labeled as 1 and 2 possess similar energy level diagram. Once they are coupled, the energy levels shift in the resulting QDM and their corresponding wavefunctions hybridize. One exemplary configuration of negatively charged biexciton XX^-, composed of two excitons and an extra electron ($X + X + e$), is shown in QD_1, where one electron occupies the p-shell. In a QDM, however, there exists further states with s-like character for the carriers to populate and form higher order complexes. (b) Spectral linewidths of partially entangled photons P_1 and P_2, separated by δ in energy, before (Γ) and after ($\Gamma^{'}$) broadening. Photons emitted within the highlighted overlap are quantum correlated.

5.2 Theoretical approach and basic concepts

The energy level structure of a typical single QD is composed of s, p, d and higher shells in resemblance to the atomic states, where the s-shell is referred to as the ground state. In a quantum dot molecule (QDM), the orbitals of each individual shell from single dots are mixed and their corresponding energy levels shift based on the coupling strength. The electron and hole s-shells of a single dot, s_e and s_h, can host up to two interacting excitons X (a biexciton XX) thus formation of any higher order complex, such as negatively charged biexciton XX^- ($X + X + e$), inevitably involves the p-shells; see Figure 5.1(a). However, p-shell carriers are not immune to phonon-mediated decays into the ground state, plus the initialization and quantum manipulation of carrier spin in the s-shell is generally preferred.

The QDM structure we address is a symmetric double dot embedded inside a III-V nanowire. Analogous to any other quantum confined structure, the starting point to study the QDM is to find its bound states, namely the molecular orbitals. Since we will be dealing with multi-particle states in the following sections, we refer to these molecular orbitals also as single particle states. To solve for the molecular orbitals we consider the whole QDM as a confining heterostructure and diagonalize the modified Luttinger-

Kohn hamiltonian introduced in Ref. [76]. The molecular orbitals could be approximately represented by the linear combination of dot-localized orbitals beyond the thin-barrier limit [158]. The molecular orbitals construct the basis set required to form the Hilbert space of multi-particle states. An electric field applied along the nanowire axis is able to change the character of molecular orbitals into the dot-localized orbitals, thus tailor the corresponding Coulomb interactions. We solve for the single and multi-particle states at several different axial electric fields and resolve the photoluminescence intensity of multi-particle transitions at grid points and midpoints by interpolation.

The QDM is designed such that the electron molecular orbitals are weakly quantized over the entire molecule and their orbitals negligibly deform in response to the axial electric field, preserving the multi-particle correlations and switching additional transitions, required for the cascade emission, on. The electron molecular orbitals remain weakly localized even after the introduction of Coulomb interactions in the multi-particle states. This is because the hole molecular orbitals are likewise delocalized at zero axial field. In contrast to the electron states, hole single particles, however, quickly localize in response to the electric field. We will demonstrate that the variation range of Coulomb interactions versus electric field is negligible compared to the electron tunneling energy.

In Sec. 5.5, we study the charged biexciton cascade in QDMs in the presence of hole tunneling. The emergence of favorable cascade transitions depends on the spin-fine structure of the contributing complexes, namely XX^- and X^- (XX^+ and X^+), and localization of the molecular orbitals under the variable electric field. Furthermore, the color distinguishability of bright transitions relies on the hole hybridization energy, the existing Coulomb interactions, and the Zeeman energy shift induced by the magnetic field. The field-dependent photoluminescence spectrum of the QDM is calculated for different transitions contributing in $XX^- \to X^- \to e$ and $XX^+ \to X^+ \to h$ cascades. These spectra indicate that merely a few spectral components, corresponding to both initial and final favorable spin configurations, are bright. Unfavorable spin configurations refer to those multi-particle states that the Coulomb blockade or Pauli spin blockade prevent them to form.

The problem of hybrid entanglement between the spin and photons urges coherent control of the electron or hole spin by means of an external magnetic field. Carrier spin preparation is normally accomplished through exciting the singly-charged QD into the charged exciton ($X^- = X+e$ or $X^+ = X+h$) state and waiting until the spontaneous decay leaves the QD either in $|\uparrow\rangle$ or $|\downarrow\rangle$ states, while the spin state is coherently controlled through a Raman transition driven by a few picosecond pulse at its qubit resonance frequency [159, 160]. Formation of charged biexcitons, XX^- and XX^+, from $|\uparrow\rangle$ or $|\downarrow\rangle$ states is then feasible through a two-photon excitation process [161].

Spectral response of QDM to magnetic field appears in the Zeeman shift of multi-particle states and their spin coupling, thus directly influences the color and linewidth distinguishability of transitions. Along with the Zeeman shift, the exchange interaction causes energy splittings in the spin fine structure of multi-particle states. By performing a detailed configuration interaction (CI) calculation, we however demonstrate that the scale of Zeeman splittings rapidly exceeds the exchange splittings, thus the energy indistinguishability of transitions is primarily violated by Zeeman effect. To obtain a clear sense of the magnetic field intensity required for spin state initialization and manipulation in QDs, we rely on earlier experiments reporting acceptable fidelities [162, 163].

A viable solution for erasing these sub-meV energy splittings is to employ high-efficiency downconversion technique. The method comprises cross-correlating the emitted photons from QD with a few-picosecond pulse in a nonlinear medium such as periodically poled lithium niobate (PPLN) waveguide [164]. The time resolution of pulses determines the arrival time of single photons and therefore broadens their linewidths (lifetime of exciton is commonly beyond 0.5 ns $\gg$ few ps). This idea could be extended to an arbitrary stream of anti-bunched photons, including entangled photons. Figure 5.1(b) schematically shows how the portion of fully entangled photons being delivered by the source can be increased through the linewidth broadening. Twin photons P_1 and P_2 have an initial linewidth equivalent to Γ and their color mismatch is δ. Assuming that δ remains constant, the overlap region, which implicitly represents the fraction of quantum correlated photons, grows by enhancing the linewidth $\Gamma \rightarrow \Gamma^{'}$. To quantitatively measure the energy coincidence of photons, we utilize the concept of concurrence developed for entanglement in both regular and time reordering schemes [165, 166, 102]. In the spin fine structure of a typical QD, concurrence is generally a function of energy mismatches and linewidths of excitonic levels. We calculate the evolution of concurrence versus the magnetic field intensity and photon linewidth. The results reveal that a sufficiently high concurrence could be reached by manipulating the linewidths properly. It is worth noting that the QDM with strongly correlated excitons can be exploited to generate higher order entangled photon states or hybrid spin-photon states, and the current work serves as a prototypical study on the application of QDMs in creating tripartite Greenberger-Horne-Zeilinger (GHZ) and W-states [167].

5.3 Hybridization in double quantum dot: antibonding character of the hole versus the interdot spacing

The double quantum dot we study consists of two $In_{0.5}Ga_{0.5}As$ insertions with the ideal $D_{\infty h}$ symmetry embedded inside a [001]-oriented GaAs core-shell nanowires; see Figure 5.2(a). The QD diameter and its vertical aspect ratio, $a_h = h_D/D_D$, are chosen 20 nm and 0.25 respectively. This ratio leads to comparable mutual interactions between electrons and holes, thus the multi-particle states accumulate less correlation energy [67]. The interdot spacing D_s determines the wavefunction symmetry of the hole particle ground state $|h_0\rangle$ and the sign of its tunneling matrix element t_h to hop up to the first excited state $|h_1\rangle$. Our numerical calculations at the single particle level demonstrate that the $|h_0\rangle$ symmetry reversal, as well as the sign inversion of tunneling matrix element [168] (t_h becoming negative), occur at $D_s \simeq 1.8$ nm. The dominant heavy hole-like part of the ground state envelope function $\varphi^{h_0}_{J=3/2,J_z=3/2}$ is illustrated in Figures 5.2(d-e), where its parity flips moving from $D_s = 1$ to 2 nm. The physics of the above symmetry reversal is discussed in Appendices A and B.

The molecular ground and first excited states of the hole, $|h_0\rangle$ and $|h_1\rangle$, are hybridizations of the two dot-localized s-shell states, $|s_{h,R}\rangle$ and $|s_{h,L}\rangle$. These two mixtures are highly correlated at small double-dot spacing, where $|s_{h,R}\rangle$ and $|s_{h,L}\rangle$ orbitals spread uniformly over the QDM, and become $|s_{h,R}\rangle$-like or $|s_{h,L}\rangle$-like when the spacing is sufficiently increased. An analogous situation occurs for the molecular ground $|e_0\rangle$ and first excited $|e_1\rangle$ states of the electron in terms of losing the correlation versus D_s. Figures 5.2(c-d) illustrate the evolution of the corresponding electron and hole energies, E_{e_0}, E_{e_1}, E_{h_0} and E_{h_1} against the interdot spacing. A reasonable range of interdot distance can be $4 < D_s < 6$ nm due to the following reasons:

1) hole hybridization energy is suppressed within this range since the tunneling component caused by the spin-orbit interaction weakly exceeds the diagonal tunneling matrix element (the definitions of these tunneling components are explained in Supplemental Information).

2) the electron first excited state (predominantly s-like) is noticeably coupled to the second excited state (predominantly p-like) given $D_s < 3$ nm as a result of their trivial energy spacing; this leads to a pronounced correlation between the two molecular states $|e_1\rangle$ and $|e_2\rangle$ for $D_s < 3$ nm.

3) D_s could be increased limitedly because the hole tunneling matrix element rapidly vanishes. Hereinafter and in order to observe the field-induced spectrum of the molecule

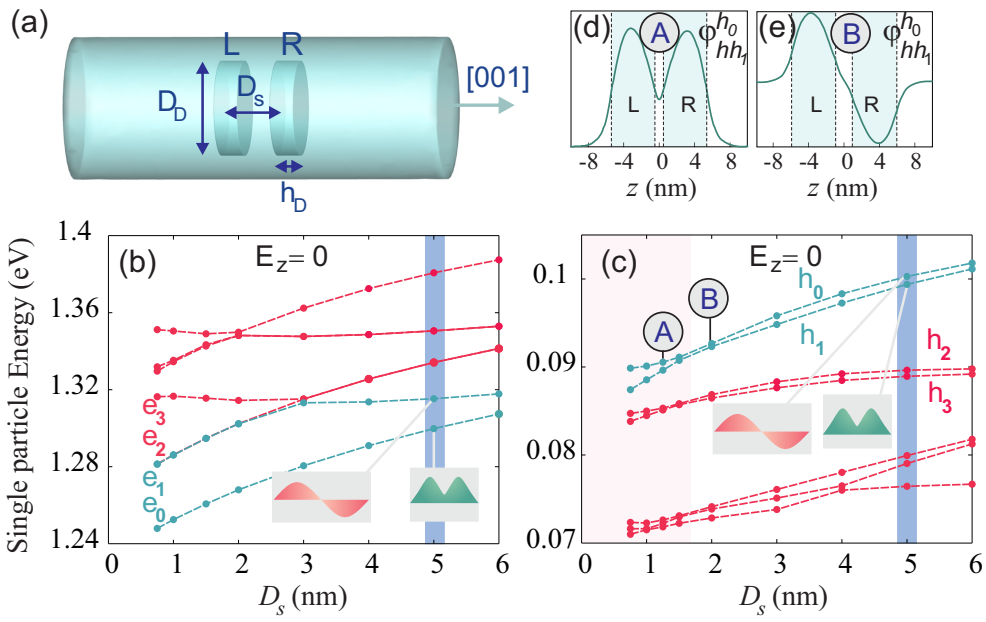

Figure 5.2: (a) Schematic of QDM embedded in a [001]-oriented core-shell nanowire. D_s: the interdot spacing between the left (L) and right (R) single dots. h_D: height of the single QD, D_D: diameter of single QD. Although the structure of QDM is assumed symmetric, the strain field relaxes away from the substrate and becomes axially asymmetric. (b), (c) Electron and hole molecular energies versus the interdot spacing. First and second electron excited states are energetically inseparable for $D_s < 3$ nm as the whole QDM acts similar to a single dot for electrons at the thin barrier limit. The highlighted region in (c) specifies where the hole ground state is bonding (axially symmetric). Hole tunneling matrix element becomes negative at $D_s = 1.8$ nm where the hole ground and first excited states anticross. (d), (e) Envelope function of the hole ground state $\varphi^{h_0}_{3/2,3/2}$ plotted along the nanowire axis at $D_s = 1$ and 2 nm showing its bonding and antibonding nature versus D_s. The highlighted region shows where the hole ground state is symmetric.

at a fixed interdot spacing we set D_s equal to 5 nm.

It is noteworthy to mention that the tunneling energy is a joint function of both axial localization and interdot spacing. If the individual QDs are weakly confining, the effective mass of hole particle along the main quantization axis decreases and the tunneling energy increases. For a certain level of confinement, the hole tunneling energy grows rapidly as the interdot spacing decreases, and regardless of its sign inversion, it vanishes sufficiently beyond the thick barrier limit.

5.4 Single particle mixed states versus the axial electric field

In the next step, an axial electric field E_z ($z \equiv [001]$) is applied in order to tailor the absorption energies of the QDM. Owing to the $D_{\infty h}$ symmetry of single QDs, the orbital densities are rather equivalent once $E_z = 0$, neglecting trivial asymmetries caused by the strain-induced fields; see Figure 5.3(a-c). Both electron and hole molecular orbitals exhibit $\sim D_{2d}$ symmetry, spreading throughout the molecule where each orbital lobe is C_{2v}-symmetric. Immediately upon applying the axial electric field, the heavy hole with highest energy $|h_0\rangle \equiv |h_1^s\rangle$ moves toward lower potential energy, in QD_R, and effectively evacuates QD_L at $E_z \simeq 3\mathrm{kV/cm}$ acquiring C_{2v} symmetry; $|h_0\rangle = |s_{h,R}\rangle$. The very same situation occurs for $|h_1\rangle \equiv |h_2^s\rangle$ under negative comparable electric fields. The Galium intermixing in the QD composition facilitates both hybridization and interdot diffusion of the electron and hole. As implied from its dispersion, the electron orbital is stiff against electric field variations, otherwise it would gain considerable kinetic energy [67]; see Figure 5.3(c) right panel. Thus $|e_0\rangle \equiv |e_1^s\rangle$ and $|e_1\rangle \equiv |e_2^s\rangle$ orbitals sustain their spreadout over both QDs maintaining the interdot coupling, $|e_0\rangle = |s_{e,L}\rangle + |s_{e,R}\rangle$ and $|e_1\rangle = |s_{e,L}\rangle - |s_{e,R}\rangle$.

S-shell electron and hole energies undergo an anticrossing in proximity to $E_z = 0$; see Figure 5.3(d). In accordance with trivial orbital deformations, the s-shell electron energies experience relatively small variations as compared to the s-shell hole energies. Along with the relatively large energy spacing between $|e_0\rangle$ and $|e_1\rangle$, this leads to the predominant hole contribution in any conversion between the excitonic configurations at low electric fields ($E_z \leq 1.5\,\mathrm{kV/cm}$). Owing to the strain-induced potentials, electrons and holes do not necessarily localize symmetrically in response to negative and positive electric fields, prohibiting a perfectly symmetric evolution of spectral features versus the axial electric field.

Since the electrons are weakly localized in our range of electric field, the correct representation is to assign $|P\rangle = |s_{e,L}\rangle + |s_{e,R}\rangle$ and $|N\rangle = |s_{e,L}\rangle - |s_{e,R}\rangle$ to the associated molecular states away from the resonance. In the case of holes, however, we refer to the molecular states as $|R\rangle = |s_{h,R}\rangle$ and $|L\rangle = |s_{h,L}\rangle$ away from the resonance as their orbital could be well approximated by the dot-localized states there.

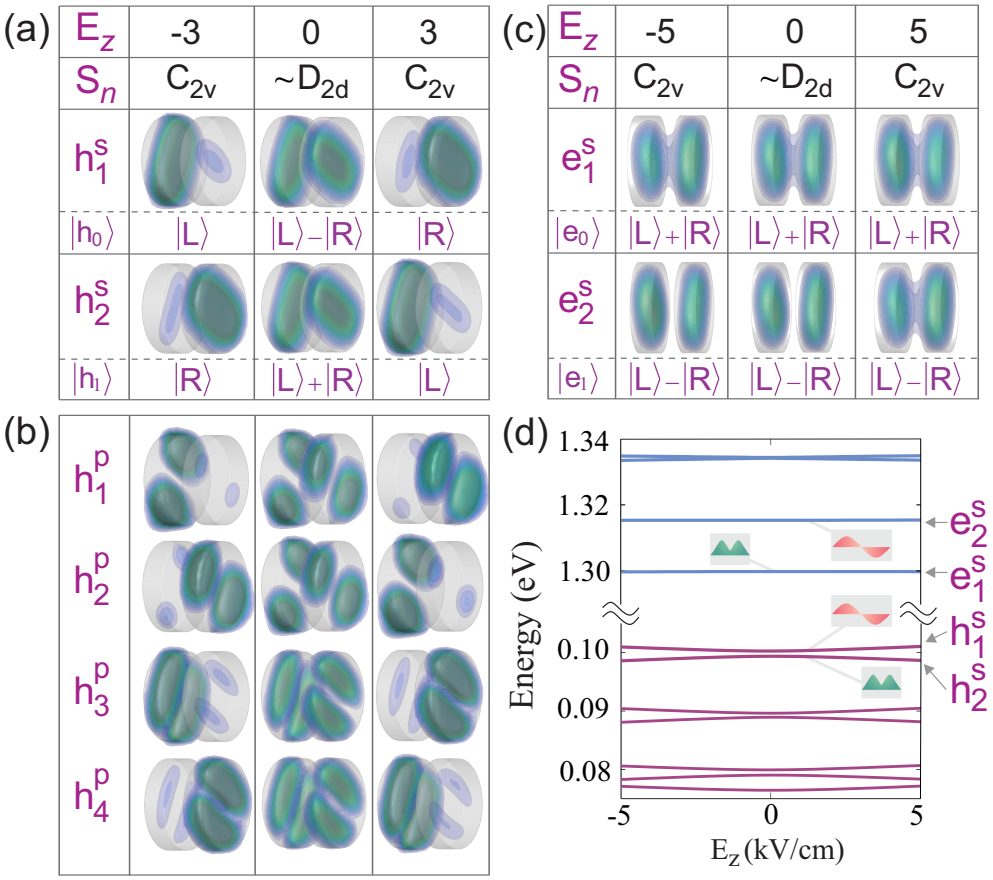

Figure 5.3: (a-b) S- and p-shell hole molecular orbitals versus the electric field indicated in kV/cm. Hole orbitals become localized inside single dots at $E_z = \pm 3$ kV/cm, thus their wavefunction could be approximated by the dot-localized states. Applying axial electric field reduces the symmetry character of orbitals from $\sim D_{2d}$ down to C_{2v} (c) Electron molecular orbitals. Owing to the small effective mass of electron, its molecular orbitals reshape reluctantly in response to E_z. The electron wavefunction remain as the linear mixture of dot-localized states within $-5 < E_z < 5$ kV/cm. The [001] axis is slightly rotated with respect to the left panel (a and b) in order to illustrate the diffusion of electron orbital inside the GaAs barrier ($t_e > t_h$). (d) Electron (four states, $2s$ and $2p$) and hole (seven states, $2s$, $4p$ and $1d$) energies as a function of the axial electric field.

5.5 Charged Biexciton Cascades in QDMs: Role of hole tunneling in the energy coincidence of transitions

Since generating multi-partite correlated states in our scheme relies on the cascade recombination of charged multi-particle complexes, namely XX^- and XX^+, inspecting the contributing transitions of QDM in the presence of hole tunneling sheds light into the essential properties we seek in the energetic of emitted photons. To this end, we consider the exemplary cascades sketched in Figure 5.4 and calculate the transition energies of the diagram. We focus on the cross-entanglement scheme where the hole tunneling energy plays a substantial role. In this scheme, the energy coincidence between $XX_k^- \to X_i^-$ and $X_j^- \to e$ (or $XX_k^+ \to X_i^+$ and $X_j^+ \to h$) $i \neq j$ transitions must be established; i (j) and k sweep over possible spin configurations of X^- and XX^-. In the diagram shown in Figure 5.4, the XX^- spin configurations are $|e_{\sigma_{e_1}} e_{\sigma_{e_2}} e_{\sigma_{e_3}} h_{\sigma_{h_1}} h_{\sigma_{h_2}}\rangle = |P_\uparrow P_\downarrow N_\uparrow R_\Downarrow L_\Uparrow\rangle$ and $|P_\uparrow P_\downarrow N_\downarrow R_\Downarrow L_\Uparrow\rangle$, where one electron molecular state is fully occupied and other states are singly filled up. Upon two inequivalent $|P_\uparrow R_\Downarrow\rangle$ and $|P_\downarrow L_\Uparrow\rangle$ recombinations starting from $|P_\uparrow P_\downarrow N_\uparrow R_\Downarrow L_\Uparrow\rangle$ ($|P_\uparrow P_\downarrow N_\downarrow R_\Downarrow L_\Uparrow\rangle$), two negative trion states, $|e_{\sigma_{e_1}} e_{\sigma_{e_2}} h_{\sigma_{h_1}}\rangle = |P_\downarrow N_\uparrow L_\Uparrow\rangle$ ($|P_\downarrow N_\downarrow L_\Uparrow\rangle$) and $|P_\uparrow N_\uparrow R_\Downarrow\rangle$ ($|P_\uparrow N_\downarrow R_\Downarrow\rangle$), emerge whose energy spacing, labeled by $\Delta_1^{X^-} + \delta_{\text{exc}}^{X^-,1}$ ($\Delta_2^{X^-} + \delta_{\text{exc}}^{X^-,2}$) in Figure 5.4, lies in the hole tunneling matrix element along with the direct and exchange Coulomb interactions. The absorption energy detuning between σ_1^+-photon in path $\mathcal{P}_1$ and σ_4^+-photon in path $\mathcal{P}_4$ under zero magnetic field, $\delta^{\sigma_{1,4}^+}$ ($\approx \delta^{\sigma_{4,1}^-}$, neglecting the difference between exchange interactions), is given by

$$\delta^{\sigma_{1,4}^+} = 2t_h + J_{hh}^{LR} + J_{ee}^{NN} - J_{eh}^{NR} - J_{eh}^{NL} + \Delta_{\text{corr}}^{XX_1^-} - \Delta_{\text{corr}}^{X_1^-} - \Delta_{\text{corr}}^{X_4^-} + \Delta_{\text{exc}}^{XX_1^-} - \Delta_{\text{exc}}^{X_1^-} - \Delta_{\text{exc}}^{X_4^-}, \quad (5.1)$$

where $t_h = (E_h^L - E_h^R)/2$ represents the hole tunneling matrix element, J_{ab}^{AB} stands for the mutual direct Coulomb interaction between particles a and b in the molecular states A and B, and $\Delta_{\text{corr}}^{\alpha}$ ($\Delta_{\text{exc}}^{\alpha}$) denote the correlation (exchange) energy stored in the complex α. Superscript AB denotes the potential of a single particle resting in molecular state A being felt by another single particle localized in state B. In order to write down above equation, the total energies of initial and final complexes in each transition are derived and subtracted. Eq. 5.1 holds once the two paths (here $\mathcal{P}_1$ and $\mathcal{P}_4$) do not share identical initial (negative biexciton) and ground (electron) states.

As implied by Eq. 5.1, $\delta^{\sigma_{1,4}^+}$ can be suppressed upon comparable attractive (J_{eh}^{AB}) and repulsive (J_{hh}^{AB} or J_{ee}^{AB}) Coulomb interactions assuming t_h, $\Delta_{\text{corr}}^{\alpha}$, $\Delta_{\text{exc}}^{\alpha} \ll J_{ab}^{AB}$ [80]. Fulfilling the condition $J_{hh}^{LR} + J_{ee}^{LL} = J_{eh}^{LR} + J_{eh}^{LL}$ then requires a relative similarity between the

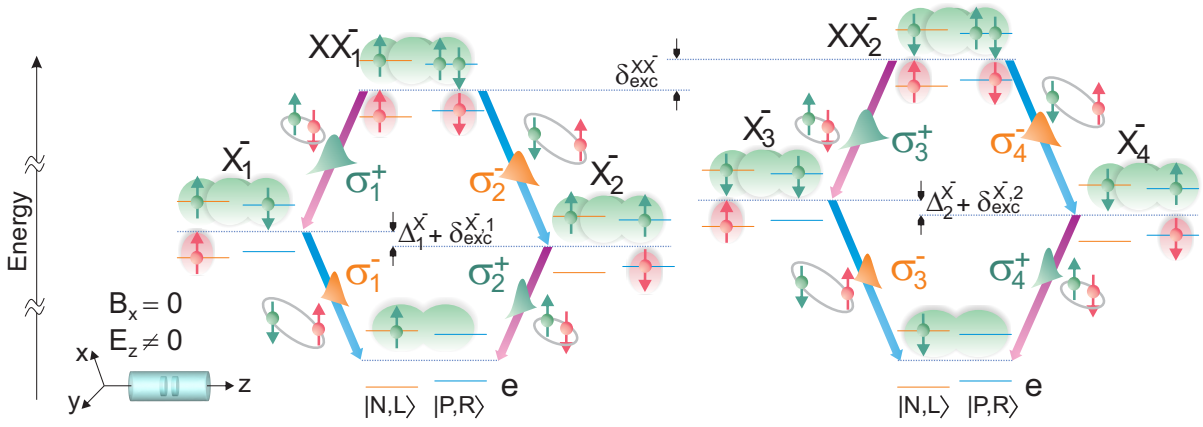

Figure 5.4: Cascade decays initiated from $|P_\uparrow P_\downarrow N_\uparrow R_\Downarrow L_\Uparrow\rangle$ and $|P_\uparrow P_\downarrow N_\downarrow R_\Downarrow L_\Uparrow\rangle$ negative biexcitons down to intermediate negative trion and electron states, producing right σ^+ and left σ^- polarized photons. The axial electric field is assumed nonzero, $E_z \neq 0$, squeezing hole orbitals into dot-localized states. Weak localization of electron is schematically represented by its orbital filling the whole QDM. $\mathbf{B}_x = 0$, thus spin configurations are still not Zeeman-shifted. Spin-photon pair entanglement could be established between each two paths of the left and right panels (subscripts denote the path numbers). Due to the spin-orbit interaction, degeneracies in the charged configurations are lifted (i.e. nonzero $\delta_{\text{exc}}^{X^-,1}$, $\delta_{\text{exc}}^{X^-,2}$ and $\delta_{\text{exc}}^{XX^-}$) even at zero magnetic field. $\Delta_1^{X^-} + \delta_{\text{exc}}^{X^-}$ ($\Delta_2^{X^-} + \delta_{\text{exc}}^{X^-}$) represents the energy spacing of intermediate trions ruled by the hole tunneling matrix element and Coulomb interactions.

electron molecular states as well as left- and right-localized hole states. The necessity of this resemblance further unfolds when considering a single QD: XX^- forms once a biexciton fills up the s-shell and a single electron resides the p-shell. Since transitions between the s and p shells are ideally forbidden $M_{sp} \ll M_{ss}$, M_{pp} (M_{AB} stands for the oscillator strength of transition between the states A and B), either (a) one recombination within each path is optically unfavorable or (b) the final metastable state varies between s and p shell, hindering the energy coincidence. In the QDM proposed here, this coincidence is likely to occur merely when the two decaying paths share the same ground state, $|N_{\uparrow,\downarrow}\rangle$ or $|P_{\uparrow,\downarrow}\rangle$, as the electron tunneling matrix element exceeds few meVs.

All charged configurations in Figure 5.4 further split after introducing a magnetic field in the Voigt geometry (transverse to the primary quantization axis, $\mathbf{B}_x \neq 0$). The induced energy splitting $\triangle_{\mathbf{B}}^{\alpha_i,\alpha_j}$ between charged configurations α_i and α_j then relies on their Zeeman mixing renormalized by the few-body correlations. The order of this splitting under adequately intense magnetic field ($> 200\,\mu$eV) is large enough compared to the dephasing linewidth of σ^+ (or σ^-) transition to impair the certainty in the phase of spin-photon pair wavefunction. Applying weak magnetic fields, on the other hand, could not maintain enough fidelity of the few-photon-based spin readout [162]. Notice that in addition to the recombinations shown in Figure 5.4, dark excitons ($e_\uparrow h_\Uparrow$ or $e_\downarrow h_\Downarrow$) become optically active in the Voigt geometry and give rise to extra cascade combinations; this is further detailed in Sec. VI. Above criteria could be safely applied to the other existing $XX^- \rightarrow X^- \rightarrow e$ cascades and also to $XX^+ \rightarrow X^+ \rightarrow h$ cascades.

Accounting only for the bright transitions, the spin-photon pair entangled states from paths $\mathcal{P}_{1,4}$ and $\mathcal{P}_{2,3}$ are

$$1/\sqrt{2}(|\sigma^+(\omega_1)\sigma^+(\omega_4)\rangle \otimes |\downarrow\rangle + |\sigma^-(\omega_4)\sigma^-(\omega_1)\rangle \otimes |\uparrow\rangle) \tag{5.2}$$

and

$$1/\sqrt{2}(|\sigma^-(\omega_2)\sigma^-(\omega_3)\rangle \otimes |\downarrow\rangle + |\sigma^+(\omega_3)\sigma^+(\omega_2)\rangle \otimes |\uparrow\rangle), \tag{5.3}$$

respectively, where $\hbar\omega_1^{\pm} = \hbar\omega_4^{\pm} \pm \delta^{\sigma^+_{1,4}} + \mathcal{O}_1(\delta_{\text{exc}}, \Delta_{\mathbf{B}}) = \hbar\omega_3^{\pm} + \mathcal{O}_2(\delta_{\text{exc}}, \Delta_{\mathbf{B}}) = \hbar\omega_2^{\pm} \pm \delta^{\sigma^+_{1,4}} + \mathcal{O}_3(\delta_{\text{exc}}, \Delta_{\mathbf{B}})$, and $\mathcal{O}(\delta_{\text{exc}}, \Delta_{\mathbf{B}})$ represents the energy correction due to the exchange and Zeeman splittings. As offered by Figure 5.3(d), the hole anticrossing and thus the negative trion splittings, $\Delta_1^{X^-}$ and $\Delta_2^{X^-}$, are in the order of 0.9 meV ($t_h < 0.45$ meV) at D_s= 5 nm. This small tunneling energy allows for the hole to readily commute between the dots and render higher energy resolutions in the detuning $\delta^{\sigma^+_{1,4}}$ adjustment.

Complex	Label	s-shell configs. (No spin)		s-shell bright channels (Spin included)		
				Total	Direct	Indirect
N-trion (X^-)	eeh	6	$X^- \to e$	24	12	12
P-trion (X^+)	hhe	6	$X^+ \to h$	24	12	12
N-biexciton (XX^-)	$eeehh$	6	$XX^- \to X^-$	72	36	36
P-biexciton (XX^+)	$hhhee$	6	$XX^+ \to X^+$	72	36	36

Table 5.1: Labels and number of s-shell configurations of multi-particle complexes studied here. All four complexes X^-, X^+, XX^- and XX^+ have six spin-excluded components free of exchange interactions. Two last columns show the number of direct, $e_{\uparrow}^{P|N} h_{\Downarrow}^{R|L}$ or $e_{\downarrow}^{P|N} h_{\Uparrow}^{R|L}$, and indirect, $e_{\uparrow}^{N|P} h_{\Downarrow}^{R|L}$ or $e_{\downarrow}^{N|P} h_{\Uparrow}^{R|L}$, bright excitons existing in each complex.

5.6 Photoluminescence spectra of charged complexes under electric field

In this section, we present the results of CI calculations incorporating the Coulomb direct and exchange interactions in a universal few-body hamiltonian constructed from the single particle orbitals (see Appendix A). Table 5.1 shows different classes of excitonic complexes studied here. Consider the case that electron molecular orbitals were strongly localized in different dots: $|P\rangle = |s_{e,R}\rangle$ and $|N\rangle = |s_{e,L}\rangle$. The s-shell transitions then could be categorized into direct and indirect as shown in Table 5.1. The indirect transitions are switched off in such a QDM hosting weakly correlated excitons. In a relatively symmetric QDM with weakly localized electrons, however, they have the chance to recombine with either left- or right-localized holes depending on the total energy of the final complex or particle. This will be detailed in the following.

5.6.1 Negatively charged exciton, $X^- \to e$ transition

Neglecting the spin degree of freedom, 12 transitions could occur between the negative exciton and the single electron levels ($6X^- \times 2e$). Among these, a part of tunneling-assisted transitions are ruled out depending on how the single particles redistribute their orbitals according to the Coulomb interactions. The formation mechanism of X^- consists of initializing one electron spin in the ground state followed by a photoexcitation creating an electron-hole pair. The favorable configuration for the two electrons is to occupy different molecular states $|P\rangle$ and $|N\rangle$ as a consequence of repulsive interaction. $|P\rangle$ and $|N\rangle$,

however, remain as a strong superposition of $|s_{e,L}\rangle$ and $|s_{e,R}\rangle$ in our range of electric field. The hole particle may exist either in the left or in the right QD, whether it is energetically favorable or not. For the sake of simplicity, hereafter, we represent $|s_{e,L}\rangle$ and $|s_{e,R}\rangle$ by $|L\rangle$ and $|R\rangle$, respectively.

Figure 5.5 illustrates the photoluminescence intensity of $X_e^-(\equiv X^- \to e)$ transitions versus the axial electric field and the associated energies. The transition from the initial configuration i to the final configuration f is represented by i_f and all spectral components are plotted with reference energy located at the QDM center. A relatively large energy spacing between $|P\rangle$ and $|L\rangle$ translates to two families of transitions appearing in the spectrum. Among all the features, four components around 1.155 eV and 1.17 eV exhibit bright photoluminescence intensity. a) Bright transitions: $X^-\{eeh\}_{e\{e\}} \equiv PNR_N$, PNL_N, PNR_P and PNL_P for $E_z < 0.5\,\mathrm{kV/cm}$. Note that in this representation, particles flip their localization ($R \rightleftharpoons L$) once the electric field is reversed, except those particles undergoing an anticrossing. We observe no pronounced distinction between the M_{NR} (M_{PL}) and M_{NL} (M_{PR}) oscillator strengths. This primarily relates to the conformity of electron configurations in the two initial states of these transitions bearing a hole anticrossing, and also to the extension of electron orbitals spreading over the entire molecule: PNR_N and PNL_N transitions are coupled sharing the same final state ($|N\rangle$ for $E_z < 0.5\,\mathrm{kV/cm}$) and $\langle P|R\rangle \approx \langle P|L\rangle$ remains unaffected upon heavy hole tunneling.

The anticrossing energy $\Delta^{X^-}_{NR-NL} \approx 0.8\,\mathrm{meV}$ at $E_z = 0.5\,\mathrm{kV/cm}$ is comparable to twice the heavy hole tunneling matrix element $\sim 0.86\,\mathrm{meV}$ (see Appendix B) but has been slightly renormalized by the Coulomb correlations accumulated in X^-. b) Semi-bright transitions, including NNL_N, NNR_N, PPL_P and PPR_P ($E_z > 0.5\,\mathrm{kV/cm}$), have two electrons residing the same molecular state in their initial trion. The photoexcited X^- state is then unfavorable to form, thus the oscillator strength drops significantly regardless of whether recombining particles resting in the same dot or not. c) Dark transitions, such as PPR_N, exist where one electron post-tunneling is involved after recombination (not shown here). We attribute the asymmetry evident in the trion features mostly to the modest asymmetry of the electron and hole orbitals in response to oppositely-oriented axial fields.

5.6.2 Negatively charged biexciton, $XX^- \to X^-$ transition

In contrast to X^-, favorable XX^- configurations accommodate two holes separated in different dots while one electron molecular state is fully and the other one is singly populated. Figure 5.6 shows the two transition families experiencing the hole anticrossings around 1.158 eV and 1.175 eV. Analogous to X^-, the bright components comprise the following

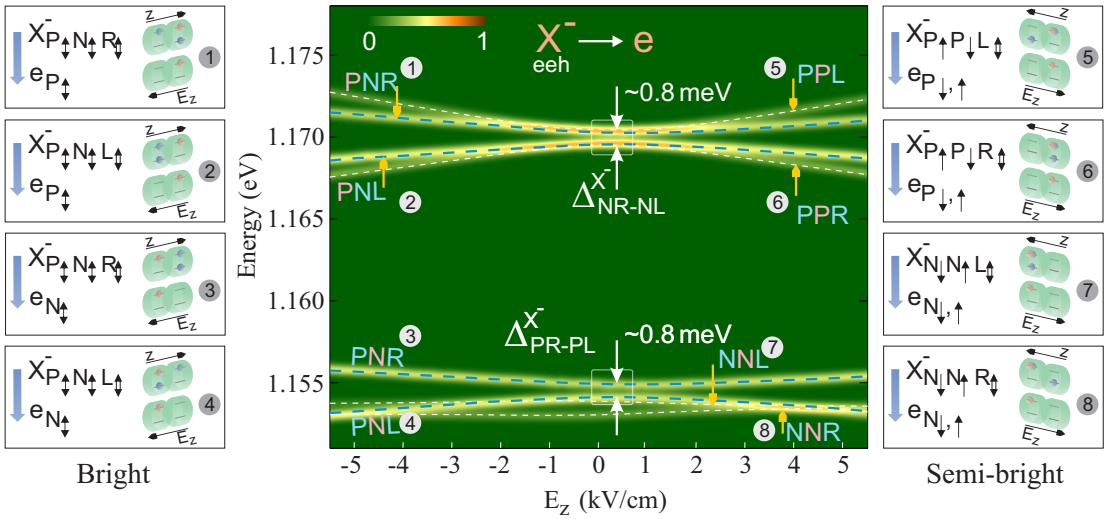

Figure 5.5: Left and right panels: electron and hole configurations in the bright and semi-bright spectral components of negative trion X^-. Center: photoluminescence intensity of X^- bright and semi-bright components plotted against the axial electric field and $X^- \to e$ transition energy. Recombining particles are coloured blue. The averaged energies associated with different components are highlighted by dashed lines: blue, favorable bright configurations; white, semi-bright configurations. Squares show the region of trion-bound hole anticrossing: $\Delta^{X^-}_{LR-LL}$ and $\Delta^{X^-}_{RR-RL} \approx 0.8\,\text{meV}$ comparable to the magnitude of hole anticrossing gap; the subscript shows the recombining excitons in each anticrossing.

recombinations: $XX^-\{eeehh\}_{X^-\{eeh\}} \equiv PNNRL_{PNL}$, $PNNRL_{PNR}$, $PPNRL_{PNR}$ and $PPNRL_{PNL}$. A part of the semi-bright components originate from those configurations having two holes in the same dot, that is $XX^-\{eeehh\}_{X^-\{eeh\}} \equiv eeeRR_{eeR}$ or $eeeLL_{eeL}$, where the unlabeled electron could choose both $|P\rangle$ and $|N\rangle$ molecular states. The rest form once the fully-populated electron molecular orbital of the trion state reshapes along the direction of electric field, rather than in the opposite direction. Some features, including bright components, are subjected to sizeable energy shifts up to 8 meV as a function of the electric field. All XX^- configurations comprising separated holes rise in energy once the electric field is suppressed since J_{hh}^{LR} increases. This increase returns to the significant enhancement of the $\langle h_0|h_1\rangle$ spatial overlap despite the quick decrease in the $|R\rangle$ and $|L\rangle$ orbital densities. In those components where the two holes populate the same QD, $J_{hh}^{LL,RR}$ drops at smaller electric fields because both $\langle h_{0;\Uparrow}|h_{0;\Downarrow}\rangle$ ($\langle h_{1;\Uparrow}|h_{1;\Downarrow}\rangle$) and the orbital densities diminish.

We focus on the two lower-energy bright $XX^- \rightarrow X^-$ transitions previously illustrated in Figure 5.4, $PPNRL_{PNR}$ and $PPNRL_{PNL}$. Assuming exactly identical initial configurations (spin included), the two transitions are tunnel coupled through their final trion states and separated by $\sim \Delta_h^{X^-} = \Delta_{NR-NL}^{X^-}$ splitting at $E_z = 0.5\,\mathrm{kV/cm}$. The highlighted energy lines in Figure 5.6, however, merely indicate the average energy of each component regardless of its spin fine structure. Comparing Figures 5.5 and 5.6, we notice that $PPNRL_{PNR}$ ($PPNRL_{PNL}$) and PNL_N (PNR_N) transitions almost energetically coincide at $E_z = -5\,\mathrm{kV/cm}$. Neglecting the correlation energies in Eq. 5.1, J_{hh}^{LR} is subjected to $\sim 5\,\mathrm{meV}$ (50.25 to 46.25 meV) reduction in magnitude due to the h_0-h_1 spatial splitting caused by a negative electric field equivalent to $5\,\mathrm{kV/cm}$. J_{ee}^{NN} remains almost unchanged (48.5 meV), while J_{eh}^{NL} and J_{eh}^{NR} each undergo -0.4 meV and 1.6 meV shift. The size of QDM and the interdot spacing allow for less confinement along the angular momentum quantization axis z as compared to the previously reported single or stacked QDs [156, 169]. The moderate axial confinement then leads to the smooth variation of h-h interaction while e-h and e-e interactions stay roughly fixed. Although $|h_0\rangle$ and $|h_1\rangle$ molecular orbitals are spatially separated at such fields, their excitons are correlated via the bound electrons.

5.6.3 Positively charged complexes, $X^+ \rightarrow h$ and $XX^+ \rightarrow X^+$ transition

Analogous to the negative trion, formation of a positive trion consists of spin initialization and photoexcitation, but the hole spin is coherently controlled here. Favorable arrangements include the electron neighboring the initial hole whereas the subsequent hole moving to the other dot. This is implied by Figure 5.7(a) where the bright features correspond

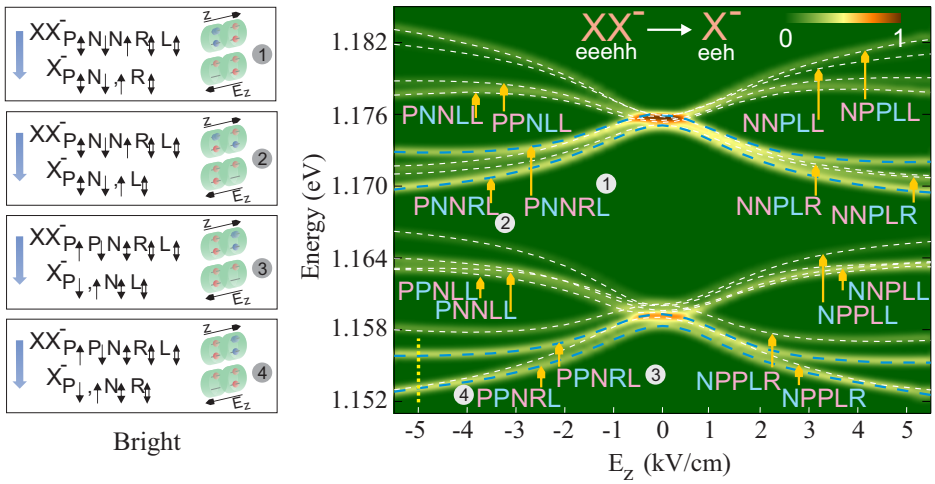

Figure 5.6: Left: electron and hole configurations in the bright spectral components of negatively charged biexciton XX^-. Right: photoluminescence intensity of XX^- versus the axial electric field. Blue (white) dashed lines identify bright (semi-bright) transitions. There exist four bright components, in which both initial (XX^-) and final (X^-) configurations are favorable to form: $PNNRL_{PNR}$, $PNNRL_{PNL}$, $PPNRL_{PNL}$ and $PPNRL_{PNR}$. By comparing to Figure 5.5, we realize that $\delta^{\sigma^+_{1,4}}$ ($\delta^{\sigma^-_{1,4}}$) is minimized at $E_z = -5\,\mathrm{kV/cm}$ (marked by yellow dotted line) where $PPNRL_{PNR}$ ($PPNRL_{PNL}$) and PNL_N (PNR_N) coincide.

to separated holes: $X^+\{hhe\}_{h\{h\}} \equiv LRN_L$, LRN_R ($E_z > 0$), RLN_R and RLN_L ($E_z < 0$). Regardless of the number of transitions, small energy corrections, and the spectral redshift, we seek band bendings akin the $XX^- \rightarrow X^-$ transitions since the energy evolution of each component versus the electric field is primarily attributed to the changes in J_{hh}^{LR} (J_{hh}^{LL} or J_{hh}^{RR} in semi-bright features). In contrast to XX^- and X^+, XX^+ contains three interacting hole particles, complicating the photoluminescence spectrum. The highly favorable configurations develop with segregated electrons, however, the e-e repulsion does not severely influence the formation of pair electrons in our range of axial field, because the energy difference between $P_\uparrow$-$P_\downarrow$ (or $N_\uparrow$-$N_\downarrow$) and $P_\updownarrow$-$N_\updownarrow$ repulsions is insignificant. Transitions in Figure 5.7(b) can be divided into two classes based on their final trion state: a) components in which the hole particles in the final state live in the same dot. These transitions are more responsive toward h-h repulsion compared to b) components with segregated holes in their final trion, thus bearing higher energy shift at larger fields. No features from $XX^+ \rightarrow X^+$ and $X^+ \rightarrow h$ spectra coincide due to the relatively large hybridization energy of the extra electron living in XX^+. This signifies that multipartite energy matching via both negatively and positively charged complexes is, in general, feasible in QDMs where electron and hole tunneling matrix elements are tantamount [170].

5.7 Analytical hamiltonian: Effect of particle interactions on the spin fine structures

In this section, we develop a simplified version of the XX^- and X^- hamiltonians to comprehend the effect of Coulomb interactions on the spin-conserved tunnelings. Providing an analytical model aids us to visualize the behavior of XX^- and X^- spin fine structure versus electric field, without getting involved with the details of CI method. We confine our study to the favorable configurations of XX^- and X^- shown in Figure 5.4. For simplicity, we consider the e-h exchange interactions of single particles residing different molecular states equal, $\delta_{\text{exc}}^{NL} = \delta_{\text{exc}}^{PR} = \delta_{\text{exc}}^{NR} = \delta_{\text{exc}}^{PL} = \delta_{\text{exc}}^{eh}$. This assumption is valid within our range of electric fields where electron and hole molecular orbitals consistently maintain their overlap integral rather unchanged. The 4×4 few-body hamiltonian describing the non-degenerate bright configurations of the negative trion $X_{eeh=PNh}$ could be expanded on basis states $N_\uparrow P_\downarrow L_\Uparrow$, $N_\uparrow P_\downarrow R_\Uparrow$, $N_\downarrow P_\downarrow L_\Uparrow$ and $N_\downarrow P_\downarrow R_\Uparrow$

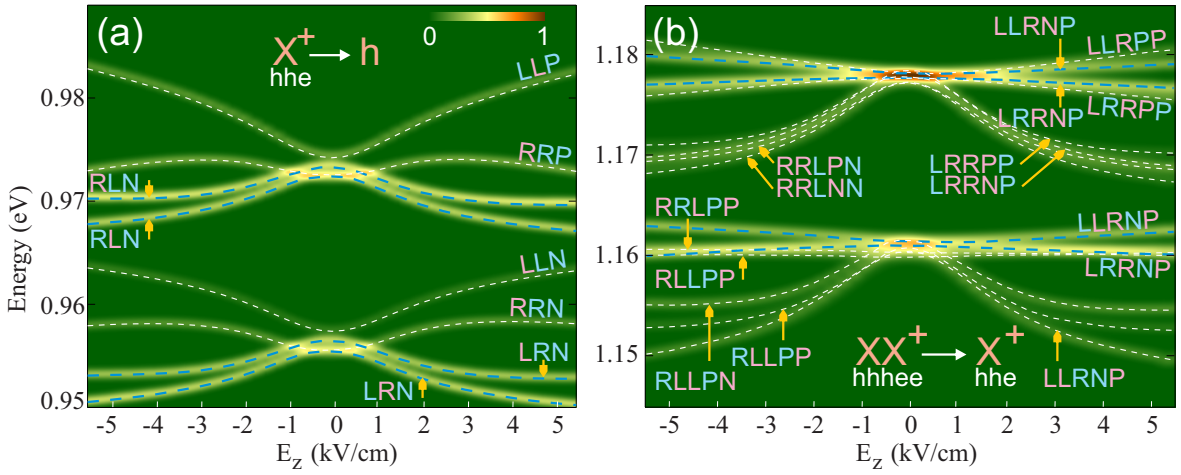

Figure 5.7: Photoluminescence intensity depicted for (a) positive trion X^+ and (b) positive biexciton XX^+ against the axial electric field and transition energies. Bright components in X^+ spectrum form with spatially separated holes. The $XX^+ \to X^+$ spectrum is, by average, 20 meV blueshifted with respect to the $X^+ \to h$ bright transitions due to the electron hybridization energy. Bright components of XX^+ include initial configurations with separated electrons and final configurations X^+ with separated holes: $LLRNP_{LRN}$, $LRRNP_{LRN}$, $LLRNP_{LRP}$ and $LRRNP_{LRP}$. Semi-bright transitions in $XX^+ \to X^+$ comprise either two neighboring electrons in the initial state or two neighboring holes in the final state. The energy splitting between the RLN_L and RLN_R (LRN_L and LRN_R) components at small fields primarily correspond to hole anticrossing in their final states.

$$\mathcal{H}^{\mathrm{B}}_{X^-} = \begin{pmatrix} \zeta_L^{X^-} & -t_h & 0 & 0 \\ -t_h & \zeta_L^{X^-} + \Delta J^{X^-} - \zeta_{E_z} & 0 & 0 \\ 0 & 0 & \zeta_L^{X^-} + 2\delta_{\mathrm{exc}} & -t_h \\ 0 & 0 & -t_h & \zeta_L^{X^-} + \Delta J^{X^-} - \zeta_{E_z} + 2\delta_{\mathrm{exc}} \end{pmatrix}. \quad (5.4)$$

Here, $\zeta_L^{X^-}$ is the total energy of $N_\uparrow P_\downarrow L_\Uparrow$, ζ_{E_z} signifies the energy shift caused by the electric field when the reference energy is located at center of the left QD, $\zeta_{E_z} = \overline{e}E_z(D_s + h_D)$, $\overline{e}$ is the unit charge, and $\Delta J^{X^-} = J_{eh}^{PL} + J_{eh}^{NL} - J_{eh}^{NR} - J_{eh}^{PR}$. The slight difference between s-shell molecular orbitals leads to nonzero ΔJ^{X^-}. The mean value of the e-h exchange energy $\delta_{\mathrm{exc}}^{eh}$ is calculated by averaging over $\langle\psi_\uparrow^e\psi_\Downarrow^h|\,\mathcal{C}\,|\psi_\Downarrow^h\psi_\uparrow^e\rangle - \langle\psi_\uparrow^e\psi_\Uparrow^h|\,\mathcal{C}\,|\psi_\Uparrow^h\psi_\uparrow^e\rangle$ versus E_z, where $\mathcal{C}$ is the Coulomb interaction operator.

We notice that the bright states $N_\uparrow P_\downarrow L_\Uparrow$ ($\equiv N_\downarrow P_\uparrow L_\Uparrow \equiv N_\uparrow P_\downarrow L_\Downarrow \equiv N_\downarrow P_\uparrow L_\Downarrow$) and $N_\uparrow P_\downarrow R_\Uparrow$ ($\equiv N_\downarrow P_\uparrow R_\Uparrow \equiv N_\uparrow P_\downarrow R_\Downarrow \equiv N_\downarrow P_\uparrow R_\Downarrow$) are fourfold degenerate, while $N_\downarrow P_\downarrow L_\Uparrow$ ($\equiv N_\uparrow P_\uparrow L_\Downarrow$) and $N_\downarrow P_\downarrow R_\Uparrow$ ($\equiv N_\uparrow P_\uparrow R_\Downarrow$) are twofold degenerate as long as $\delta_{\mathrm{exc}}^{NL} = \delta_{\mathrm{exc}}^{PR} = \delta_{\mathrm{exc}}^{NR} = \delta_{\mathrm{exc}}^{PL}$ and the trivial anisotropic exchange interactions are discarded. These assumptions are not necessarily valid in a strained QDM as could be revealed by our CI calculations, but facilitate providing a semi-quantitative description of the exchange couplings. The total energy spectrum of $X^-_{eeh=NPh}$ as a function of the axial electric field is plotted in Figure 5.8(a), where the direct Coulomb interactions are artificially discarded $\Delta J_1^{X^-} = 0$, and (b) where the states are Coulomb correlated $\Delta J_1^{X^-} \neq 0$. The quadruplets labeled by $N_\uparrow P_\downarrow L_\Uparrow$ and $N_\uparrow P_\downarrow R_\Uparrow$ (analogous to the doublets labeled by $N_\downarrow P_\downarrow L_\Uparrow$ and $N_\downarrow P_\downarrow R_\Uparrow$) evolve to resonance where the anticrossing caused by the hole tunneling appears, $\Delta_h^{X^-} = 2\sqrt{t_h^2 + (2\delta_{\mathrm{exc}}^{eh})^2} \simeq 892$ μeV having $2\delta_{\mathrm{exc}}^{eh} = 122\,\mu$eV and $t_h = 430\mu$eV. Relatively trivial variations of $\Delta J_1^{X^-}$, shown in the inset of Figure 5.8(b), is a consequence of electron delocalization and comparable direct and indirect e-h interactions, thus $\Delta_h^{X^-}$ is not noticeably renormalized.

Negative biexciton includes two hole particles, thus the spin-conserved tunneling of the hole is restricted by the Pauli exclusion principle. This spin blockade leads to six $XX^-_{eeehh=N_\uparrow P_\uparrow P_\downarrow hh}$ doublets considering the twofold spin degeneracy of each electron. In order to resolve the corresponding energy state diagram, we consider the basis states $N_\uparrow P_\uparrow P_\downarrow L_\Downarrow R_\Uparrow$ ($\equiv N_\downarrow P_\uparrow P_\downarrow L_\Downarrow R_\Uparrow$), $N_\uparrow P_\uparrow P_\downarrow L_\Uparrow R_\Downarrow$ ($\equiv N_\downarrow P_\uparrow P_\downarrow L_\Uparrow R_\Downarrow$), $N_\uparrow P_\uparrow P_\downarrow L_\Downarrow R_\Downarrow$ ($\equiv N_\downarrow P_\uparrow P_\downarrow L_\Uparrow R_\Uparrow$), $N_\uparrow P_\uparrow P_\downarrow L_\Uparrow R_\Uparrow$ ($\equiv N_\downarrow P_\uparrow P_\downarrow L_\Downarrow R_\Downarrow$), $N_\uparrow P_\uparrow P_\downarrow R_\Uparrow R_\Downarrow$ ($\equiv N_\downarrow P_\uparrow P_\downarrow R_\Uparrow R_\Downarrow$) and $N_\uparrow P_\uparrow P_\downarrow L_\Uparrow L_\Downarrow$ ($\equiv N_\downarrow P_\uparrow P_\downarrow L_\Uparrow L_\Downarrow$), then construct the 6×6 few-body hamiltonian $\mathcal{H}^{\mathrm{B}}_{XX^-}$ as

$$\begin{pmatrix} \Delta J_1^{XX^-} - \zeta_{E_z} & 0 & 0 & 0 & -t_h & -t_h \\ 0 & \Delta J_1^{XX^-} - \zeta_{E_z} & 0 & 0 & -t_h & -t_h \\ 0 & 0 & \Delta J_1^{XX^-} - \zeta_{E_z} + 2\delta_{\text{exc}} & 0 & 0 & 0 \\ 0 & 0 & 0 & \Delta J_1^{XX^-} - \zeta_{E_z} - 2\delta_{\text{exc}} & 0 & 0 \\ -t_h & -t_h & 0 & 0 & \Delta J_2^{XX^-} - 2\zeta_{E_z} & 0 \\ -t_h & -t_h & 0 & 0 & 0 & \zeta_L^{XX^-} \end{pmatrix}, \tag{5.5}$$

$$\Delta J_1^{XX^-} = \zeta_L^{XX^-} + J_{eh}^{NL} + 2J_{eh}^{PL} - J_{eh}^{NR} - 2J_{eh}^{PR} + J_{hh}^{LR} - J_{hh}^{LL} \tag{5.6}$$

and

$$\Delta J_2^{XX^-} = \zeta_L^{XX^-} + 2(J_{eh}^{NL} - J_{eh}^{NR} + 2J_{eh}^{PL} - 2J_{eh}^{PR}) + J_{hh}^{RR} - J_{hh}^{LL}. \tag{5.7}$$

where $\zeta_L^{XX^-}$ is the total energy of $N_\uparrow P_\uparrow P_\downarrow L_\Uparrow L_\Downarrow$. Assuming that the direct and indirect interactions are comparable, $\Delta J_1^{XX^-} = \zeta_L^{XX^-}$ and $\Delta J_2^{XX^-} = \zeta_L^{XX^-}$, we observe the singlet states $N_\uparrow P_\uparrow P_\downarrow L_\Uparrow L_\Downarrow$ and $N_\uparrow P_\uparrow P_\downarrow R_\Uparrow R_\Downarrow$ undergoing an "anticrossing" with an energy gap equivalent to $\Delta_h^{XX^-} = 2\sqrt{2t_h^2 + (2\delta_{\text{exc}}^{eh})^2} \simeq 1.24$ meV; see Figure 5.8(c). The two singlets, however, first couple to $N_\uparrow P_\uparrow P_\downarrow L_\Downarrow R_\Uparrow$ or $N_\uparrow P_\uparrow P_\downarrow L_\Uparrow R_\Downarrow$ rather than undergoing a direct anticrossing since the two-hole tunneling is prohibited in our model. The triplet states $N_\uparrow P_\uparrow P_\downarrow L_\Downarrow R_\Downarrow$ and $N_\uparrow P_\uparrow P_\downarrow L_\Uparrow R_\Uparrow$ are separated by $\zeta_{\text{exc}}^{XX^-} = 4\delta_{\text{exc}}^{eh}$ and pass through the anticrossing region without tunnel coupling to the singlet states, because the spin state is conserved during the tunneling. The remaining states, $N_\uparrow P_\uparrow P_\downarrow L_\Downarrow R_\Uparrow$ and $N_\uparrow P_\uparrow P_\downarrow L_\Uparrow R_\Downarrow$, form a singlet-triplet pair in proximity to the anticrossing. Their degeneracy seen in Figure 5.8(c) returns back to the assumption of all exchange interactions being equivalent. Beyond the thin barrier limit, δ_{exc}^{NR} exchange interaction is negligible, thus $N_\uparrow P_\uparrow P_\downarrow L_\Downarrow R_\Uparrow$ and $N_\uparrow P_\uparrow P_\downarrow L_\Uparrow R_\Downarrow$ split by $\zeta_{\text{exc}}^{XX^-} = 2\delta_{\text{exc}}^{eh}$ as illustrated in the inset of Figure 5.8(c).

In Figure 5.8(d), the energy state diagram of $XX^-_{eeehh=N_\uparrow P_\uparrow P_\downarrow hh}$ is depicted against the electric field, taking the Coulomb interactions into account ($\Delta J_1^{XX^-} \neq \zeta_L^{XX^-}$ and $\Delta J_2^{XX^-} \neq \zeta_L^{XX^-}$). *h-h* repulsive interactions significantly change as a function of axial localization, leading to large variations in J_{hh}^{LL}, J_{hh}^{LR} and $\Delta J_1^{XX^-}$ versus the electric field as shown in the inset. The Coulomb splitting drastically renormalizes the energy levels of the quadruplet $N_\uparrow P_\uparrow P_\downarrow L_\Downarrow R_\Uparrow$, $N_\uparrow P_\uparrow P_\downarrow L_\Uparrow R_\Downarrow$, $N_\uparrow P_\uparrow P_\downarrow L_\Downarrow R_\Downarrow$, $N_\uparrow P_\uparrow P_\downarrow L_\Uparrow R_\Uparrow$, and decouples the hole spin singlets, $N_\uparrow P_\uparrow P_\downarrow L_\Uparrow L_\Downarrow$, and $N_\uparrow P_\uparrow P_\downarrow R_\Uparrow R_\Downarrow$, from $N_\uparrow P_\uparrow P_\downarrow L_\Downarrow R_\Uparrow$ and $N_\uparrow P_\uparrow P_\downarrow L_\Uparrow R_\Downarrow$, in the vicinity of the anticrossing gap. The splitting can be suppressed by intermixing the

dot-barrier materials and thus delocalizing the $|h_0\rangle$ and $|h_1\rangle$ molecular orbitals. Since the negative trion states are rather insensitive to Coulomb interactions, the anticrossings visible in the $N_\uparrow P_\uparrow P_\downarrow hh \rightarrow NPh$ transitions are mainly due to the tunnel-coupling of final states. Extending the same principles to positively charged complexes, the spin fine structure of the positive trion X^+ should exhibit a similar pattern as XX^- as long as the hole tunneling is concerned. The presence of three holes in the positive biexciton XX^+, however, further complicates the effective hamiltonian. We do not study the total energy of XX^+ here, but we predict observing trivial decouplings because the h-h repulsions effectively cancel out each other, i.e. $J_{hh}^{LL} + 2J_{hh}^{RL} - J_{hh}^{RR} - 2J_{hh}^{LR} \leq 2t_h$.

5.8 Cascade Transitions under Transverse Magnetic Field

CI method incorporates both isotropic and anisotropic e-h exchange interactions $\delta_{\text{exc}}^{eh} = -\beta^{\text{exc}} \boldsymbol{\sigma}_e \cdot \mathbf{J}_h$, where β^{exc} is the coupling coefficient and $\mathbf{J}_h$ is the hole angular momentum operator. β^{exc} coefficients of mutual e-h exchange interactions are calculated using $\langle \psi_{\sigma_e}^e \psi_{\sigma_h}^h | \mathcal{C} | \psi_{\sigma_h}^h \psi_{\sigma_e}^e \rangle = \langle \psi_{\sigma_e}^e | V_{\sigma_e,\sigma_h}^{e,h} | \psi_{\sigma_h}^h \rangle$, where $V_{\sigma_e,\sigma_h}^{e,h}$ is the mean-field potential caused by the mixed orbital $\langle \psi_{\sigma_e}^e | \psi_{\sigma_h}^h \rangle$ [125]. Upon applying a transverse (non-axial) magnetic field in the Voigt geometry, the magnetic-field-induced coupling terms between the bright and dark excitons appear, enhancing the energy splittings and providing access to the desirable spin states. The off-diagonal mixing matrix elements $\langle \alpha_i | \mathcal{H}_{\mathbf{B}}^{ij} | \alpha_j \rangle$ between two arbitrary configurations α_i and α_j is given by $\mathcal{H}_{\mathbf{B}}^{ij} = \frac{\mu_B}{2} g_{eff}^{\perp} \mathbf{B}_\perp \cdot \boldsymbol{\sigma}_{ij}$, where $g_{eff}^{\perp}$ stands for the effective transverse g-factor at a particular axial electric field, and $\boldsymbol{\sigma}_{ij}$ is the spin flip operator associated with configurations α_i and α_j. The dark-bright mixing gives rise to a nonzero many-body oscillator strength of dark states, introducing extra optically-active decays in proximity to the unperturbed transitions. Activation of dark transitions may lead to the emergence of unwanted spectral features and several Λ systems [171], comprising metastable electron and hole ground states with unwanted spin configurations. Therefore, they shall be eliminated from the spectral window before being subjected to any additional post-processing.

One striking feature in the energy level diagram of QDMs, as compared to single QDs, is the existence of available bright channels leading to both $|e_\uparrow\rangle$ and $|e_\downarrow\rangle$ electron final states. Hence, the requisite for activating dark states via a transverse magnetic field is basically eliminated, and the Faraday configuration (parallel to the strong quantization axis) could also be employed for the spin control or tuning the charged complexes. Our single particle calculations based on the gauge invariant discretization method [163] show

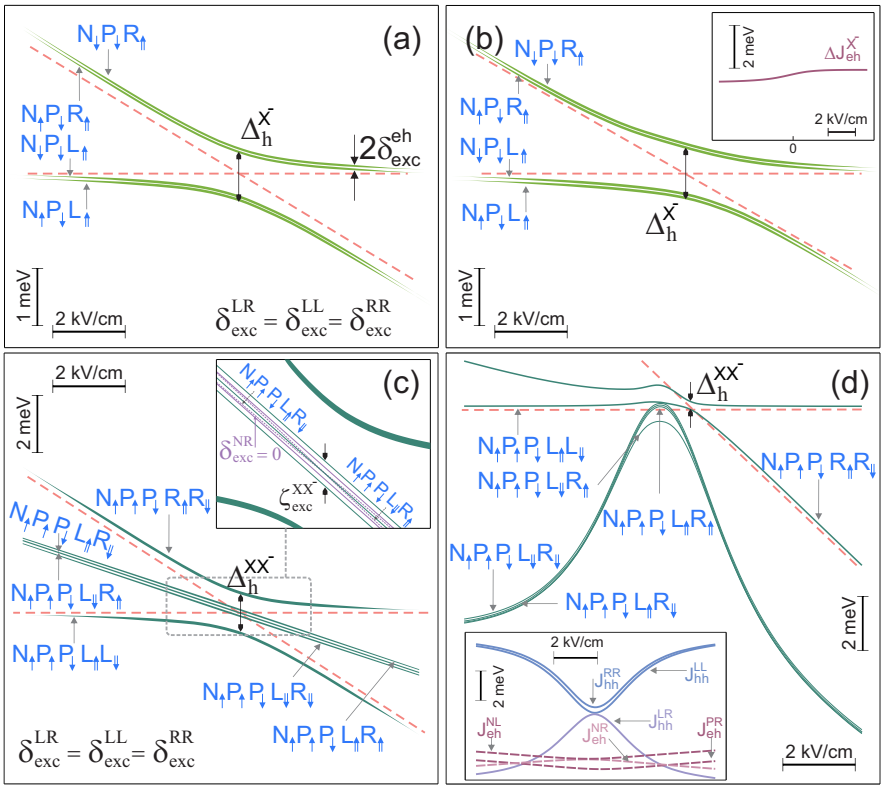

Figure 5.8: (a) Energy level diagram of the irreducible trion basis set plotted with respect to the reference energy $\zeta_L^{X^-}$ as a function of the axial electric field once the direct Coulomb interactions are switched off. $N_\uparrow P_\downarrow L_\Uparrow$ and $N_\uparrow P_\downarrow R_\Uparrow$ ($N_\downarrow P_\downarrow L_\Uparrow$ and $N_\uparrow P_\downarrow R_\Uparrow$) are tunnel coupled, $\Delta_h^{X^-} \simeq 892$ μeV, $2\delta^{eh}_{\rm exc} = 122$ μeV. (b) $\Delta J^{X^-} \neq 0$ (inset), but the spin fine structure exhibits a similar pattern to (a) because the attractive interactions are comparable and evolve smoothly as a function of the electric field. (c) Energy state diagram of negative biexciton basis set calculated with respect to $\zeta_L^{XX^-}$ having the Coulomb interactions discarded. $\Delta_h^{XX^-} \simeq 1.24$ meV, $N_\uparrow P_\uparrow P_\downarrow L_\Downarrow R_\Downarrow$ and $N_\uparrow P_\uparrow P_\downarrow L_\Uparrow R_\Uparrow$ are each separated from the $N_\uparrow P_\uparrow P_\downarrow L_\Downarrow R_\Uparrow$-$N_\uparrow P_\uparrow P_\downarrow L_\Uparrow R_\Downarrow$ doublet by $2\delta^{eh}_{\rm exc}$ ($\zeta^{XX^-}_{\rm exc} = 4\delta^{eh}_{\rm exc}$). The inset illustrates the situation where the $\delta^{NR}_{\rm exc}$ and $\delta^{PL}_{\rm exc}$ interactions are assumed to be weak. The violet lines show the new energies of the quadruplet with $N_\uparrow P_\uparrow P_\downarrow L_\Downarrow R_\Uparrow$ and $N_\uparrow P_\uparrow P_\downarrow L_\Uparrow R_\Downarrow$ crossing. (d) Coulomb interactions are switched on, $\Delta J_1^{XX^-} \neq \zeta_L^{XX^-}$ and $\Delta J_2^{XX^-} \neq \zeta_L^{XX^-}$. Noticeable change in $\Delta J_1^{XX^-} \simeq J_{hh}^{LR} - J_{hh}^{LL}$ decouples the quadruplet from the $N_\uparrow P_\uparrow P_\downarrow L_\Uparrow L_\Downarrow$ and $N_\uparrow P_\uparrow P_\downarrow R_\Uparrow R_\Downarrow$ singlets. Inset: evolution of attractive and repulsive interactions as a function of the axial electric field.

that due to the orbital resemblance, the hole effective g-factors are comparable for the low-lying s-shells, that is $g^x_{|s_{h,L}\rangle} = 0.262$ and $g^x_{|s_{h,L}\rangle} = 0.258$, and smaller than the electron effective g-factors, $g^x_{|s_{e,N}\rangle} = -1.08$ and $g^x_{|s_{e,P}\rangle} = -1.042$, at $E_z = -5\,\mathrm{kV/cm}$. We comment that strong localization of hole orbitals under electric field results in smaller g-factors and less Zeeman splitting of charged states. The reason lies in the fact that g-factor can be explained as the measure of deformation the orbital undergoes in response to the external magnetic field. Once the hole orbital becomes squeezed in the real space, its Fourier transform spreads out in k-space. The hole particle then gains further kinetic energy if its orbital reshapes. The reluctance to exchange the kinetic energy prohibits the orbital to deform by the magnetic field and the g-factor drops. Therefore, although excitons are fully entangled in the vicinity of anticrossing, they suffer from larger Zeeman shifts under the magnetic field.

Figure 5.9(a) and (b) illustrate the energy spectrum of XX^- and X^- for different spin configurations in $NPPLR$ and NPL components, respectively, as a function of the transverse magnetic field $\mathbf{B}_x$ at $E_z = -5\,\mathrm{kV/cm}$. We selected three exemplary configurations from the XX^- energy state spectrum comprising two bright recombinations with electrons localized in $|P\rangle$. Transitions labeled as σ_1^+, σ_3^+ and σ_5^- correspond to the bright $\langle P|R\rangle$ recombinations. The oscillator strength of $XX^-\{NPPLR\}_{X^-\{NPL\}}$ transitions is given in Figure 5.9(c). The anticrossings visible at low magnetic fields correspond to the coupling to dark trion features or the bright-bright trion mixing; for example, $\delta_h^L = 11\,\mu\mathrm{eV}$ is the hole anticrossing energy between $N_\downarrow P_\uparrow R_\Uparrow$ and $N_\downarrow P_\uparrow R_\Downarrow$ states. Such anticrossing behaviour changes the dominant character of Zeeman-coupled spin configurations in the course of magnetic field variations. The measure of anticrossing energy pertains to the effective g-factor of the coupled spin states. The primary character of each spin configuration at $\mathbf{B}_x = 3\mathrm{T}$ is indicated in Figure 5.9(a-b) and (e-f).

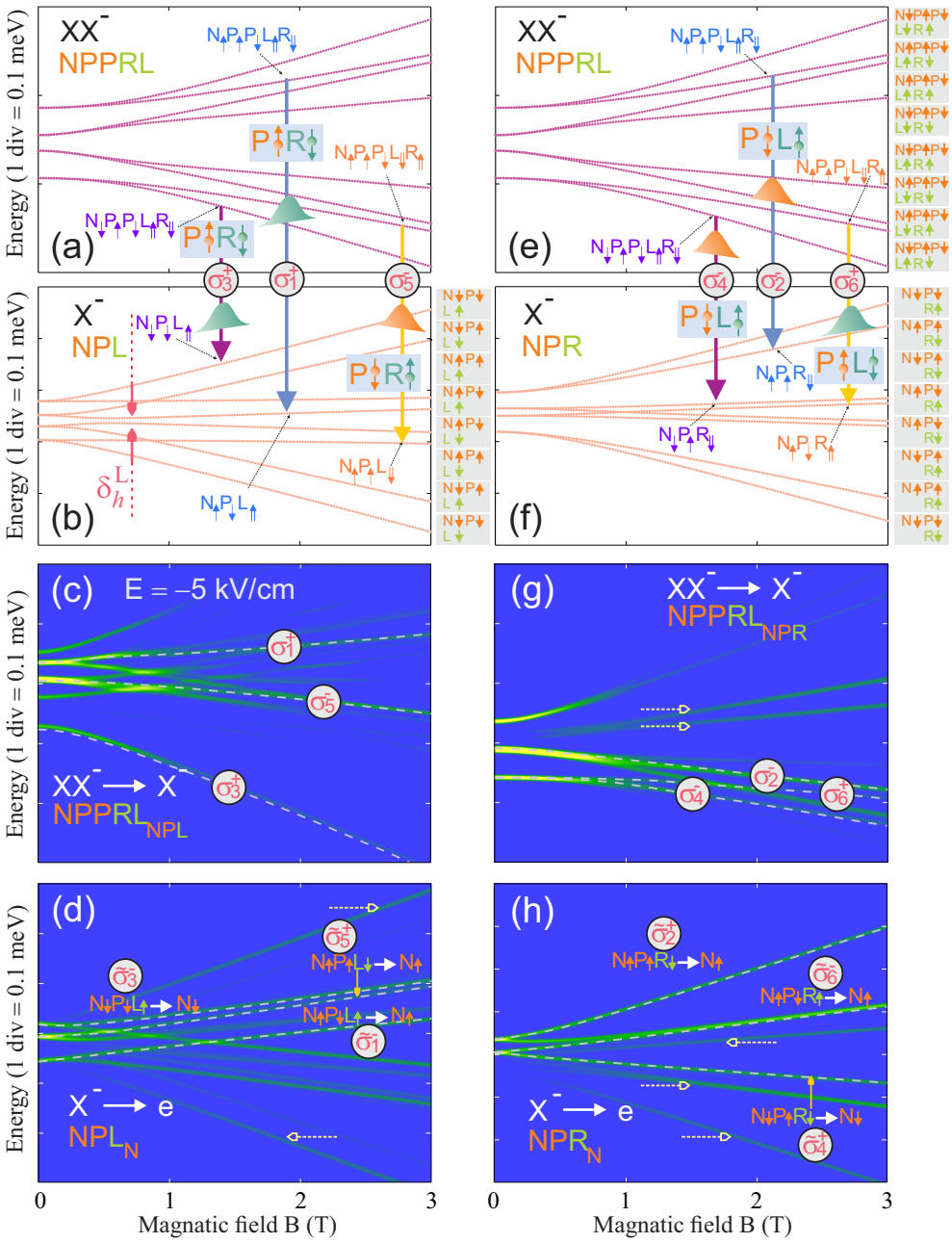

Figure 5.9: (a) and (e) Negative biexciton $NPPLR$ and, (b) and (f), negative trions, NPL and NPR, energies versus the [100]-oriented magnetic field at $E_z = -5\,\mathrm{kV/cm}$. The dominant character attributed to each component at $\mathbf{B}_x = 3\mathrm{T}$ is indicated at the right side of each panel. Configurations with all the spins flipped are approximately degenerate at $\mathbf{B}_x = 0$. Intermediate trions configured in NPL and NPR form following $\langle P_{\sigma_e}|R_{\sigma_h}\rangle$ and $\langle P_{\sigma_e}|L_{\sigma_h}\rangle$ recombinations, respectively. Three pairs of $XX^-_{X^-}$ bright transitions, (c) and (g), exhibiting large enough oscillator strengths are selected: σ_1^+ (σ_2^-), σ_3^+ (σ_4^-) and σ_5^- (σ_6^+). The subsequent X_e^- transitions, (d) and (h), are labeled by $\tilde{\sigma}_1^-$ ($\tilde{\sigma}_2^+$), $\tilde{\sigma}_3^-$ ($\tilde{\sigma}_4^+$) and $\tilde{\sigma}_5^+$ ($\tilde{\sigma}_6^-$). The energies of final electron states $\{N_\uparrow, N_\downarrow\}$ are not shown here. Horizontal arrows mark dark states gaining noticeable oscillator strengths upon Zeeman mixing.

The asymmetric character of s-shell molecular orbitals reveals comparing Figures 5.9(b) and (f) where localization of the trion-bound hole is merely altered, but the effective g-factors of trions are different. Similar to Figure 5.9(c), the oscillator strengths of the trions are shown in Figure 5.9(d) labeled by $\tilde{\sigma}_1^+$, $\tilde{\sigma}_3^+$ and $\tilde{\sigma}_5^-$. Compared to $\sigma_{i=1,3}^+$ (σ_5^-), the trion transitions $\tilde{\sigma}_{i=1,3}^-$ ($\tilde{\sigma}_5^+$) undergo relatively smaller energy change versus $\mathbf{B}_x$. The maximum energy variation observed for each individual transition however does not exceed 200 μeV under this range of magnetic field $\mathbf{B}_x < 3$T. Right panel of Figure 5.9 depicts the same set of data for $XX^-\{NPPLR\}_{X^-\{NPR\}}$ transitions: the initial XX^- states are identical but the intermediate trion states here emerge following $\langle P|L\rangle$ recombination, also the polarization of the emitted photon is reversed. The spectral dispersion through coupling to multiple states is considerably suppressed in both $XX_{X^-}^-$ and X_e^- spectra as compared to the alternative path due to the less number of crossings (anticorssings) seen in the NPR trion.

5.9 Photon pair concurrence

Full analysis of the spin-photon pair entanglement should be performed in an experimental framework or via a mathematical model incorporating the timing details and spin dynamics. An explicit parameter to incorporate the energy and linewidth of two arbitrary transitions in QDM spectrum is the photon-pair concurrence. In our particular case, the tripartite concurrence could be estimated once the spin dynamics is known [172]. Here we exclusively analyze the photon indistinguishability through calculating the concurrence C which is ideally $C = 1$ for the maximally entangled state in the regular scheme but never reaches above 0.73 in the time reordering scheme (cross entanglement). In order to verify the entanglement between the photon pair and the third particle (electron spin), their correlations in the current spin-polarization basis as well as the rotated basis shall be measured. Previous observation of these correlations are reported for the spin-single photon entanglement [173]. In the following, we narrow down our model to the cross-entanglement scheme. The findings are then extensible to the regular scheme.

According to Figure 5.4, the concurrence of photon pairs relies upon $\Gamma_{XX^-\to X_\lambda^-}$, $\Gamma_{X_\lambda^-\to e}$, $\lambda \in \{\sigma^+, \sigma^-\}$, and the normalized detuning $\Delta_\omega^{\aleph} = [\delta^{\sigma_{1,4}^+} + \mathcal{O}(\delta_{\text{exc}}, \Delta_{\mathbf{B}})]/2\Gamma_{X_{\sigma^+}^-\to e}$, where $\Gamma_{\alpha_i\to\alpha_j}$ stands for half the spontaneous emission rate of the recombining exciton: the concurrence drops with increasing $\Gamma_{XX^-\to X_\lambda^-}/\Gamma_{X_\lambda^-\to e}$ and $\Delta_\omega^{\aleph}$ [102]. Both these parameters can be optimized via frequency conversion technique to maximize the concurrence. Figure 5.10 schematically shows the setup for spectral filtering the polarized emission of QDM and manipulating the linewidths of $XX_{X^-}^-$ and X_e^- photons: The desired polarization of pho-

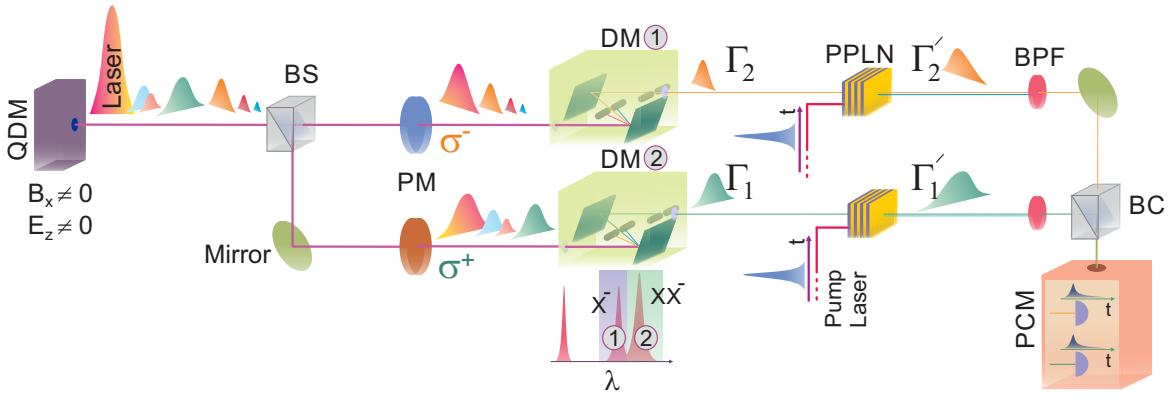

Figure 5.10: Simplified experimental setup of the X^- and XX^- polarization and spectral filtering and the subsequent frequency conversion. Excitation setup including pump and rotation is not shown here. The linewidths of emitted photons, Γ_1 and Γ_2, are broadened through the downconversion process (periodically poled lithium niobate, PPLN) once the unwanted spectral components are properly filtered out. QDM, quantum dot molecule; BS, beam splitter; PM, polarization module composed of polarizer, half and quarter wave plates; DM, double monochromator; BC, beam combiner; BPF, bandpass filter; PCM, photon counting module including single photon detectors.

tons is selected by the polarization module (PM). Except $XX^-_{X^-}$ and X^-_e, other spectral features are then filtered out via a double monochromator (DM). At this step, the photon linewidths, $\Gamma_2 = \Gamma_{XX^- \longrightarrow X^-_\lambda}$ and $\Gamma_1 = \Gamma_{X^-_\lambda \longrightarrow e}$, are broadened via cross-correlating the corresponding photons with an ultrafast laser in a PPLN waveguide. This process leads to both frequency and linewidth conversion of initial $XX^-_{X^-}$ and X^-_e photons and their concurrence. Assuming that the dephasing linewidth could become as narrow as 30 μeV in defect-free NWQDs [174], the normalized detuing drops significantly subsequent to the frequency conversion process, which is able to enhance Γ even by one order of magnitude [173].

Above linewidths relate to the photon emission rates proportional to $\langle XX^-_\lambda | \mathcal{H}_{\text{em}} | X^-_\lambda \rangle$ and $\langle X^-_\lambda | \mathcal{H}_{\text{em}} | e \rangle$. Here, $\mathcal{H}_{\text{em}}$ is the coupling hamiltonian to the optical modes l, $\mathcal{H}_{\text{em}} = \sum_{c;l;\lambda} g^c_{l\lambda} \hat{a}^\dagger_{l\lambda} \hat{b}_\lambda$ + H.c. where $g^c_{l\lambda}$ is the oscillator strength of transition $c = \{XX^-_\lambda \rightarrow X^-_\lambda, X^-_\lambda \rightarrow e\}$, $\hat{b}_{\sigma^+} = \hat{h}_\Downarrow \hat{c}_\uparrow$, $\hat{b}_{\sigma^-} = \hat{h}_\Uparrow \hat{c}_\downarrow$, and $\hat{a}^\dagger_{l\lambda}$ creates a photon in lth optical mode with polarization λ. Figures 5.11(a) and (d) depict the energy evolution of photons created in paths $\mathcal{P}_1$ and $\mathcal{P}_4$ ($\mathcal{P}_2$ and $\mathcal{P}_3$) as a function of the transverse magnetic field. For the sake of simplicity, we assume that the average linewidth of upper transitions in Figure 5.4 diagram after frequency conversion is twice the linewidth of lower ones: $\gamma_p = \Gamma'_{XX^- \rightarrow X^-_\lambda} / \Gamma'_{X^-_\lambda \rightarrow e} \approx 2$;

$\Gamma^{'}_{\sigma_1^+} = \Gamma^{'}_{\sigma_4^-} = 2\Gamma^{'}_{\tilde{\sigma}_1^-} = 2\Gamma^{'}_{\tilde{\sigma}_4^+}$. Although this ratio is independent of the dephasing linewidth and primarily relies on the time resolution of the laser source pumping the PPLN, our assumption does not pose any constraint to the generality of results. We further assume that the frequencies of single photons are down-converted with the same ratio, i.e. $\omega^{'}_{i=1,2,3,4} = \eta\omega_{i=1,2,3,4}$. The concurrence of the photon pairs in paths $\mathcal{P}_1$ and $\mathcal{P}_4$ is then given by [102, 175]

$$C = \frac{4}{\pi^2}\int\int \frac{\Gamma_{\sigma_1^+}\Gamma_{\tilde{\sigma}_4^+} W_o(\omega_m,\omega_n)}{(\omega_m+\omega_n-\Omega_{1;XX^-}-i\Gamma^{'}_{\sigma_1^+})(\omega_m+\omega_n-\Omega_{4;XX^-}+i\Gamma^{'}_{\sigma_4^-})}\times \frac{d\omega_m d\omega_n}{(\omega_m-\omega^{'}_{3;X^-}-i\Gamma^{'}_{\tilde{\sigma}_1^-})(\omega_m-\omega^{'}_{4;X^-}+i\Gamma^{'}_{\tilde{\sigma}_4^+})} \tag{5.8}$$

where $\Omega_{1;XX^-} = \omega^{'}_1 + \omega^{'}_3$ and $\Omega_{4;XX^-} = \omega^{'}_2 + \omega^{'}_4$; see Figure 5.11(c). The simplest additional phase above $W_o(\omega_m,\omega_n)$ can be a linear phase with time delay τ_o, that is $W_o(\omega_m,\omega_n) = \exp[i(\omega_m-\omega_n)\tau_o]$. Since the detuning between the two paths $\mathcal{P}_1$ and $\mathcal{P}_4$, $\Delta_\omega = |\omega^{'}_1-\omega^{'}_4|+|\omega^{'}_3-\omega^{'}_2|$, is constantly nonzero in our setup, the time delay suggested by Pathak and Hughs, $\tau_o = \ln(1+\Gamma^{'}_{XX^-\to X_\lambda^-}/2\Gamma^{'}_{X_\lambda^-\to e})/\Gamma^{'}_{XX^-\to X_\lambda^-}$, does not necessarily optimize the concurrence here. The optimum τ_o, however, could be resolved empirically once the actual level broadenings are determined. The concurrence of photon pairs versus the magnetic field and $\Gamma^{'}_{XX^-\to X_\lambda^-}$ is plotted in Figure 5.11(b). The magnetic field magnitude is set above 2 T where the spin initialization and readout are experimentally feasible. The transition oscillator strengths are comparable and steady in this range, permitting the detuning Δ_ω to be the only parameter restraining the concurrence. According to the continuous increase in $\omega^{'}_1$-$\omega^{'}_4$ splitting, local extremum occurs at $\Delta_\omega^{\min}$ at which $\tilde{\sigma}_1^-$ and σ_4^- coincide. The inset shows how noticeably the concurrence is improved once $\Gamma^{'}_{XX^-\to X_\lambda^-}$ increases from 100 μeV up to 200 μeV. Figure 5.11(e) depicts the same plot for the concurrence of photon states across generations in $\mathcal{P}_2$ and $\mathcal{P}_3$. Energy detunings $|\omega^{'}_4-\omega^{'}_1|$ and $|\omega^{'}_2-\omega^{'}_3|$ evolve oppositely versus the magnetic field, thus the concurrence remains insensitive toward its variations, see inset Figure 5.11(e).

Above example demonstrates that level broadenings up to half the photon-photon detuning energy ($\sim 200\,\mu$eV) could improve the cascade concurrence considerably. On the other hand, exerting the magnetic field in the Faraday configuration would keep the dark states inactive and conserve the bright transition oscillator strengths undispersed by prohibiting any spin-flip mixing. Coherent control of the spin rotation may then be more favorable in Faraday configuration owing to its clean emission spectrum. We note that

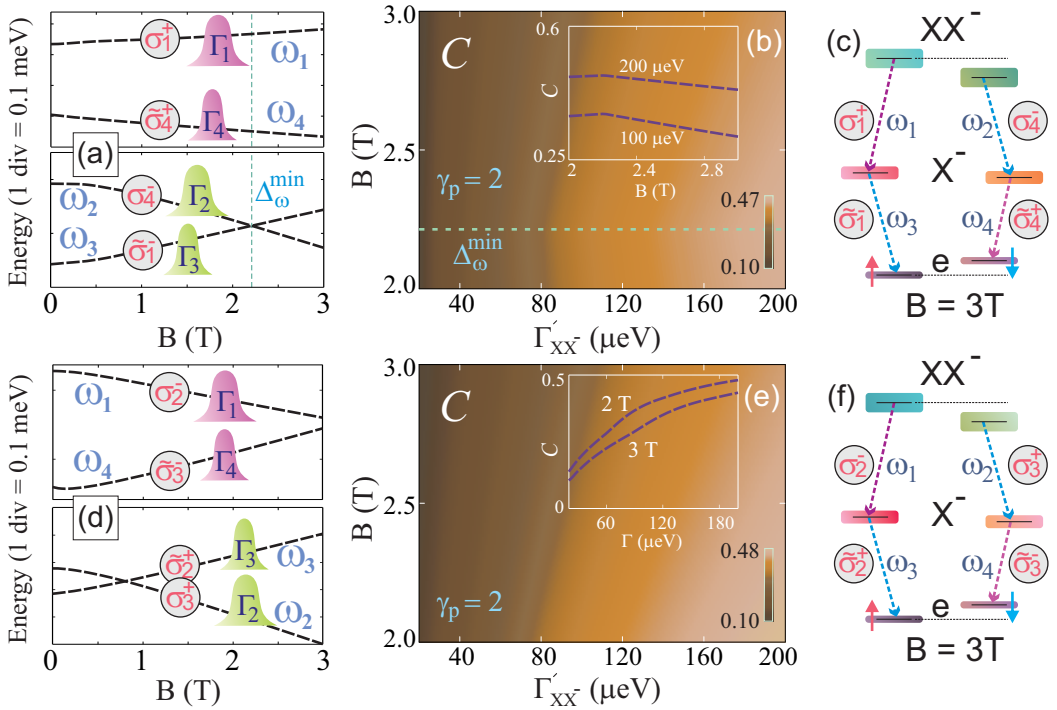

Figure 5.11: (a), (d) Energy of photon pairs created across generations in cascade paths $\mathcal{P}_1$ and $\mathcal{P}_4$, $\mathcal{P}_2$ and $\mathcal{P}_3$. The respective linewidths of photons before frequency conversion are illustrated in a sense that upper transitions possess less dephasing lifetime. The frequency of each transition is labeled according to the $XX^- \rightarrow X_\lambda^- \rightarrow e$ energy diagrams shown in (c) and (f). (b) Concurrence of $\mathcal{P}_1$-$\mathcal{P}_4$ cascades versus magnetic field and $\Gamma'_{XX^- \rightarrow X_\lambda^-}$; $\gamma_p = 2$. The inset shows concurrence as a function of $\mathbf{B}_x$ for $\Gamma'_{XX^- \rightarrow X_\lambda^-}$ =100 μeV and 200 μeV. Maximum value appears at $\Delta_\omega^{\min}$ where $\omega_2 = \omega_3$. (e) Concurrence of photon pairs in $\mathcal{P}_2$-$\mathcal{P}_3$ cascades; $\gamma_p = 2$. Inset: concurrence versus $\Gamma'_{XX^- \rightarrow X_\lambda^-}$ plotted for $\mathbf{B}_x$= 2 T and 3 T.

intermediate exchange-coupled trion states are assumed to be immune to the single spin flip, e.g. $N_{\uparrow}P_{\downarrow}L_{\Uparrow} \rightarrow N_{\downarrow}P_{\downarrow}L_{\Uparrow}$, or the cross-dephasing process, e.g. $N_{\uparrow}P_{\downarrow}L_{\Uparrow} \rightarrow N_{\downarrow}P_{\uparrow}L_{\Downarrow}$, during the excitation cycle. Principally, weak axial quantization of molecular orbitals gives rise to smaller spin relaxation times of the exciton-bound electron and hole [143, 144]. The hole molecular orbitals are squeezed at higher electric field here, but the electron orbitals preserve a fixed volume regardless of the electric field magnitude.

Apart from the photons across generations in Figure 5.4, entanglement between the photons within generations could also be established via the frequency conversion technique. The first emitted photons in paths $\mathcal{P}_1$ and $\mathcal{P}_3$ (or second emitted photons in $\mathcal{P}_2$ and $\mathcal{P}_4$) are in fact energetically separated only by the measure of exchange and Zeeman splittings. This implies that the charged biexciton cascades offer several path options to produce tripartite entangled states. In addition, we predict that higher values of concurrence are obtainable by tailoring the XX^- and X^- level broadenings with different scales as concurrence grows monotonously while $\Gamma'_{XX^-\rightarrow X^-_{\lambda}}/\Gamma'_{X^-_{\lambda}\rightarrow e}$ decreases [102]

5.10 Quantum dot molecules in [111] nanowires

Before ending this chapter, let us address the case of the [001] nanowire replaced with its [111] counterpart. The strain-driven asymmetry of single particle states seen above, and also the asymmetry of transition energies versus the axial electric field are more pronounced in [111]-oriented double QDs as a result of the built-in piezoelectric field; see Sec. 3.5.2 and [139]. The advantage of [111]-oriented quantization, however, is that orbitals save their C_{3v} symmetry irrespective of the electric field amplitude. As mentioned above, the symmetry conversion from D_{2d} down to C_{2v} upon applying the axial electric field on [001]-QDMs lifts the bright exciton degeneracies. In contrast, the elevated C_{3v} symmetry predicted in [111]-QDMs is immune to the symmetry-breaking Stark effect.

Figure 5.12(a) shows the molecular orbitals for a $InAs_{0.2}P_{0.8}$ QDM embedded inside an InP nanowire. Each individual dot is 4 nm thick and 20 nm in diameter. Interdot spacing is set to 6 nm, and the shell thickness is 15 nm. The barrier region is considered InP to delocalize the electron molecular orbitals: the electron hybridization energy is ≈ 12 meV. The 6 nm interdot spacing provides a hole antibonding ground state and $t_h = 0.17$ meV tunneling energy; see Figure 5.12(b) bottom panel. This tunneling energy is comparable to the e-h exchange interaction energy, which leads to interesting properties in the multiparticle energy spectrum of the QDM. For example, in Figure 5.8(a) or (b) we notice that t_h is large enough that the exchange-coupled trion states jointly evolve towards the two asymptotes: basically the tunnel-coupled states are far away from the exchange-coupled

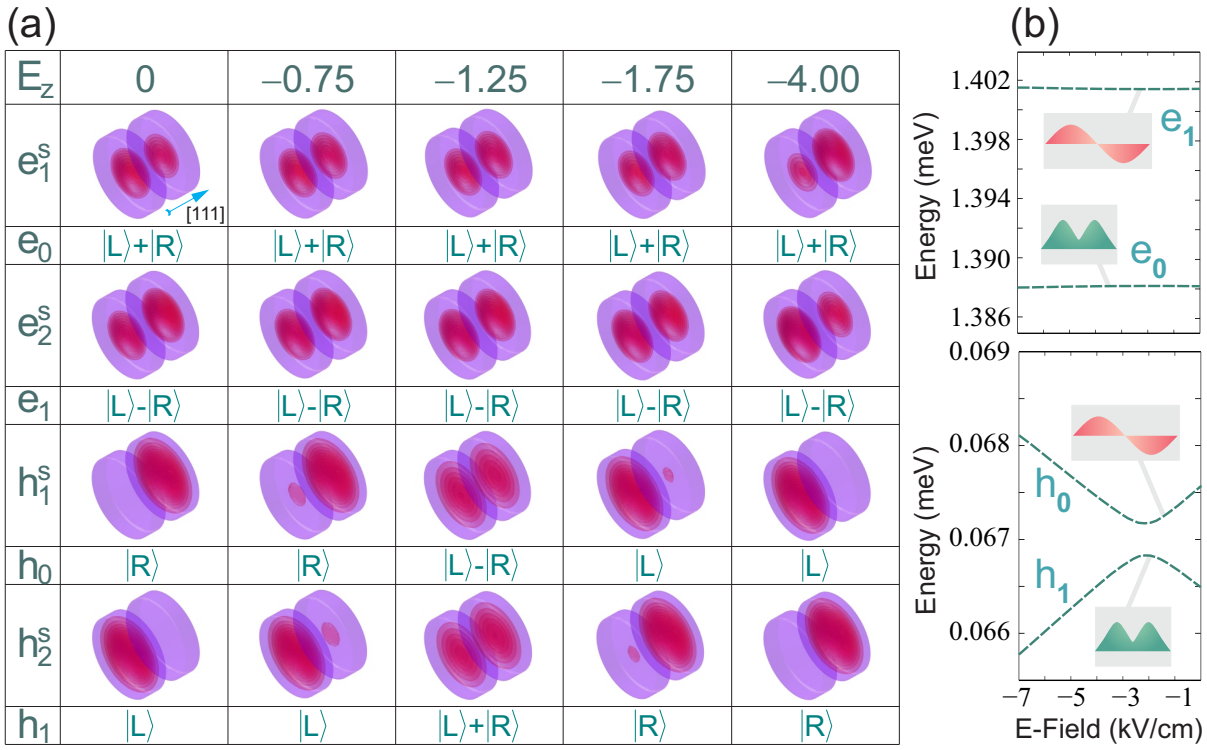

Figure 5.12: (a) Electron and hole s-shell molecular orbitals versus [111]-oriented electric field (the measure of axial electric field E_a is $\sqrt{3}E_z$). Analogous to In(Ga)As QDMs, hole molecular orbitals get localized rapidly away from the anticrossing point, $E_a = -1.25\sqrt{3}$ (kV/cm), while electron orbitals remain almost delocalized as electric field scans over the studied range. (b) Energy of the electron (top panel) and hole (bottom panel) ground and first excited states.

states. However, if the e-h exchange energy exceeds t_h, the tunnel-coupled and exchange-coupled states may cross. This means that it may be more favorable for a particular trion configuration to undergo a coherent tunneling rather than flipping one of its spins through the exchange coupling. The effect of this behaviour on the spin relaxation rates of bound electrons and holes is under question and has not been addressed in the literature to the best of our knowledge. In terms of mesoscopic properties, [111]-oriented double dots resemble [001]-oriented QDMs and the analysis given in the previous sections qualitatively apply to these structures as well.

5.11 Summary

We investigated the feasibility of producing tripartite spin-photon pair entanglement from charged biexcitons in quantum dot molecules. In the proposed structure, two quantum dots are coupled sharing their s-shell ground states with a relatively small hybridization energy of the hole particle ($t_h < 0.5$ meV) that facilitates switching between different configurations without extensive cost of tunneling energies. We particularly analyzed the case of In(Ga)As stacked QDs embedded in [001]-oriented GaAs nanowires. However, the results can be generalized to other types of QDMs sustaining strongly correlated orbitals. We showed that the weak quantization of electron opens new channels of recombination for higher order entanglement. Our calculations in the few-body framework revealed that charged biexcitons and excitons exhibit dominant spectral features as a direct consequence of existing mutual interactions. The variety of available transitions then narrows down to a few favorable initial and final states. Neglecting the small exchange splittings, $XX^- \rightarrow X^- \rightarrow e$ cascades represent relative energy matching under axial electric filed, while $XX^+ \rightarrow X^+ \rightarrow h$ channels lack any color coincidence under our range of fields. This is primarily attributed to the large electron hybridization energy. By providing an exemplary cascade of $XX^- \rightarrow X^- \rightarrow e$ transitions, we examined the double dot spin fine structure and Zeeman shifts under the magnetic field in the Voigt geometry. The strong quantization of the hole particle away from anticrossing lead to its small transverse g-factor, thus charged complexes undergo less Zeeman shift. Upon empirically approved range of magnetic field required for the spin manipulation ($\mathbf{B} < 3$T), photon energy detunings were calculated below $400\,\mu$eV. Sufficient photon concurrence is then achievable by manipulating the level broadenings through the frequency conversion technique. Our analysis is a demonstration of how properly-sorted multi-particle states could be exploited to create multi-partite entangled states in an engineerable solid state source.

Chapter 6

Quantum optics experiments on single nanowire quantum dots

6.1 Introduction

To demonstrate that NWQDs are able to generate single photons, their operation within the quantum regime has to be investigated via quantum optics experiments. Such experiments demand for a low temperature ambient to suppress the background noise and phonon scattering processes. The unique signature of single photon emission is the antibunching character of the photon stream, where, unlike the coherent state of a laser or bunched photons emitted from a filament, individual photons are rather equally spaced in time [176]. To show the antibunching phenomenon and prove the quantum nature of the photon emitter, the so called "cross-correlation" measurements need to be accomplished [177]. Witnessing the quantum correlation between two photons further complicates the measurement conditions as the indistinguishability and sequence of correlated photons also comes to the picture [148, 59].

In this chapter, we address our main challenges towards designing efficient NWQDs. Different figures of merit, such as axial quantization, emission wavelength, symmetry character of orbitals, binding energies of excitonic complexes and collection efficiency of photons, have been taken into consideration to set the structural parameters of the QD segment and nanowire. Most of the principles we apply follow our theoretical findings in Chapters 3 and 4. Through cross-correlation measurements, we show that these QDs exhibit a decent performance in terms of single photon emission at low temperatures. Perhaps the striking feature of the QDs developed here is their very small FSS compared to the self-assembled

QDs. The measured FSS of our QDs barely exceeds 15 μeV showing a substantial improvement compared to 80-120 μeV FSS of regular self-assembled QDs [6]. This result fairly agrees with our theoretical predictions in Chapter 4. In addition to the small FSS, observation of cascade recombination, evidenced by XX-X cross-correlation measurements, offers this type of QDs as potential source of polarization-entangled photons. Relying on the polarization sensitive tomography measurements [95], we observe quantum correlation between twin XX-X photons.

6.2 Nanowire QD structure

We are able to grow ternary In(As)P insertions inside InP nanowires. Based on theoretical results in Chapter 3, several considerations should be taken here: a) The strain force between the ternary insertion and nanowire core must be optimized to avoid electron surface states. This strain is dependent on the insertion intermixing. Fortunately, the shell thickness in our nanowires is thick enough to relax the strain energy introduced by the small QD segment; see below. b) The emission wavelength has to be set based on the detection efficiency of available detectors (900-950 nm). c) The symmetry character of orbitals is crucial for vanishing FSS. (111) growth orientation automatically fulfils this requirement. d) We prefer a small binding energy of ground state XX as it is beneficial for realizing XX-X energy coincidence via applying electric field. This translates to weaker axial localization. e) Spin relaxation time: the spin relaxation rate increases with dark-bright exchange splitting Δ_{bd}, and Δ_{bd} is principally an e-h exchange interaction, thus the QD axial localization plays an important role in tailoring the spin flip time. In [111]-NWQDs, Δ_{bd} increases with a_h, leading to shorter spin flip times. Considering all above factors, we design the QD insertion with the following structural parameters: 1) QD material: $InAs_{0.2}P_{0.8}$, 2) QD diameter: 20-34 nm, 3) QD height: 6-8 nm (a_h = 0.25-0.4), 4) shell thickness: 10-15 nm (excluding the cladding; see the next section).

6.2.1 Light extraction efficiency

Light extraction efficiency depends on the nanowire structure and the underlying substrate. A nanowire made of InP with refractive index $n = 12$ can support several optical modes as a cylindrical waveguide. The number of guided modes indeed depends on the nanowire diameter. The single QD emits at 900-950 nm, and a 30-35 nm core-shell nanowire barely supports an optical mode at this wavelength. An extra thick cladding layer surrounding the whole core-shell nanowire and made of the same material leads to HE, EH, TE and TM

modes forming in the nanowire-cladding structure [178]. The QD emission then couples into the guided modes rather than being scattered to air at the nanowire sidewalls. To enhance the extraction efficiency the nanowire-cladding can be tapered at the top.

The schematic of clad NWQD is shown in Figure 6.1(a). The nanowires are grown on top of a (111)B InP substrate. Thus the refractive indices of cladding and substrate are identical, leading to loss of at least half of the power. In practice, the nanowires can be transferred with flexible polydimethylsiloxane (PDMS) films onto a gold coated substrate [179]. This way, an important part of the downward QD emission, coupled to the optical modes, will be reflected at the InP/gold interface. The back-reflected electric field may then interfere constructively or destructively with the upward electric field depending on the QD position. To obtain a constructive interference, the QD has to be located at the antinodes of the electric field.

Figure 6.1(b) illustrates the dispersion curves for different sets of guided modes, including HE_{mn}, EH_{mn}, TE_{mn} and TM_{mn}, supported by an InP cylindrical waveguide. The dispersion is plotted versus the nanowire diameter at a fixed wavelength $\lambda = 910$ nm. To solve for the dispersion curves of guided modes, we employed the characteristic equations given in Ref. [180]. This plot provides us the insight to set the cladding diameter to have a single mode waveguide. The QD can be assumed as a point source located at the nanowire axis since its diameter is less than 35 nm. Hence, its emission will not couple into the TE_{01} and TM_{01} as their electric-field mode profile contains a node at the nanowire axis. However, we set the nanowire diameter to 200 nm to avoid any partial coupling into the other modes. To confirm that the QD emission is coupled only to the fundamental mode HE_{11}, we solved for the corresponding field distribution and compared it to our finite difference time domain (FDTD) simulation results[1]. To perform the FDTD simulations, a cylinder on top of a substrate is defined in a 3D box, and the entire box is discretized uniformly. An in-plane (perpendicular to the nanowire axis) point source located at the nanowire axis models the QD dipole emission. The resemblance between the field distribution of $|E|$ in FDTD model and $|H_{11}|$ mode profile from the analytical solution ensures that the QD dipole is primarily coupled to the nanowire fundamental mode, see Figure 6.1(c) and (d).

The effective refractive index of the fundamental mode HE_{11} is $n_{\mathrm{eff,HE_{11}}} \approx 1.71$ from Figure 6.1(b). The QD then can be spaced at $h_{\mathrm{DS}} = m\lambda/4n_{\mathrm{eff,HE_{11}}}$ $(m = 1, 3, 5, \ldots)$ points from the InP/gold interface. To obtain a conclusive picture, different structures are simulated in FDTD and the results are shown in Figure 6.1(g-l). Figure 6.1(g) illustrates $|E|^2$ in a 3 μm long and 200 nm thick InP nanowire, schematically depicted in Figure 6.1(e), in which the QD is located at $5\lambda/4n_{\mathrm{eff,HE_{11}}} = 655$ nm away from the InP substrate.

[1]The finite difference time domain simulations are implemented in Meep developed by the Ab-Initio research group at MIT.

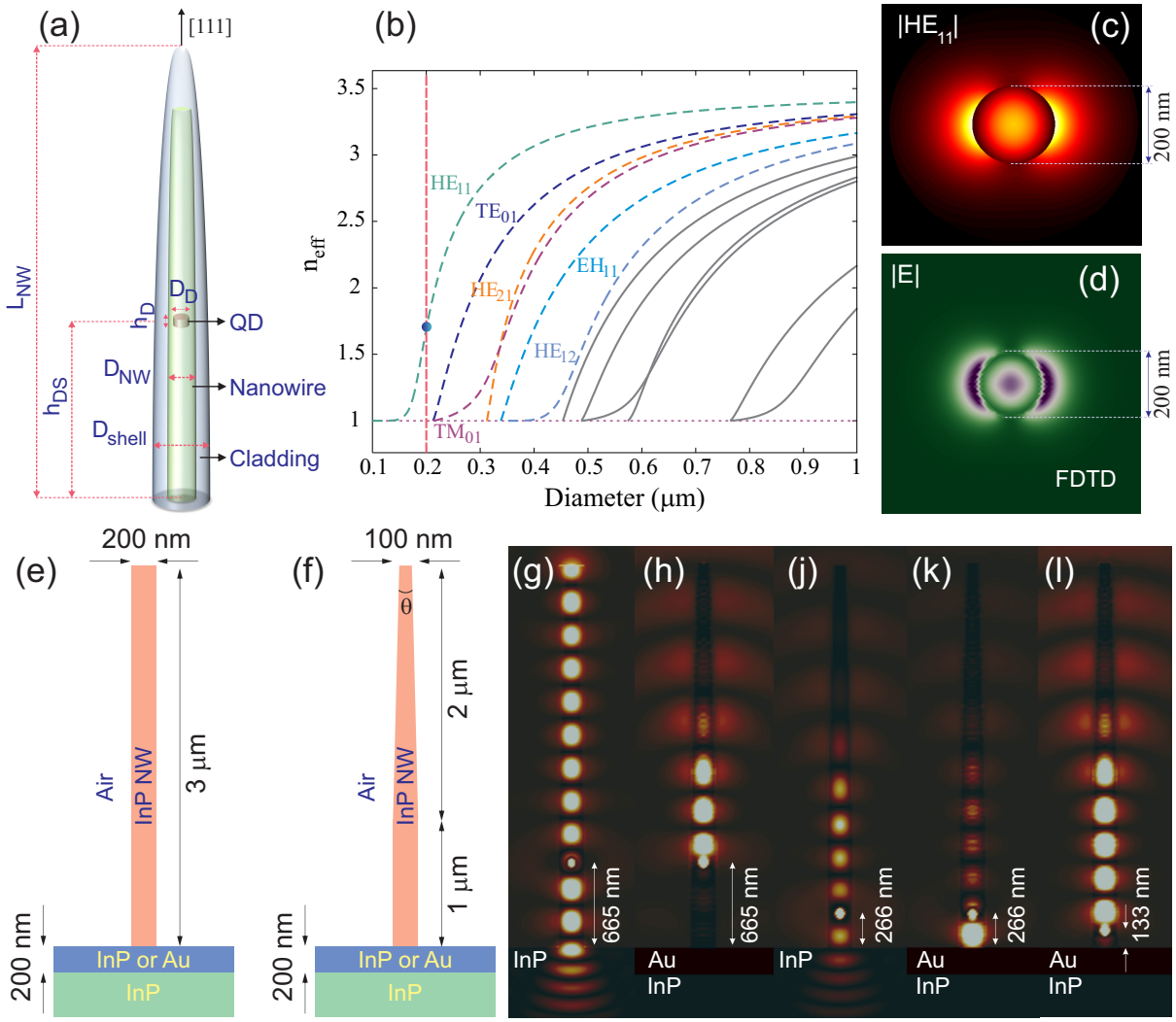

Figure 6.1: (a) Schematic of clad NWQD tapered at the top. h_{D}: QD height, D_{D}: QD diameter, D_{NW} nanowire diameter, D_{shell}, cladding diameter, h_{DS}: dot spacing from substrate, L_{NW}: nanowire length. (b) Dispersion curves of a cylindrical InP nanowire with $\varepsilon_r = 12$ at 910 nm. 200 nm-thick Nanowire supports only the fundamental HE_{11} mode at this wavelength. (c) The mode profile of HE_{11} at nanowire cross-section; $D_{\mathrm{shell}} = 200$ nm. (d) Norm of the electric field displayed at the cross section of 200 nm-thick nanowire excited with an in-plane dipole at 910 nm. (e) and (f) Schematic representation of nanowire-substrate side view. Dimensions are indicated for untapered and tapered nanowire; $\theta = 1.43°$. (g-l) The $|E|^2$ intensity solved by FDTD and plotted for a 2D-cut along the nanowire axis in different structures: (g) untapered, InP substrate; (h), (k), (l) tapered, gold-coated InP substrate with the QD located at $5\lambda/4n_{\mathrm{eff,HE}_{11}}$, $2\lambda/4n_{\mathrm{eff,HE}_{11}}$, and $\lambda/4n_{\mathrm{eff,HE}_{11}}$; (j) tapered, InP substrate.

Fundamental mode HE_{11} forms in the nanowire waveguide. A large fraction of the upward propagating field is reflected at InP/air interface, while the entire downward field enters the InP substrate and dispersed. Such nanowire-substrate configuration is very inefficient once the optical objective collects the light from the top. The same structure is modified in Figure 6.1(h) by tapering the nanowire tip and replacing the bare InP substrate with a gold-coated InP substrate. The length of tapered section is 2 μm with tapering angle $\theta = 1.43°$. The ratio of the untapered/tapered sections is set to 1/2 to obtain a proper waveguiding and gradually scatter the field into air within a smaller numerical aperture. The downward field reflected from the InP/Au interface interfere constructively with the upward field, thus a substantial portion of emitter power is delivered to the tapered region. In practice, the surrounding air region is replaced with PDMS that has ~ 1.4 refractive index and further enhances the extraction efficiency from the nanowire.

To demonstrate the effect of destructive interference, the QD dipole is relocated to a node of electric field at $2\lambda/4n_{\text{eff,HE}_{11}} = 266$ nm. In Figure 6.1(j), the tapered nanowire is grown on bare InP substrate, therefore, the location of QD dipole has no impact on the field power delivered to the tapered region. However, once the InP substrate is coated with a 200 nm gold layer, Figure 6.1(k), the destructive interference prohibits the main part of the field power to reach the nanowire tip. In our fabricated samples, the QD is located ~ 150 nm away from the bottom of nanowire close to a field antinode, $\lambda/4n_{\text{eff,HE}_{11}} = 133$ nm, Figure 6.1(l). However, the nanowires have not been transferred to a gold-coated substrate, hence the field distribution resembles Figure 6.1(j).

6.2.2 Fabrication steps

Nanowires are grown on a (111)B S-doped InP substrate coated with a 20 nm SiO_2 layer. In order to define the gold catalyst size, this layer is electron-beam patterned with arrays of holes. The diameter of these holes (30 to 90 nm) determine the size of gold catalyst. The actual diameter of the cladding is defined after isotropic wet etching the substrate with HF solution. Gold is then deposited within the center of SiO_2 hole through the metal lift off process. Above mechanism provides the ability to selectively position the nanowires with definite spacing [66].

The growth process of clad nanowires include two primary steps: a) Phase I: The nanowire core region is grown employing the chemical beam epitaxy (CBE) with trimethyl-indium (TMI) in the vapor-liquid-solid (VLS) mode at 420° C. Stabilizing the temperature at 420° ensures the InP vertical growth merely at the interface of InP and gold catalyst and prevents any radial growth [66]. The QD diameter is determined in this step depending on the gold catalyst size. Also, the QD height is decided by the time interval that AsH_3

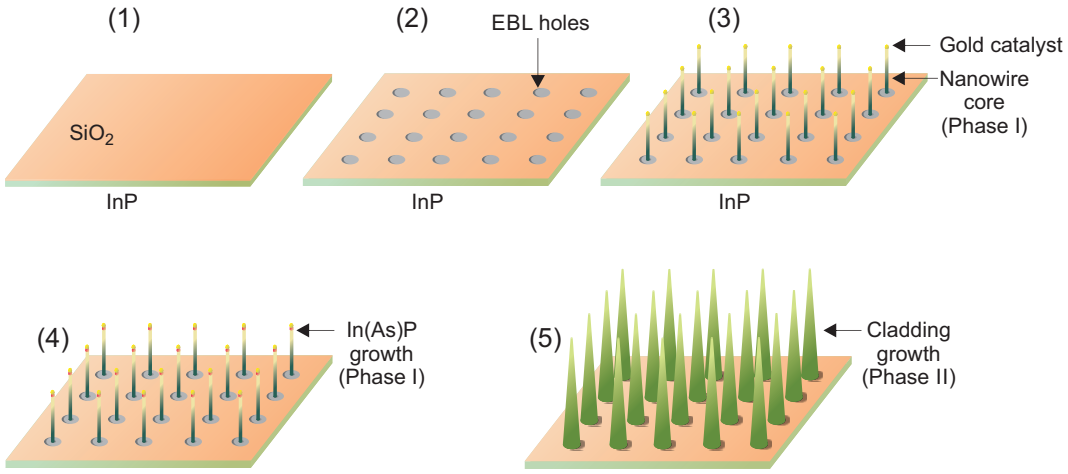

Figure 6.2: NWQD growth process: (1) SiO_2 spin coating the InP substrate. (2) Opening holes in the SiO_2 layer by wet etching. Gold catalyst will be deposited by a lift off process subsequently. (3) Nanowire core region growth at 420° C. (4) Incorporating the QD insertion by switching from PH_3 to AsH_3. (5) InP clad radial growth at 515° C.

replaces PH_3 (almost 2-3 seconds) in the growth chamber. The QD/InP-substrate spacing for the samples we study in the following is set to $\sim$ 150 nm for future post-growth manipulations, see Sec. 6.2.1. b) Phase II: Radial growth of the cladding is accomplished at higher temperatures, nominally 515° C, where axial growth is significantly suppressed at the nanowire tip and noncatalyzed radial growth dominates [66]. The axial growth becomes almost 4 times slower compared to Phase I (catalyzed growth), thus the final height of clad nanowires reaches almost twice the core height.

Figure 6.3 depicts the scanning electron microscopy (SEM) and transmission electron microscopy (TEM) images of typical nanowires we use for quantum optics measurements [2]. Clad wires can be untapered (a-b) or tapered (c-d) with different lengths. The variety in length and cladding thickness aids us obtain some statistics on the extraction efficiency of nanowires. Since the nanowire length is short compared to the QD resonance wavelength, then longer wires provide decent guided modes, leading to brighter emission. In a short nanowire, the optical mode happens to be scattered at nanowire ends prior to its formation. In contrast, a thicker nanowire, supporting more guided modes, does not necessarily secure a higher efficiency. In fact, the QD dipole partially couples into each guided mode depending on its mode profile and dispersion. We experimentally observed

[2]Nanowires are grown by Dan Dalacu in Philip Poole's group at National Research Council, Ottawa, Canada. SEM and TEM images presented in this chapter are taken in the same group.

brighter emission (improved collection efficiency) for cladding thickness D_{shell} = 150-200 nm. To facilitate the optical access, single vertically standing wires are positioned at the center of squares made of similar wires. Isolating individual NWQDs is crucial to capture photons merely from a single emitter.

6.3 Setup

The QD samples are investigated using a confocal microscopy setup equipped with Janis Research ST-500 continuous flow cryostat, HeNe cw laser and Ti:Sapphire ps pulsed laser (Spectra Physics Tsunami). The objective used for excitation and collection from the top is a Mitutoyo Plan Apo Infinity-Corrected long working distance (WD = 6 mm) with NA equivalent to 0.68 and 100x magnification. The spectrometer is composed of an Acton SP-2750i 750 mm monochromator and a set of different resolution gratings (including 600, 1200 and 1500 grooves/mm). To filter out specific excitonic resonances, a home-made spectrometer made of slitless monochromator with 1200 grooves/mm grating is employed. The spectroscopy camera is Princeton Instruments VersArray (Liquid-N_2-cooled) with efficiency of $\sim$ 36% at 910 nm and $\sim$ 17% at 970 nm. The spectral resolution of the setup is roughly 0.02 nm. To perform time-correlation measurements, Perkin Elmer avalanche photodiodes (APD, Single Photon Counting Module Array) are used. The resolution time for these APDs reaches down to 128 ps. Regarding that the intrinsic lifetimes of X and XX are longer than 0.9 ns in our samples (see Sec. 6.4.3), above APDs could resolve the cross-correlation counts appropriately. We switch to fast single-photon detection modules from Micro Photon Devices with 8 ps time resolution. The electronics include HydraHarp 400 Time-Correlated Single Photon Counting (TCSPC) module from PicoQuant for recording detection events[3].

A simplified schematic of the setup including the essential components is given in Figure 6.4. Setup benefits from two types of excitation: 1) Continuous wave (cw) HeNe laser at 632.8 nm as a non-resonant pump, which excites electron-hole pairs above the wurtzite InP band gap ($\simeq$ 1.493 eV) [181, 142]. 2) Non-resonant and upper shell excitation at 808 nm and 870 nm, respectively, via Ti:Sapphire pulsed laser with 80 MHz repetition rate. The spontaneous emission of QD is collected via an objective and dispersed in the 750 mm monochromator, then captured by the VersArray detector at the exit slit of spectrometer. In the particular configuration shown here, vertically standing wires are

[3]The quantum optics experiments were performed using the quantum dot setup developed in G. Weihs' group at the Institute for Experimental Physics, Innsbruck, Austria. The experimental data are produced by the author of this thesis in company with Tobias Huber and Ana Predojevic from G. Weihs' group.

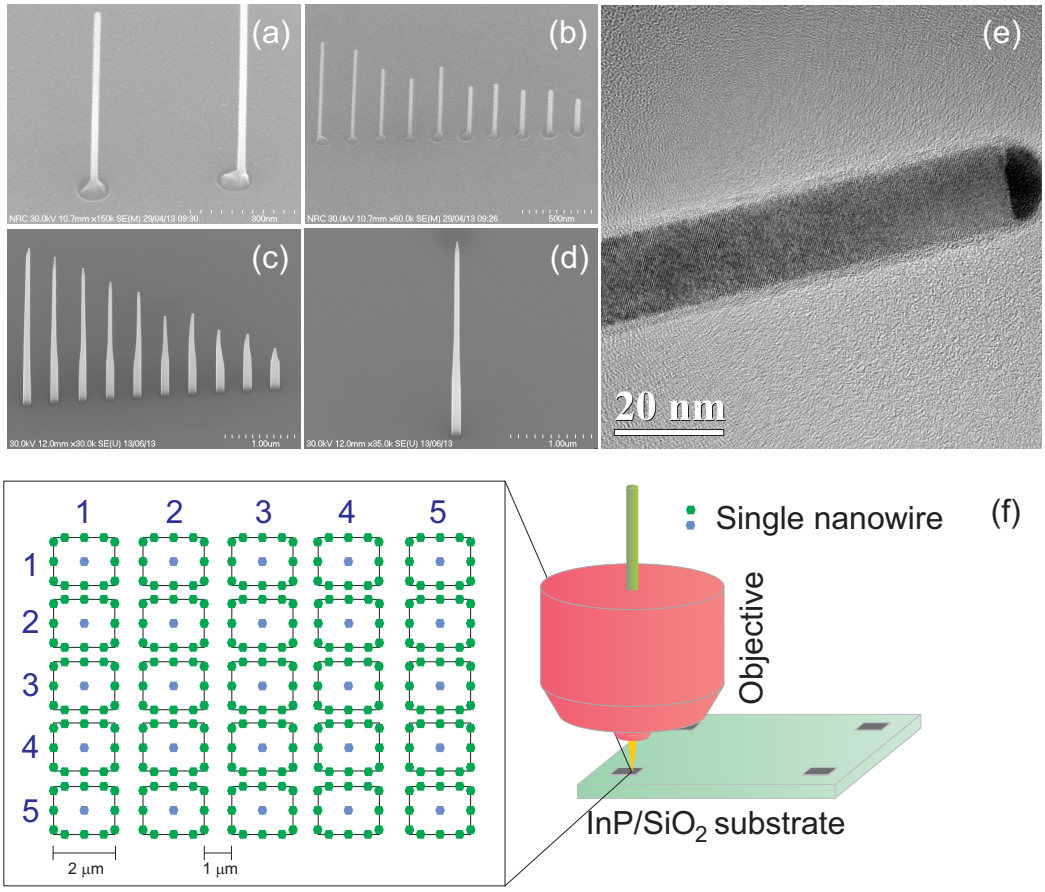

Figure 6.3: (a-b) SEM image of clad untapered nanowires embedding single QDs. Wires are selectively-positioned. (c-d) Clad tapered nanowires. Wires are closely spaced in (c), while we normally isolate a single wire for convenient optical access, as shown in (d). (e) TEM image of unclad InP nanowire in wurtzite phase. (f) In the investigated samples, single wires are positioned at the center of squares made of identical wires. The diameter of wires change from 20 nm to 34 nm in 2 nm steps.

excited from the top, and their emission is collected from the same objective. We have the additional option to excite via a different objective from the side to enhance the accuracy of collection alignment. The spot size of the objective (commonly $\sim 1\mu$m) is dynamically changed to optimize the collection efficiency according to the excitation power and QD brightness. Excitation power is being continuously monitored at the objective entrance by a power meter, not to exceed 500 μW and cause the spectral diffusion.

In order to perform time-correlation measurements on an individual sharp line, e.g. X, it is spectrally selected through a double monochromator and delivered to the single photon counting module (APDs) after a 50/50 beam splitter. Cross-correlation counts between two different lines are recorded by directing each line to a certain SPCM. We also implemented a polarization control module made of a polarizer, half wave plate (HWP) and quarter wave plate (QWP), which enables us study the cross-correlation counts in different polarization states. During the cross-correlation and time-resolved measurements, SPCMs and Ti:Sapphire laser are synchronized via a correlation card (not shown in Figure 6.4) to keep track of the photon detection times.

6.4 Micro-photoluminescence spectrum and time-correlation measurements

6.4.1 Photoluminescence spectrum at low power excitation

In order to resolve the QD luminescence, the standing nanowires are illuminated along their axis, see Figure 6.3(f), so that the propagation vector of the excitation (emission) beam and nanowire axis are parallel. We intentionally avoided transferring the nanowires from their as-grown substrate to the lying configuration. The reason lies in the nanowire selectivity on the polarization of electric field as described in Sec. 3.3. The PL of lying nanowires excited from the top is shown to be highly linear-polarized due to the significant difference between the nanowire and air refractive indices [182, 183]. This prohibits optical access to the intrinsic polarization characters of excitons in the NWQD. For example, access to all basis sets of polarization is necessary in measuring the total angular momentum of the exciton for entanglement experiments. Similarly, spin state manipulation of electron (hole) demands for circularly polarized light. Circular polarization in nanowires requires careful alignment along the axis since nanowire has a cylindrical symmetry.

First mission is to look for the QDs showing low background emission, negligible line mixing (e.g. spectral overlap between X and XX lines) and adequate counts from the sharp

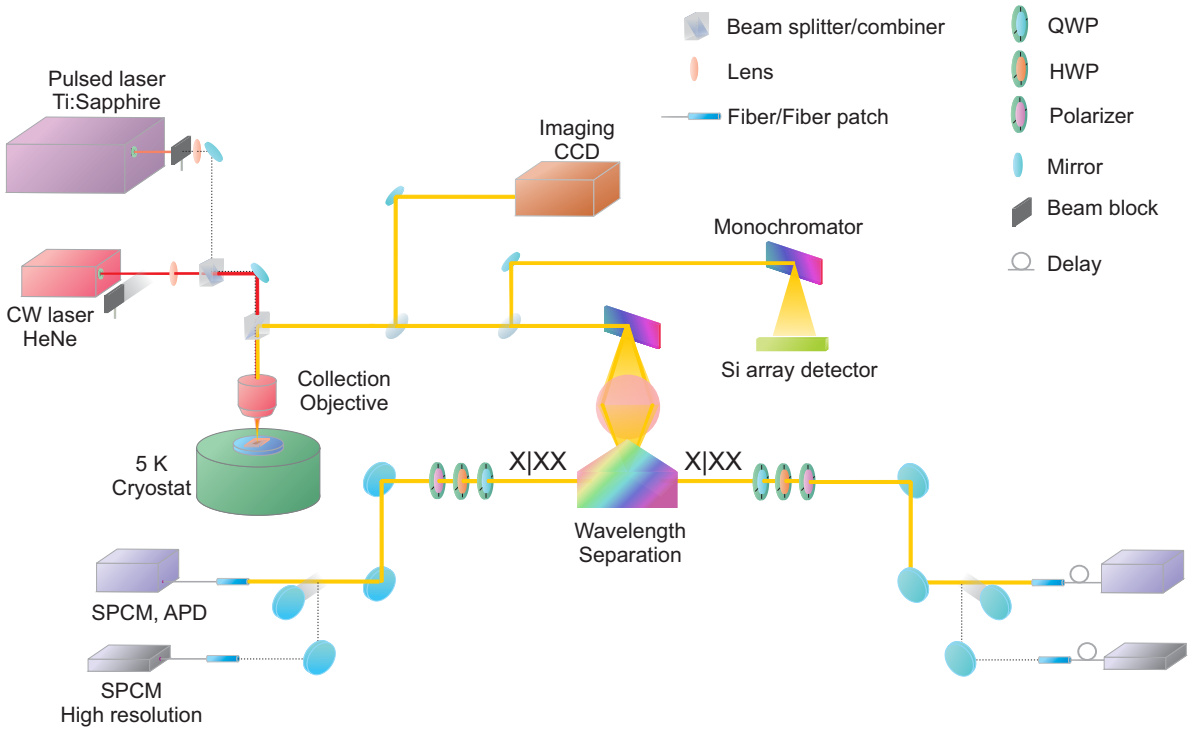

Figure 6.4: Simplified schematic of micro-PL and time correlation setup. HeNe laser is utilized for nanowire above band-gap excitation, resolving the PL spectrum and single line time-correlation $g^{(2)}$ measurement. Pulsed laser is used in lifetime measurements and cross-correlation experiments. Spectral filtering the excitonic lines is doable via a double monochromator since the binding energies are small.

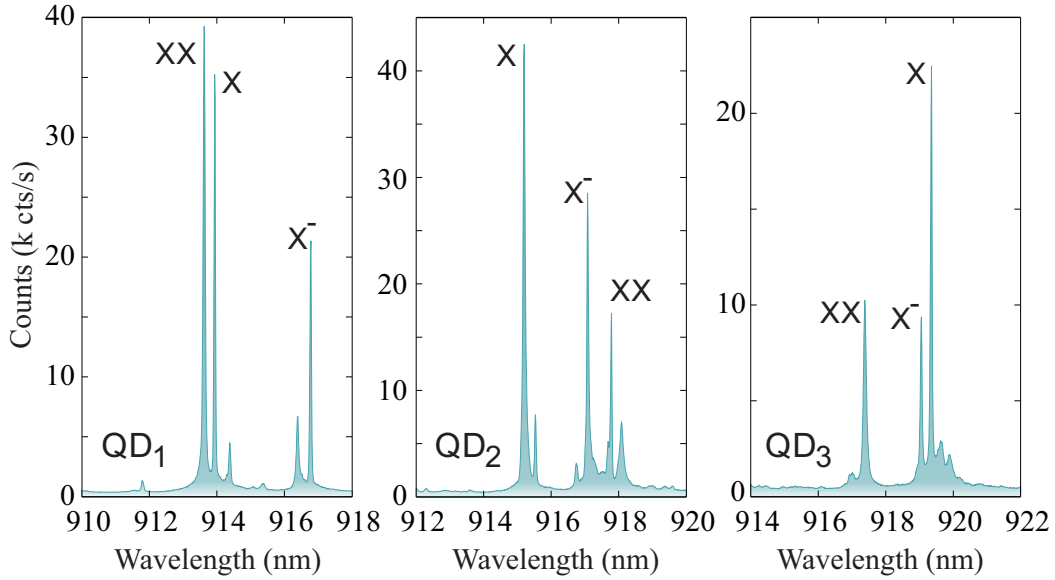

Figure 6.5: Photoluminescence spectra of three different NWQDs. The binding energy of XX is below 4.5 meV, in agreement with the theoretical predictions. Most of the dots show antibinding XX (QD_1 nad QD_3), however a few QDs have binding biexciton (QD_2). The excitation power applied to resolve above spectra is measured < 200 nW at the objective input.

lines, namely X, XX, X^- and X^+. The broad spectral features normally do not provide desirable autocorrelation $g^{(2)}(0)$ and emitted photons are not antibunched. Figure 6.5 illustrates the typical photoluminescnece intensity of NWQDs. The character of X and XX lines are determined based on cross-correlation measurements that will be explained in the following. The vertical aspect ratio is kept in the $a_h = 0.3$-0.4 range to minimize the XX binding energy as much as possible. Most of the QDs exhibit antibinding XX, i.e. $E(XX_0) > E(X_0)$. The character of charged trions can be revealed under a magnetic field. We symbolically assign X^- to these sharp lines as they show no sign of cascade cross-correlation with either of X and XX lines, however they could be other types of charged complexes, for example X^+. Determination of the actual character of charged complexes is beyond the scope of this work.

6.4.2 Time-correlation measurements

In order to characterize the spectral features, we performed autocorrelation measurements using Perkin Elmer APDs and a HydraHarp 400 TCSPC module. Qualitatively, XX resonance is simple to identify as its intensity presents a nonlinear increase versus the excitation

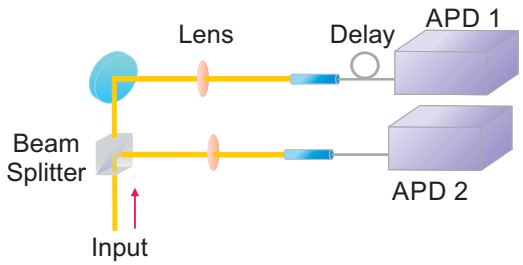

Figure 6.6: HBT setup: photon stream from the QD is sent to a 50:50 beam splitter. Photons in the upper channel undergo a time delay before arriving at APD.

power. Although we normally observe a sub-quadratic power dependency XX certainly grows faster than X and $X^{\pm}$ which show a linear or sub-linear trend. True characterization of spectral features, however, requires investigating the quantum correlation of their corresponding photons. Before describing on how to observe such a correlation in practice, let us elaborate on the concept of time correlation or conditional probability of two individual photons.

In quantum optics, the time dependence of a semi-classical electromagnetic field is described by quantum operators and the time-correlation function is defined as

$$g^{(2)}(\tau) = \frac{\langle \hat{a}^{\dagger}(t)\hat{a}^{\dagger}(t+\tau)\hat{a}(t+\tau)\hat{a}(t)\rangle}{\langle \hat{a}^{\dagger}(t)\hat{a}(t)\rangle^{2}} \tag{6.1}$$

based on photon creation $a^{\dagger}(t)$ and annihilation $a(t)$ operators. If the two photons emitted at t and $t+\tau$ are uncorrelated, meaning that the probability of their coincidence in time corresponds to the product of probabilities of photon emission at each time, then $g^{(2)}(\tau) = 1$. However, if the probability of detecting photon $t+\tau$ is conditional on the detection event of photon t, then $g^{(2)}(\tau) < 1$ and the two photons are correlated in time. The correlation function at $\tau = 0$, $g^{(2)}(0)$, represents the normalized conditional probability of two photons emitted simultaneously. To better understand the concept of $g^{(2)}(0)$ for a particular number state, $|n\rangle$, we represent it based on the number operator ($\hat{n}\,|n\rangle = n\,|n\rangle$) [92]:

$$g^{(2)}(0) = \frac{\langle \hat{n}(\hat{n}-1)\rangle}{\langle \hat{n}\rangle^{2}} \tag{6.2}$$

For a two-photons state $|n\rangle = |2\rangle$, $g^{(2)}(0) = 1/2$. Thus the mandatory figure of merit of a single photon emitter is $g^{(2)}(0) < 1/2$. In the case of pure single photon emission with no coincidence over time we have $g^{(2)}(0) = 0$.

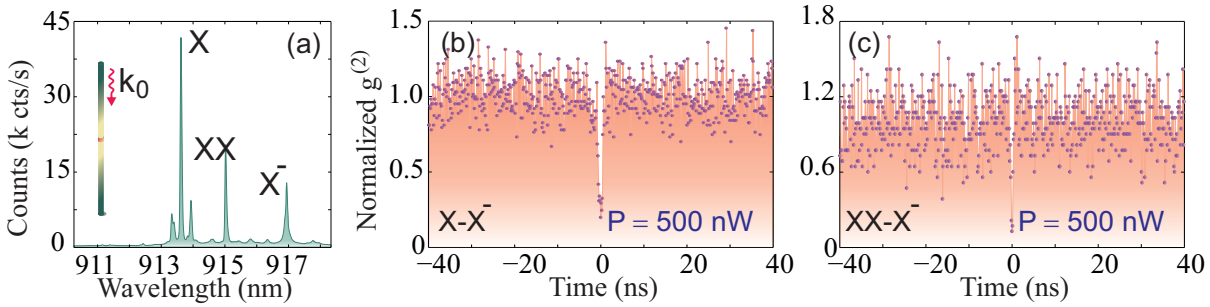

Figure 6.7: (a) PL spectrum of 6 nm-high and 28 nm in diameter NWQD measured at excitation power $P = 500$ nW and $T = 5°$K. Nanowire is excited along its axis. (b-c) Normalized $g^{(2)}_{X,X^-}(\tau)$ and $g^{(2)}_{XX,X^-}(\tau)$ counts measured at excitation power $P = 500$ nW, confirming that the third sharp line at ~ 917 nm in (a) is a charge exciton.

To confirm the character of different features we do the following steps:

1. Resolving autocorrelation counts $g^{(2)}(\tau)$ for each individual sharp feature in the spectral window to verify its anti-bunched stream of photons. For this purpose, all other features are filtered out and the photons from the sharp line are directed to a 50:50 beam splitter of a Hanbury Brown and Twiss (HBT) setup, see Figure 6.6 [184]. The outputs of the beam splitter are connected to the start and stop APDs to record the photon counts against the difference of their arrival time τ. In practice, background light, very small contribution from nearest-neighbor spectral lines and two photon coincides prohibit reaching the absolute zero.

2. Resolving cross-correlation counts $g^{(2)}_{\alpha_1,\alpha_2}(\tau)$ between two different sharp lines originating from different excitonic complexes α_1 and α_2. Here, photons from each line are sent to different APDs. If two complexes are X and XX, an antisymmetric $g^{(2)}_{\alpha_1,\alpha_2}(\tau)$ with a noticeable rise in counts appears. This rise is a signature of the second photon emission ($X \longrightarrow G$) immediately (in the order of the exciton lifetime) after initial recombination ($XX \longrightarrow X$). An asymmetric $g^{(2)}$ pattern without any rise in counts implies that the two complexes do not contribute in a cascade and one of them is probably charged exciton.

Single photon emission

Figure 6.7(b) and (c) depict $\{X^-, X\}$ and $\{X^-, XX\}$ cross-correlation counts (item 2) for the QD whose spectrum is shown in Figure 6.7(a). Emergence of no rise in the cross-

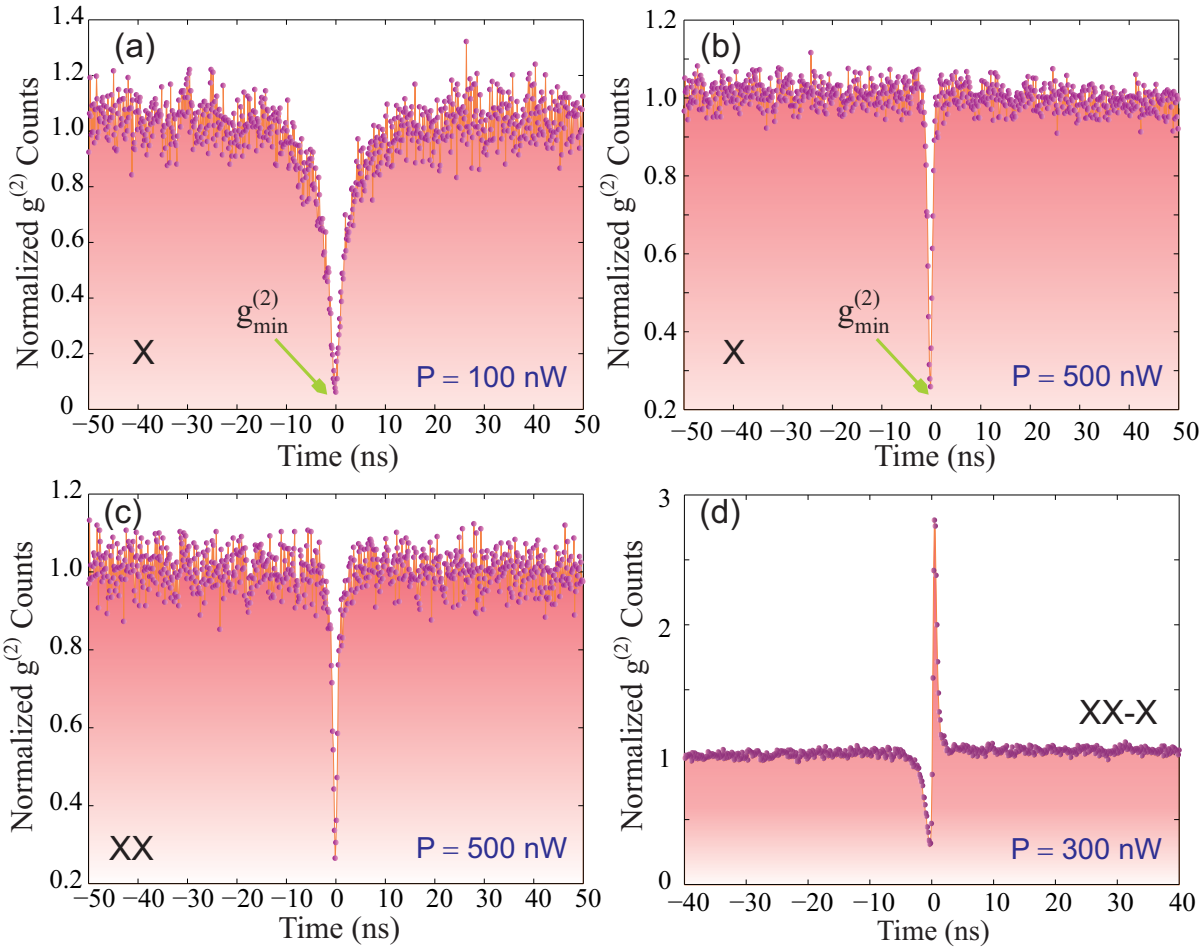

Figure 6.8: (a-b) Normalized autocorrelation counts from the X line at power pumping P = 100 nW (low) and 500 nW. Under CW excitation, the exponential constant of $g^2(\tau)$ function is power-dependent. (c) Normalized autocorrelation counts of XX line at P = 500 nW showing antibunching character of $XX \rightarrow X$ photons. (d) Normalized cross-correlation counts between XX and X lines at P = 300 nW showing a clear signature of cascade recombination. The time resolution is set to 128 ps for all experiments.

correlation histogram implies no cascade emission between X^- and the other two lines. Thus we conclude this spectral feature corresponds to a charged trion. $g^{(2)}_{X,X^-}(0) < 0.25$ indicates that formation of charged biexciton at P = 500 nW is still unlikely to happen. The quality of the NWQDs as a single photon emitter is inspected by the time-correlation function of its X line. In most of the dots we observed a strong X emission and a $g^{(2)}_X(0) <$ 0.15. The correlation function of the QD in Figure 6.7(a) is plotted in Figure 6.8(a) at

$P = 100$ nW, exhibiting $g_X^{(2)}(0) < 0.15$. The value of $g_{\min}^{(2)}$ does not reach zero in the presence of stray background light. To consider the stray background light, we fit the data to $g_X^{(2)}(\tau, \tau_X) = 1 + r^2(g_n^{(2)}(\tau, \tau_X) - 2)$, where $g_n^{(2)}(\tau, \tau_X) = 1 - ae^{-\tau/\tau_X}$ and $1/r$ is the signal to noise ratio. Having $a = 2.42 \times 10^4$, $r = 0.00626$ and $\tau_X = 2.3$ ns the curve perfectly fits the exponential decay in proximity to $\tau = 0$. Then, $g_X^{(2)}(0, \tau_X) \approx 0.06$ which is a clear signature of antibunched photons and proves that the NWQD is a single photon source. The rate of exponential decay τ_X corresponds to the X "effective" lifetime. The measure of X intrinsic lifetime can be derived only by time-resolved PL measurements or alternatively by $g_X^{(2)}$ at very low excitation powers where the chance of re-excitations is trivial. As could be understood from Figure 6.8(b) effective lifetime is dependent on the excitation power. At higher pumping levels, the number of photo-generated electron-hole pairs in the barrier increases quickly. Consequently, they decay down to the QD higher shells and ground state with higher rates, enhancing the chance of spontaneous recombination in the QD s-shell. Moreover, $g_{\min}^{(2)}$ is increased up to ≈ 0.25 which indicates the spectral diffusion from the two adjacent lines seen in Figure 6.7(a). In order to confirm the single photon emission from the XX line, i.e. $XX \rightarrow X$ transition, we perform the autocorrelation measurement on XX at ≈ 915 nm. Figure 6.8(c) depicts the normalized $g_{XX}^{(2)}$ counts at $P = 500$ nW. The exponential decay was fitted with $g_{XX}^{(2)}(\tau, \tau_{XX}) = 1 + r^2(g_n^{(2)}(\tau, \tau_{XX}) - 2)$, having $a = 1.198 \times 10^4$, $r = 0.007942$ and effective biexciton lifetime $\tau_{XX} = 0.59$ ns. To observe a clean $g^{(2)}$ histogram with deeper dip at $\tau = 0$, one alternative is to pump at p-shell with a contentious wave Ti:Sapphire laser to suppress the background light.

XX-X cascade

The above experiments clearly verify the performance of the NWQDs in the single photon regime. The primary condition to be assessed for the entangled photon pair generation is the presence of cascade between XX and X lines. Figure 6.8(d) illustrates the normalized cross-correlation counts (item 2) of XX and X lines under cw excitation. The probability is reduced at the negative times, indicating that immediately after a $X \rightarrow G$ transition, the $XX \rightarrow X \rightarrow G$ sequence is terminated and it takes some time for the QD to capture electron/hole in its ground state; hence, the two photon emission is essentially prohibited at $t < 0$. The rise observed at the positive times signifies the immediate (perhaps in the order of X lifetime) emission of second photon from the intermediate X state. By fitting exponential curves to the $g^{(2)}$ counts in 6.8(d), we obtain $\tau_X = 1.03$ ns and $\tau_{XX} = 0.51$ ns at $P = 300$ nW. As we already have shown that both exciton and biexciton exhibit antibunching behavior at $P = 500$ nW, it is confirmed that they both generate antibunched photons at $P = 300$ nW, as well. The cross-correlation counts do not reach zero at $\tau = 0$ because of the background light.

Single photon emission from X and XX lines was also examined under the non-resonant pulse excitation at 808 nm, with 180 nW excitation power, 2 ps long pulses and 80 MHz repetition rate. We did not observe a reasonably bright emission of X under p-shell quasi-resonant excitation at $\sim$ 870-890 nm, therefore, we switched back to the non-resonant pumping. Figure 6.9(a) and (b) show the unnormalized autocorrelation counts of X and XX resonances, respectively. The clear drop of coincidences at time delay $\tau = 0$ reflects the single photon emission from each line. The coincidence peaks are equally separated by $\sim$ 12.5 ns according to the laser repetition rate. The XX-X cross-correlation counts are shown in Figure 6.9(c). The principal peak at $\tau = 0$ is the signature of cascade emission as previously verified under the cw pumping. This reflects that XX-X cascade decay takes place under both cw and pulsed non-resonant excitation in NWQDs.

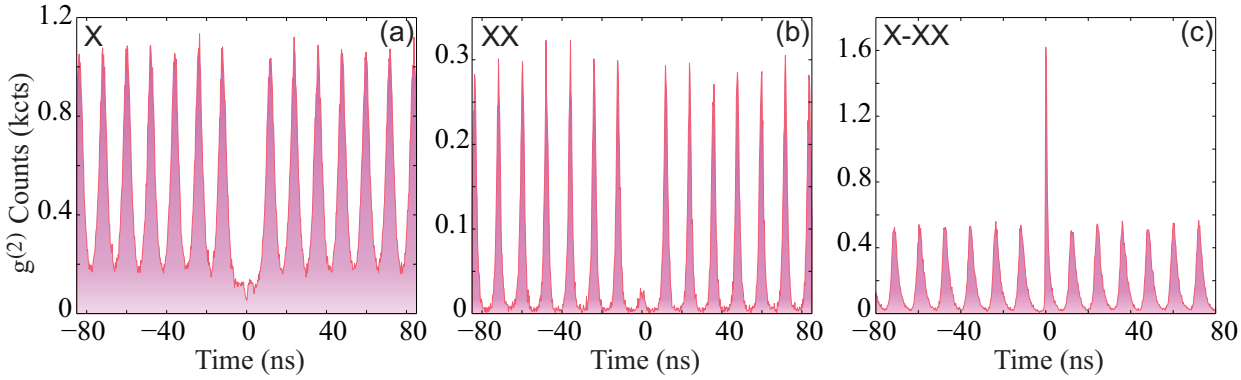

Figure 6.9: (a), (b) autocorrelation counts of X and XX lines under non-resonant pulsed excitation at 808 nm. Multiphoton coincidence counts vanish at zero time delay. (c) XX-X cross-correlation counts with the same pumping parameters as (a). The rise of coincidence counts in proximity to $\tau = 0$ demonstrates the cascade recombination.

6.4.3 Time-resolved PL measurement

The time-resolved PL experiment was performed to better understand the dynamic of s-shell exciton and biexciton and measure the their intrinsic lifetimes. We used the same setup as in Sec. 6.4.2 with Ti:Sapphire pulsed laser, 2 ps pulse duration and 80 MHz repetition rate (repetition period 12.5 ns). Considering the fact that X lifetime typically does not exceed a few nanoseconds, this repetition rate is adequately long to ascertain that the exciton has decayed within each excitation period. The fast single-photon detection module (with 8 ps time resolution) was synchronized with the laser emission and correlation

card in order to record the time delay between the laser excitation pulse and photodetection events on single-photon detection module. The statistical histogram of recorded counts versus delay time is shown in Figure 6.10. We observe a clean exponential decay at relatively low excitation powers (P = 180 nW) under non-resonant pulsed pumping. X counts are fitted to a monoexponential decay with time constant τ_X = 2.25 ns. The long radiative lifetime of X implies the high quality of nanowires and absence of the fast non-radiative processes. XX counts can be fitted to a monoexponential by discarding the tail of recorded data $\tau > 5$ ns, and the time constant is estimated to be τ_{XX} = 0.95 ns. The $\sim$ 2:1 ratio between τ_X and τ_{XX} is in agreement with previously reported data on InAs QDs [185]. This ratio decreases upon larger excitation powers. The slow varying component appearing at the tail of XX counts might be originated from refilling of the biexciton state by thermal excitation or spin relaxation, although the latter is unlikely in this time scale.

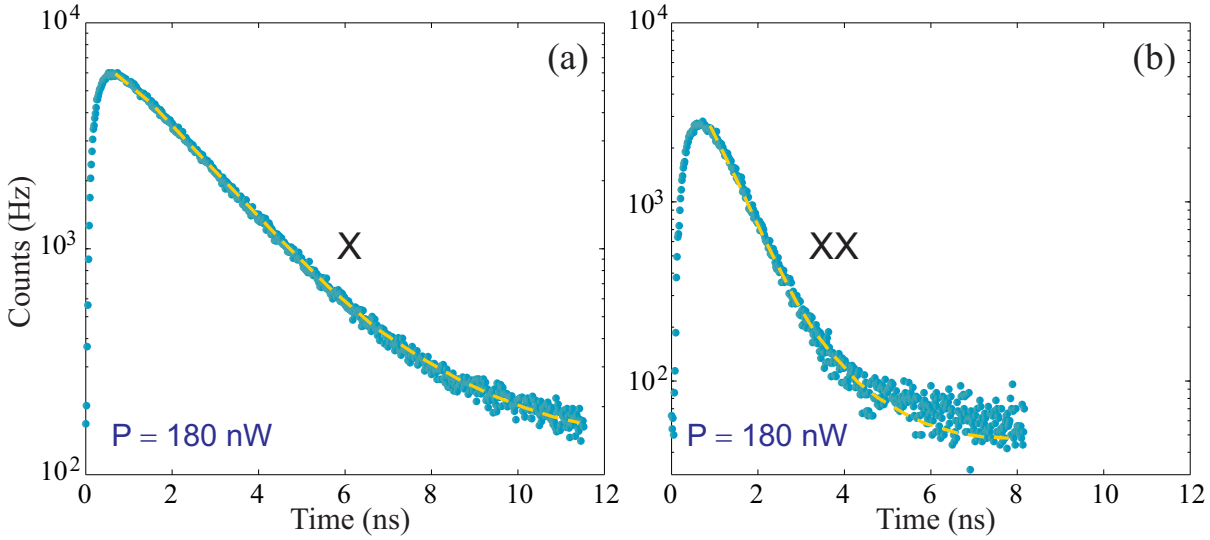

Figure 6.10: (a-b) Time-resolved lifetime measurement of X and XX lines under pulsed excitation: 2 ps pulse duration, 80 MHz repetition rate, excitation power P = 180 nW. Dashed lines show the exponential fits: τ_X = 2.25 ns and τ_{XX} = 0.95 ns.

6.4.4 Fine structure splitting

After identifying the QDs showing cascade recombination, their exciton FSS shall be measured. Referring back to Chapter 3, we expect to observe very trivial FSS values because of

the C_{3v} symmetry of electron and hole wavefunctions. We perform a polarization-sensitive spectroscopy measurement to resolve the FSS as it is essentially the energy difference between the H- and V-polarized photons. To this end, we use a Glan-Thompson polarizer followed by a HWP after the collecting objective. The HWP is initially set to 0° so that the polarization of the beam sent to the CCD is H. By rotating the HWP in small increments (10°) we gradually switch from H-polarized photons to V ones. The X and XX lines shift according to this change of polarization, however the shift is not detectable on CCD and can be resolved only by curve fitting. To track the exact position of X and XX spectral peaks, we fit these lines to Lorentzian lineshapes. The positions of peaks varies sinusoidally versus the HWP angle, as shown in Figure 6.11. The green points in this figure indicate where the spectral peaks after fitting are located. The peak-to-peak amplitude of the sine curve determines the FSS in the QD.

Figure 6.11(a-d) show the FSS of four selected QDs with very similar axial localization but different diameters: (a) 22 nm and (b) 24 nm. For each diameter, we tested at least 5 dots and measured similar fine structure splittings. Several conclusions could be made based on our statistics on the FSS data:

1. NWQDs with some certain dimensions exhibit a substantial reduction compared to the regular self-assembled QDs (in the order of 100 μeV) [6]. Notice that we are able to deterministically suppress the FSS in contrast to the self-assembled QDs where small fine structure splittings are randomly reported in an ensemble of QDs with large FSS.

2. The NWQDs do not show exactly zero FSS, in contrast to the predictions we made based on numerical simulations. We believe that nonzero FSS returns back to inhomogeneity of As intermixing inside the QD insertion.

3. We clearly recognize a diameter-dependence of the FSS: anisotropic exchange interaction, as the origin of FSS, has a Coulombic nature and drops once the orbitals dilute.

4. By increasing the diameter and decreasing the carrier localization, we lose oscillator strength. This was confirmed by the PL measurements as we consistently recorded less counts on both CCD and APDs for QD with $D_D > 30$ nm. Thus, there exists a lower bound for FSS upon the QD size.

Considering the fact that the FWHM of most resonances is between 30 and 50 μeV, observing a trace of entanglement should be likely with above FSS values. Such significant decrease in the FSS paves the way towards realizing QD-based entangled photon sources without any need to post-processing.

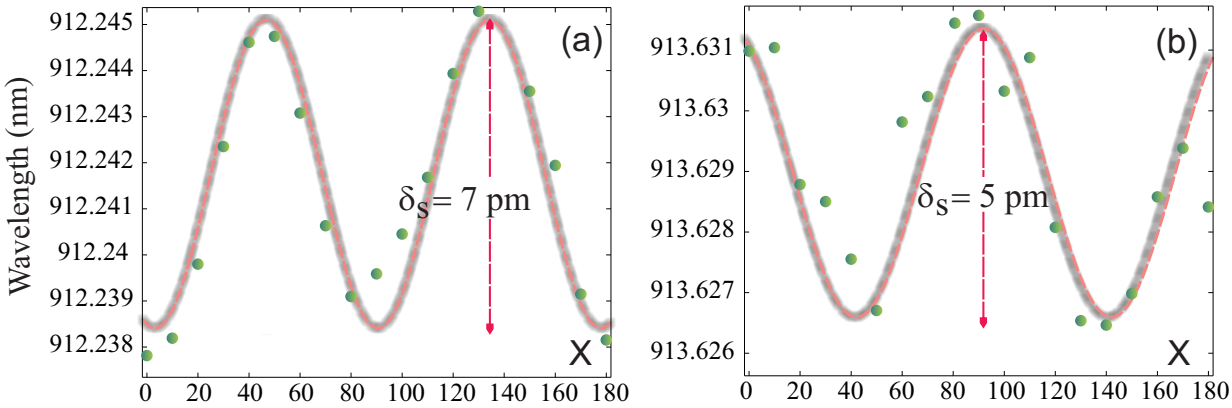

Figure 6.11: Sinusoidal fits to the peak values of X emission versus the polarization angle. The peak-to-peak value determines the FSS. (a) $\delta_s = 10.28$ μeV, $D_D = 22$ nm, b) $\delta_s = 7.4$ μeV, $D_D = 24$ nm. Although the FSS is decreased by increasing the diameter, the number of counts we measured for the QDs with diameters larger than 30 nm were not adequate to perform the high-resolution correlation measurements. This is attributed to the weak localization of electron and hole and weak oscillator strength.

6.5 Observation of Entanglement

Entanglement is a time-dependent process. Even in the presence of FSS, there is a chance of observing entanglement in the early times after the biphoton emission; for a succinct explanation of this time-dependency see the discussion given in Sec. 4.7. In order to investigate the existence of entanglement in NWQDs, we performed a full tomography measurement on the polarization states of photon pairs. This way, the density matrix ρ_{bi} of photon pair could be reconstructed based on the cross-correlation counts recorded in the tomography experiment. The density matrix of a photon pair with two polarization states (qubit) associated with each individual photon is a 4×4 complex matrix in different polarization basis sets. To perform a full tomography measurement, cross-correlation counts of XX and X photons must be resolved in different bases, namely rectilinear, diagonal and circular. It is mathematically proven that the density matrix ρ_{bi} in each basis set can be reconstructed by 16 projective cross-correlation measurements $\{XX, X\} \in \{HH, HV, VV, VH, RH, RV, DV, DH, DR, DD, RD, HD, VD, VR, HR, RR\}$ [186], where the biphoton projected states are indicated by the first letter for XX photons and the second letter for X photons. The reconstruction procedure is fully described in Ref. [186]. To project the QD emission into different bases, the polarization module shown in Figure 6.4 is utilized. Since the natural basis emitted by the NWQS is circular, we first rotated its emission to the rectilinear basis and then selected the desirable projections.

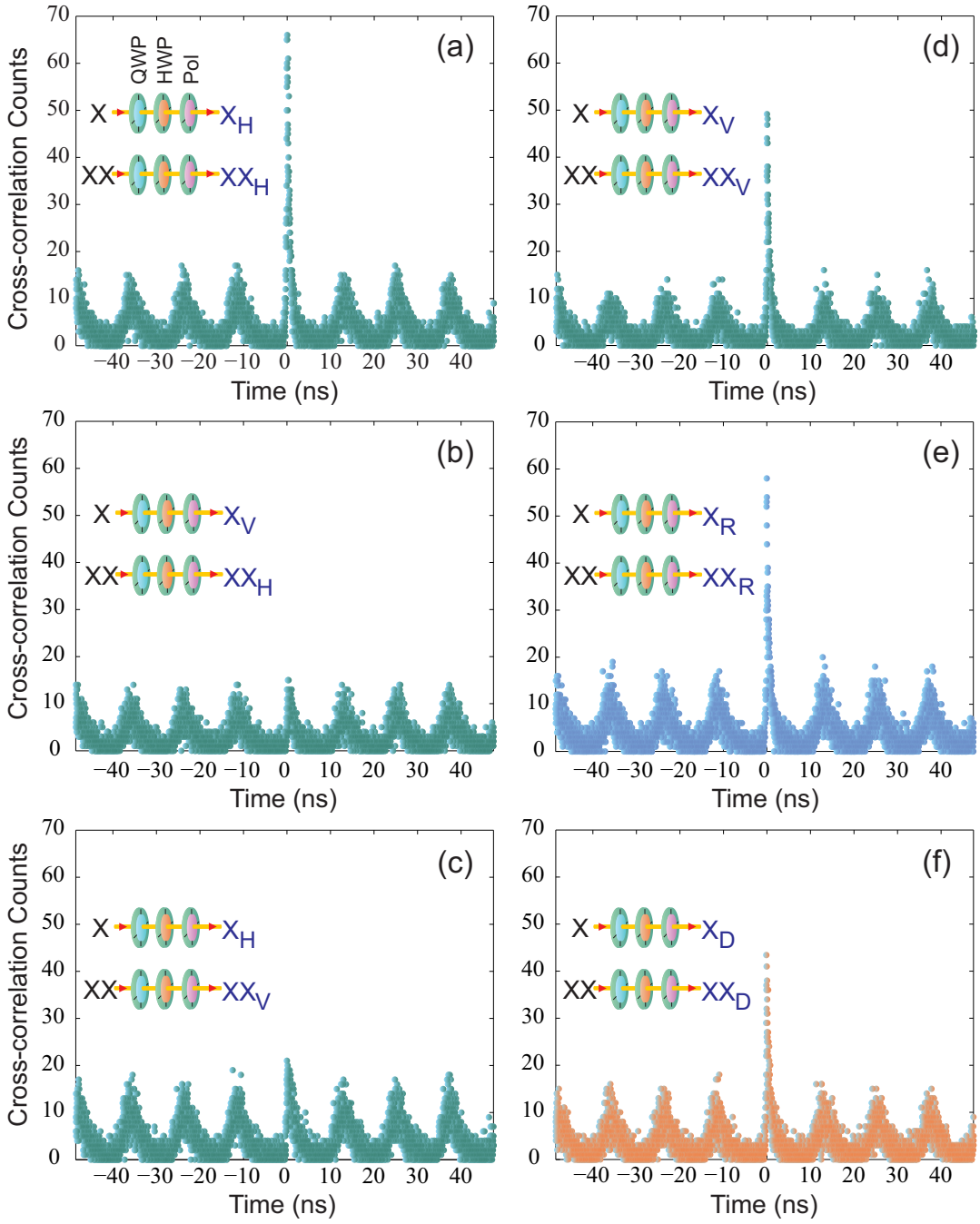

Figure 6.12: The cross-correlation counts measured for the XX and X photons in the following bases: (a) HH, (b) HV, (c) VH, (d), VV, (e) RR and (f) DD. Insets show the polarization state of XX and X photons after the polarization module, consisting of QWP, HWP and polarizer. The central peaks denote the correlation between XX and X photons in different polarization states.

For the tomography experiment, nanowires were excited by Ti:Sapphire pulsed laser at 808 nm, 80 MHz repetition rate and 2 ps pulse duration. The outcoming photons are sent to high-resolution SPCMs after proper spectral and polarization filtering. Figure 6.12 illustrates the cross-correlation counts in HH, HV, VH, VV, DD, and RR projection bases. The insets show what projection has been selected for either XX or X photon by the polarization module. The central peak in HH, VV, DD, and RR projections clearly signify the XX-X cascades and the correlation of corresponding photons. In fact, the average number of counts in the peaks at zero delay dominates the average number of counts in other peaks because of the larger probability of detecting the X photon in the same excitation period that XX photon is detected. Appearance of the central peak in HH and VV projections and its absence in HV and VH projections imply that the photons are quantum correlated in the rectilinear basis and the biphoton state can be approximately written as a linear combination of HH and VV states. The same correlation is seen in the diagonal basis, Figure 6.12(f). However, the emergence of RR cascade, instead of RL, may imply that the XX and X photons are only classically correlated in the circular basis. Appearance of both RR and RL (not shown here) is not surprising, as the minimum FSS we measured on the NWQDs never went below $\sim 5\mu$eV. We, however, notice that the certain verification of entanglement must be assessed via the biphoton density matrix.

The statistical nature of cross-correlation patterns in Figure 6.12 does not allow for an accurate understanding of the entanglement evolution in time. The full description is principally incorporated in the density matrix of photon pair ρ_{bi} resolved form a specific time window after the XX-X cascade event. This window is referred to as gating time and is basically a post-selection of counts in the cross-correlation pattern. The idea behind this post-selection is simple: in a QD with nonzero FSS, the randomized phase difference between the HH and VV components destroys the time-integrated entanglement. Therefore, a trace of entanglement should be observable early after the photon pair emission. By monitoring the elements of the density matrix within the gating time, the entangled biphoton state then can be identified.

The real and imaginary parts of the biphoton density matrix ρ_{bi} are shown in Figure 6.13(a-b) ~ 35 ps after the emission event. The stronger matrix elements are located on the diagonal with dominant outer elements $\langle HH|\,\rho_{\text{bi}}\,|HH\rangle$ and $\langle VV|\,\rho_{\text{bi}}\,|VV\rangle$. The amplitude of these two elements denote the strength of polarization correlation. The inner diagonal elements represent the uncorrelated light primarily originated form the background light and different dephasing processes. ρ_{bi} resembles the density matrix of $|HH\rangle + i\,|VV\rangle$, i.e. $(|HH\rangle + i\,|VV\rangle) \otimes (\langle HH| - i\,\langle VV|)$, shown in 6.13(c-d). Therefore, the biphoton state emitted from the NWQD is an entangled state within a small time window right after the cascade event. According to Sec. 2.5.3, the fidelity with the ideal state $|HH\rangle + i\,|VV\rangle$ is

$(\rho_{\mathrm{bi},11} + \rho_{\mathrm{bi},44})/2 - \mathrm{Im}\{\rho_{\mathrm{bi},14}\} = 0.78$.

We should note that the entanglement fades out rapidly into a classically correlated state for longer gating times and the fidelity drops below 0.5 at $\sim$ 60 ps. Such a short entanglement lifetime, as compared to the exciton lifetime, points out that entanglement is a delicate property and the FSS of NWQD has to be further suppressed to achieve durable entangled states.

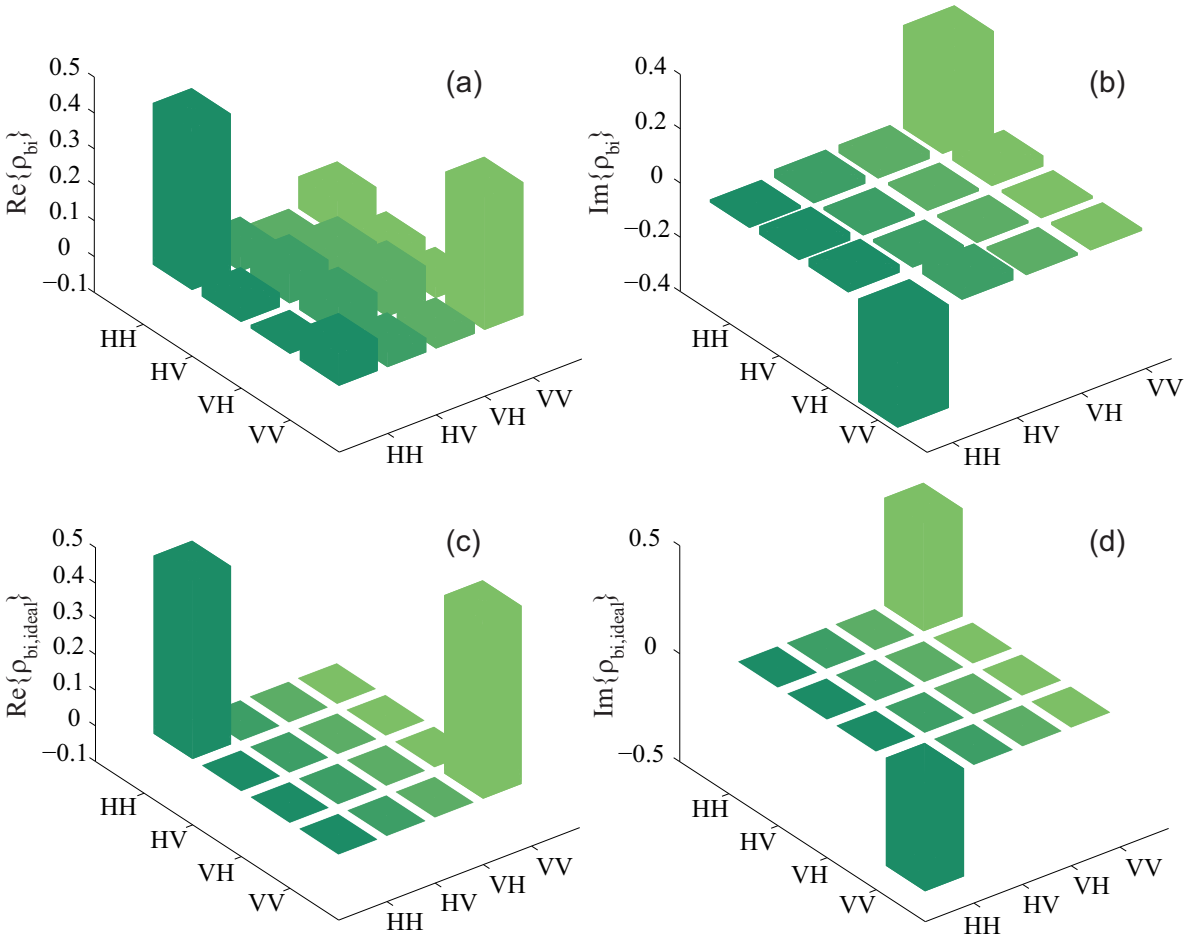

Figure 6.13: (a) and (b), real and imaginary components of the biphoton density matrix reconstructed from the full tomography measurements. The gating time is 35 ps. (c) and (d) show the real and imaginary components of the density matrix for the ideal entangled state $|HH\rangle + i\,|VV\rangle$.

6.6 Summary

NWQDs present good performance as a single photon source in terms of the time correlation function. The $g^{(2)}$ counts collected from exciton, biexciton and charged exciton resonances contain a sharp dip, indicating their excellent quality of single photon emission at low excitation powers. Both non-resonant continuous wave and pulsed pumping experiments verify the antibunching regime. The cross-correlation between X and XX resonances demonstrate a clear signature of cascade emission required for the entangled photon generation. The XX binding energy in most of the QDs is less than 1 meV, which is favourable for the cross-entanglement scheme. Moreover, the bright exciton splitting shows a substantial reduction in NWQDs compared to self-assembled QDs. We did not observe zero FSS, as anticipated by our theoretical modelings, and its origin is yet under question. However, the FSS/FWHM ratio was still small enough to promise a trace of polarization entanglement, particularly upon proper time gating of the detectors. The presence of entanglement early after the biphoton emission event was confirmed by our full tomography measurements. However its duration was rather small as compared to the exciton lifetime. In order to enhance the photon collection efficiency, the nanowires are tapered and the thickness of their cladding was optimized to support a single optical mode at QD emission wavelength.

Chapter 7

Conclusions and outlook

This work was a combination of two approaches: theoretical modeling and experimental analysis. Although the nature of concepts studied in the two approaches did not allow for rechecking every piece of theoretical predictions by experiments, in some important cases we noticed a decent agreement between the numerical results and experimental observations. In Sec. 7.1, I summarize the conclusions and contributions we made to the field in this work. In Sec. 7.2 an outlook will be provided based on the ongoing state of this research.

7.1 Conclusions and Contributions

For the first time, I studied the electronic properties of NWQDs at two different levels: single particle level and few-particle level. To this end, I started with developing a rich finite-element computational package based on modified $\mathbf{k} \cdot \mathbf{p}$ model and configuration interaction (CI) method which is currently not available in the quantum dot community. The package is able to simulate other nanostructures such as self-assembled QDs, quantum wells and wires. The application of this package on self-assembled QDs is reflected in my proposal on "Entangled photon pair generation in hybrid superconductor-semiconductor quantum dot devices", *Phys. Rev. B*, **84**, 104504 (2011), which has not been included in this thesis. Different physical and structural effects are incorporated in the numerical modeling to solidify the correctness of predictions:

1. Strain-induced potentials: hydrostatic, biaxial and shear strain components were numerically calculated by CM model and plugged into the $\mathbf{k} \cdot \mathbf{p}$ hamiltonian as hydrostatic and biaxial potential along with the off-diagonal coupling terms cause by the shear strain.

2. Piezoelectric potential: caused by charges originated from shear strain components. It was self-consistently solved with the strain distribution.

3. Band mixing: that is the wavefunction coupling between the HH, LH and SO parts of hole orbitals. The anisotropies in geometry directly, via off-diagonal components of kinetic hamiltonian $\mathcal{H}_k$, and indirectly, via off-diagonal components of strain hamiltonian $\mathcal{H}_s$, give rise to this wavefunction coupling.

4. Spin-orbit coupling inherently incorporated into the $\mathbf{k} \cdot \mathbf{p}$ hamiltonian.

5. Many-body effects: direct Coulomb interactions, exchange interactions and correlations. This accounts for minor reshaping of electron and hole orbitals ina strongly confining QD, Coulomb blockade, and energy renormalizations.

6. Electric field Stark effect and magnetic field Zeeman effect.

Items 1-4 were addressed in Chapter 3, items 5 and 6 are detailed in Chapters 4 and 5.

The modelings at the single particle level, Chapter 3, enabled us quantitatively understand the impact of strain-induced potentials on the electron/hole orbital symmetry and their dipole strength. For example, one of the challenges we faced in the early stages of NWQD growth was the very weak emission counts as it could not be detected by the micro-PL setup. The numerical simulations revealed the formation of electron orbital in the vicinity of QD sidewalls driven by hydrostatic strain. This unfolded the importance of radial growth to relax the accumulated stress forces. Moreover, exciton and biexciton wavelengths showed a strong dependency on axial quantization rather than lateral quantization. Indeed, this criterion principally applies to vertical aspect ratios $a_h < 0.5$, particularly in [111]-oriented NWQDs where the LH character grows quickly with the QD height. In general, to keep the character of ground state pure (HH $> 95\%$) the axial quantization has to be considerably stronger than lateral confinement, as frequently seen in flat self-assembled QDs.

The symmetry of electron and hole orbitals in NWQDs is elevated compared to the self-assembled QDs. Cylindrical NWQDs in [001]-oriented nanowires show D_{2d} symmetry, which preserves the degeneracy between two bright excitons. The yield of growing [001] straight GaAs wires is, however, low [187] and [111] orientation is favourable. Regardless of vertical anisotropy, electron and hole wavefunctions possess C_{3v} symmetry in [111]-oriented NWQDs. Threefold in-plane symmetry leads to zero FSS.

The model then evolves to the few-particle level, Chapters 4, where a realistic picture of NWQD energy level structure emerges. In this picture the conditional probability density

of electrons and holes, as fermions, in a multiexciton complex is covered. In particular, ground state X, XX, X^- and X^+ states in NWQD are studied in detail. The binding energies of XX, X^- and X^+ with respect to exciton primarily rely on the direct Coulomb interactions, and correlations act like a correction to keep the energy of complex minimized: wherever the difference between attractive and repulsive interactions grows, more correlation energy is accumulated. The measure of XX binding energy is of importance in the cross entanglement scheme, where XX and X have to come into resonance by an external electric field. In practice, the range of electric field that can be applied in a nanosclae device is limited, therefore, small XX binding energy is of interest: binding energy is smaller in NWQDs with larger vertical aspect ratio ($a_h > 0.3$).

We defined an orbital-dependent kinetic energy to track the exchange between kinetic and potential energies of electrons and holes and their orbital deformations. The kinetic energy a particle stores depend on its effective mass and orbital extent. We showed holes are responsive to changes in the confinement as they exchange small kinetic energy upon orbital deformations. This concept could be generally applied to any type of confining nanostructure. The electron with a flat dispersion is reluctant to reshape under size variations of NWQD. Therefore, its Coulomb interactions smoothly change with changing NWQD height or diameter.

The results given in Chapters 3 and 4 are mostly design-oriented and useful for understanding the trend of different mesoscopic effects under structural parameters. Indeed, a material-dependent analysis would even further enrich the modelings. However, the conclusions already made can qualitatively describe the system to a great extent suited for empirical testing. Results are presented for zinc-blende materials because of the availability of their $\mathbf{k} \cdot \mathbf{p}$ parameters. In the mesoscopic scale, where the tiny details of atomic structure are discarded, the validity of relevant outcomes remains intact: orbital deformation and symmetry, Coulomb interactions, and binding energies are well-described in a mesoscopic perspective. Consequently, the overall behaviour should be extendible to wurtzite material as well. Our findings in Chapters 3 and 4, along with our analysis on hexagonal NWQDs, are presented in M. Khoshnegar et al., "Single- and few-particle states in core-shell nanowire quantum dots", *Phys. Rev. B*, **86**, 205318 (2012).

In Chapter 5, I further extend the model to quantum dot molecules. This structure provides more versatility for tuning the energy level structure, carrier localization and interactions. The hybridized states render new transition channels in the s-shell, thus the number of s-shell excitons is not limited to 2 anymore. I demonstrate that the hole particle shows nontrivial hole tunneling coefficient easily controllable with axial electric field. Upon double dot symmetry, the electron remains delocalized instead and maintains the oscillator strength of newly opened channels. New channels with persistent brightness

during hole tunneling promise for higher order entangled states. The very important concept in the operation of QDM as an entangled photon source is the emergence of merely a limited number of spectral features as revealed by the configuration interaction calculations: Coulomb blockade decides what configurations, or equivalently what spectral features, are favorable to form. I believe such spectral features should be observable in QDM spectroscopy.

The significance of the proposed model in Chapter 5 is twofold: a) For the first time, the concept of few-body interactions in a nanowire quantum dot molecule with hybridized states is dealt with. The few-particle complexes (i.e. X, XX, X^- and X^+) exhibit unique spectral behaviour directly related to the electron and hole hybridization energies. b) A proposal for generating tripartite GHZ entangled state is given based on a flexible nanostructure. Almost every spectral characteristic, including operating wavelength, tunneling coefficient and color indistinguishability, is adjustable by QD size and interdot spacing. Such tunability is impossible to reach in other solid-state-based systems such as NV centers in diamond [35]. The versatile energy levels structure allows for realizing W-states or triphoton entangled states. The deficiency of the proposed setup perhaps lies in establishing the absolute color indistinguishability of generated photon: although it is quite practical to integrate a QD with nonlinear waveguides to downconvert emitted photons on-chip, post-processing of each individual transition in an entangled state demands for high wavelength selectivity. It would be desirable to post-select and manipulate each linewidth separately to increase the photon concurrence. Hence, implementation of the whole setup on a single integrated chip still remains questionable. On the other hand, a QDM seems to be a promising source of higher order entangled states in time-bin entanglement, in which the color coincidence is not a priori [188].

The photon statistics experiments explained in Chapter 6 study the performance of NWQDs in quantum regime. The autocorrelation and cross-correlation functions of X and XX resonances signify both single photon emission and cascade recombination, introducing NWQDs as a viable competitor of self-assembled quantum dots serving as quantum photon source. Site-controlled nanowires allow for proper optical isolation and suppressing the background light, which usually deteriorate $g^{(2)}$ function in self-assembled devices. The small FSS and tunable binding energy, both anticipated by numerical modeling, are outstanding features of NWQDs towards producing entangled photons. Moreover, in terms of light collection efficiency, the nanowire shape can be flexibly tailored to waveguide and transmit a larger fraction light radiated by QD. Our full tomography measurements show that a trace of entanglement exists in NWQDs with narrow emission linewidth and small FSS. By reconstructing the polarization density matrix of photon pairs ρ_{bi}, we realized that the biphoton correlated state resembles $|HH\rangle + i\,|VV\rangle$ immediately after the cascade

event. The fidelity to the above maximally entangled state was calculated to be 0.78. The entanglement lifetime was, however, short. Our experiments led to the first observation of photon entanglement in NWQDs. However, there still exist some open questions on how to improve the quality of QD segments, completely vanish the FSS, and prolong the entanglement lifetime.

7.2 Outlook and future

7.2.1 Vertical gating the nanowires

Although FSS is relatively small in NWQDs, an electrical control over the exciton bright states is preferable for entanglement purposes. Similarly, tuning the XX binding energy requires for an external electric field in the time reordering scheme. Moreover, hole tunneling in a QDM is a field-dependent process. Electrical contacting of the nanowires horizontally lying on the substrate is convenient and well-established [189]. The challenge arises from the fact that nanowire emission is highly polarized. To realize the polarization entanglement, it has to be reconstructed in all basis sets. However, nanowires lying on substrate can only provide one linear basis if their radiation is perpendicularly collected. A viable solution will be using a wrap-gate transistor configuration to provide electrostatic gate control (e.g. see Ref. [189] where InGaAs nanowires are wrap-gated and vertically contacted). In a wrap-gate vertical transistor, the "source" and "drain" metallic contacts at the bottom and top of the nanowire apply an axial Stark effect, while the surrounding gate provide radial control. In our applications, where optical pumping is accomplished via an objective, Schottky contacts suffice for axial control. In this case, a detailed electrostatic modeling is needed to understand the net field distribution of vertical contacts in the presence of gate.

7.2.2 Coupled QD

The proposal given in Chapter 5 on QDMs relies on independent growth of individual dots with a relatively short interdot spacing. This means it is presumed that the growth of first QD does not affect the size of the second QD and the symmetry of double dot. Although the asymmetry of double dot, if not very significant, does not change the results qualitatively, an unknown growth dependent effect would lead to an inconclusive empirical-based design. For example, the initial design in Sec. 5.10, i.e. $D_D = 20$ nm, $h_D = 4$ nm and $D_s = 6$ nm is based on zinc-blende parameters. The ground state X transition is

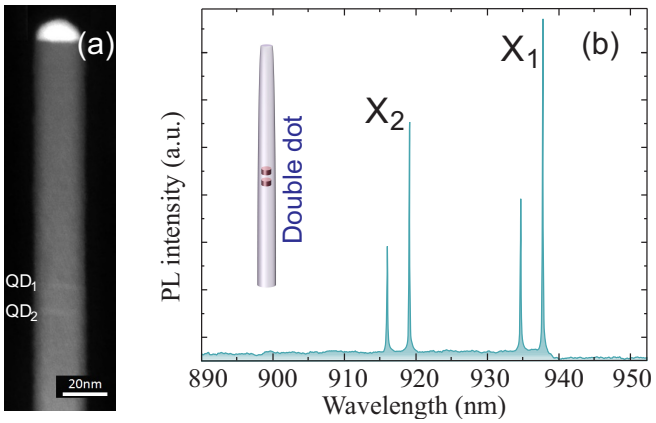

Figure 7.1: (a) TEM image of nanowires embedding double dots with 20 nm interdot spacing. (b) Spectrum of double quantum dot comprising two exciton emissions at $\sim$ 940 nm and $\sim$ 920 nm. The growth times of single dots are identical, thus the X_1-X_2 splitting results from either QD-QD wavefunction coupling or growth-dependent dissimilarity of QDs.

then calculated to be $\sim$ 1.28 eV ($J_{eh} = 45$ meV). Knowing the fact that energy band gap of wurtzite InP increases by $\sim$ 0.15-0.2 eV, enlarging the height of QD to 6-8 nm and the interdot spacing to $\sim$ 10 nm should lead to coupled dots with delocalized electrons emitting at a close wavelength. In a recent double dot growth ($InAs_{0.15}P_{0.85}$/InP), we noticed that such energies are obtained upon larger interdot spacings 15-20 nm, see Figure 7.1[1]. As could be inferred from the double dot spectrum, the low energy resonance X_1 at $\sim$ 940 nm is separated by $\sim$ 20 meV from X_2. This energy spacing results from either the electron hybridization of the two dots or growth-dependent dissimilarity of individual QDs. In the former case, QD-QD coupling has prompted the energy splitting. In the latter case, however, the size variation has led to the appearance of two different resonances.

Provided that the two QDs are genuinely coupled, its signature should be observed in the cross-correlation between X_1 and X_2 lines: if two QDs are decoupled, they emit single photons independently. Consequently, no dip is traceable in the cross-correlation counts. In contrast, the energy of X_1 exciton is dependent on the presence of X_2 exciton if the two dots are coupled. Thus the whole QDM does not emit two single photons from X_1 and X_2 lines simultaneously, and cross-correlation dip is observed. Performing such experiments sheds light into the nature of correlated excitons in a QDM without access to an external electric field.

A sensible concept in producing quantum correlated photons in solid state systems is

[1]TEM images is taken in Philip Poole's group at National Research Council, Ottawa, Canada.

that having access to more sequential decays offers higher order states. This is exactly where the coupled structures such as QDMs could play an essential role. Their function particularly becomes more logical in those schemes where the precise energy indistinguishability of constituting photons is not a prerequisite (e.g. in time-bin entanglement). Besides that, I believe that transition from the regular single core-shell NWQDs to QDMs leads to essential advancements in the performance of nanowire-based quantum photon sources: more tunable *s*-shell transitions, controllable tunneling energies, peculiar antibonding character of hole wavefunction and smaller fine structure splitting of bright excitons are all promising features for potential quantum photonics applications, which are, of course, beyond my current vision.

APPENDICES

Appendix A

Single Particle Hamiltonian

To calculate the single particle energies we employ the eight-band Luttinger-Kohn Hamiltonian with the inclusion of strain and piezoelectricity, $\mathcal{H}_{\mathbf{k}\cdot\mathbf{p}} = \mathcal{H}_k + \mathcal{H}_s + \mathcal{H}_p$, where $\mathcal{H}_k$, $\mathcal{H}_s$ and $\mathcal{H}_p$ are the kinetic, strain-induced and piezoelectric parts of $\mathbf{k}\cdot\mathbf{p}$ Hamiltonian [77, 78]. The total wavefunction in the eight-band Hamiltonian is classified into eight spinors $|c_{1,2}\rangle = |c_{l=0}^{n;s=\pm1/2}\rangle$, $|hh_{1,2}\rangle = |hh_{l=1,J_z=\pm3/2}^{n;s=\pm1/2}\rangle$, $|lh_{1,2}\rangle = |lh_{l=1,J_z=\pm1/2}^{n;s=\pm1/2}\rangle$ and $|so_{1,2}\rangle = |so_{l=0,J_z=\pm1/2}^{n;s=\pm1/2}\rangle$ associated with the conduction, heavy hole (hh), light hole (lh) and spin-orbit split-off (so) bands, respectively. Note that we use lower case letters in this appendix only for the sake of simplicity in the representation, and the above spinors are exactly the same as spinors introduced in Sec. 2.1. s, l and J_z denote the spin orientation, angular momentum and z-projection of total angular momentum of the single particle ($J = l + s$), and n represents the state number. $\mathcal{H}_{\mathbf{k}\cdot\mathbf{p}}$ is solved throughout the structure with appropriate boundary conditions (see Ref. [67]) to find the energy eigenvalues and also the envelope functions $\varphi_{c,hh,lh,so}^{e;h}$ corresponding to each spinor; $\psi_{J,J_z}^{e;h} = \varphi_{J,J_z}^{e;h}\,|J, J_z\rangle$, where $J \in \{3/2,\, 1/2\}$ and $J_z \in \{\pm3/2,\, \pm1/2\}$. The diagonal matrix elements of CB and VB spinors in $\mathcal{H}_{\text{tot}}$ are

$$\mathcal{H}_c = \langle c_{1,2}|\,\mathcal{H}_{\text{tot}}\,|c_{1,2}\rangle = E_c + \frac{\hbar^2}{2m_0}(p_\perp^2 + p_\parallel^2) + a_c(\epsilon_\perp + \epsilon_\parallel) + V_p, \tag{A.1}$$

$$\begin{aligned}\begin{matrix}\mathcal{H}_{hh}\\ \mathcal{H}_{lh}\end{matrix} &= \langle \begin{matrix}hh_{1,2}\\ lh_{1,2}\end{matrix} |\,\mathcal{H}_{\text{tot}}\,| \begin{matrix}hh_{1,2}\\ lh_{1,2}\end{matrix} \rangle = E_v - \frac{\hbar^2}{2m_0}\gamma_1(p_\perp^2 + p_\parallel^2)\\ &\mp \frac{\hbar^2}{2m_0}\gamma_2(p_\perp^2 - 2p_\parallel^2) - a_v(\epsilon_\perp + \epsilon_\parallel) \mp b_v(\epsilon_\parallel - \tfrac{1}{2}\epsilon_\perp) + V_p,\end{aligned} \tag{A.2}$$

$$\mathcal{H}_{so} = \langle so_{1,2}| \mathcal{H}_{\text{tot}} |so_{1,2}\rangle = E_v - \frac{\hbar^2}{2m_0}\gamma_1(p_\perp^2 + p_\parallel^2) - \Delta_{so} - a_v(\epsilon_\perp + \epsilon_\parallel) + V_p, \tag{A.3}$$

with momentum operators $p_\parallel = -i\partial_z$, $p_\perp = -i(\partial_x + \partial_y)$, and strain components $\epsilon_\parallel = \epsilon_z$ and $\epsilon_\perp = \epsilon_x + \epsilon_y$ provided that QD growth orientation is along z axis. $E_{c(v)}$ determines the CB (VB) edge and $\gamma_{i=1,2,3}$ are the Luttinger parameters [130]. $a_{c(v)}$, b_v, V_p and Δ_{so} represent conduction (valence) hydrostatic deformation, [001]-shear deformation, piezoelectric and spin-orbit coupling potentials, respectively [76]. The hh, lh and so-components of hole orbital are coupled as a consequence of biaxial and shear strain together with the spin-orbit interaction [105], i.e.

$$\begin{aligned}\mathcal{H}^r_{hh-lh} = \langle lh_2| \mathcal{H}_{\text{tot}} |hh_1\rangle = -\sqrt{3}\frac{\hbar^2}{2m_0}[\gamma_2(p_x^2 - p_y^2) \\ - 2i\gamma_3 p_x p_y] + \frac{\sqrt{3}}{2}b_v(\epsilon_{xx} - \epsilon_{yy}) - id_v\epsilon_{xy} = \langle hh_2| \mathcal{H}_{\text{tot}} |lh_1\rangle ,\end{aligned} \tag{A.4}$$

$$\begin{aligned}\mathcal{H}^s_{hh-lh} = \langle hh_2| \mathcal{H}_{\text{tot}} |lh_2\rangle = \sqrt{3}\gamma_3\frac{\hbar^2}{m_0}(p_z p_x - ip_z p_y) \\ - d_v(\epsilon_{xz} - i\epsilon_{yz}) = -\langle lh_1| \mathcal{H}_{\text{tot}} |hh_1\rangle ,\end{aligned} \tag{A.5}$$

$$\mathcal{H}^r_{hh-so} = \langle hh_2| \mathcal{H}_{\text{tot}} |so_2\rangle = \sqrt{2}\langle lh_2| \mathcal{H}_{\text{tot}} |hh_1\rangle = -\langle so_1| \mathcal{H}_{\text{tot}} |hh_1\rangle , \tag{A.6}$$

$$\mathcal{H}^s_{hh-lh} = \langle so_2| \mathcal{H}_{\text{tot}} |hh_1\rangle = 1/\sqrt{2}\langle hh_2| \mathcal{H}_{\text{tot}} |lh_2\rangle = \langle hh_2| \mathcal{H}_{\text{tot}} |so_1\rangle \tag{A.7}$$

where d_v is the [111]-deformation potential.

Appendix B

Tunneling Matrix Element

Here we introduce different components participating in the hole effective tunneling matrix element. The interplay between the magnitude of different tunneling terms leads to a peculiar evolution of the ground state parity versus the interdot spacing. According to the $D_{\infty h}$ symmetry of the QDM structure, both $|h_0\rangle$ and $|h_1\rangle$ are primarily hh-like (see Table B.1), that is $\rho_{hh}^{h_0;h_1} = |\varphi_{hh}^{h_0;h_1}|^2 \gg \rho_{c,lh,so}^{h_0;h_1}$, independent of the interdot spacing. This confirms the fact that predominant contributions in the effective tunneling matrix element partially originate from the interdot diffusion of hh-orbital (t_{hh}) along with its coupling to the lh- and so-orbitals (t_{co}), that is $t_h = t_{hh} - t_{co}$, where $t_{hh} = 1/2(E_{hh}^{h_1} - E_{hh}^{h_0})$, $t_{co} = E_{r;s}^{h_1;lh} - E_{r;s}^{h_0;lh} + E_{r;s}^{h_1;so} - E_{r;s}^{h_0;so}$,

$$E_{hh}^{h_1,h_0} \approx \sum_{J_z} \langle \psi_{3/2,J_z}^{h_1,h_0} | \, \mathcal{H}_{hh} \, | \psi_{3/2,J_z}^{h_1,h_0} \rangle \,, \tag{B.1}$$

$$E_{r;s}^{h_1,h_0;lh} \approx 2 \langle \psi_{hh_1}^{h_1,h_0;lh} | \, \mathcal{H}_{hh-lh}^{r} \, | \psi_{lh_2}^{h_1,h_0;lh} \rangle - 2 \langle \psi_{hh_1}^{h_1,h_0;lh} | \, \mathcal{H}_{hh-lh}^{s} \, | \psi_{lh_1}^{h_1,h_0;lh} \rangle$$

$$+ 2 \langle \psi_{hh_2}^{h_1,h_0;lh} | \, \mathcal{H}_{hh-lh}^{s\dagger} \, | \psi_{lh_2}^{h_1,h_0;lh} \rangle + 2 \langle \psi_{hh_2}^{h_1,h_0;lh} | \, \mathcal{H}_{hh-lh}^{r\dagger} \, | \psi_{lh_1}^{h_1,h_0;lh} \rangle \,, \tag{B.2}$$

and $E_{r;s}^{h_1,h_0;so}$ are obtained by replacing so wavefunctions instead of lh in Eq. B.2. We also account for the lh-induced part of diagonal tunneling matrix elements in Eq. B.1. The primary approximation above is the elimination of trivial coupling terms bearing no hh component. By the same token, so-related terms effectively do not contribute in the hole tunneling as compared to lh-related terms and could be safely removed. All above energy terms include two components originating from the kinetic and strain-induced parts of $\mathcal{H}_{\mathbf{k}\cdot\mathbf{p}}$ in Appendix A. Having $\mathcal{H}_{\mathbf{k}\cdot\mathbf{p}}$ diagonalized, both components can be resolved

D_s (nm)	0.75	1.0	1.5	2.0	3.0	4.0	5.0	6.0
hh_0 (%)	87.0	87.5	88.5	90.6	92.1	93.0	93.6	94.0
lh_0 (%)	11.9	11.5	10.5	8.6	7.2	6.4	5.8	5.4
hh_1 (%)	86.5	87.7	89.4	89.8	91.9	93.3	94.2	94.7
lh_1 (%)	12.4	11.3	9.7	9.3	7.3	5.9	5.1	4.7
t_h (meV)	1.22	0.76	0.17	-0.39	-0.51	-0.48	-0.43	-0.30

Table B.1: hh and lh percentages in the two first hybridized states versus the interdot distance.

applying single particle orbitals into above equations. Last row in Table B.1 compiles calculated hole tunneling energies versus the interdot spacing. The anticrossing observed in the vicinity of $D_s = 1.8$ nm in Figure 5.2(c) occurs when t_{co} dominates t_{hh} and the antibonding character of the ground state reveals. We note that the presence of D_{2d}-symmetric piezoelectric potential prevents us from attributing a definite parity (axially symmetric or antisymmetric) to the s-shell wavefunctions particularly away from the double dot axis.

References

[1] Nicolas Gisin, Grgoire Ribordy, Wolfgang Tittel, and Hugo Zbinden. Quantum cryptography. *Reviews of Modern Physics*, 74(1):145–195, Jan 2002.

[2] E. Knill, R. Laflamme, and G. J. Milburn. A scheme for efficient quantum computation with linear optics. *Nature*, 409(6816):46–52, Jan 2001.

[3] Michael Varnava, Daniel Browne, and Terry Rudolph. How good must single photon sources and detectors be for efficient linear optical quantum computation? *Physical Review Letters*, 100(6):060502, Feb 2008.

[4] Edo Waks, Kyo Inoue, Charles Santori, David Fattal, Jelena Vuckovic, Glenn S. Solomon, and Yoshihisa Yamamoto. Secure communication: Quantum cryptography with a photon turnstile. *Nature*, 420(6917):762–762, Dec 2002.

[5] Michael A. Nielsen and Isaac L. Chuang. *Quantum Computation and Quantum Information: 10th Anniversary Edition*. Cambridge University Press, 2011.

[6] P. Michler. *Single Semiconductor Quantum Dots*. Springer, Berlin, 2009.

[7] W. Buttler, R. Hughes, P. Kwiat, G. Luther, G. Morgan, J. Nordholt, C. Peterson, and C. Simmons. Free-space quantum-key distribution. *Physical Review A*, 57(4):2379–2382, Apr 1998.

[8] Tobias Schmitt-Manderbach, Henning Weier, Martin Furst, Rupert Ursin, Felix Tiefenbacher, Thomas Scheidl, Josep Perdigues, Zoran Sodnik, Christian Kurtsiefer, John Rarity, and et al. Experimental demonstration of free-space decoy-state quantum key distribution over 144km. *Physical Review Letters*, 98(1), Jan 2007.

[9] Chandra M Natarajan, Michael G Tanner, and Robert H Hadfield. Superconducting nanowire single-photon detectors: physics and applications. *Superconductor Science and Technology*, 25(6):063001, Jun 2012.

[10] Leonard Mandel and Emil Wolf. *Optical Coherence and Quantum Optics*. Cambridge University Press, 1995.

[11] Paul Kwiat, Klaus Mattle, Harald Weinfurter, Anton Zeilinger, Alexander Sergienko, and Yanhua Shih. New high-intensity source of polarization-entangled photon pairs. *Physical Review Letters*, 75(24):4337–4341, Dec 1995.

[12] H. Arnaut and G. Barbosa. Orbital and intrinsic angular momentum of single photons and entangled pairs of photons generated by parametric down-conversion. *Physical Review Letters*, 85(2):286–289, Jul 2000.

[13] Paul G. Kwiat, Edo Waks, Andrew G. White, Ian Appelbaum, and Philippe H. Eberhard. Ultrabright source of polarization-entangled photons. *Physical Review A*, 60(2):R773–R776, Aug 1999.

[14] Y. H. Shih and C. O. Alley. New type of Einstein-podolsky-rosen-bohm experiment using pairs of light quanta produced by optical parametric down conversion. *Physical Review Letters*, 61(26):2921–2924, Dec 1988.

[15] J. Brendel, N. Gisin, W. Tittel, and H. Zbinden. Pulsed energy-time entangled twin-photon source for quantum communication. *Physical Review Letters*, 82(12):2594–2597, Mar 1999.

[16] Christian Kurtsiefer, Markus Oberparleiter, and Harald Weinfurter. Generation of correlated photon pairs in type-ii parametric down conversion-revisited. *Journal of Modern Optics*, 48(13):1997–2007, Nov 2001.

[17] Albert Einstein. *Einstein's Miraculous Year: Five Papers That Changed the Face of Physics*. Princeton University Press, 2005.

[18] X. Zou and L. Mandel. Photon-antibunching and sub-poissonian photon statistics. *Physical Review A*, 41(1):475–476, Jan 1990.

[19] C. Monroe. Quantum information processing with atoms and photons. *Nature*, 416(6877):238–246, Mar 2002.

[20] J. McKeever. Deterministic generation of single photons from one atom trapped in a cavity. *Science*, 303(5666):1992–1994, Mar 2004.

[21] Matthias Keller, Birgit Lange, Kazuhiro Hayasaka, Wolfgang Lange, and Herbert Walther. Continuous generation of single photons with controlled waveform in an ion-trap cavity system. *Nature*, 431(7012):1075–1078, Oct 2004.

[22] Martin Mucke, Joerg Bochmann, Carolin Hahn, Andreas Neuzner, Christian Nolleke, Andreas Reiserer, Gerhard Rempe, and Stephan Ritter. Generation of single photons from an atom-cavity system. *Physical Review A*, 87(6), Jun 2013.

[23] Th. Basche, W. Moerner, M. Orrit, and H. Talon. Photon antibunching in the fluorescence of a single dye molecule trapped in a solid. *Physical Review Letters*, 69(10):1516–1519, Sep 1992.

[24] B. Lounis and W. E. Moerner. Single photons on demand from a single molecule at room temperature. *Nature*, 407(6803):491–493, Sep 2000.

[25] S.G. Lukishova, A.W. Schmid, A.J. McNamara, R.W. Boyd, and C.R. Stroud. Room temperature single-photon source: single-dye molecule fluorescence in liquid crystal host. *IEEE Journal of Selected Topics in Quantum Electronics*, 9(6):1512–1518, Nov 2003.

[26] A. Gruber. Scanning confocal optical microscopy and magnetic resonance on single defect centers. *Science*, 276(5321):2012–2014, Jun 1997.

[27] A. Drabenstedt, L. Fleury, C. Tietz, F. Jelezko, S. Kilin, A. Nizovtzev, and J. Wrachtrup. Low-temperature microscopy and spectroscopy on single defect centers in diamond. *Physical Review B*, 60(16):11503–11508, Oct 1999.

[28] Christian Kurtsiefer, Sonja Mayer, Patrick Zarda, and Harald Weinfurter. Stable solid-state source of single photons. *Physical Review Letters*, 85(2):290–293, Jul 2000.

[29] N. Bar-Gill, L.M. Pham, C. Belthangady, D. Le Sage, P. Cappellaro, J.R. Maze, M.D. Lukin, A. Yacoby, and R. Walsworth. Suppression of spin-bath dynamics for improved coherence of multi-spin-qubit systems. *Nature Communications*, 3:858, May 2012.

[30] B. J. M. Hausmann, J. T. Choy, T. M. Babinec, B. J. Shields, I. Bulu, M. D. Lukin, and Marko Lonar. Diamond nanophotonics and applications in quantum science and technology. *physica status solidi (a)*, 209(9):1619–1630, Sep 2012.

[31] Jennifer T. Choy, Birgit J. M. Hausmann, Thomas M. Babinec, Irfan Bulu, Mughees Khan, Patrick Maletinsky, Amir Yacoby, and Marko Loncar. Enhanced single-photon emission from a diamond-silver aperture. *Nature Photonics*, 5(12):738–743, Oct 2011.

[32] Andreas W. Schell, Johannes Kaschke, Joachim Fischer, Rico Henze, Janik Wolters, Martin Wegener, and Oliver Benson. Three-dimensional quantum photonic elements based on single nitrogen vacancy-centres in laser-written microstructures. *Scientific Reports*, 3, Apr 2013.

[33] P. Neumann, R. Kolesov, B. Naydenov, J. Beck, F. Rempp, M. Steiner, V. Jacques, G. Balasubramanian, M. L. Markham, D. J. Twitchen, and et al. Quantum register based on coupled electron spins in a room-temperature solid. *Nature Physics*, 6(4):249–253, Feb 2010.

[34] E. Togan, Y. Chu, A. S. Trifonov, L. Jiang, J. Maze, L. Childress, M. V. G. Dutt, A. S. Srensen, P. R. Hemmer, A. S. Zibrov, and et al. Quantum entanglement between an optical photon and a solid-state spin qubit. *Nature*, 466(7307):730–734, Aug 2010.

[35] P. Neumann, N. Mizuochi, F. Rempp, P. Hemmer, H. Watanabe, S. Yamasaki, V. Jacques, T. Gaebel, F. Jelezko, and J. Wrachtrup. Multipartite entanglement among single spins in diamond. *Science*, 320(5881):1326–1329, Jun 2008.

[36] P. Michler. A quantum dot single-photon turnstile device. *Science*, 290(5500):2282–2285, Dec 2000.

[37] R. Thompson, R. Stevenson, A. Shields, I. Farrer, C. Lobo, D. Ritchie, M. Leadbeater, and M. Pepper. Single-photon emission from exciton complexes in individual quantum dots. *Physical Review B*, 64(20):201302(R), Oct 2001.

[38] S. M. Ulrich, M. Benyoucef, P. Michler, N. Baer, P. Gartner, F. Jahnke, M. Schwab, H. Kurtze, M. Bayer, S. Fafard, and et al. Correlated photon-pair emission from a charged single quantum dot. *Physical Review B*, 71(23), Jun 2005.

[39] Charles Santori, David Fattal, Jelena Vuckovic, Glenn S. Solomon, and Yoshihisa Yamamoto. Indistinguishable photons from a single-photon device. *Nature*, 419(6907):594–597, Oct 2002.

[40] A. J. Bennett, D. C. Unitt, A. J. Shields, P. Atkinson, and D. A. Ritchie. Influence of exciton dynamics on the interference of two photons from a microcavity single-photon source. *Optics Express*, 13(20):7772, 2005.

[41] S. Varoutsis, S. Laurent, P. Kramper, A. Lemaitre, I. Sagnes, I. Robert-Philip, and I. Abram. Restoration of photon indistinguishability in the emission of a semiconductor quantum dot. *Physical Review B*, 72(4):041303(R), Jul 2005.

[42] Yu-Ming He, Yu He, Yu-Jia Wei, Dian Wu, Mete Atature, Christian Schneider, Sven Hofling, Martin Kamp, Chao-Yang Lu, and Jian-Wei Pan. On-demand semiconductor single-photon source with near-unity indistinguishability. *Nature Nanotechnology*, 8(3):213–217, Feb 2013.

[43] Z. Yuan. Electrically driven single-photon source. *Science*, 295(5552):102–105, Dec 2001.

[44] A. J. Bennett, D. C. Unitt, P. See, A. J. Shields, P. Atkinson, K. Cooper, and D. A. Ritchie. Microcavity single-photon-emitting diode. *Applied Physics Letters*, 86(18):181102, 2005.

[45] Raj B Patel, Anthony J Bennett, Ken Cooper, Paola Atkinson, Christine A Nicoll, David A Ritchie, and Andrew J Shields. Quantum interference of electrically generated single photons from a quantum dot. *Nanotechnology*, 21(27):274011, Jul 2010.

[46] A. Bennett, D. Unitt, P. See, A. Shields, P. Atkinson, K. Cooper, and D. Ritchie. Electrical control of the uncertainty in the time of single photon emission events. *Physical Review B*, 72(3):033316, Jul 2005.

[47] Pierre M. Petroff. Semiconductor self-assembled quantum dots: Present status and future trends. *Advanced Materials*, 23(20):2372–2376, May 2011.

[48] M. B. Ward, T. Farrow, P. See, Z. L. Yuan, O. Z. Karimov, A. J. Bennett, A. J. Shields, P. Atkinson, K. Cooper, and D. A. Ritchie. Electrically driven telecommunication wavelength single-photon source. *Applied Physics Letters*, 90(6):063512, 2007.

[49] Asli Ugur, Stefan Kremling, Fariba Hatami, Sven Hofling, Lukas Worschech, Alfred Forchel, and W. Ted Masselink. Single-photon emitters based on epitaxial isolated InP/ingap quantum dots. *Applied Physics Letters*, 100(2):023116, 2012.

[50] M. Reischle, J. Beirne, G, W.-M. Schulz, M. Eichfelder, R. Rossbach, M. Jetter, and P. Michler. Electrically pumped single-photon emission in the visible spectral range up to 80 k. *Optics Express*, 16(17):12771, Aug 2008.

[51] Satoshi Kako, Charles Santori, Katsuyuki Hoshino, Stephan Gotzinger, Yoshihisa Yamamoto, and Yasuhiko Arakawa. A gallium nitride single-photon source operating at 200 k. *Nature Materials*, 5(11):887–892, Oct 2006.

[52] Hiroyuki Naiki, Sadahiro Masuo, Shinjiro Machida, and Akira Itaya. Single-photon emission behavior of isolated cdse/zns quantum dots interacting with the localized surface plasmon resonance of silver nanoparticles. *The Journal of Physical Chemistry C*, 115(47):23299–23304, Dec 2011.

[53] J. P. Reithmaier, G. Sek, A. Loffler, C. Hofmann, S. Kuhn, S. Reitzenstein, L. V. Keldysh, V. D. Kulakovskii, T. L. Reinecke, and A. Forchel. Strong coupling in a single quantum dot-semiconductor microcavity system. *Nature*, 432(7014):197–200, Nov 2004.

[54] A. Kiraz, P. Michler, C. Becher, B. Gayral, A. Imamoglu, Lidong Zhang, E. Hu, W. V. Schoenfeld, and P. M. Petroff. Cavity-quantum electrodynamics using a single inas quantum dot in a microdisk structure. *Applied Physics Letters*, 78(25):3932, 2001.

[55] Dirk Englund, David Fattal, Edo Waks, Glenn Solomon, Bingyang Zhang, Toshihiro Nakaoka, Yasuhiko Arakawa, Yoshihisa Yamamoto, and Jelena Vuckovic. Controlling the spontaneous emission rate of single quantum dots in a two-dimensional photonic crystal. *Physical Review Letters*, 95(1):013904, Jul 2005.

[56] Matthew Pelton, Charles Santori, Jelena Vuckkovic, Bingyang Zhang, Glenn Solomon, Jocelyn Plant, and Yoshihisa Yamamoto. Efficient source of single photons: A single quantum dot in a micropost microcavity. *Physical Review Letters*, 89(23):233602, Nov 2002.

[57] C. Schneider, M. StrauB, T. Sunner, A. Huggenberger, D. Wiener, S. Reitzenstein, M. Kamp, S. Hofling, and A. Forchel. Lithographic alignment to site-controlled quantum dots for device integration. *Applied Physics Letters*, 92(18):183101, 2008.

[58] P. Atkinson, M.B. Ward, S.P. Bremner, D. Anderson, T. Farrow, G.A.C. Jones, A.J. Shields, and D.A. Ritchie. Site control of inas quantum dot nucleation by ex situ electron-beam lithographic patterning of GaAs substrates. *Physica E: Low-dimensional Systems and Nanostructures*, 32(1-2):21–24, May 2006.

[59] Oliver Benson, Charles Santori, Matthew Pelton, and Yoshihisa Yamamoto. Regulated and entangled photons from a single quantum dot. *Physical Review Letters*, 84(11):2513–2516, Mar 2000.

[60] Alain Aspect, Philippe Grangier, and Gerard Roger. Experimental tests of realistic local theories via bell's theorem. *Physical Review Letters*, 47(7):460, 1981.

[61] M. Bayer, G. Ortner, O. Stern, A. Kuther, A. Gorbunov, A. Forchel, P. Hawrylak, S. Fafard, K. Hinzer, T. Reinecke, and et al. Fine structure of neutral and charged excitons in self-assembled in(ga)as/(al)gaas quantum dots. *Physical Review B*, 65(19):195315, May 2002.

[62] Mikael T. Bjork, Claes Thelander, Adam E. Hansen, Linus E. Jensen, Magnus W. Larsson, L. Reine Wallenberg, and Lars Samuelson. Few-electron quantum dots in nanowires. *Nano Letters*, 4(9):1621–1625, Sep 2004.

[63] Marcel A. Verheijen, George Immink, Thierry de Smet, Magnus T. Borgstrom, and Erik P. A. M. Bakkers. Growth kinetics of heterostructured gap-gaas nanowires. *Journal of the American Chemical Society*, 128(4):1353–1359, Feb 2006.

[64] S. De Franceschi, J. A. van Dam, E. P. A. M. Bakkers, L. F. Feiner, L. Gurevich, and L. P. Kouwenhoven. Single-electron tunneling in InP nanowires. *Applied Physics Letters*, 83(2):344, 2003.

[65] A. Fuhrer, C. Fasth, and L. Samuelson. Single electron pumping in inas nanowire double quantum dots. *Applied Physics Letters*, 91(5):052109, 2007.

[66] Dan Dalacu, Alicia Kam, D Guy Austing, Xiaohua Wu, Jean Lapointe, Geof C Aers, and Philip J Poole. Selective-area vapour-liquid-solid growth of inp nanowires. *Nanotechnology*, 20(39):395602, Sep 2009.

[67] M. Khoshnegar and A. H. Majedi. Single- and few-particle states in core-shell nanowire quantum dots. *Physical Review B*, 86(20), Nov 2012.

[68] Magnus T. Borgstrom, Valery Zwiller, Elisabeth Muller, and Atac Imamoglu. Optically bright quantum dots in single nanowires. *Nano Letters*, 5(7):1439–1443, Jul 2005.

[69] Ethan D. Minot, Freek Kelkensberg, Maarten van Kouwen, Jorden A. van Dam, Leo P. Kouwenhoven, Valery Zwiller, Magnus T. Borgstrom, Olaf Wunnicke, Marcel A. Verheijen, and Erik P. A. M. Bakkers. Single quantum dot nanowire LEDs. *Nano Letters*, 7(2):367–371, Feb 2007.

[70] M C Plante and R R LaPierre. Control of GaAs nanowire morphology and crystal structure. *Nanotechnology*, 19(49):495603, Dec 2008.

[71] Alexander Kley, Paolo Ruggerone, and Matthias Scheffler. Novel diffusion mechanism on the GaAs(001) surface: The role of adatom-dimer interaction. *Physical Review Letters*, 79(26):5278–5281, Dec 1997.

[72] M. Grundmann, O. Stier, and D. Bimberg. Inas/GaAs pyramidal quantum dots: Strain distribution, optical phonons, and electronic structure. *Physical Review B*, 52(16):11969–11981, Oct 1995.

[73] R. Seguin, A. Schliwa, S. Rodt, K. Potschke, U. Pohl, and D. Bimberg. Size-dependent fine-structure splitting in self-organized inas/GaAs quantum dots. *Physical Review Letters*, 95(25):257402, Dec 2005.

[74] L. K. Shalm, D. R. Hamel, Z. Yan, C. Simon, K. J. Resch, and T. Jennewein. Three-photon energy-time entanglement. *Nature Physics*, 9(1):19–22, Nov 2012.

[75] G R Liu and S S Quek Jerry. A finite element study of the stress and strain fields of inas quantum dots embedded in GaAs. *Semiconductor Science and Technology*, 17(6):630–643, Jun 2002.

[76] Thomas Bahder. Eight-band k.p model of strained zinc-blende crystals. *Physical Review B*, 41(17):11992–12001, Jun 1990.

[77] Craig Pryor. Eight-band calculations of strained inas/GaAs quantum dots compared with one-, four-, and six-band approximations. *Physical Review B*, 57(12):7190–7195, Mar 1998.

[78] Weidong Sheng, Shun-Jen Cheng, and Pawel Hawrylak. Multiband theory of multi-exciton complexes in self-assembled quantum dots. *Physical Review B*, 71(3):035316, Jan 2005.

[79] Shun Lien Chuang. *Physics of Photonic Devices (Wiley Series in Pure and Applied Optics)*. Wiley, 2009.

[80] Andrei Schliwa, Momme Winkelnkemper, Anatol Lochmann, Erik Stock, and Dieter Bimberg. In(ga)as/GaAs quantum dots grown on a (111) surface as ideal sources of entangled photon pairs. *Physical Review B*, 80(16):161307, Oct 2009.

[81] O. Gywat. *Spins in Optically Active Quantum Dots: Concepts and Methods*. Wiley-VCH, Weinheim, 2010.

[82] A. Bracker, E. Stinaff, D. Gammon, M. Ware, J. Tischler, A. Shabaev, Al. Efros, D. Park, D. Gershoni, V. Korenev, and et al. Optical pumping of the electronic and nuclear spin of single charge-tunable quantum dots. *Physical Review Letters*, 94(4), Feb 2005.

[83] T. Dietl, Awschalom D., Kaminska M., and Ohno H. *Spintronics, Volume 82 (Semiconductors and Semimetals)*. Academic Press, 2008.

[84] D. Bimberg. *Semiconductor Nanostructures(Nano-Science and Technology)*. Springer, Berlin, 2010.

[85] B. D. Gerardot, S. Seidl, P. A. Dalgarno, R. J. Warburton, D. Granados, J. M. Garcia, K. Kowalik, O. Krebs, K. Karrai, A. Badolato, and et al. Manipulating exciton fine structure in quantum dots with a lateral electric field. *Applied Physics Letters*, 90(4):041101, 2007.

[86] Garnett W. Bryant, Natalia Malkova, and James Sims. Mechanism for controlling the exciton fine structure in quantum dots using electric fields: Manipulation of exciton orientation and exchange splitting at the atomic scale. *Physical Review B*, 88(16):161301(R), Oct 2013.

[87] N. Skold, A. Boyer de la Giroday, A. J. Bennett, I. Farrer, D. A. Ritchie, and A. J. Shields. Electrical control of the exciton fine structure of a quantum dot molecule. *Physical Review Letters*, 110(1):016804, Jan 2013.

[88] Rinaldo Trotta, Eugenio Zallo, Elisabeth Magerl, Oliver G. Schmidt, and Armando Rastelli. Independent control of exciton and biexciton energies in single quantum dots via electroelastic fields. *Physical Review B*, 88(15):155312, Oct 2013.

[89] E. Blackwood, M. Snelling, R. Harley, S. Andrews, and C. Foxon. Exchange interaction of excitons in GaAs heterostructures. *Physical Review B*, 50(19):14246–14254, Nov 1994.

[90] M. Bayer, O. Stern, A. Kuther, and A. Forchel. Spectroscopic study of dark excitons in inxga1-xas self-assembled quantum dots by a magnetic-field-induced symmetry breaking. *Physical Review B*, 61(11):7273–7276, Mar 2000.

[91] J. Tischler, A. Bracker, D. Gammon, and D. Park. Fine structure of trions and excitons in single GaAs quantum dots. *Physical Review B*, 66(8):081310(R), Aug 2002.

[92] Rodney Loudon. *The Quantum Theory of Light (Oxford Science Publications)*. Oxford University Press, USA, 2000.

[93] Christopher Gerry and Peter Knight. *Introductory Quantum Optics*. Cambridge University Press, 2004.

[94] Charles Santori, David Fattal, Jelena Vuckovic, Glenn S Solomon, and Yoshihisa Yamamoto. Single-photon generation with inas quantum dots. *New Journal of Physics*, 6:89–89, Jan 2004.

[95] N. Akopian, N. Lindner, E. Poem, Y. Berlatzky, J. Avron, D. Gershoni, B. Gerardot, and P. Petroff. Entangled photon pairs from semiconductor quantum dots. *Physical Review Letters*, 96(13):130501, Apr 2006.

[96] R. Mark Stevenson, Andrew J. Hudson, Anthony J. Bennett, Robert J. Young, Christine A. Nicoll, David A. Ritchie, and Andrew J. Shields. Evolution of entanglement between distinguishable light states. *Physical Review Letters*, 101(17):170501, Oct 2008.

[97] A. J. Hudson, R. M. Stevenson, A. J. Bennett, R. J. Young, C. A. Nicoll, P. Atkinson, K. Cooper, D. A. Ritchie, and A. J. Shields. Coherence of an entangled exciton-photon state. *Physical Review Letters*, 99(26):266802, Dec 2007.

[98] Charles Santori, David Fattal, Matthew Pelton, Glenn S. Solomon, and Yoshihisa Yamamoto. Polarization-correlated photon pairs from a single quantum dot. *Physical Review B*, 66(4):045308, Jul 2002.

[99] S. M. Ulrich, S. Strauf, P. Michler, G. Bacher, and A. Forchel. Triggered polarization-correlated photon pairs from a single cdse quantum dot. *Applied Physics Letters*, 83(9):1848, 2003.

[100] Gabriel Bester, Xifan Wu, David Vanderbilt, and Alex Zunger. Importance of second-order piezoelectric effects in zinc-blende semiconductors. *Physical Review Letters*, 96(18):187602, May 2006.

[101] Michael E. Reimer, Marek Korkusinski, Jacques Lefebvre, Jean Lapointe, Philip J. Poole, Geof C. Aers, Dan Dalacu, W. Ross McKinnon, Simon Frederick, Pawel Hawrylak, and Robin L. Williams. Voltage induced hidden symmetry and photon entanglement generation in a single, site-selected quantum dot. 2007.

[102] J. Avron, G. Bisker, D. Gershoni, N. Lindner, E. Meirom, and R. Warburton. Entanglement on demand through time reordering. *Physical Review Letters*, 100(12):120501, Mar 2008.

[103] R. J. Young, R. M. Stevenson, A. J. Shields, P. Atkinson, K. Cooper, D. A. Ritchie, K. M. Groom, A. I. Tartakovskii, and M. S. Skolnick. Inversion of exciton level splitting in quantum dots. *Physical Review B*, 72(11):113305, Sep 2005.

[104] D. J. P. Ellis, R. M. Stevenson, R. J. Young, A. J. Shields, P. Atkinson, and D. A. Ritchie. Control of fine-structure splitting of individual inas quantum dots by rapid thermal annealing. *Applied Physics Letters*, 90(1):011907, 2007.

[105] Andrei Schliwa, Momme Winkelnkemper, and Dieter Bimberg. Impact of size, shape, and composition on piezoelectric effects and electronic properties of in(ga)as/gaas quantum dots. *Physical Review B*, 76(20):205324, Nov 2007.

[106] M. Reimer, M. Korkusiski, D. Dalacu, J. Lefebvre, J. Lapointe, P. Poole, G. Aers, W. McKinnon, P. Hawrylak, and R. Williams. Prepositioned single quantum dot in a lateral electric field. *Physical Review B*, 78(19):195301, Nov 2008.

[107] Mohsen Ghali, Keita Ohtani, Yuzo Ohno, and Hideo Ohno. Generation and control of polarization-entangled photons from GaAs island quantum dots by an electric field. *Nature Communications*, 3:661, Feb 2012.

[108] A. J. Bennett, M. A. Pooley, R. M. Stevenson, M. B. Ward, R. B. Patel, A. Boyer de la Giroday, N. Skld, I. Farrer, C. A. Nicoll, D. A. Ritchie, and et al. Electric-field-induced coherent coupling of the exciton states in a single quantum dot. *Nature Physics*, 6(12):947–950, Oct 2010.

[109] Ming Gong, Weiwei Zhang, Guang-Can Guo, and Lixin He. Exciton polarization, fine-structure splitting, and the asymmetry of quantum dots under uniaxial stress. *Physical Review Letters*, 106(22):227401, May 2011.

[110] Jianping Wang, Ming Gong, Guang-Can Guo, and Lixin He. Eliminating the fine structure splitting of excitons in self-assembled inas/GaAs quantum dots via combined stresses. *Applied Physics Letters*, 101(6):063114, 2012.

[111] F. Ding, R. Singh, J. D. Plumhof, T. Zander, V. Kpek, Y. H. Chen, M. Benyoucef, V. Zwiller, K. Drr, G. Bester, and et al. Tuning the exciton binding energies in single self-assembled InGaAs/GaAs quantum dots by piezoelectric-induced biaxial stress. *Physical Review Letters*, 104(6), Feb 2010.

[112] Stefan Seidl, Martin Kroner, Alexander Hogele, Khaled Karrai, Richard J. Warburton, Antonio Badolato, and Pierre M. Petroff. Effect of uniaxial stress on excitons in a self-assembled quantum dot. *Applied Physics Letters*, 88(20):203113, 2006.

[113] A. Mohan, M. Felici, P. Gallo, B. Dwir, A. Rudra, J. Faist, and E. Kapon. Polarization-entangled photons produced with high-symmetry site-controlled quantum dots. *Nature Photonics*, 4(5):302–306, Mar 2010.

[114] Robert J Young, R Mark Stevenson, Paola Atkinson, Ken Cooper, David A Ritchie, and Andrew J Shields. Improved fidelity of triggered entangled photons from single quantum dots. *New Journal of Physics*, 8(2):29–29, Feb 2006.

[115] Xin Yan, Xia Zhang, Xiaomin Ren, Hui Huang, Jingwei Guo, Xin Guo, Minjia Liu, Qi Wang, Shiwei Cai, and Yongqing Huang. Growth of inas quantum dots on GaAs nanowires by metal organic chemical vapor deposition. *Nano Letters*, 11(9):3941–3945, Sep 2011.

[116] Keitaro Ikejiri, Yusuke Kitauchi, Katsuhiro Tomioka, Junichi Motohisa, and Takashi Fukui. Zinc blende and wurtzite crystal phase mixing and transition in indium phosphide nanowires. *Nano Letters*, 11(10):4314–4318, Oct 2011.

[117] Maria Tchernycheva, George E. Cirlin, Gilles Patriarche, Laurent Travers, Valery Zwiller, Umberto Perinetti, and Jean-Christophe Harmand. Growth and characterization of InP nanowires with inasp insertions. *Nano Letters*, 7(6):1500–1504, Jun 2007.

[118] Hadas Shtrikman, Ronit Popovitz-Biro, Andrey Kretinin, and Moty Heiblum. Stacking-faults-free zinc blende GaAs nanowires. *Nano Letters*, 9(1):215–219, Jan 2009.

[119] U. Krishnamachari, M. Borgstrom, B. J. Ohlsson, N. Panev, L. Samuelson, W. Seifert, M. W. Larsson, and L. R. Wallenberg. Defect-free InP nanowires grown in [001] direction on InP (001). *Applied Physics Letters*, 85(11):2077, 2004.

[120] Maarten H. M. van Weert, Nika Akopian, Umberto Perinetti, Maarten P. van Kouwen, Rienk E. Algra, Marcel A. Verheijen, Erik P. A. M. Bakkers, Leo P. Kouwenhoven, and Val Zwiller. Selective excitation and detection of spin states in a single nanowire quantum dot. *Nano Letters*, 9(5):1989–1993, May 2009.

[121] Maarten P. van Kouwen, Michael E. Reimer, Anne W. Hidma, Maarten H. M. van Weert, Rienk E. Algra, Erik P. A. M. Bakkers, Leo P. Kouwenhoven, and Val Zwiller. Single electron charging in optically active nanowire quantum dots. *Nano Letters*, 10(5):1817–1822, May 2010.

[122] S. L. Altmann and P. Herzig. *Point-Group Theory Tables*. Clarendon Press, Oxford, 1994.

[123] A. D. Andreev, J. R. Downes, D. A. Faux, and E. P. O'Reilly. Strain distributions in quantum dots of arbitrary shape. *Journal of Applied Physics*, 86(1):297, 1999.

[124] S. Schulz, M. A. Caro, E. P. O'Reilly, and O. Marquardt. Symmetry-adapted calculations of strain and polarization fields in (111)-oriented zinc-blende quantum dots. *Physical Review B*, 84(12):125312, Sep 2011.

[125] O. Stier, M. Grundmann, and D. Bimberg. Electronic and optical properties of strained quantum dots modeled by 8-band k.p theory. *Physical Review B*, 59(8):5688–5701, Feb 1999.

[126] A. Williamson, L. Wang, and Alex Zunger. Theoretical interpretation of the experimental electronic structure of lens-shaped self-assembled inas/GaAs quantum dots. *Physical Review B*, 62(19):12963–12977, Nov 2000.

[127] Oliver Stier. *Electronic and Optical Properties of Quantum Dots and Wires, Berlin Studies in Solid State Physics*, volume 7. Wissenschaft und Technik Verlag, Berlin, 2001.

[128] S. L. Chuang. *Physics of Optoelectronic Devices*. Wiley-Interscience, New York, 1995.

[129] M. E. Pistol and C. Pryor. Band structure of segmented semiconductor nanowires. *Physical Review B*, 80(3), Jul 2009.

[130] I. Vurgaftman, J. R. Meyer, and L. R. Ram-Mohan. Band parameters for iii-v compound semiconductors and their alloys. *Journal of Applied Physics*, 89(11):5815, 2001.

[131] S. Raychaudhuri and E. T. Yu. Calculation of critical dimensions for wurtzite and cubic zinc blende coaxial nanowire heterostructures. *Journal of Vacuum Science & Technology B: Microelectronics and Nanometer Structures*, 24(4):2053, 2006.

[132] Karen L. Kavanagh, Igor Saveliev, Marina Blumin, Greg Swadener, and Harry E. Ruda. Faster radial strain relaxation in inas-gaas core-shell heterowires. *Journal of Applied Physics*, 111(4):044301, 2012.

[133] P. Harrison. *Quantum Wells, Wires and Dots: Theoretical and Computational Physics of Semiconductor Nanostructures*. Wiley-Interscience, New York, 2000.

[134] K. F. Karlsson, M. A. Dupertuis, D. Y. Oberli, E. Pelucchi, A. Rudra, P. O. Holtz, and E. Kapon. Fine structure of exciton complexes in high-symmetry quantum dots: Effects of symmetry breaking and symmetry elevation. *Physical Review B*, 81(16):161307, Apr 2010.

[135] R. Seguin, A. Schliwa, T. D. Germann, S. Rodt, K. Potschke, A. Strittmatter, U. W. Pohl, D. Bimberg, M. Winkelnkemper, T. Hammerschmidt, and et al. Control of fine-structure splitting and excitonic binding energies in selected individual inas/gaas quantum dots. *Applied Physics Letters*, 89(26):263109, 2006.

[136] H. van Kesteren, E. Cosman, W. van der Poel, and C. Foxon. Fine structure of excitons in type-ii GaAs/alas quantum wells. *Physical Review B*, 41(8):5283–5292, Mar 1990.

[137] F. Bras, P. Boucaud, S. Sauvage, G. Fishman, and J. M. Gerard. Temperature dependence of intersublevel absorption in inas/GaAs self-assembled quantum dots. *Applied Physics Letters*, 80(24):4620, 2002.

[138] K. F. Karlsson, V. Troncale, D. Y. Oberli, A. Malko, E. Pelucchi, A. Rudra, and E. Kapon. Optical polarization anisotropy and hole states in pyramidal quantum dots. *Applied Physics Letters*, 89(25):251113, 2006.

[139] Yann-Michel Niquet and Dulce Mojica. Quantum dots and tunnel barriers in inasinp nanowire heterostructures: Electronic and optical properties. *Physical Review B*, 77(11):115316, Mar 2008.

[140] R. S. Knox. *Theory of Excitons, Solid State Physics*. Academic Press, San Diego, 1963.

[141] A. Barenco and M. Dupertuis. Quantum many-body states of excitons in a small quantum dot. *Physical Review B*, 52(4):2766–2778, Jul 1995.

[142] Niklas Skold, Mats-Erik Pistol, Kimberly Dick, Craig Pryor, Jakob Wagner, Lisa Karlsson, and Lars Samuelson. Microphotoluminescence studies of tunable wurtzite inas0.85p0.15 quantum dots embedded in wurtzite InP nanowires. *Physical Review B*, 80(4):041312, Jul 2009.

[143] E. Tsitsishvili, R. Baltz, and H. Kalt. Exciton spin relaxation in single semiconductor quantum dots. *Physical Review B*, 67(20):205330, May 2003.

[144] E. Tsitsishvili, R. v. Baltz, and H. Kalt. Exciton-spin relaxation in quantum dots due to spin-orbit interaction. *Physical Review B*, 72(15):155333, Oct 2005.

[145] H. Sasakura, C. Hermannstdter, S. N. Dorenbos, N. Akopian, M. P. van Kouwen, J. Motohisa, Y. Kobayashi, H. Kumano, K. Kondo, K. Tomioka, and et al. Longitudinal and transverse exciton-spin relaxation in a single inasp quantum dot embedded

inside a standing InP nanowire using photoluminescence spectroscopy. *Physical Review B*, 85(7):075324, Feb 2012.

[146] Marek Korkusinski, Michael Reimer, Robin Williams, and Pawel Hawrylak. Engineering photon cascades from multiexciton complexes in a self-assembled quantum dot by a lateral electric field. *Physical Review B*, 79(3):035309, Jan 2009.

[147] J. Cirac, P. Zoller, H. Kimble, and H. Mabuchi. Quantum state transfer and entanglement distribution among distant nodes in a quantum network. *Physical Review Letters*, 78(16):3221–3224, Apr 1997.

[148] E. Moreau, I. Robert, L. Manin, V. Thierry-Mieg, J. Gerard, and I. Abram. Quantum cascade of photons in semiconductor quantum dots. *Physical Review Letters*, 87(18):183601, Oct 2001.

[149] R. Stevenson, R. Young, P. See, D. Gevaux, K. Cooper, P. Atkinson, I. Farrer, D. Ritchie, and A. Shields. Magnetic-field-induced reduction of the exciton polarization splitting in inas quantum dots. *Physical Review B*, 73(3), Jan 2006.

[150] M. Khoshnegar and A. H. Majedi. Entangled photon pair generation in hybrid superconductor-semiconductor quantum dot devices. *Physical Review B*, 84(10), Sep 2011.

[151] Ranber Singh and Gabriel Bester. Nanowire quantum dots as an ideal source of entangled photon pairs. *Physical Review Letters*, 103(6), Aug 2009.

[152] J. Persson, T. Aichele, V. Zwiller, L. Samuelson, and O. Benson. Three-photon cascade from single self-assembled InP quantum dots. *Physical Review B*, 69(23), Jun 2004.

[153] M. Scheibner, M. Doty, I. Ponomarev, A. Bracker, E. Stinaff, V. Korenev, T. Reinecke, and D. Gammon. Spin fine structure of optically excited quantum dot molecules. *Physical Review B*, 75(24):245318, Jun 2007.

[154] Andreas Fuhrer, Linus E. Froberg, Jonas Nyvold Pedersen, Magnus W. Larsson, Andreas Wacker, Mats-Erik Pistol, and Lars Samuelson. Few electron double quantum dots in inas/InP nanowire heterostructures. *Nano Letters*, 7(2):243–246, Feb 2007.

[155] A. S. Bracker, M. Scheibner, M. F. Doty, E. A. Stinaff, I. V. Ponomarev, J. C. Kim, L. J. Whitman, T. L. Reinecke, and D. Gammon. Engineering electron and hole tunneling with asymmetric inas quantum dot molecules. *Applied Physics Letters*, 89(23):233110, 2006.

[156] Gabriel Bester, J. Shumway, and Alex Zunger. Theory of excitonic spectra and entanglement engineering in dot molecules. *Physical Review Letters*, 93(4), Jul 2004.

[157] J. Climente, M. Korkusinski, G. Goldoni, and P. Hawrylak. Theory of valence-band holes as luttinger spinors in vertically coupled quantum dots. *Physical Review B*, 78(11), Sep 2008.

[158] E. A. Stinaff. Optical signatures of coupled quantum dots. *Science*, 311(5761):636–639, Feb 2006.

[159] M. Atature. Quantum-dot spin-state preparation with near-unity fidelity. *Science*, 312(5773):551–553, Apr 2006.

[160] A. Ramsay, S. Boyle, R. Kolodka, J. Oliveira, J. Skiba-Szymanska, H. Liu, M. Hopkinson, A. Fox, and M. Skolnick. Fast optical preparation, control, and readout of a single quantum dot spin. *Physical Review Letters*, 100(19), May 2008.

[161] S. Stufler, P. Machnikowski, P. Ester, M. Bichler, V. Axt, T. Kuhn, and A. Zrenner. Two-photon rabi oscillations in a single inxga1-xas/gaas quantum dot. *Physical Review B*, 73(12):125304, Mar 2006.

[162] David Press, Thaddeus D. Ladd, Bingyang Zhang, and Yoshihisa Yamamoto. Complete quantum control of a single quantum dot spin using ultrafast optical pulses. *Nature*, 456(7219):218–221, Nov 2008.

[163] Till Andlauer, Richard Morschl, and Peter Vogl. Gauge-invariant discretization in multiband envelope function theory and g factors in nanowire dots. *Physical Review B*, 78(7), Aug 2008.

[164] Serkan Ates, Imad Agha, Angelo Gulinatti, Ivan Rech, Matthew T. Rakher, Antonio Badolato, and Kartik Srinivasan. Two-photon interference using background-free quantum frequency conversion of single photons emitted by an inas quantum dot. *Physical Review Letters*, 109(14), Oct 2012.

[165] William K. Wootters. Entanglement of formation of an arbitrary state of two qubits. *Physical Review Letters*, 80(10):2245–2248, Mar 1998.

[166] W. A. Coish and J. M. Gambetta. Entangled photons on demand: Erasing which-path information with sidebands. *Physical Review B*, 80(24):241303(R), Dec 2009.

[167] Dik Bouwmeester, Jian-Wei Pan, Matthew Daniell, Harald Weinfurter, and Anton Zeilinger. Observation of three-photon greenberger-horne-zeilinger entanglement. *Physical Review Letters*, 82(7):1345–1349, Feb 1999.

[168] M. Doty, J. Climente, M. Korkusinski, M. Scheibner, A. Bracker, P. Hawrylak, and D. Gammon. Antibonding ground states in inas quantum-dot molecules. *Physical Review Letters*, 102(4):047401, Jan 2009.

[169] Hanz Y. Ramirez and Shun-Jen Cheng. Tunneling effects on fine-structure splitting in quantum-dot molecules. *Physical Review Letters*, 104(20):206402, May 2010.

[170] Jie Peng and Gabriel Bester. Charged excitons and biexcitons in laterally coupled (in,ga)as quantum dots. *Physical Review B*, 82(23):235314, Dec 2010.

[171] Xiaodong Xu, Yanwen Wu, Bo Sun, Qiong Huang, Jun Cheng, D. G. Steel, A. S. Bracker, D. Gammon, C. Emary, and L. J. Sham. Fast spin state initialization in a singly charged inas-GaAs quantum dot by optical cooling. *Physical Review Letters*, 99(9):097401, Aug 2007.

[172] Xiu-Hong Gao, Shao-Ming Fei, and Ke Wu. Lower bounds of concurrence for tripartite quantum systems. *Physical Review A*, 74(5):050303(R), Nov 2006.

[173] Kristiaan De Greve, Leo Yu, Peter L. McMahon, Jason S. Pelc, Chandra M. Natarajan, Na Young Kim, Eisuke Abe, Sebastian Maier, Christian Schneider, Martin Kamp, and et al. Quantum-dot spin-photon entanglement via frequency downconversion to telecom wavelength. *Nature*, 491(7424):421–425, Nov 2012.

[174] Dan Dalacu, Khaled Mnaymneh, Jean Lapointe, Xiaohua Wu, Philip J. Poole, Gabriele Bulgarini, Val Zwiller, and Michael E. Reimer. Ultraclean emission from inasp quantum dots in defect-free wurtzite InP nanowires. *Nano Letters*, 12(11):5919–5923, Nov 2012.

[175] P. Pathak and S. Hughes. Comment on "entanglement on demand through time reordering". *Physical Review Letters*, 103(4):048901, Jul 2009.

[176] Charles Santori, David Fattal, and Yoshihisa Yamamoto. *Single-photon Devices and Applications*. Wiley-VCH, 2010.

[177] Peter Michler. *Single Quantum Dots: Fundamentals, Applications and New Concepts (Topics in Applied Physics)*. Springer, 2003.

[178] Amnon Yariv and Pochi Yeh. *Photonics: Optical Electronics in Modern Communications (The Oxford Series in Electrical and Computer Engineering)*. Oxford University Press, USA, 2006.

[179] A J Standing, S Assali, J E M Haverkort, and E P A M Bakkers. High yield transfer of ordered nanowire arrays into transparent flexible polymer films. *Nanotechnology*, 23(49):495305, Dec 2012.

[180] A. Kapoor and G.S. Singh. Mode classification in cylindrical dielectric waveguides. *Journal of Lightwave Technology*, 18(6):849–852, Jun 2000.

[181] A. De and Craig E. Pryor. Predicted band structures of III-V semiconductors in the wurtzite phase. *Physical Review B*, 81(15):155210, Apr 2010.

[182] J. Wang. Highly polarized photoluminescence and photodetection from single indium phosphide nanowires. *Science*, 293(5534):1455–1457, Aug 2001.

[183] Lei Fang, Xianwei Zhao, Yi-Hsin Chiu, Dongkyun Ko, Kongara M. Reddy, Thomas R. Lemberger, Nitin P. Padture, Fengyuan Yang, and Ezekiel Johnston-Halperin. Comprehensive control of optical polarization anisotropy in semiconducting nanowires. *Applied Physics Letters*, 99(14):141101, 2011.

[184] R. Hanbury Brown and R. Q. Twiss. A test of a new type of stellar interferometer on sirius. *Nature*, 178(4541):1046–1048, Nov 1956.

[185] Charles Santori, Glenn Solomon, Matthew Pelton, and Yoshihisa Yamamoto. Time-resolved spectroscopy of multiexcitonic decay in an inas quantum dot. *Physical Review B*, 65(7):073310, Feb 2002.

[186] Daniel F. V. James, Paul G. Kwiat, William J. Munro, and Andrew G. White. Measurement of qubits. *Physical Review A*, 64(5):052312, Nov 2001.

[187] S C Ghosh, P Kruse, and R R LaPierre. The effect of GaAs(100) surface preparation on the growth of nanowires. *Nanotechnology*, 20(11):115602, Mar 2009.

[188] P. K. Pathak and S. Hughes. Coherent generation of time-bin entangled photon pairs using the biexciton cascade and cavity-assisted piecewise adiabatic passage. *Physical Review B*, 83(24):245301, Jun 2011.

[189] Xiangfeng Duan, Yu Huang, Yi Cui, Jianfang Wang, and Charles M. Lieber. A iiiv nanowire channel on silicon for high-performance vertical transistors. *Nature*, 409(6816):66–69, Jan 2001.